ABSTRACT

Title of Dissertation: EXPERIMENTAL AND NUMERICAL INVESTIGATION OF TANGENTIALLY-INJECTED SLOT FILM COOLING

Andrew P. Voegele, Doctor of Philosophy, 2013

Dissertation directed by: Associate Professor, Arnaud Trouvé
Department of Fire Protection Engineering
Associate Professor, André Marshall
Department of Fire Protection Engineering

Film cooling is a technique used in gas turbine engines, and blades and rocket nozzles to protect critical surfaces from the hot combustion gases. In film cooling applications, a relatively cool thin fluid is injected along surfaces and subsequently mix with the hot mainstream, thus leading to a reduction of protection at the wall. The breakdown of this film involves complex physics including intense turbulent mixing, heat transfer, conduction, radiation and variable density effects to name a few.

In this dissertation, film cooling is both experimentally measured and numerically simulated. The experiments feature non-intrusive Particle Image Velocimetry to provide two-dimensional planes of mean and fluctuating velocity, which are critical in order to characterize and understand the turbulent flow phenomena involved in film cooling. Additionally, through the use of micro-thermocouples, the thermal flow fields and wall temperatures are non-intrusively measured, with very small radiative errors. The film cooling flows are experimentally varied to cover a variety of breakdown regimes for both adiabatic (or idealized walls with no heat loss) and non-adiabatic walls (or walls with a

carefully controlled heat loss through them). The subsequent experimental dataset is a unique and comprehensive set of turbulent measurements characterizing and demonstrating the film breakdown and the turbulent flow physics.

The experiments are then numerically simulated using an in-house variable density, Large Eddy Simulation (LES) Computational Fluid Dynamics (CFD) code developed as part of this dissertation. In addition to accurately predicting important turbulent kinematic and thermal flow phenomena, the key wall parameters were predicted to within 3% for the adiabatic cases and to within 6% for the non-adiabatic cases, with a few exceptions. Turbulent inflow techniques, crucial for the success of LES of film cooling, are examined. In addition to the turbulent flow physics, radiation and conduction physics at the wall were also simulated with good fidelity. The combined experimental and numerical approach was used to uniquely form a comprehensive study, examining many aspects of film cooling phenomena relevant for engineering applications.

EXPERIMENTAL AND NUMERICAL INVESTIGATION OF TANGENTIALLY-INJECTED SLOT FILM COOLING

by

Andrew P. Voegele

Dissertation submitted to the Faculty of the Graduate School of the
University of Maryland, College Park, in partial fulfillment
of the requirements for the degree of
Doctor of Philosophy
2013

Advisory Committee:

Associate Professor Arnaud Trouvé, Co-Chair
Associate Professor André Marshall, Co-Chair
Associate Professor Christopher Cadou
Associate Professor Kenneth Yu
Professor Doron Levy, Dean's Representative

Dedication

I dedicate this work to my family: my mom, my dad, my grandmother, my two sisters: Alex and Coco and my young niece: Joey. I can describe myself in a variety of ways; but at the foundation, the core, is always my family.

Acknowledgements

This work had been sponsored by NASA's Constellation University Institutes Project (CUIP). Appreciation is expressed to Claudia Meyer of the NASA Glenn Research Center, program manager of the University Institute activity. A special thanks is given to Joe Ruf, Kevin Tucker and Chris Morris at NASA Marshall Space Flight Center for their help and insight for this work. A special thanks is owed to Joe Ruf, in particular, who mentored me during my time at NASA Marshall and encouraged me to expose myself to many of the projects while there. Additionally, much of the numerical work in this dissertation used the Extreme Science and Engineering Discovery Environment (XSEDE), which is supported by National Science Foundation grant number OCI-1053575.

I also need to thank my advisors Dr. Marshall and Dr. Trouvé. Dr. Marshall truly has been supportive, patient and engaging throughout the course of my dissertation, often extending meetings to develop my critical reasoning and help develop physical insight into problems. Dr. Trouvé also was incredibly supportive and essentially taught me ways of analyzing and understanding CFD problems, including the development of physical and numerical insight into the physics of turbulent flows. I would also like to thank Dr. Cadou who helped find support for me in the final phases of my dissertation, allowed me to co-teach a class with him providing excellent teaching suggestions and also for being available to discuss and aide my specific research. Finally I also owe gratitude to my other committee members Dr. Yu and Dr. Levy.

They say it takes a village to raise a child; frankly I think it takes a village to earn a PhD as well. I cannot express enough appreciation for my colleague and friend, Fernando Raffan, without him much this research would not be possible. He really almost mentored me in the beginning of my time here, which eventually turned into more collaborative relationship. I truly appreciate his support and willingness to discuss not only research but also any problems I may have. Similarly I'd like to thank my lunch buddies, Camilo Aguilera, Dan Waters and John Alexis Guerra Gomez, who have provided entertaining bright spots in my day, even when I was struggling through my research. Thank you to all my aerospace and soccer buddies. I also owe debts of gratitude to Luis Bravo for his help in developing LES BLAC and to Carlos Cruz, whom I have actually never met, but who generated a lot of the groundwork for my PhD topic. I'd like to thank current and former members of my lab: Kiran Dellimore, Daanish Maqbool, Anand, Shyam Menon, Jeff St. Clair and Matt Collett. Also I want to acknowlege my CFD group: Vivien Lecoustre, Sebastian Vilfayeau, Zohreh Ghorbani, Ben Trettel, Praveen Narayanan, Christine Pongratz, Salman Verma, Ayodeji Ojofeitimi, Arthur Piquet and probably a few more.

I truly cannot state the importance of my friends and family in helping me finish this PhD. All of my friends from UVA: Mark, Lauren, Kenzie, Jessica, Ben T., Kara, Tony, Brian, Matt, Ben W., Tudor, Bevin, Kacee and Abby, were supportive and always there if I needed to see a friendly face. I especially would like to thank David and Becky, who are like family to me, and were truly there for

all of my triumphs, failures, joys and heartaches. I could not ask for better and more loyal friends; words cannot express the gratitude I have for them.

Speaking of family, I definitely need to thank my mom and dad, my step-mom, my brother-in-law, my two sisters: Alex and Coco, and my grandmother, who not only provided unwavering support and encouragement, but also were the ones to develop my love for knowledge, which led to me wanting to get a PhD in the first place. I truly do not know who, what or where I would be without their presences in my life. Finally I'd like to thank God, for giving me love, patience, support and enlightenment during both the fun and trying times.

Table of Contents

List of Tables

List of Figures

Nomenclature

α ……thermal diffusivity
δ ……..change, differencing operator or Kroenecker delta
Δ ……change or spacing
γ ……ratio of specific heats
η ……effectiveness
μ ……..dynamic viscosity
λ ……wavelength
ρ ……density
θ ……...non-dimensional temperature or angle
φ ……scalar quantity
σ ……Stefan-Boltzmann constant
τ ……..time scale or shear stress tensor
ν ……kinematic viscosity
ω ……..chemical source term
A ……area
B ……heat flux coefficient
BR ……blowing ratio
c ……..wave speed
c_p ……specific heat capacity
C_m .....mixing coefficient
d ……...diameter
D ……..diameter
FDTC ……..fully developed turbulent channel
FPS ……flat plate simulation
f ……function or mixture fraction
$f^{\#}$ ……..f stop number
G ……filter
h ……..convection coefficient or enthalpy
I ……...intensity
k ……...thermal conductivity
KE ……..kinetic energy
L ……Leonard's Stress or Length
m ……mass or path length
M ……magnification or Mach Number
MS ……minimum shear
Nu ……Nusselt Number
p ……...pressure
P ……...pressure
Pr ……Prandtl Number
Q ……heat or thermal energy
q ……..heat flux or subgrid-scale heat flux vector
R ……radius or Reynolds stress
Re ……..Reynolds number

RHS ……...right hand side
r ……mass flux vector or radius
s ……slot height
S ……..strain rate tensor
t ……thickness of splitter plate, or test plate, time or subgrid scale stress tensor
tke ……...turbulent kinetic energy
T ……temperature
TR ……..temperature ratio
u or U ……...streamwise component of velocity or velocity
v ……wall-normal component of velocity
V ……...velocity magnitude or vertical component of velocity
VF ……...view factor
VR ……velocity ratio
WJ ……wall jet
WW ……...wall wake
w ……spanwise component of velocity
x ……streamwise coordinate
y ……...wall-normal coordinate
z ……spanwise coordinate

Superscripts

. ……rate
`` ……flux
→ ……vector
` ……....fluctuating component
~ ……favre-averaged
- ……..averaged or filtered
n ……time step number
it ……..iteration number
* ……non-dimensional or sub-variable
+ ……wall units

Subscripts

AD …….....adiabatic
air ……..air
avg ……average
aw ……adiabatic wall
b ……bead
back ……backside
casing ……..casing
c ……coolant
conduction ……...conduction
constant ……constant
CL ……center line
e ……..approximate image
f ……..fluid

g ……...gas
k ……kolmogorov
L ……laminar
min ……minimum
max,allowable ……..maximum allowable
max ……...maximum
p ……particle
q ……heat flux component
radiation ……..radiation
RMS ……root-mean squared
slot ……...slot condition
solid ……occurring in the solid
surr ……...surroundings
SS ……stainless steel
sgs ……...sub-grid scale
t ……turbulent sub-grid scale
τ ……frictional scale
total ……total
testplate ……...test plate
X ……..x-component
uv ……...stream-wise, wall-normal component
v ……viscous
wall ……wall
w ……wall
xy ……x and y component
Y ……...y-component
Z ……...z-component
0 ……...integral scale
∞ ……mainstream

1. Introduction

Long distance, expedient travel became possible with the advent of modern airplanes. As aircraft become increasingly complex, coupled with the rising cost of fuel, increasing airline expenses will be passed on to travelers. From 2000 to 2011, the total annual consumption of fuel by U.S.-based airlines dropped from 19.026 to 16.385 billion gallons [1]. The cost of this fuel, however, more than tripled over the same span increasing from 15.198 billion dollars to 46.881 billion dollars [1]. As their expenses keep increasing, airline companies need their aircraft to become as efficient as possible. One major source of inefficiency is the propulsion cooling system. Lefebvre [2] estimates that about 1/3 of the gas turbine air intake is used on engine cooling, which results in no net propulsion, meaning this cooling air does not propel the aircraft.

Space travel has also become possible in recent history with human-rated spacecraft, featuring large multiple stage rockets. A rule of thumb is that it takes about $10,000 to put one pound of payload into low earth orbit [3]. So in order to put a single human into orbit requires over $1,000,000. In rocket engines, both the fuel and oxidizer are carried on board, so any cooling apparatus or coolant is extra weight, which greatly increases space transportation costs.

In order to mitigate these cooling losses, many studies have investigated different methods of cooling their engines. These techniques allow the engine, both gas turbines and rockets, to operate at temperatures well above the failure temperatures of the wall material used in these engines. Generally, the higher the temperature of the working gas, the more work that can be extracted and converted into propulsion. Stated another way, the higher the thermal energy of the propellant, the more energy there is to be converted

into kinetic energy, which will propel the aircraft. To give an idea of the temperature scale, the typical combustor temperature of a gas turbine engine is nominally 2280 K [2], while rocket engines feature combustor temperatures in the range of 2700 to 3400 K [4].

1.1 Film Cooling Problem

One cooling technique used in both rockets and gas turbines is called film cooling. Film cooling involves the injection of a relatively cool gas along critical surfaces, creating an insulating layer that protects the wall from the hot combustion exhaust. In rocket applications, the fuel-rich exhaust, exiting the gas generators that run the fuel pumps, is fed into coolant manifolds, where it is injected along the walls of the nozzle and combustion chamber. In jet engines, the coolant is actually bypass air that is captured at the intake and is fed into cooling plenums before being injected onto the turbine blades or along the combustor liner. Schematics of both the gas turbine engine combustor liner and the rocket film cooling application are seen in Figures 1 and 2, respectively.

Film cooling involves the mixing between two highly turbulent streams, in the presence of intense heat transfer, radiation, large pressure gradients and combustion in

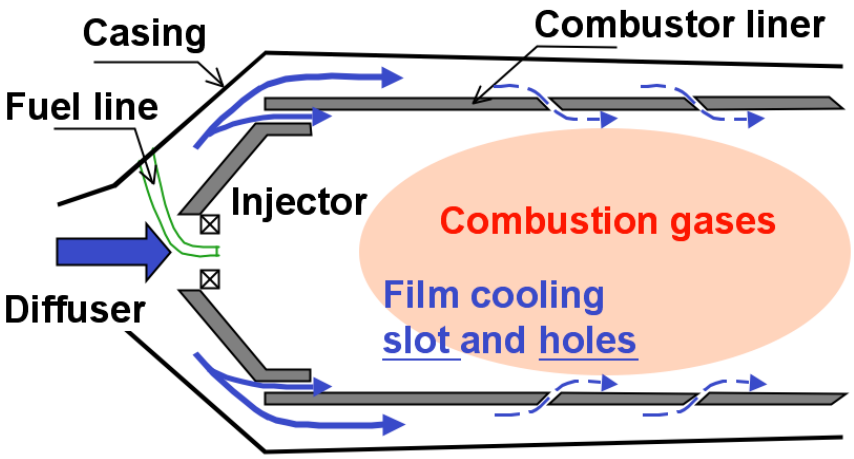

Figure 1- Schematic of film cooling in gas turbine combustor. Image adapted from Raffan [5].

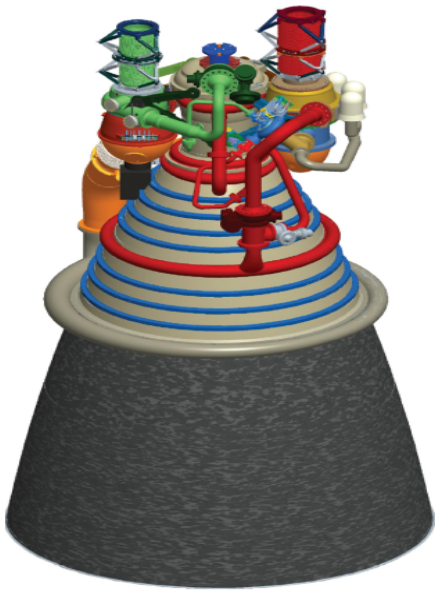

Figure 2- Schematic of a rocket using film cooling. Rendering of the J-2X engine, featuring film cooling along the nozzle extension [6]. Public Image adapted from NASA [6].

the vicinity of walls. As the two streams mix, the flow properties rapidly change, which makes many of the common constant property assumptions used in engineering analysis invalid. Due to the complex mixing dynamics involved, film cooling has been a problem of numerous research studies all focused on understanding and modeling these flows.

1.2 Film Cooling Set-up and Basics

A canonical film cooling configuration is shown in Figure 3. Notice this configuration features tangentially-injected slot film cooling, as opposed to film cooling via holes or inclined slots. Hole film cooling is most commonly seen in gas turbine engines along the turbine blades. In this study, canonical slot film cooling will be explored because this configuration allows an array of physics to be studied that are more

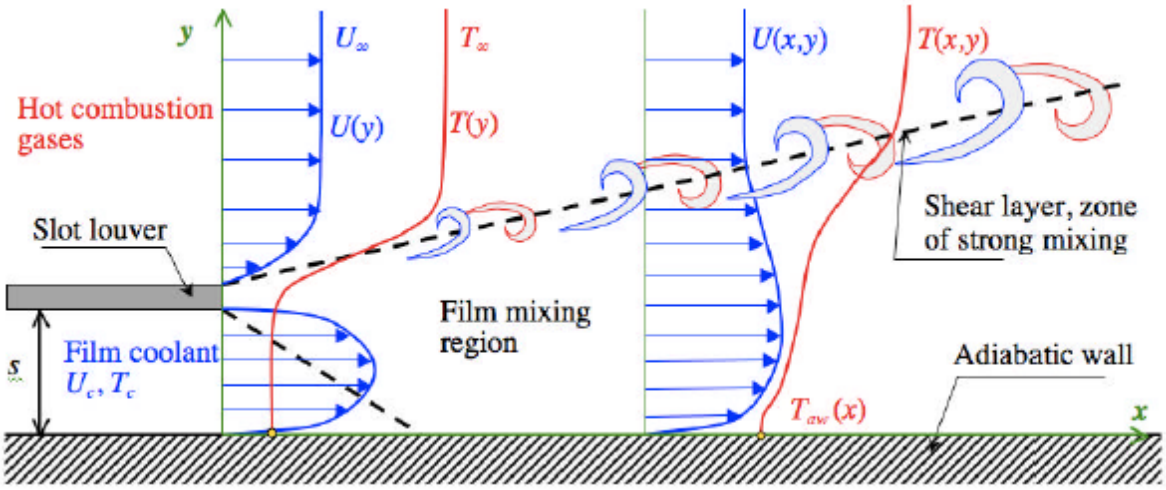

Figure 3- Canonical slot film cooling configuration. Image adapted from Cruz [7].

generally applicable across a range of practical applications. This flexibility is in contrast with film cooling via hole geometries, where a variety of 3-D geometry-dependent, flow effects become immediately apparent and dominate the mixing between the film and mainstream. The additional mixing mechanisms make it difficult to extract information that is relevant to general engineering flows and not a specific configuration.

In the canonical configuration (Figure 3), a splitter plate separates the hot mainstream combustion gases from the film coolant. The film coolant is injected along a critical surface to protect it from the hot gases. Once injected, the coolant begins to mix with the mainstream, thus heating up and affording less protection for the wall. The job of propulsion engineers is to ensure that enough coolant is injected to keep the wall temperature below critical material limits. The film mixing region is driven by turbulent shear existing between the coolant and hot mainstream. Shear layer vorticies form due to Kelvin-Helmholtz instabilities causing bulk fluid mixing, substantially enhancing overall mixing.

The major parameters used to characterize film cooling flows are the temperature ratio, the velocity ratio, the blowing ratio, the turbulence levels in the two streams and the Reynold's number of the two streams. The definitions for the temperature, velocity and blowing ratios are seen in Eqns. 1-3, respectively, while the coolant Reynolds number is given in Eqn. 4. It should be noted, the mach numbers (not shown here) of the two streams can become important in compressible environments, and will significantly alter the shear physics of the two streams.

$$TR = \frac{T_\infty}{T_C} \qquad \text{Eq. (1)}$$

$$VR = \frac{V_C}{V_\infty} \qquad \text{Eq. (2)}$$

$$BR = \frac{\rho_C V_C}{\rho_\infty V_\infty} \qquad \text{Eq. (3)}$$

$$\mathrm{Re}_C = \frac{\rho_C V_C s}{\mu_C} \qquad \text{Eq. (4)}$$

The blowing ratio, temperature ratio and velocity ratio are all somewhat coupled, but each parameter is a characteristic quantity of different film cooling processes. The velocity ratio describes the shear existing between the coolant and mainstream. Three different shear regimes exist in slot film cooling applications. A wall wake, minimum shear and wall jet film cooling problems have velocity ratios of less than unity, approximately unity and greater than unity, respectively. Each of these shear regimes have characteristic structures that determine the way the film mixes and breaks down. The wall wake, where the mainstream is moving faster than the coolant, develops turbulent shear structures with a clockwise orientation when using the reference frame

provided in Figure 3. The wall jet, where the coolant moves faster than the mainstream, develops shear structures with a counter-clockwise orientation. Lastly the minimum shear has no preferred orientation, meaning it will have both counter-clockwise and clockwise shear structures. In the minimum shear case the two characteristic speeds are approximately the same. Consequently, this regime has the least amount of shear. The spreading, driven by shear, therefore occurs more slowly for a minimum shear scenario than for a wall wake or wall jet, which have relatively higher shear.

The blowing ratio, meanwhile, determines the mixing layer orientation. The blowing ratio is a ratio of mass fluxes and gives information about the momentum of the flow. Blowing ratios that are greater than one correspond to scenarios where the coolant has a higher mass flux than the mainstream and therefore will in a mean sense spread into the mainstream. Conversely, film cooling with blowing ratios less than one will have mean preferential spreading towards the wall, or stated differently the mixing layer will be oriented towards the wall. Lastly blowing ratios of approximately unity will have a relatively symmetric spread. The blowing ratio implicitly carries with it information about the density ratio between the two streams, which is important when intense heat transfer occurs or when the coolant and mainstreams are different gases.

The temperature ratio governs not only the density ratio for single species mixing but also governs the amount of heat transfer occurring. Since heat transfer is proportional to a temperature difference, the temperature ratio gives an idea of the strength of the heat transfer. The larger the temperature ratio generally means the larger the heat transfer. As will be discussed later, the density ratio also plays a role in film cooling mixing.

The slot Reynold's number in some senses characterizes the turbulence existing at the slot exit. The turbulence at the slot exit in turn governs the mixing in the near injector region close to the wall. If this Reynold's number is very high, the mixing will occur more vigorously than for less turbulent cases. While there are many other important parameters governing the film mixing, as will be described later, the parameters summarized above are the most fundamental and the most often used to characterize film cooling studies.

The adiabatic wall effectiveness, shown in Equation 5, is the quantity of interest in most film cooling research studies. In engineering applications, the wall temperature needs to be kept below material limits. The adiabatic wall effectiveness is a non-dimensional wall temperature in the presence of no wall heat transfer. It can be thought of as an efficiency describing how well the coolant is protecting the wall. When the adiabatic wall effectiveness is one, the film is perfectly protecting the wall. By contrast, when it is zero, the film no longer affords the wall any protection from the hot combustions gases. Similarly the flow effectiveness, reproduced below in Equation 6, gives a description for how well mixed the flow is at a given spatial location.

$$\eta_{ad} = \frac{\left(T_\infty - T_{ad,W}\right)}{\left(T_\infty - T_C\right)} \qquad \text{Eq. (5)}$$

$$\eta = \frac{\left(T_\infty - T\right)}{\left(T_\infty - T_C\right)} \qquad \text{Eq. (6)}$$

It should be noted that normally in research studies radiation is ignored because the film mixing is most often dominated by the turbulent convective mixing due to shear between the mainstream and film. The non-linear nature of radiation makes it difficult to predict.

Therefore, temperatures regimes are often selected to isolate turbulent mixing from radiative effects.

In most research studies, adiabatic wall boundary conditions are most often explored because heat transfer effects through the wall, which are heavily configuration and application specific, are not present. In real-world applications, some sort of backside-cooling is almost always used which further cools the wall temperature past the adiabatic wall temperature, thus further protecting the wall. However, unless the backside heating is very large, the wall protection remains largely governed by the film mixing with the mainstream, which is more easily explored in the adiabatic cases. The adiabatic cases are, therefore, more generalizable and representative of all film cooling cases. Adiabatic cases are also useful because they effectively define the worst case film cooling conditions, without involving the complications of modeling or measuring the solid conductive heat transfer. Lastly, most film cooling heat transfer correlations feature use of the local adiabatic wall temperature as opposed to the coolant temperature because this temperature is a good reference temperature for the actual local heat transfer through the wall. The wall heat flux is often written as the product of the convection coefficient and the difference between the actual wall temperature and the adiabatic wall temperature as is seen below in Equation 7.

$$q_w'' = h\left(T_W - T_{ad,W}\right) \qquad \text{Eq. (7)}$$

1.3 Review of Experimental Work

1.3.1 Experimental and Modeling Work

In this section, a review of the existing experimental and modeling work will be given to provide perspective for the current film cooling research. The focus of the review will be on important mixing mechanisms or characteristics governing film cooling decay. Also fundamental and historical studies will be summarized to give context for the work that followed.

1.3.1.1 Wieghardt experiments & models

Wieghardt [8] performed one of the seminal film cooling studies in which he established much of the film cooling scaling that is still used today. Wieghardt studied film heating for de-icing applications on aircraft. While the direction of heat transfer is reversed, film heating is analogous to film cooling because the turbulent mixing processes are similar; meaning experimental trends of both film cooling and film heating will collapse when proper non-dimensionalization is used. Wieghardt's experimental study featured slot film heating, with an injection angle of about 30 degrees relative to the mainstream flow over a variety of blowing ratios.

One of Wieghardt's main findings was that the temperature profiles downstream were nearly self-similar, when based on the local adiabatic wall temperature. His semi-empirical approach established a non-dimensional, self-similar temperature, which is primarily a function of the wall-normal direction, y. The form of the function is based on an energy balance and boundary layer assumptions with an assumed turbulent, power law velocity field. The specific coefficient in the exponent was selected to provide a good fit with his experimental results. Wieghardt's expression is reproduced below in Equation 8.

$$\theta = \frac{T - T_\infty}{T_{ad,W} - T_\infty} \approx e^{-0.768\left(\frac{y}{\delta_T}\right)^{\frac{13}{6}}}$$ Eq. (8)

Here T, T_∞, $T_{ad,W}$ refer to the flow, mainstream and adiabatic wall temperature, respectively, while δ_T is the thermal thickness, which *is* a function of downstream distance. The similarity regions normally apply only far downstream of injection because the inlet is characterized by rapid streamwise variations that are not present in the far-injection field. These rapid streamwise gradients make boundary layer assumptions untenable. The definition of δ_T is seen in Equation 9 and has a form similar to the more traditional enthalpy thickness. For film cooling, Weidghardt's non-dimensionalized temperature needs to be slightly recast and is called the flow effectiveness. The adiabatic wall effectiveness and the flow effectiveness, already given in Equation 5 and 6, respectively, describe the effectiveness at the wall and in the flow. To summarize, Wieghardt [9] assumed: 1). the film cooling flow resembles a boundary layer, 2). viscous dissipation is negligible, 3). the thermal heat conductivity is only a function of x, 4). all other constant property assumptions are valid (Cp, μ, etc.), 5). the eddy heat conductivity is much larger than the molecular heat conductivity, 6). the flow is similar, 7). the velocity follows a power law distribution [8-9]. While not true, these assumptions allow film cooling analysis to become more tractable.

$$\delta_T = \int_0^\infty \left(\frac{T - T_\infty}{T_{ad,W} - T_\infty} \right) dy = \int_0^\infty \theta dy$$ Eq. (9)

Tribus and Klein [11] used Wieghardt's scaling coupled with a simplified analytical boundary layer solution to generate a semi-empirical equation for the adiabatic effectiveness based on the slot Reynold's number, the blowing ratio and the non-

dimensional axial distance based on slot height. Tribus and Klein's expression for Wieghardt's non-dimensionalized wall temperature is given as

$$\theta_W = c_1 \mathrm{Re}_C^{0.2} \left(\frac{x}{BR \cdot s} \right)^{-0.8} \qquad \text{Eq. (10)}$$

where c1 was selected as 4.62 so as to fit Wieghardt's data best. This modeling approach identifies the coolant Reynolds number, the blowing ratio, the streamwise distance and the slot height as critical parameters determing the wall temperature profile. The form of this approach is the basis for many future modeling research studies.

Hartnett et al. [12] measured several film cooling wall wake flows using the same injection configuration as Wieghardt. The study provided velocity profiles and temperature profiles at several streamwise locations downstream of injection. Hartnett et al. then used the form of the equation generated by Tribus and Klein [11] on their experimental data to develop a slightly different adiabatic wall effectiveness correlation by selecting a different value of c_1. For these wake flows, Wieghardt's scaling collapsed the data well for (x / BR / s) > 60. In addition to these correlations, Hartnett et al. modified their own correlation to incorporate the Prandtl number.

Stollery and El-Ehwany [9-10] used a simple energy and mass balance, along with the key assumption that the boundary layer thickness grows proportional to Reynolds number based on the streamwise distance to the negative one-fifth power (a flat plate Blasius assumption). In this study, the authors provide the same boundary layer model expression as the other previous analyses but the assumptions and approach are much simpler. An added benefit of this approach is that the analysis still holds true for velocity ratios greater than unity, which was not previously true. Stollery and El-Ehwany also postulated that three distinct regimes exist in terms of the experimental development of

the flow: 1. Initial region, 2. Wall jet region (existing for BR > 1), 3. Boundary layer region (very far away from injection). This separation of regions is the basis for film cooling zonal models that will be discussed briefly in the subsequent section

1.3.1.2 Other film cooling models

Hatch and Papell [13] developed a semi-empirical film cooling correlation that accounts for variable-density flows, including different gas species, over a wide temperature and velocity range. The correlation contains coolant flow rate instead of a blowing ratio and was developed for tangential injections using a simple heat balance. The purpose of using mass flow rates instead of blowing ratio was to make the correlation more general for a wide range of mainstream temperatures, velocities and gas species. The previous correlations were deemed to be too specific to accurately model their experimental data. In their analysis, the coolant was seen as its own discrete layer, with assumptions that temperature gradients in the coolant and in the streamwise directions were small. The authors were able to generate an exponential expression featuring the convective heat transfer coefficient, the length of the plate, the cooling flow rate, the coolant heat capacity and a variable x' that depends on several more flow properties. Their correlation reproduced their own experiments within 5 % of the observed temperatures for both helium and air coolants.

After the findings of Hatch and Papell [13] that previous correlations were too specific, Papell and Trout [14], and Papell [15] developed a series of empirical relationships based on their own wide range of experimental data for the effectiveness from tangential film injections and later from inclined injections. They identified important design parameters, such as the non-dimensional downstream distance based on

the slot height, the temperature ratio and the blowing ratio. Then they created an empirical power law relationship using these parameters. No attempt was made here to develop a theoretical model, but their hope was to study a large variable space to make their correlations useful to designers. They explored a range of different mainstream mach numbers, slot heights, blowing ratios and temperature ratios.

Ballal and Lefebvre [16] suggested two changes to the previous boundary layer correlations of Stollery and El-Alwhany [9-10]. First they used experimental data to estimate values of the skin friction coefficients, which in previous studies were based on Blasius scaling. The skin friction estimate helped provide better predictions of the adiabatic wall effectiveness, especially within 40 slot heights of injection. Next by emprically changing the exponent of the Reynold's number, their correlation further improved the effectiveness performance compared to the experimental data they were using (especially for blowing ratios that imply moderate wall wake or minimum shear cases). Lastly, the authors proposed a jet model for larger velocity ratios based on a mass balance featuring a different form of the effectiveness correlation. Using experimental data to find new empirical coefficients, this new correlation gave better performing effectiveness results for jets flows than previous correlations.

Simon [17] developed a zonal model approach for wall jet flows that included the turbulence intensity, velocity ratio and temperature ratio. The zonal approach divides the film cooling domain into two distinct regions: the fully mixed region and the potential core region. The boundary between these two regions is the lower extent of the shear mixing layer that develops between the mainstream and coolant. In the potential core region, the flow is comprised primarily of unmixed coolant, resulting in different trends

than in the fully mixed region, where the coolant and mainstream are mixing in a mean sense. In each of these regions, the relative importance of the turbulence intensity of the coolant and mainstream greatly varies. Futhermore, Simon used the experimental values of Marek and Tacina [18] to get a different form of C_m (a turbulent mixing coefficient used in effectiveness correlations that will be discussed later), with different power relations and coefficients incorporating turbulence intensity. The Simon model estimated the effectiveness to within 4% of the studies examined, a marked improvement over the approximate 30% spread of previous modeling attempts.

1.3.1.3 Additional Findings and Film Cooling Effects

Hartnett et al. [12] in 1961 also studied non-adiabatic film cooling flows. In this study, they showed that the turbulent heat transfer correlations will work for film cooling arrangements especially far downstream, if the adiabatic wall temperature and not the coolant temperature is used as the reference temperature, as is shown in Equation 7. This finding was originally postulated by Sceza [19].

Goldstein [20] also presented the heat transfer equation shown in Equation 7. The form of this equation is particularly useful, he explains, because when the surface is perfectly insulated (adiabatic), the heat transfer equation will predict zero wall heat transfer. Goldstein goes on to state that the adiabatic wall temperature is more important and harder to predict than the convective heat transfer coefficient, which is often close to the value without a film. This statement highlights why the adiabatic wall temperature is the focus of most film cooling studies. Lastly, Goldstein points out that in the absence of backside cooling the adiabatic wall temperature is the minimum possible temperature in the film cooling system because radiation effects cause the wall temperature to increase.

1.3.1.4 Geometric Effects

Burns and Stollery [21], and Kacker and Whitelaw [22] experimentally explored the effect of the louver lip thickness over a range of velocity ratios and showed that the film performance deteriorated with increasing louver lip thicknesses, regardless of blowing ratio or downstream distance. Further, Burns and Stollery stated that boundary layer correlation models need to incorporate this louver lip thickness, especially when the louver lip thickness becomes large [21]. With thicker louver lips, the wake region behind the lip becomes larger meaning the turbulent mixing will also increase. This increase in mixing causes the enhanced degradation of the film. In addition to their louver thickness parametric studies, Burns and Stollery [21] also confirmed that the boundary layer model is not appropriate for distances less than 100 slot heights from injection due to axial gradients and non-equilibrium mixing.

1.3.1.5 Compressibility, Variable Density Effects

Burns and Stollery [21] were one of the first to explore the effect of using a foreign gas as a coolant (a coolant gas that is different from the mainstream gas); in their case studying both an argon mixture and helium. Rocket cooling applications often feature the use of fuel-rich exhaust gas that acts as a film coolant in the rocket nozzle. Therefore film cooling with multiple gas species is representative of the film cooling conditions for rocket engineering applications. Arctan-12 and Helium were the coolants injected into air. They found that helium, the least dense coolant in this study, provided the worst effectiveness results for a given velocity ratio. Stated differently, the greater mass flux of the coolant the better the film cooling performance at a non-dimensional downstream distance based only on slot height. The effectiveness measurement was based on a heat

and mass transfer analogy, where the mass concentration was measured and converted into an analogous adiabatic wall effectiveness. This equivalent effectiveness is often called the impervious effectiveness in the literature.

Also, the authors [21] explored the effect of the mainstream boundary layer thickness. Two mainstream boundary layers were created using different wire trips in the thin louver geometry with a velocity ratio of approximately unity. These boundary layers were explored for three different density ratios. In the near-injector field for the smallest coolant to mainstream density ratio, the effectiveness of the smaller mainstream boundary layer case was much higher than that of the thick mainstream boundary layer. Conversely, for an intermediate value of the density ratio the reverse trend was observed. For the largest density ratio, little separation between the thick and thin mainstream boundary layers was observed. Burns and Stollery concluded that the influence of mainstream boundary layer thickness is minor but can be important for low values of density ratio due to a relative momentum deficit in the boundary layer compared to the momentum of the coolant.

Similar to Burns and Stollery [21], Pederson et al. [23] studied the effect of density differences between the coolant and mainstream by also studying foreign gas injection for hole film cooling. Pederson et al. legitimized using the heat and mass transfer Reynold's analogy to invoke an adiabatic effectiveness based on heat transfer results. In this analogy, a mass transfer effectiveness can be measured instead of the physical adiabatic wall effectiveness, which is experimentally difficult to measure non-intrusively. The typical effectiveness in the mass transfer analogy uses the mass fraction of the coolant gas instead of the flow temperature. The downstream distances also must be normalized

in a special way to incorporate Schmidt number effects for the mass transfer analogy. The streamwise distance parameter defined by Pederson et al. is shown in Equation 11. Here C and ∞ denotes conditions in the coolant and main streams, respectively, while μ is the viscosity. When using these scalings, the effectiveness from different experiments, using either heat transfer film cooling or the corresponding mass transfer film cooling, collapsed. However Pederson et al. did admit that an exact heat and mass transfer analogy does not truly exist for variable property flows, as mechanisms for heat transfer and mass transfer are not truly analogous.

$$\xi = \frac{x}{BR \cdot s}\left(\frac{\mu_C}{\mu_\infty}\mathrm{Re}_C\right)^{-0.25} \qquad \text{Eq. (11)}$$

Goldstein [20] showed that the effectiveness could be defined in multiple ways in compressible, high speed applications. The recovery temperature of the coolant flow can replace the static coolant temperature, while the mainstream recovery temperature replaces the mainstream static temperature. When compressibility effects can be neglected, the effectiveness based on recovery temperatures reduces to Equation 5. Goldstein further showed that an iso-energetic effectiveness can be defined when the coolant and mainstream flow have the same stagnation temperatures. Using the iso-energetic effectiveness, the effectiveness is unity at the injection plane, which is not generally true of the effectiveness based on recovery temperature. The iso-energetic effectiveness was also found to make compressible film cooling correlate well with low Mach number experimental results better than the effectiveness based on the recovery temperatures.

Hansmann et al. [24] explored slot film cooling in the presence of high temperature and velocities under conditions more representative of propulsion applications, where

compressibility effects are non-negligible. Both air and helium were used to study mass density effects at these high speeds. At such high speeds, adiabatic boundary conditions are very difficult to achieve due to aerodynamic heating, resulting in large heat loads a the wall. Instead Hansmann et al. defines effectiveness as one minus the ratio of the wall heat transfer rate for the film cooling case to the wall heat transfer rate for a case with no film cooling, reproduced below in Equation 12. For a given blowing ratio, helium was found to produce higher effectiveness than air. However since wall wakes were being explored in this study, helium would have a higher velocity ratio for a given blowing ratio, meaning the shear between the two streams is smaller resulting in reduced mixing. Meanwhile at constant velocity ratio, air outperformed helium due to the higher coolant mass flux.

$$\eta = 1 - \frac{\dot{q}_c}{\dot{q}_0} \qquad \text{Eq. (12)}$$

Jones [25] showed that the heat and mass transfer analogy can be further applied to account for differences in specific heat and thermal conductivity, where the analog to mass transfer is not direct. The approximate method developed by Jones takes experimental data measuring the scalar mixing of two streams and converts this mixing into an equivalent heat transfer/enthalpy space. The corrections applied agreed with experimental data very well. Furthermore, when using carbon dioxide, for example, the correction needed is small. Sulfur hexafluoride and argon injection was also studied and collapsed well with analogous experiments.

1.3.1.6 Turbulence

Juhaz and Marek [26] performed one of the seminal film cooling studies in their presentation of film cooling data in the presence of high freestream turbulence. In actual

engineering applications, film cooled regions are composed of highly turbulent, high temperature fluids. Juhaz and Marek, studied a range of turbulence intensities for a variety of wall wake blowing ratios. They explored different slot geometries over a range of freestream and coolant conditions, consistent with those seen in combustor applications. Next Juhaz and Marek analyzed previous correlations, mentioned above in Section 1.3.1.1, and found the data collapse to be poor. They rederived a simple effectiveness mixing model featuring a turbulent mixing coefficient. They found that C_m needed to be changed from 0.01 (the coefficient of previous studies) to 0.15. After this change, the correlation developed in this report collapsed the experimental data to within 20%. As the name suggests, the turbulent mixing coefficient, C_m, is heavily linked to the turbulence levels in the experimental wind tunnels. The higher freestream turbulence cases in this study caused a much more rapid decay of film cooling effectiveness than was seen in previous film cooling literature. C_m in this study was deemed to be primarily dependent on then wall-normal turbulence intensity. In a subsequent study, Marek and Juhaz [27] showed that while the effects are small, C_m is also a function of the axial or streamwise turbulent intensity.

Ko [28] in 1980 performed an array of experimental studies of turbulent slot film cooling flows, using a hotwire anemometer to get information on the streamwise fluctuating velocity, streamwise turbulence intensity and temperature distribution for a range of blowing ratios. Ko used these measurements to calculate a new value of C_m for their experimental data, according to the correlations of Marek and Juhaz [26]. Also heat transfer measurements were made in the case of a non-adiabatic wall, to show heat transfer is increased in the presence of turbulence.

Lebedev et al. [29] also extensively characterized a wide arrange of mainstream flow turbulence levels over a range of wall wake blowing ratios. This study featured a film heating arrangement. Additional blowing ratios that spanned minimum shear and wall jet regimes were explored in a subsequent paper [30]. They also used a hot-wire anemometer to provide streamwise velocity and turbulence intensity profiles at the injection plane of the mainstream flow. The subsequent adiabatic wall effectiveness was reported and once again the turbulence was shown to degrade coolant protection, with less influence of mainstream turbulence seen at the larger blowing ratios. The increasing turbulence was also shown to decrease the decay in both the near-injector (near the injection plane) and far-injector (far from the injection plane) regions.

1.3.1.7 Comprehensive Characterization

Due to the complexity of film cooling, it is difficult to experimentally characterize film cooling in a comprehensive way. Most studies either capture only the turbulent kinematics with limited temperature measurements, or comprehensive temperature measurements with limited kinematic data. Additionally these studies focus on one shear regime, most often a wall wake case. However in CFD validation for example, both mean and turbulent information is needed at not only the injection plane but at several locations downstream. Only in this way can a CFD simulation show that the physical mechanisms responsible for mixing are being properly resolved. Characterizing the velocity, temperature and turbulence is therefore crucial for CFD development. Additional understanding of the film cooling processes from these comprehensive experiments may also be gained.

Cruz [7], Cruz and Marshall [31], and Raffan [5] performed 2D film cooling experiments for multiple velocity ratios (corresponding to multiple blowing ratios) on an adiabatic and non-adiabatic wall in an open-loop, hot wind tunnel facility. These experiments featured microthermocouple probes and Particle Image Velocimetry (PIV) that non-intrusively provided mean and higher ordered statistics on the velocity and temperature fields. Using PIV, instantaneous flow structures were captured, showing the coherent turbulent shear structures inherent in these 2D film cooling flows. Additionally, derived skin friction and convective heat transfer coefficients are provided as a function of downstream distance. Unfortunately, the test section encountered leaks contaminating the film cooling mixing. Despite this leakage, this study showed the ability to capture a comprehensive database of experimental film cooling, allowing for careful CFD validation.

1.3.2 Summary of Previous Experimental/Modeling Work

The experimental work in the literature on the whole primarily focuses on exploring single parameters that govern film cooling flows. The experiments are used to update and fine-tune engineering correlations that are generally only applicable in the far-field, where boundary layer assumptions are tenable. The experiments on the whole focus on the adiabatic wall effectiveness, which is the quantity of merit in film cooling studies. Also most experiments do not give both mean and turbulent information that is especially useful for CFD validation. The turbulent information that does exist is often incomplete and primarily involves intrusive measurement techniques. The various correlations show significant scatter varying from one data set to the next, normally due to the difficulty in predicting the turbulent mixing coefficient.

Further, the length of the potential core, or the region of near perfect effectiveness existing just downstream of injection, is of great importance to film cooling designers. Just after this potential core, the film experiences a rapid breakdown as the mixing layer impinges on the wall. In engineering design, the film would need to be replenished soon after this impingement point, making this prediction of the potential core length rather important compared to far-field predictions.

To illustrate the importance of the near-injector mixing, consider the toy problem of turbine blades in gas turbine engines. Lefebvre [2] indicates that the maximum operating temperature of commonly used alloys for the combustor liner is about 1100 K. The nominal cooling air temperature, which is bypass air that still goes through the compressor is 800 K. The exit combustor temperature is nominally 2280 K. In these circumstances, the minimum allowable effectiveness would be 0.80. Given this result, the effectiveness behavior far downstream of the impingement point, which is below 0.80, is far less important than the near-injector physics governing the higher effectivenesses. This far-injector field is not the primary region of concern for designers and therefore should be of secondary interest in a study. Unfortunately, most film cooling analytical models and to a lesser extent experimental, and numerical (as will be shown) studies, focus on the far-field decay, where convenient boundary layer assumptions can be made. Therefore the correlations either need to be updated to accurately incorporate the near-injector mixing, which has thus far not been possible, or CFD needs to be more widely validated to accurately predict film cooling flows. In order to accurately do either of these approaches, a large comprehensive experimental dataset is needed that measures film cooling mixing across all three velocity ratios in the presence of important film cooling

physics, like mass density effects, turbulence and wall heat transfer.

1.4 Review of Numerical Work

The advent of modern computing has allowed CFD to play a key role in the design and analysis of complicated flow paths. With these added resources, engineers and researchers have been able to further explore complicated film cooling flows in hopes of optimizing CFD's accuracy and overall system performance. Direct Numerical Simulation (DNS), Large Eddy Simulation (LES) and Reynolds Averaged Navier-Stokes Simulations (RANS) have been used to numerically tackle film cooling flows depending on the complexity of the problem and the desired fidelity of the results. RANS, which involves temporally averaging the Navier Stokes over a long period of time relative to characteristic turbulent time scales, is widely considered the lowest fidelity technique. The effect of turbulence is essentially entirely modeled and added to the mean flow quantities. LES, meanwhile, involves spatially filtering the Navier-Stokes equations. In this technique, all flow scales greater than the filter width are resolved, while the scales smaller than the filter width are modeled. Proper LES simulations will resolve the large flow structures that are more geometry dependent, while the smaller structures that are more universal and dissipative in nature are modeled. DNS resolve all the relevant flow scales all the way down to the dissipative Kolmogorov scales. No filtering or special treatment is required, but the grid density and time step must be sufficiently fine to resolve gradients on the order of the Kolmogorov scales. While DNS provides the highest fidelity results, the fine resolution requirements add significantly to computational overhead and makes DNS calculations overly prohibitive for most engineering flows.

LES simulations provide a balance between the level of accuracy, and the grid restriction and therefore are more applicable for modern engineering applications.

1.4.1 RANS

Early numerical studies featured RANS based computations to predict film cooling flows. For example, Kacker and Whitelaw [32] performed one of the first fundamental RANS film cooling parametric studies. Many of the important film cooling design parameters were explored, including the velocity ratio, louver lip thickness, coolant and free stream Reynolds number, coolant velocity profile, coolant turbulence intensity and free stream turbulence intensity. Due to the limited computational capabilities at the time, however, several restrictive simplifying assumptions were made, e.g., constant property assumptions. Additionally, a van-Driest like mixing turbulence model was used with a tuned mixing length based on experimental data. The two-dimensional elliptic stream function and vorticity equations for boundary layer flows were solved on somewhat coarse grids that used wall functions to alleviate the fine grid requirement near the wall. This seminal study did establish many of the film cooling parametric trade-offs that exist. The solutions featured the Reynold's analogy, where the species mixing between the coolant and mainstream is considered analogous to the heat transfer between two different temperature streams. The effective Schmidt number, akin to the turbulent Prandtl number was chosen according to experimental data as 0.4, with an inflow boundary condition prescribed from experimental data.

Stoll and Staub [33] used a k-ε turbulence model in a parabolic finite difference code to compare simulated wall heat flux values to measurements from their film cooling experiment in a converging-diverging nozzle. A variable turbulent Prandtl number was

calculated from an engineering correlation developed for boundary layer and mixing flows. Several supersonic wall wake experiments were simulated, all in the presence of a favorable pressure gradient. In the near wall region, the law of the wall was used to recreate the near wall velocity in the viscous sublayer. The simulations captured the wall pressure very well, while underpredicting the wall heat flux. Other kinematic and thermal data were not reported.

Zhou et al. [34] used a modified k-ε model on a finite-volume code to simulate two dimensional, normally injected, adiabatic slot film cooling. Using a steady RANS formulation, they simulated two wall wake cases. The turbulent Prandtl number and the thermal governing equation were not reported. For both cases, the mean velocity and turbulent kinetic energy distributions in the film cooling domain show significant deviation from the experimental values. In terms of effectiveness, the authors used the heat and mass transfer analogy to compute heat transfer effects. For one case, they found excellent agreement between the simulation and the experiment both in the near injector region and in the far field. The effectiveness differs more dramatically for other. In normally injected films, the extent of film attachment to the wall, and not the shear between the two streams, is the primary factor determining the wall protection afforded by normally injected films.

Jansson et al. [35] used both a k-ε model and an algebraic stress model to simulate flat plate slot film cooling for a blowing ratio and velocity ratio close to unity, or a minimum shear cases. They performed adiabatic film cooling flows for lip thickness to slot height ratios of 0.1 and 1, while the turbulent Prandtl number was prescribed between 0.5 and 0.9 depending on the region of the flow. The simulation for the smaller louver lip

thickness results captured the overall mean velocity and temperature trends well. For the larger lip thickness ratio, in which large-scale vortex shedding occurred, unsteady RANS calculations were used to resolve the turbulent periodicity in the flow. The mean velocity field was captured fairly well, while the mean temperature field significantly deviated from experimental values especially in the near wall region. The streamwise progression of the adiabatic wall effectiveness in either case was not reported.

More recently, Lakehal [36] used a modified k- ε model that was tuned for jets in crossflow using DNS data to simulate hole film cooling performed by Sinha et al [37]. Lakehal produced very accurate film cooling effectivenesses, both along the hole centerline and laterally outwards for a very complex film cooling flow. Velocity and flow temperature comparisons were not reported.

Zhang et al. [38] studied liquid film cooling in a rocket combustion chamber using a k-ε model with Van Driest damping near the wall. They compared the simulated liquid film length and found their results to be within about 10 percent of experimentally measured values, but provided little other comparisons.

Cruz [7] used the Spalart-Allmaras model in a finite-difference code to simulate slot film cooling experiments of multiple blowing ratios with both adiabatic and constant temperature walls, which were done by Cruz [7], Raffan [5], and Cruz and Marshall [31]. The Spalart-Allmaras model, with a constant turbulent Prandtl number of 0.85, in general captured the adiabatic wall effectiveness to within about 12%. The mean temperature profiles at different downstream distances showed similar fidelity when compared to experimentally measured values, while the velocity profiles showed more significant deviation in the far field. Cruz showed that improved accuracy was gained with respect to

semi-empirical models developed in other studies. The large discrepancies were attributed to the constant density assumption used in the finite difference code and the entrainment of air into the experimental flow path (noted previously), which accelerates the flow. In general, the effectiveness showed an initially prolonged ideal effectiveness near the inlet. As stated before, these zero-pressure gradient simulations were validated against experimental data that contained flow acceleration.

Dellimore [39] also simulated the adiabatic experiments of Cruz [7] using the Spalart Allmaras but the turbulent Prandtl number was tuned to 0.5 to achieve better agreement in the effectiveness and temperature profiles. These results showed an initially prolonged effectiveness of unity, also seen in Cruz's RANS data [7] and then rapidly decayed. Dellimore [40], in a later study, using a constant turbulent Prandtl number of 0.7, simulated the overall temperature trends fairly well, while the momentum field had a maximum error of 33.1%. This flow entrainment of the experimental data, Dellimore [40] argues caused a pressure gradient that accelerates or decelerates the fluid depending on the velocity ratio and the region of the flow. The adiabatic wall effectiveness is predicted to within 10% of the experimental values for the wall wake, minimum shear and wall jet cases, respectively. The effectiveness decay in the near injector region is underpredicted, similar to the other tangentially injected slot film cooling studies.

Voegele [41-42] performed similar parametrics to the studies of Cruz [7] and Dellimore [40], except validating against corrected experimental data. Voegele showed that all RANS studies experienced a delayed onset of mixing that is crucial in the near-injector field. Since this near-injector field is the region of interest in most film cooling applications, it is this critical region that must be accurately predicted. Voegele [42]

noted that RANS simulations featuring constant turbulent Prandtl number would not accurately predict film cooling decay since the real turbulent Prandtl number is variable. Constant turbulent Prandtl number film cooling studies captured film cooling effectiveness to within 10% of the experiments. While this error may not seem large, Voegele [42] stated that due to the non-linear nature of this problem, the film protection length (the distance from injection where the film adequately protects the wall) could be overestimated by over 30%.

1.4.2 LES

LES provides higher fidelity CFD solutions since more turbulence scales of the flow are directly simulated, as opposed to the RANS approach where turbulence is completely modeled. The limited success of the RANS based approaches, as noted by Voegele [41-42], necessitates the need for a higher fidelity technique when simulating subsonic, tangentially-injected, slot film cooling.

1.4.2.1 LES FILM COOLING

Guo et al. [43], Tyagi and Acharya [44], and Muldoon and Acharya [45] explored hole film cooling using LES, LES and DNS approaches, respectively. They were successfully able to reproduce important kinematic and thermal flow features, in addition to reproducing velocity and temperature fields very close to experimental values.

Cruz [7] performed LES on a 2D film cooling wall jet using an incompressible, constant property, finite difference code. The effectiveness and temperature profiles produced promising results and were close to experimentally measured values. The peak velocities were underpredicted, which was attributed mostly to the constant density formulation. The experiments used for validation, however, experienced an experimental

leak, contaminating downstream results. Voegele [41] went on to perform the wall jet, constant density, constant property, LES calculations following the methods of Cruz [7] but validated against a new corrected adiabatic experiment. He found that the constant density results compared very well with experiments, except in the far-field where variable-mass density effects were postulated to become important.

Konopka et al. [46] performed LES calculations of the wall-wake, zero-pressure gradient, supersonic film cooling data of Juhany et al. [47]. The effectiveness results compare very well with the experimental results except in the far field approximately 100 slot heights downstream of injection. They also present kinematic results for their film cooling data but have no experimental data to validate their results against. Additionally they performed both favorable and adverse pressure gradient wall wake cases without experimental comparisons. In a subsequent study, Konopka et al. [48] explores the same wall wake configuration in order to examine the effect of injecting a laminar film as opposed to a film with artificial turbulence. The laminar film based on recovery temperatures has a higher effectiveness than the turbulent film case except downstream for slot heights greater than 60.

1.4.2.2 LES Film Cooling Inlets

Simon [17] and Goldstein [20] both demonstrated the importance of inlet parameters on the near-injector mixing. If experimentally the inlet conditions are of interest, realistic numerical simulations will place similar import on the inlet boundary condition. Morever, LES in particular requires realistic flow structures to be convected into the domain in order to have physical shear mixing near the injector plane. Therefore

determining a proper LES technique to adequately accomplish this inflow specification is crucial.

As part of his simulation, Cruz [7] developed a precursor simulation technique to provide time varying inflow conditions that contain realistic boundary layer structures that convect into the film cooling domain. This method of Cruz [7] is based off of a larger group of methods where separate LES calculations are run *a priori* and a library of streamwise planes are saved from this precursor simulation. These slices are then used as an inflow boundary condition for the LES simulation of interest. Not only did Cruz [7] and Voegele [41] use this technique with great success for film cooling, but Li et al. [49] and Piomelli et al. [50] also used this method for the calculation of mixing layers and accelerating boundary layers, respectively.

Konopka et al. [46, 48] used the inflow method of El-Askaray [51]. El-Askaray modified Lund et al.'s [52] rescaling method to account for compressibility. The method of Lund et al. allows for spatially developing boundary layers to be calculated as a pseudo-periodic simulation. In this method, a zero-gradient, spatially-developing boundary layer is simulated with inflow and outflow boundary conditions, as opposed to periodic boundary conditions. The outflow values are used in a feedback loop to adjust the inflow to get correct mean information (e.g., the correct skin friction and momentum thickness) at some downstream distance. This inflow represents a reduced cost compared to a spatially developing boundary layer simulation, while physically meaningful turbulent structures are still generated. Keating and Piomelli [53] note that the drawback to this technique is that there must be some equilibrium region where experimental data

exists upstream of a simulation inflow. Additionally, using the method of Lund et al. [52] can introduce "spurious periodicity" into the simulation of interest [53].

Keating and Piomelli [53] performed a review of several different inflow generation techniques for a spatially developing boundary layer simulation. The following inflow boundary conditions were explored: 1). Synthetic turbulence - a random number generator is used in conjunction with preserving appropriate first-order and second-order velocity statistics, 2). "Recycled Inflow" – variants of the method described by Lund et al. [52], 3). Precursor simulation - more general version of the method used by Cruz [7] and Voegele [41]. The precursor simulation technique provided the highest fidelity results in terms of skin friction coefficient and energy spectra, but was the most expensive calculation. The synthetic turbulence technique provided the lowest fidelity results but had the advantage of being the cheapest of the calculations.

1.4.2.3 LES Wall Modeling

While less computationally expensive than DNS, wall-resolved LES still remains overly prohibitive at large Reynolds numbers due to the grid and time resolution requirements needed to resolve the small near-wall structures. Piomelli and Balaras [54], in their review of LES wall modeling techniques, go over the various LES and DNS computational costs. DNS requires the resolution of the Kolmogorov scales of turbulent motion. The computational expense, which is proportional to the number of grid points multiplied by the number of time steps, scales like the Reynold's number to the third power [54]. Wall-resolved LES, meanwhile almost needs DNS-like resolution in the wall region (the inner layer of the boundary layer) but has less stringent grid and time step

requirements in the outer layer, where large geometry dependent structures are resolved and the finer turbulent structures are modeled. The inner layer scaling requires a computational expense that is proportional to the Reynold's number to the 2.4 power. The outer layer computational expense, meanwhile, is proportional to the Reynolds number to the 0.6 power, representing a much less demanding cost [54].

The idea of wall modeling takes advantage of the coarser requirements in the outer layer by modeling the inner layer effects on the outer layer by means of a wall model. Therefore using a wall model, the total computational expense scales with the outer layer scaling, alleviating the restrictions of the wall-resolved LES requirements. To more fully emphasize this point, Piomelli and Balaras [54] estimated that 99% of the grid points in a wall-resolved LES are used to resolve the inner layer of a boundary layer with a characteristic Reynolds number of order 10^6; this inner layer, however, comprises only 10% of the total boundary layer. The accuracy of the wall-modeled LES calculations is not surprisingly heavily dependent on the wall model. The wall model, according to Piomelli and Balaras [54], especially needs to model the wall shear stress correctly, since the grid is too coarse to evaluate the near-wall gradient or the near-wall hair-pin structures via finite differencing in wall-modeled approaches.

Two different branches of LES wall-modeling have become popular: 1. Equilibrium models, 2. Zonal models. Equilibrium models use the logarithmic law of the wall (log-law) to reconstruct the wall shear stress based on the velocity at a point in the logarithmic layer. The log-law assumes that the shear stress is constant in the near-wall region through the logarithmic layer, which is positioned at the lower extent of the outer flow. Therefore, the shear stress can be calculated at the first interior grid point (assuming this

point is in the logarithmic layer) and can be used to calculate the wall shear stress through the log-law. The log-law thus effectively defines a boundary condition on the velocity equation that approximates the momentum flux of many turbulent flows. As the name suggests, equilibrium models only apply for equilibrium flows and is dependent on the form of the log-law. These models often fail in non-equilibrium regions, such as separated regions.

Zonal models, on the other hand, define a separate mesh near the wall that is fine in the wall-normal direction but maintains the same streamwise and spanwise spacing as the outer flow. On this separate mesh a set of simplified equations, most often the boundary layer equations, are solved to recreate the wall shear stress based on the conditions existing at the first outer layer point, which should once again be in the logarithmic layer. When the boundary layer equations are used on this interior mesh, the method is called the two-layer model (TLM) and was first used by Balaras and Benocci [55]. The TLM computational expense scales only approximately with the outer layer scaling because some expense is added due to the boundary layer solution on the inner mesh. However since the interior mesh is only refined in the wall-normal direction and the equation set is much simpler, the overall cost is mitigated. Detached eddy simulation (DES), proposed by Spalart et al. [56], is performed when certain regions of the flow solve the LES equations, while other regions employ the RANS equations. DES is primarily used on separated flows, where the RANS equations are used upstream of separation in the inner layer of the boundary layer and LES is used downstream of separation. The two sets of regions are often formulated using an eddy-viscosity approach. In this method, the

transition between the two regions involves blending between the eddy-viscosities of the RANS and LES equations.

So far no wall-modeled LES calculations have been performed on tangentially-injected, slot film cooling. Martini et al. [57] performed a DES calculation of slot film cooling injected along an incline with internal struts and holes in the slot. While the film is formed in a slot, this configuration is similar to injection through discrete holes, as no continuous film is formed. This geometry, therefore, does not define a canonical configuration. They examined three different internal configurations over three blowing ratios that spanned wall wake and minimum shear film cooling regimes. The DES approach predicted the experimental adiabatic, laterally-averaged film cooling effectiveness compared to the RANS k-ω approach. Roy et al. [58] and Kapadia et al. [59] also both used DES to study hole film cooling and showed great promise in capturing the film cooling trends at lower cost. These studies [57-59], to this author's knowledge, comprise the only literature of LES wall-modeled film cooling.

1.4.3 Summary of Previous Numerical Work

Most of the numerical literature uses RANS techniques that are unable, without model tuning, to capture the near-injector mixing trends that are crucial for film cooling predictions. The next logical progression is to use a higher-fidelity technique to capture adiabatic slot film cooling, but there is very little literature studying LES and DNS of slot film cooling. Almost all the literature focuses on overall mixing, with very little attention being paid to the near-injector mixing where actual film cooling is performed. Similarly heat transfer comparisons are equally missing.

In addition to wall-resolved LES, wall models can be used to reduce the grid restrictions near the wall. However studies exploring wall-modeled LES in slot film cooling applications are almost non-existent. A little more information on LES inlets is available in the literature, but almost no parametric studies have been performed that compares the performance of LES inlet techniques in film cooling configurations. It should be noted that there have been a few LES film cooling studies of note that deal with hole film cooling [43-45, 57-59]. Hole film cooling, however, features different mixing mechanisms than slot film cooling. Nonetheless, these LES studies demonstrate the promising performance of LES in film cooling configurations.

1.5 Objectives

The experimental literature review revealed that there is a need for slot film cooling data that provides a comprehensive set of kinematic and thermal data, from which CFD model validation can be performed. Since turbulence is the dominant mixing mechanism in this flow, CFD engineers require not only mean information but fluctuating information as well. Almost no studies provide fluctuating velocity information, with even fewer providing the fluctuating thermal information, all in addition to the mean kinematic and thermal data. Similarly, no studies give such comprehensive measurements across the three shear regimes (VR < 1, VR ~ 1, VR > 1), which comprise very different film cooling mixing.

Most studies, similarly, do not physically study heat transfer but rather make use of the heat and mass transfer analogy. Both adiabatic and non-adiabatic studies are of interest in film cooling flows, since flows of engineering interest will always have heat

transfer. The wall heat flux equation depends on both adiabatic and non-adiabatic conditions. Since no obvious heat-mass transfer analogy exists for the non-adiabatic wall, heat transfer reduction from backside cooling cannot be evaluated when the heat and mass transfer analogy is employed. One goal of this PhD work is therefore to provide a comprehensive experimental data set that reports and measures:

- Mean and fluctuating kinematic profiles at several streamwise stations for both adiabatic and non-adiabatic walls
- Mean thermal profiles at several streamwise stations for both adiabatic and non-adiabatic walls
- Adiabatic effectiveness across the three shear regimes (VR < 1, VR ~ 1, VR > 1)
- Non-adiabatic wall temperatures across the three shear regimes (VR < 1, VR ~ 1, VR > 1)
- Mean and thermal conditions close to the injector plane to allow for CFD inflow generation

Such a study would constitute a major step forward in the film cooling literature and would allow film cooling engineers to better design correlations and understand film cooling mixing dynamics. Additionally, a convenient dataset will be generated for CFD modelers to validate their codes in a turbulent environment in the presence of heavy thermal mixing, where constant property assumptions cannot be made.

As was seen in the literature review, modeling correlations have failed to capture the near-injector mixing that is of primary interest in film cooling studies. These failures translate to a need to numerically model this problem instead. Since RANS CFD was

shown to perform poorly for subsonic adiabatic slot film cooling, a higher fidelity technique is needed. Numerically, LES has yet to be studied in detail for subsonic slot film cooling flows. The film cooling literature for LES either focuses on: 1). hole film cooling [43-45, 57-59], which is not canonical, 2). constant density subsonic film cooling [7, 41], which is not true in engineering applications or 3). supersonic slot film cooling [46, 48], where the heavy, initial turbulent mixing is not nearly as dominant as in subsonic applications. In the following dissertation, comprehensive LES parametric studies will be performed. This PhD work will include exploring:

- LES wall-resolved, adiabatic simulations across the three shear regimes (VR < 1, VR ~ 1, VR > 1)
- LES wall-resolved, non-adiabatic simulations across the three shear regimes (VR < 1, VR ~ 1, VR > 1)
- LES inlet generation parametrics studying inflow techniques
- Development of film cooling insight, especially when used in tandem with experimental information
- LES validation against experimental data also presented in this dissertation

The LES studies will generate significant understanding in the simulation of slot film cooling flows and will hopefully show their feasibility for more practical Reynold's numbers. To this author's knowledge no LES non-adiabatic slot film cooling studies have been performed. Similarly no variable density, wall jet LES film cooling studies have been performed. The research therefore will make a major contribution to the film cooling and general LES literature.

Chapter 2: Approach

In the last chapter, the current state of slot film cooling research was summarized and several key areas of research were identified. The purpose of this section is to describe the approach and methods used to accomplish the objectives detailed in Chapter 1. The research focuses on tackling film cooling both experimentally and numerically, representing a broad and comprehensive approach, allowing for deeper insight into the problem. The first section details the experimental approach including an overview of the experimental apparatus, a description of the experimental diagnostics and a discussion of the experimental uncertainty. The second section reviews the numerical approach, starting first with a description of the general LES equations and their subsequent implementation in the CFD flow solver. CFD code validation, discussions of inflow generation techniques, and LES film cooling wall modeling will then be presented.

2.1 Experimental Approach

The experimental film cooling research was performed at the Film Cooling Research Lab at the University of Maryland. A hot wind tunnel was used to a variety of different kinematic and thermal film cooling conditions. Meanwhile, a number of diagnostics were employed to characterize the turbulent film cooling mixing phenomena present in the experiments. Much of the experimental procedure and experimental apparatus was developed by Cruz [7], Cruz and Marshall [31], Raffan [5] and Raffan [60]. However in the interest of being thorough and for the convenience of the reader, the experimental approach is nonetheless reviewed below and reflects the current experimental campaign.

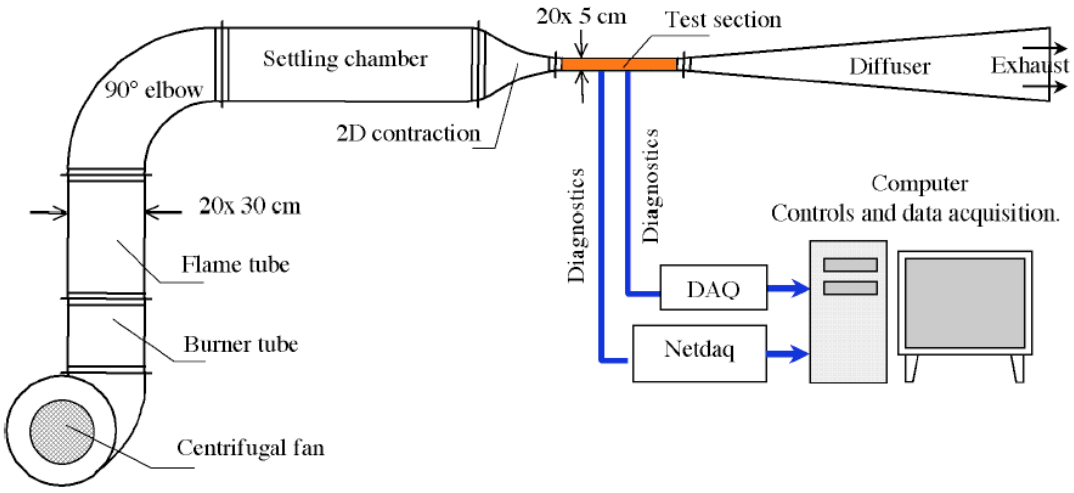

Figure 4. Schematic of the film cooling hot-wind tunnel. Adapted from Cruz and Marshall [31].

2.1.1 Experimental Apparatus

Figure 4 shows a schematic of the open-loop, hot wind tunnel used to study film cooling. This apparatus is capable of establishing a variety of film cooling conditions relevant to real-world engineering applications. The film cooling mainstream air is driven by a variable-speed, centrifugal fan, upstream of a combustion section, which in turn is used to heat the mainstream flow to the desired thermal conditions. In the combustion section, the inline methane burner produces heated visciated air. A mass flow controller provides a constant methane flow rate into the burner. Downstream of the burner, the flow enters a 90-degree elbow, equipped with turning vanes to avoid pressure losses and to mitigate asymmetric velocity profiles induced by the centrifugal fan. Next, the settling chamber further homogenizes the flow via flow conditioners. The first of these is a bed of randomly packed ceramic saddles, which serves to remove large temperature fluctuations induced by the burner. Next a honeycomb wedge is used to destroy the large-scale structures and straighten the flow. At the end of the settling chamber, a fine stainless steel

mesh is used to generate grid turbulence and further homogenize the flow. The mesh consists of 0.165 mm thick wire rods, with a characteristic spacing of approximately 0.85 mm, making for a square mesh density of about 140 squares per square centimeter. A 2D convergent section, with a 6 to 1 contraction ratio, is used to destroy any thick boundary layers and accelerate the flow to engineering-relevant conditions with the available laboratory mainstream mass flow rate [7]. After the convergent section, the mainstream flow enters the test section where detailed flow measurements are made. To reduce the undesirable wall heat transfer upstream of the test section, one-inch Kaowool boards and fiberglass are used to thermally insulate the settling chamber and the contraction section. The coolant air, driven by a high-capacity compressor at ambient laboratory conditions, is injected into the test section via a 2D tangential slot. Downstream of the test section a 2D diffuser is used to reduce aerodynamic losses. The diffuser is attached to an exhaust hood to provide test section pressures lower than atmospheric pressure.

In terms of relevant film cooling parameters, this experimental apparatus is capable of providing a range of turbulent, film cooling conditions. It can attain velocity, blowing and temperature ratios ranging from 0.5-3.0, 0.75-5.0, and 1.0-1.67, respectively. The range of Reynold's number of the coolant flow is 2000 to 8000, which all comprise a turbulent regime. While these Reynold's numbers are low compared to actual engine applications, the basic turbulent physics and mixing mechanisms are still present, allowing for a meaningful and representative film cooling study.

Test Section

The test section is a 200 mm by 50 mm rectangular channel that is 500 mm long; the test section is where the flow measurements of interest are made and can be seen in

Figure 5. The test section features quartz windows that allow for optical access, necessary for the laser-based diagnostics used in this study. The casing of the test section is made of stainless steel, while the test plate is 6.35 mm thick and consists of a high-temperature, low-thermal conductivity plastic called UDEL (k = 0.24 W/m/K) [7]. The casing is also insulated with fiberglass and Kaowool boards; these materials have low thermal conductivity also, which prevents heat loss from the test section. Several thermocouple ports exist allowing for thermal profiles to be made at many streamwise locations.

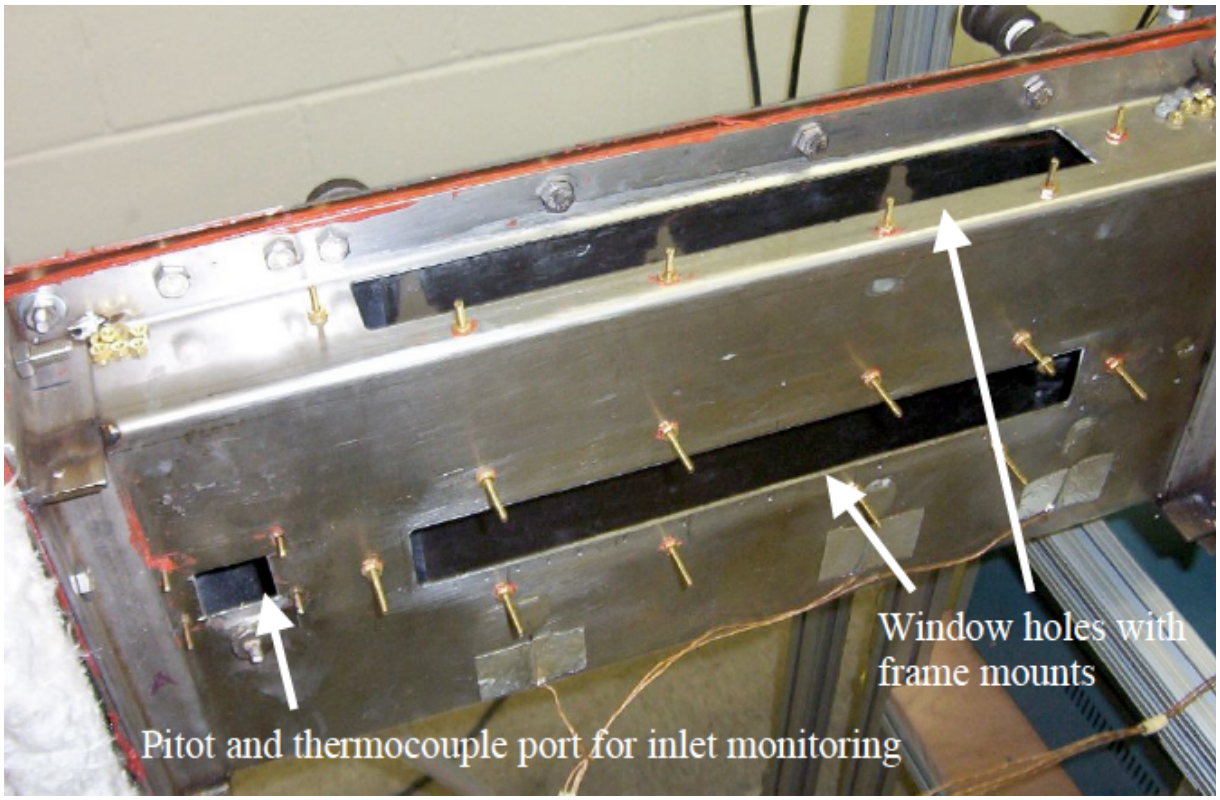

Figure 5. Picture of the test section. Adapted from Raffan [5].

The ambient coolant air is mixed in a plenum and then normally-injected into a louvered slot, where the film mixes and develops, eventually becoming a relatively uniform coolant film, resembling fully developed channel flow. The injection from the

plenum into the coolant slot is made via holes 3.17 mm in diameter and spaced 6.35 mm apart. This type of injection scheme was seen as being representative of configurations in gas turbine and rocket engines. The coolant slot height is nominally 5.3 mm for the adiabatic cases, but varies slightly from 5.3 to 6.06 mm depending on the shear case due to thermal expansion of the splitter plate.

Two different test section configurations, seen in Figure 6, are used to experimentally impose the two different thermal boundary conditions. An adiabatic wall boundary condition results when no heat transfer occurs through the wall. Strictly

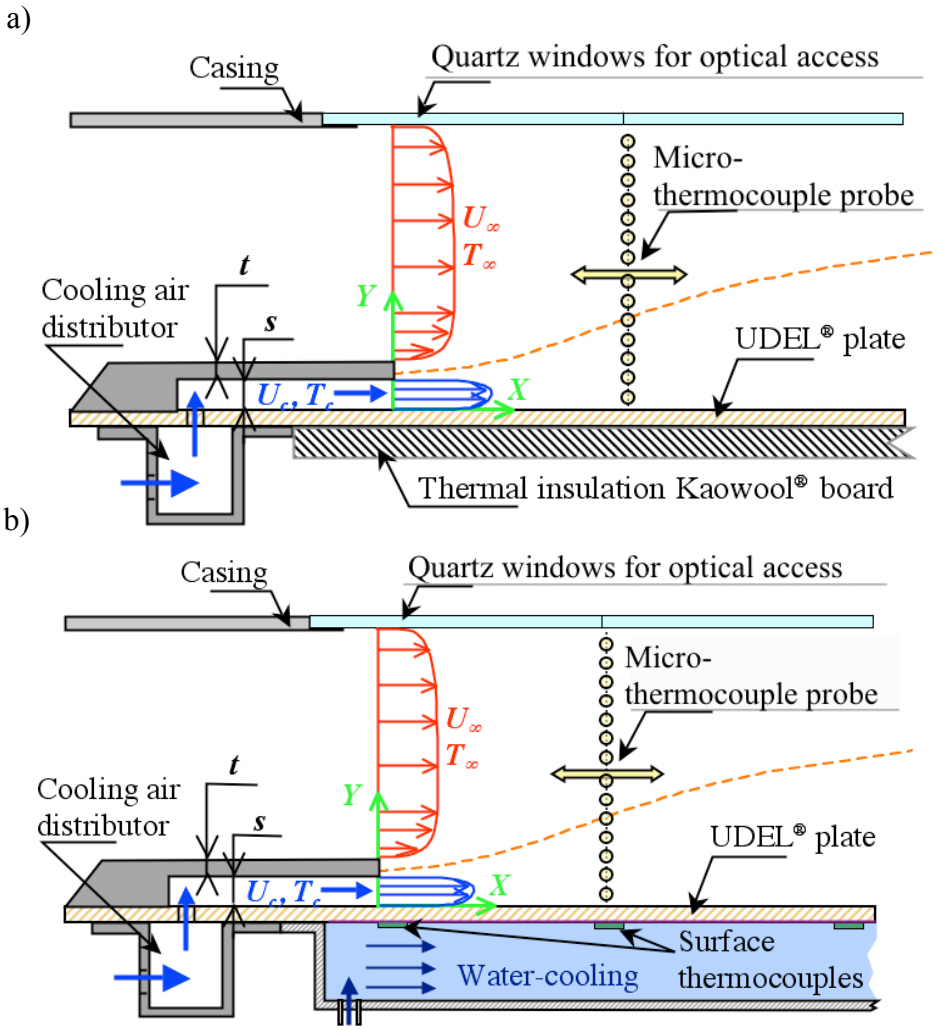

Figure 6. Schematic of the test section for a) adiabatic test plate, b) non-adiabatic test plate. Adapted from Cruz [7]

speaking, an adiabatic boundary condition is almost virtually impossible to exactly enforce. However the low conductivity materials of the insulation and test plate make the solid heat transfer negligible relative to the flow heat convection. Wall thermocouples and the near wall thermal profiles are used to confirm that the wall is adiabatic. This adiabaticity is vital in order to reconstruct an adiabatic effectiveness, the flow parameter of merit in film cooling studies. An adiabatic wall, as mentioned earlier, provides a wall boundary condition that is not configuration or application dependent, as the wall material and backside cooling can affect the overall cooling of the wall. Therefore the adiabatic wall allows for the experimental isolation of cooling protection provided by the film and not other cooling techniques often used in engines. In terms of practical use, the adiabatic wall also effectively defines the expected upper limit of the wall temperature; in engineering applications film cooling is supplemented with some kind of backside cooling to further lower the wall temperature.

The second configuration, seen in Figure 6b, is used to test film cooling in the presence of a well-defined, non-adiabatic wall. The backside insulation is removed and replaced with a water jacket, intended to remove heat from the test plate. Chilled water at approximately 10 ^{o}C is circulated through the water jacket at high flow rates, effectively providing a nearly uniform backside wall temperature. A pump drives water from a large tank. The water in the tank is also equipped with a chiller that maintains this low water temperature. This type of boundary condition is highly desirable for CFD code validation, since it is both statistically stationary and allows for simplifying assumptions to be made in the solid-state heat transfer equations. Also the use of both adiabatic and non-adiabatic boundary conditions is necessary to validate the near-wall physics of film cooling flows.

Due to near-wall noise in laser-based diagnostics and flow disturbances caused by more conventional, intrusive measurements, the near wall kinematic information is difficult to ascertain. Therefore derived wall quantities that are of tremendous importance in engineering applications, namely the skin friction coefficient, can only be approximated. The non-adiabatic boundary condition allows for a heat transfer measurement to be made, which depends on both the flow conditions but also the near-wall physics. If CFD codes can simulate the wall heat transfer correctly, in addition to the flow mixing away from the wall, the ability of CFD to capture the near-wall physics can be validated. The wall heat transfer, dependent on both kinematic and thermal information, if simulated correctly, can give confidence that both the near-wall kinematic and thermal flow fields are captured correctly by CFD solvers.

2.1.2 Experimental Diagnostics

A number of experimental diagnostics were used in this study to measure the experimental flow properties. The purpose of this section is to give some rationale for the selection of the main diagnostics in addition to the general operating principles behind the devices. The main diagnostic techniques of this study are Particle Image Velocimetry (PIV), used to capture flow kinematics, and microthermcouples, used to measure the thermal flow properties. Other diagnostic tools such as pitot tubes, surface thermocouples, rotameters and mass flow controllers were used as backup measurements to verify the main diagnostics were functioning properly. For more information on these other diagnostic tools the reader is referred to Cruz and Marshall [31], Cruz [7], Raffan [5] and Raffan [60].

2.1.2.1 PIV

Operating Principle

In PIV, a flow is seeded with tracer particles, intended to faithfully follow the fluid flow structures. Two pictures, associated with two laser pulses that illuminate the flow, are taken in rapid succession. The displacement the particles move (from the first picture to the second) divided by the time between pictures results in a velocity field for the image pair.

A PIV system consists of a CCD camera; a high-power, dual-pulsed laser; and PIV image processing software. A cylindrical lense is placed on the laser to form a thin laser sheet. This laser sheet is pulsed twice, illuminating a single plane of the flow. Each pulse should be temporally short (on the order of nanoseconds). The two laser pulses are separated in time by some small amount, which is quite large with respect to the duration of the laser pulse. The spacing in time of the laser pulses will depend on the camera field of view and the flow characteristics; however it is normally three orders of magnitude longer than the laser pulse time. Each laser pulse will illuminate the particles in the flow within the laser sheet, which ensures only in-plane motions are captured. Since the flow time scales are much larger than the laser pulse time, the particles are effectively "frozen" in a picture taken at the time of each laser pulse. A CCD camera is used to take two pictures, one of each laser pulse. If the time between the pulses and therefore pictures are selected carefully, the particles will be displaced by some small amount. Averaged displacement vectors can be drawn for groups of particles, which can be converted to a velocity if the gate time (or displacement time) between pictures is known.

While in principle this technique may not be difficult to understand, the actual implementation can be onerous and involves careful selection of PIV parameters. One such parameter is the seeding particles. The seeding particles must be carefully selected to ensure they are large enough to scatter light from the laser pulse so they appear on a picture; yet they must also be small enough to faithfully follow the flow structures. Adrian [61] provides a detailed discussion of this trade-off. Additionally the concentration of particles must be small and relatively uniform such that the fluid flow properties do not change.

Cross-Correlation

The calculation of "particle displacement" in PIV is normally calculated through the use of a cross correlation procedure. In this technique, each image pair is subdivided into smaller squares (or rectangles), called interrogation regions, which contain several particles. In each image, each particle is mapped in the image coordinate space; e.g., each particle is given a (x, y) location. The cross correlation shifts the second image by a displacement, s, and multiplies the intensity at each pixel location by the same location in the first image. The product of the intensities is then summed up over the entire interrogation region. If s is varied such that the entire interrogation region has been swept, an ideal cross-correlation peak, corresponding to a specific displacement, can be found. This displacement is the average displacement the particles in the interrogation window move between the first and second images. Once these displacements are known, velocity vectors can be formed for each interrogation region by dividing the displacement by the time between images. This cross-correlation is more formally described by Equation 13, where the cross correlation coefficient, R, is a function of the displacement

s. R is defined as the integral of the product of the intensity in image one, I_1, at a given location and the intensity of image two, I_2, at the shifted location. As one can imagine, there are finer intricacies of the cross-correlation procedure that are beyond the scope of this analysis. For more information the reader is referred to [61].

$$R(\vec{s}) = \iint I_1(\vec{x}) I_2(\vec{x} + \vec{s}) dA \qquad \text{Eq. (13)}$$

Laser Reflections & Particle Analysis

Laser wall reflections can be intense enough to saturate an image in the near-wall region and can illuminate particles out of the plane of the laser sheet. The out-of-plane particles can show up as blurry particles in PIV images. In order to mitigate these reflections, the walls are treated with black acrylic paint that absorb much of the laser light and reemits it as diffuse light. In laboratory tests, this black acrylic paint was found to reduce wall noise more than a rhodamine wall treatment, which is often used for PIV measurements with green laser light near walls.

In this study two different types of seeding were used: Titanium dioxide (TiO_2) and Bis(2-ethylhexyl) sebacate (referred to as liquid seeding in this work). The liquid seeding was preferred over TiO_2 because TiO_2 tends to deposit on the quartz windows and the wind tunnel walls during experiments, obscuring the optical access to the flow and also creating additional laser noise because of the particles blocking the black acrylic paint. Fortunately, the liquid seeding that interacted with the wall did not adhere to the wind tunnel surfaces. Unfortunately due to the lower boiling point of the alcohol-based seeding, the seeding would evaporate or boil, when exposed to the very high temperatures exiting the combustor. Therefore TiO_2 was selected in the mainstream with liquid seeding in the slot, where the temperatures were low enough such that the liquid

seeding did not appreciably evaporate. In the author's experience, the TiO_2 did not appreciably deposit on the windows when only used in the mainstream.

The following analysis will focus on the acceptable sizes of seeding particles. Using the analysis of Cruz [7], the difference in particle velocity and fluid velocity to first order is written in Equation 14. Ideally, this velocity difference is zero and the particle velocity is the same as the fluid velocity. However, since particles have their own inertia, particles can lag behind the fluid and have a velocity different from the fluid. Higher order terms that were dropped in Equation 14 include acceleration effects due to pressure gradients and buoyancy effects. Essentially this equation describes the lag in particle velocity from the fluid velocity due to inertial acceleration of the particle, which governs how fast a particle will respond to the flow. Observe that the velocity difference becomes smaller if the particle size is reduced, or the density of the particle and fluid are reduced.

$$\vec{V}_p - \vec{u} = \frac{2}{9}\frac{r_p{}^2\left(\rho_p - \rho_f\right)}{\mu}\frac{d\vec{V}_p}{dt} \qquad \text{Eq. (14)}$$

In the case of solid or liquid particles in air, the density of the particle is orders of magnitude large than the density of the fluid flow, which leads to a particle time scale shown in Equation 15. This time scale, which describes how quick a particle reacts to the flow, must be smaller than the smallest characteristic time scales of the flow. The smallest scales of the flow are on the order of the Kolmogorov scales, which estimate the

$$\tau_P = \frac{2\rho_p r_P{}^2}{9\mu} \qquad \text{Eq. (15)}$$

smallest turbulent eddies in Kolmogorov turbulence. Using turbulent theory and the energy cascade, the time scale of the Kolmogorv eddies can be written in terms of the largest flow scales (the integral scale) according to the relationship seen in Equation 16 [62, 63]. Here the subscripts K and 0 refer to the Kolmogorov and integral scales,

respectively. The integral flow scale, τ_0, is given by s/U_0, where U_0 is the integral flow velocity. The velocity of interest is the streamwise, root-mean-squared (RMS) velocity, which in this case is about 15% of the characteristic streamwise velocity. In all cases, this characteristic velocity is approximately 20 m/s, meaning the flow velocity driving particle-fluid velocity differences is 3 m/s. The Reynold's number is calculated based on this flow velocity and the slot height.

$$\tau_K \propto \tau_0 \mathrm{Re}_0^{-1/2} \qquad \text{Eq. (16)}$$

The ratio of the particle and Kolmogorv time scales can be used to form a Stokes number seen in Equation 17. In the literature, researchers have found when the Stokes number of the particle is less than 0.2, the particle follows the flow within two percent error [64]. Table 1, reproduced following the analysis of Cruz, shows the characteristic response times of TiO_2 particles selected to seed the film cooling flows in this dissertation work. The particle sizes of the TiO_2 range from 0.3 to 1 μm. The Stokes numbers for the range of particles is about 0.2, meaning the particles should follow the flow faithfully to within about 2% error. Since the PIV resolution is set to be greater than the Kolmogorov scales, this analysis gives confidence that the particles faithfully follow flow scales resolved by the PIV system. The PIV resolution is set in order to capture several particles (at least ten) in each characteristic interrogation cell. This requirement translates to interrogation cell sizes on the order of tens of micrometers. Also of note, the liquid seeding has an even lower density, meaning the response time of the liquid particle is even smaller than time scale of the solid particle. The Stoke numbers calculated in Table 1 represent conservative estimates, as the limiting viscosity and limiting slot height were chosen that would represent the largest Stoke numbers. For more information on the

seeding, seeders and how the particles are injected into the flow, see Cruz [7] and Raffan [60].

$$Stokes\ Number = \tau_P / \tau_K \qquad \text{Eq. (17)}$$

Table 1 – Particle Response time analysis based on the integral turbulent flow scale, U_0 = 3 m/s.

Particle Diameter - D (μm)	**Particle Time Scale - τ_P (μs)**	**Kolmogorov Time Scale - τ_K (μs)**	**Stokes Number**
0.3	1.07	57.51	0.02
1.0	11.85	57.51	0.21

PIV Guidelines and Difficulties

The previous analysis ensured the particles were small enough to faithfully follow the flow. The conflicting requirement is that the particles must be large enough to be seen in the image. Adrian [61] reviews some of these particle sizing and PIV guidelines. The image diameter of a primarily particle depends on the f-number, $f^{\#}$ (this controls the aperture size); the wavelength of the light, λ; and the magnification factor of the lense, M. The approximate image diameter, d_e, is given in equation 18 below [61]. The Lavision Inc. PIV system used in this work features Solo PIV dual ND:YAG lasers. The laser

$$d_e = \left(M^2 d_p{}^2 + \left(2.44(1+M) f^{\#} \lambda \right)^2 \right)^{1/2} \qquad \text{Eq. (18)}$$

outputs up to 100 mJ per pulse of green light with a wavelength of 532 nm [65]. A cylindrical lense is used to form a laser sheet approximately 1 mm thick. A CCD camera is used to then capture the two images in quick succession. In this work, an $f^{\#}$ of eight is used, which means that the focal length of the lense is eight times the diameter of the aperture. Given that the particle size, $f^{\#}$ and wavelength have all been specified, one must

adjust the magnification to ensure the apparent particle size is large enough to be seen. The first term in Equation 18 is the actual magnified size of the particle on the image plane, while the second term is the diffraction-limited spot size. For small particles (on the order of micrometers) using the previously specified $f^{\#}$ and wavelength, the diffraction limited spot size dominates over the image size of the particle [61].

In this work, the field of view is approximately 35 mm by 35 mm, while the CCD sensor is a square with an area of 15.155 mm by 15.155 mm [65]. The magnification factor is defined as the image size divided by the object size, giving a magnification factor of 0.433. For this camera the pixel size is 7.40 μm. Table 2 shows the particle image size for the range of particle sizes in both micrometers and pixels, as calculated by Equation 18. The particle size is very nearly 2 pixels, which represents the optimum particle size for the PIV cross-correlation vector post-processing [61].

Table 2 – Particle image size.

Particle Diameter - D (μm)	**Particle Image Diameter - D (μm)**	**Particle Image Diameter - D (pixel)**
0.3	14.88	2.01
1.0	14.89	2.01

Another 2D planar PIV guideline concerns the laser sheet thickness and the depth of field of the camera. The out-of-plane component of velocity must be small enough such that most of the particles do not leave the plane of illumination in the second PIV laser pulse. If this happens, the cross-correlation processing of PIV algorithms will not be able to work and spurious velocity vectors will result. In general, this criteria is not difficult to assess as the subsequent PIV velocity field will contain many spurious,

unphysical velocity vectors. Even still, more rigorous analysis is made. As given by Adrian [61], the depth of field, or the depth of the region of focus, is given in Equation 19. In the current work, the depth of field is 1.49 mm and the laser sheet thickness is

$$\delta z = 4\left(1 + M^{-1}\right)^2 f^{\#2}\lambda \qquad \text{Eq. (19)}$$

approximately 1 mm. In order for the PIV processing to correlate effectively, the out-of-plane displacement from one time to the next should be less than ¼ of the depth of field or the laser sheet thickness [66]. Since the laser sheet thickness will only illuminate particles in its plane, the only particles that can be in focus are in the laser sheet. Therefore the particles should not move more than 0.25 mm between laser pulses. This constraint is summarized in Equation 20. The out-of-plane displacement in a time interval can be approximated by the product of the length of the time interval multiplied by the out-of-plane velocity. In this work, a gate time of 8 μs was nominally used as the time between laser pulses. Therefore, the maximum allowable out-of-plane velocity is 31.25 m/s, which is greater than any in-plane velocity recorded in this experimental work. However since this experiment in the mean is two-dimensional, this out-of-plane velocity should be much less than the streamwise component of velocity, thus ensuring this requirement is met.

$$\Delta z_{\max,allowable} = \tfrac{1}{4}\delta z = w\Delta t \qquad \text{Eq. (20)}$$

An additional constraint on the velocity field is that the spatial gradients must be sufficiently small such that in a given interrogation region, the velocity of the entire region can be approximated by a single velocity. This constraint, described by Keane and Adrian [66], is represented in Equation 21, where d_1 is the size of the interrogation

region and is nominally 16 pixels. This constraint translates to a velocity change of less than 72 m/s over 1 mm, which once again is much smaller than any velocity gradient in the present experiment, except perhaps in a very small region very close to the splitter plate.

$$\left|\frac{\partial u}{\partial y}\right| < \frac{d_p}{M_0 \Delta t \frac{d_1}{2}} \qquad \text{Eq. (21)}$$

The last restriction discussed here requires the number of particles in an interrogation region to be greater than ten, which was ensured by inspection and was normally on the order of twenty particles per interrogation region [66]. Many of the other PIV restraints discussed in Keane and Adrian [66] can be compensated by the post-processing algorithms developed by LaVision [65] and are therefore not discussed here.

Near the injection, due to wall-noise and laser reflections, 1000 images were used to calculate mean and RMS statistics on the velocity field. Farther downstream only 500 images were necessary to capture statistically converged RMS statisitics. Additional PIV procedure (calibration, post-processing) and problems associated with wall-noise and laser reflections are not discussed here. Rather the reader is referred to Raffan [60], where in-depth discussions are made.

2.1.2.2 Microthermocouples

The thermal flow measurements were made by microthermocouples, a schematic for which is seen in Figure 7. The microthermocouple assemblies were fabricated in-house and features thermocouple probes with 13 μm diameter Type K thermocouple wires. The bead diameters are on the order of the wire diameters. The wires are sheathed by ceramic insulation to electrically insulate the thermocouple leads. This ceramic

insulation is then inserted into a stainless steel tube and bonded with a high-temperature adhesive. The stainless steal sheath acts as a barrier to both the high-temperature, turbulent flow and any residual PIV particles in the wind tunnel. The thermocouple leads and sheath are then attached to a male thermocouple connecter jack that connects to the Labview data acquisition system. Thermal data was recorded at 20 kHz over a period of

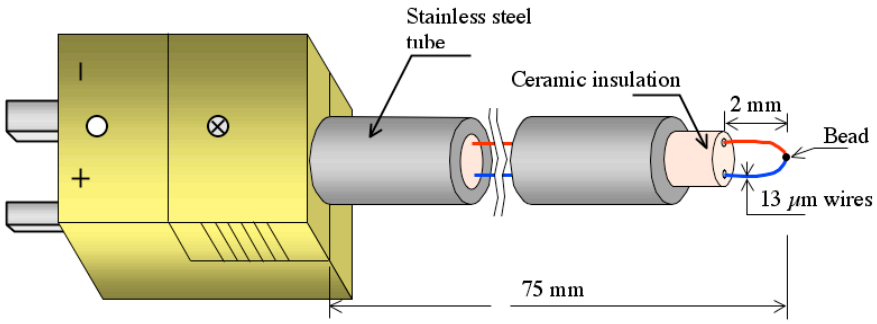

Figure 7. Schematic of Type K microthermocouple with 13 μm wires. Adapted from Cruz [7].

15 s at each temperature data point. The thermocouple bead is placed 2 mm away from the ceramic insulation to mitigate measurement errors due to flow disturbances caused by the probe and is long enough to avoid thermal conduction errors near the bead [67]. The thermocouple is inserted through small port holes at several axial locations in the test section to make thermal flow measurements. The thermocouple assembly is attached to a 10 μm-accurate traverse, which is used to give sub millimeter spatial resolution in the traversing direction (in this experiment that is the wall-normal direction).

The small bead and wire sizes were selected to effectively eliminate thermocouple radiation and conduction losses at the flow temperatures measured in this study; the thermocouple radiation and conduction errors scale with the bead and wire diameters. Using a simple heat balance on the thermocouple probe, radiative heating of the

thermocouple is balanced by convective cooling, as is shown in Equation 22. The true temperature is the gas temperature, T_g; the actual measured temperature, T_b, is affected by radiative loads from the surrounding walls, which have the temperature, T_{surr}. Here the convective coefficient has been replaced by the Nusselt number, Nu, the diameter of the bead, D_b, and the thermal conductivity of air, k_{air}. The emissivity of the bead, ε_b, is approximately 0.8 [67] and σ is the Stefan-Boltzmann constant. For small bead and wire diameters, the convection is actually dominated by the wire diameter, as the bead is effectively only a small protuberance connecting two small cylinders (the thermocouple wires) [68]. Therefore the Nusselt number equation is shown in Equation 23, where A, B and n are 0.24, 0.56 and 0.45, respectively [68]. Here the Reynolds number is based on the local flow conditions and the diameter of the wire. The radiative error is largest when the bead temperature and the Nusselt number are small. The maximum radiative uncertainty found in all the experiments corresponds to a change in temperature, ΔT, of -0.33 K, corresponding to a 0.15% flow effectiveness change. This estimate is actually conservative, since neither the view factor or the emissivity of the emitting surfaces were considered in the heat balance.

$$T_g - T_b = \Delta T = \frac{\sigma \varepsilon_b D_b}{k_{air} Nu}\left(T_b^4 - T_{surr}^4\right) \qquad \text{Eq. (22)}$$

$$Nu = A + B(\mathrm{Re})^n \qquad \text{Eq. (23)}$$

The small probe size has the added benefit of having a small amount of thermal inertia, meaning the thermocouple can respond to rapid variations in flow temperature. This trait is desirable in turbulent flows as turbulent thermal fluctuations can be measured. Even though, the thermal inertia is small, the response time of the thermocouple is large enough that the temperature signal of the turbulent fluctuations is attenuated and phase delayed by the thermocouple. Marshall [70] and Ghoddoussi [71] developed a thermocouple circuit and post-processing that attempts to recover the fluctuating gas temperature from the measured output. The temporal lag of the thermocouple can be characterized by a time constant, which can be used to reconstruct the time-varying gas temperature from the thermocouple signal. Following the analysis of Ghoddoussi [71], the gas temperature, T_g, when using a simple heat balance, can be written in terms of the bead temperature, T_b, as is shown in Equation 24. Here τ_b, given in Equation 24b refers to the thermocouple time constant, while m_b, c_p, h and A_b are the bead mass, the bead heat capacity, the convection coefficient of the bead and the surface area of the bead.

$$T_g(t) = T_b(t) + \tau_b \frac{dT_b(t)}{dt} \qquad \text{Eq. (24a)}$$

$$\tau_b = \frac{m_b c_p}{hA_b} \qquad \text{Eq. (24b)}$$

If the time constant can be determined, some fluctuating thermal flow information can be reconstructed. The time constant of the bead, unfortunately, depends not only on bead characteristics but also on the local flow around the bead, characterized by the convective heat transfer coefficient, h.

The temperature step change method [70] has been used in the past to directly determine the time constant. In this approach, the thermocouple is placed in the film cooling flow and is put through a series of heating cycles. The thermocouple response is measured and the time constant can be extracted. The time constant can be thought of as the time for the temperature difference between the bead and the gas to decay to 1/e of its initial value. In this way, the time constant is measured directly and does not require the direct calculation of h. An example of the theoretical signal and actual measured signal coming from a thermocouple after such a heating current is seen in Figure 8, reproduced from [71]. One can see initially that the thermocouple response is closely approximated by exponential decay (the theoretical solution) in the initial transient region. If several heating cycles are performed, an average local time constant can be determined. An alternate, simpler technique is to estimate the convective coefficient using a correlation, such as Equation 23. Then Equation 24 can be used to estimate the time constant. This latter approach is adopted in this work. For further details of this approach see Raffan[60]. For more information on heating circuits and the temperature compensation techniques see Ghoddoussi [71], Cruz [7] and Raffan [60]. Typical values of the temperature time constant varied between 1.5 and 3.0 ms, depending on the local flow conditions.

The voltage change of a type-K thermocouple for a given temperature change is well characterized. However the thermocouple needs to be calibrated to convert this temperature change to an absolute temperature. Therefore if a known temperature, say an ice bath at 0 ^{o}C, is applied to an uncompensated thermocouple, a reference voltage may be recorded. The voltage change relative to this reference voltage can be used to convert

temperatures relative to 0 ^{o}C. Boiling water, nominally at 100 ^{o}C, or room temperature air (measured by a reference thermocouple) can also be used as reference conditions or can be used to verify the microthermocouple probe. Many thermocouple data acquisition systems come with this reference temperature circuit built into the thermocouple data processing. However this internal calibration often reduces the high frequency response of the thermocouple, necessitating the use of an external thermocouple calibration like the one described above. In this study, an ice water bath was used to calculate the reference conditions.

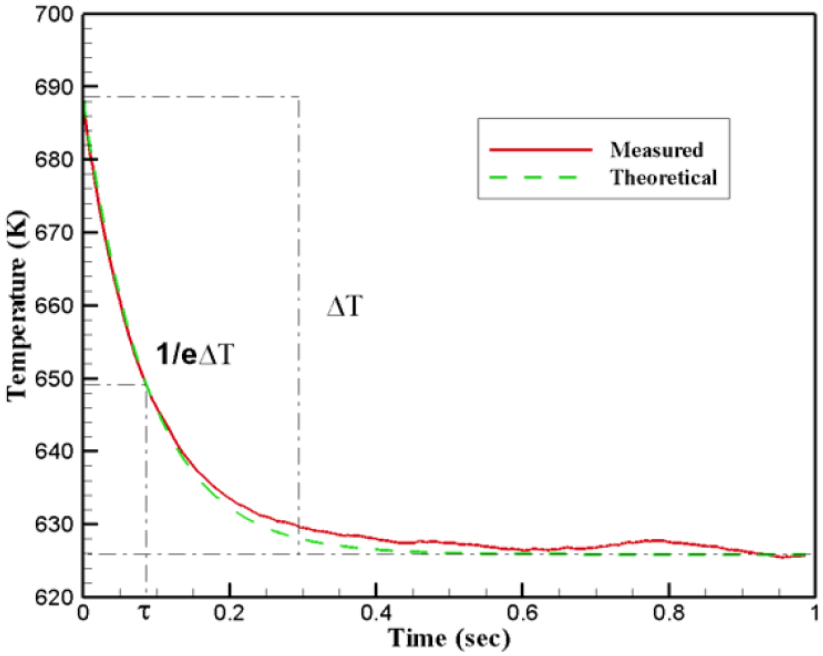

Figure 8. A typical thermocouple response to a heat cycle used to determine thermocouple time constant information. Adapted from Ghoddoussi [71].

2.1.3 Discussion of Conduction and Radiation

The non-adiabatic cases are performed such that there is a heat flux through the wall. In these cases, the wall heat transfer rate can be calculated according to Equation 23 from §1. This equation assumes 1D wall-normal heat conduction in the plate, which

holds because the plate is thin and has a large temperature difference across the plate. Since the UDEL conductivity and the plate thickness are known, the heat transfer can be calculated using the known wall temperature and backside temperature. The backside wall temperature is approximately uniform and is measured with an array of backside wall thermocouples. The flow-side wall temperature is measured with the microthermocouple probe, described previously.

In the non-adiabatic cases, the backside of the test plate is water cooled to approximately 10 ^{o}C. In actuality, the backside temperature is slightly variable along the length of the plate but the total variation is less than 3 ^{o}C. The actual distribution of backside wall temperature will be shown in §3. As is shown in Figure 6b, the heat exchanger is a co-flow device, in that the water flows in the same direction as the hot air. Since the wall is thin compared to the test plate's other dimensions and made of a thermal plastic with a small thermal conductivity, axial and spanwise heat conduction can be neglected. Additionally the temperature gradient in the wall is primarily in the wall-normal direction further validating this assumption. When the experiment has reach a steady-state, the averaged, wall heat flux via conduction is approximated by Equation 25. Here T_{solid}, T_{wall}, T_{back} and t_{wall} refer to the temperature in the solid, the flow side wall temperature, the back side wall temperature and the thickness of the test plate wall, respectively.

$$\vec{q}''_{conduction} = -k_{wall}\nabla T_{solid} \approx -k_{wall}\frac{\partial T_{solid}}{\partial y} \approx -k_{wall}\frac{\left(T_{wall} - T_{back}\right)}{t_{wall}} \qquad \text{Eq. (25)}$$

Due to the nature of this experiment and the relative differences between the test plate temperature and the casing temperature, thermal radiation heat transfer should not be entirely ignored. Fortunately, at these relatively low temperatures (when compared to rocket conditions) the working gas (air) is radiatively non-participating. The casing, however, does interact with the test plate wall. Since the experiment is an enclosure, a grey, diffuse surface is assumed, where re-reflections are ignored. These assumptions allow for a view factor analysis to approximately hold for the radiatively interacting surfaces. The definition of the view factor, $VF_{j\rightarrow i}$, from surface j to surface i is described by Equation 26 [72].

$$VF_{j\rightarrow i} = \frac{1}{A_j}\int_{A_i}\int_{A_j}\frac{\cos(\theta_i)\cos(\theta_j)}{\pi m^2}dA_j dA_i \qquad \text{Eq. (26)}$$

Note that the small solid angle relation is employed to remove the integration over the solid angle and instead integrate over surface A_j. Here m is the path length of the radiative ray, while θ is the angles made between incident or leaving radiation and the surface. The view factor can be thought of as the percentage of radiation leaving surface j that is intercepted by surface i. It is entirely determined by the geometry of the radiating surfaces. The majority of the wind tunnel is stainless steel, with an emissivity, ε_{ss}, of 0.20 [72]. The UDEL test plate has an emissivity, ε_{wall}, of approximately 0.91 [7]. Once again using the grey, diffuse surface assumptions, ignoring re-reflections, the net radiative heat flux on the test plate is given by Equation 27 [73]. This approach is taken duo to two main reasons. Firstly, when re-reflections are considered, the test plate begins to interact with itself, creating a coupled, multi-body problem due to the non-uniform temperature

along the test plate. Coupled with the fact the casing temperature distribution is known with a limited fidelity, the use of a higher order approach is not necessarily justified.

$$\dot{q}''_{radiation} = \varepsilon_{wall}\varepsilon_{SS}VF\sigma\left(T^4_{casing} - T^4_{wall}\right) \qquad \text{Eq. (27)}$$

2.1.4 Test Matrix

Table 3 shows a summary of the different experimental test conditions. The table is divided into two separate thermal wall boundary conditions: adiabatic and non-adiabatic. These two boundary conditions are further sub-divided into the three film cooling shear regimes: wall wake, minimum shear and wall jet. For the non-adiabatic cases, an average backside wall temperature, T_{back}, is provided. When combined with the wall temperature on the flow side and knowledge of thermal properties, the backside wall temperature allows for a heat flux to be calculated, as discussed above. Since the conditions between the adiabatic cases and the non-adiabatic cases are similar (in terms of kinematic mixing), a convective heat transfer coefficient can be formed from the non-adiabatic wall temperature, the adiabatic wall temperature and the wall heat flux using Eqn. 7 in §1.2. Also it should be noted here that the slot height changes for all the cases, especially between the adiabatic and non-adiabatic cases. Thermal expansion occurred in the adiabatic cases, so in an attempt to reduce the thermal expansion the slot was changed before the non-adiabatic cases and this resulted in the reduced thermal expansion effects for these cases. In terms of convention here, U_{slot} refers to the maximum velocity in the slot. Normally the film cooling literature uses the bulk velocity U_C to characterize the coolant flow; however since this quantity is an integral measure over the slot height, it is susceptible to the PIV data loss near the wall and therefore is not reported. Also it should be noted that all slot Reynolds numbers correspond to turbulent flow.

Table 3. Test Matrix of Experimental Film Cooling Conditions.

	Adiabatic Cases			Non-Adiabatic Cases		
	Wall Wake	Minimum Shear	Wall Jet	Wall Wake	Minimum Shear	Wall Jet
U_{slot} (m/s)	11.2	20.4	23.1	11.3	20.4	20.6
U_{∞} (m/s)	24.7	20.9	11.1	26.0	21.6	11.4
T_c (K)	295.1	286.1	294.0	313.5	301.8	300.8
T_{∞} (K)	463.2	455.2	464.5	457.9	451.3	460.5
VR	0.5	1.0	2.1	0.4	0.9	1.8
TR	1.6	1.6	1.6	1.5	1.5	1.5
BR	0.7	1.6	3.3	0.6	1.4	2.8
s (mm)	6.1	5.7	5.3	4.1	4.2	3.9
Re_s	4186	7787	7622	2457	4998	4723
T_{back} (K)				288	283	286

2.1.5 Experimental Uncertainty

An uncertainty analysis following the guidance of Cruz [7] and Raffan [60] is carried out to quantify the typical errors of the different experimental measurements and provide confidence in these measurements. In experimental error analysis, measurement errors are normally subdivided into two categories: systematic (or deterministic) errors and random (or stochastic) errors. Random errors are normally due to unsteadiness and physical processes that cause random fluctuations about the true value. An example of this would be uncontrolled environmental variations or slight variations in boundary conditions. Systematic errors meanwhile are a repeatable bias that can be determined prior to an experiment. An example of a systematic error is an intrusive probe, which perturbs the flow and alters the flow, thus biasing it. Another example of a systematic error occurs when improperly calibrating. In an ideal world the systematic error can be removed such that only random errors, which are not biased, remain.

Providing the measurement error is important; however sometimes reported quantities are dependent on multiple measurements. The Reynolds number is an example. In order to compute the uncertainty of a derived quantity, the errors from the constitutive components must be propagated to form a new uncertainty. Consider a derived quantity, G, that is a function, g, of N different measurements, $f_1 \ldots f_N$, as is seen in Equation 28.

$$G = g\left(f_1, f_2, ..., f_N\right) \qquad \text{Eq. (28)}$$

Since each measurement has its own uncertainty, the derived quantity in general will have some different propagated uncertainty. When the uncertainties of the measurements are normally distributed (most physical processes are) and are not correlated, the propagated uncertainty is shown in Equation 29.

$$\xi = \Delta G = \sqrt{\left(\frac{\partial g}{\partial f_1}\Delta f_1\right)^2 + \left(\frac{\partial g}{\partial f_2}\Delta f_2\right)^2 + \cdots + \left(\frac{\partial g}{\partial f_N}\Delta f_N\right)^2} \qquad \text{Eq. (29)}$$

A summary of the experimental uncertainties is reported in Table 4. The velocities have a relative uncertainty of about 2-3%. As was stated earlier, since a particle Stokes number of 0.2 is maintained, particles faithfully follow 98 % of the flow structures. Additional errors and uncertainties come from out-of-plane motion, algorithmic detection of velocity vectors, calibration uncertainty and spatial resolution of the camera. These errors are detailed more in depth in Raffan [60], where a final uncertainty estimate of approximately 3% was found. The slot height was determined from a calibrated, focused image using the PIV camera. The resolution of the image and hence this measurement was 0.05 mm.

Table 4. Table with estimated uncertainty of the experimental measurements.

	Nominal Value	Uncertainty	Relative Uncertainty (%)
	Measured Directly		
U_c (m/s)	19	0.3	1.6
U_∞ (m/s)	11	0.3	2.7
T_c (K)	294	1.3	0.4
T_∞ (K)	465	1.3	0.3
T_{back} (K)	283	1.1	0.4
T_{casing} (K)	420	1.1	0.3
s (mm)	5.3	0.05	0.9
	Propagated Uncertainty		
η	1.00	0.004	0.4
VR	1.7	0.05	3.1
TR	1.6	0.003	0.2
BR	2.7	0.09	3.1
Re_s	6352	110	1.7
$q_{radiation}$ (W/m^2)	191.7	4.9	2.6
$q_{conduction}$ (W/m^2)	68.8 - 190.2	6.3	3.3 - 9.1

In terms of the thermal measurements, the manufactures of the type-K thermocouples used in the experiment report an uncertainty of 1.1 ^oC. However this uncertainty is valid for a single measurement. Under well-controlled conditions (ambient air, quiescent flow and ice water bath), the mean temperature consistently showed variations much smaller than 1.1 ^oC. This finding seems to suggest that the thermocouple is suffering from a systematic error that consistently biases the results. The mean thermal fluctuations in the laboratory study showed variations on the order of 0.25 ^oC, which is likely due to the resolution of the DAQ system. Typically the radiative error was also found to be less than 0.20 ^oC. Therefore if the same thermocouple is used to take all the measurements in an operation involving differences in temperature, like the effectiveness, the systematic errors cancel and the 0.25 ^oC random error and the radiative errors dominate the uncertainty. However if different thermocouples are used, each

thermocouple can have a 1.1 ^{o}C systematic error that does not necessarily cancel. Table 4 shows the uncertainties of the various quantities along with their relative uncertainties. For the most part, quantities have an uncertainty smaller than 5%, with finer relative accuracy seen in the temperature fields. Please note that the uncertainty in emissivity and thermal conductivity were not included in the uncertainty analysis.

2.2 **Numerical Approach**

Another major aspect of this research involves the numerical simulation of the film cooling physics. As was described in Chapter 1, an LES approach was selected to simulate the film cooling experiments that will be presented in Chapter 3. LES BLAC, an in-house LES CFD code, was originally developed by Anthony Keating [74] and is used in the current research. As part of this work, LES BLAC had to be modified to account for non-passive scalars and changes in density due to thermal mixing. Therefore the LES equations and their implentation in LES BLAC are described below. Next validation cases are presented to assess the suitability of LES BLAC in this research. Finally, the numerical methodology for film cooling, including numerical boundary conditions, are presented. Detailed discussion of the film cooling grids and grid independence will be reserved for §4.

2.2.1 Navier Stokes Equations

LES BLAC is used to solve the Navier-Stokes equations under the low-Mach number assumption. Equations 30 and 31 show the spatial coordinate direction vector, x_i, and velocity vector, u_i, written in both vector and indicial notation. LES BLAC features the solution of two scalars: mixture fraction, f, and enthalpy, h shown in Eqn 32. In this work, air is the only gas species considered, so the mixture fraction does not need to be

calculated and will not be reported in the subsequent discussions. The index k is used exclusively for indexing the scalar being used and is not a tensor or vector designation. Therefore the typical arithmetic rules involving repeated indices and matrix multiplication do not hold for the scalar index. The Navier-Stokes equations in differential form are written in Eqns 33-34 using indicial notation and assuming the flow is a Newtonian fluid and has a low-Mach number (M < 0.3). Body and chemical source terms are not included in the following analysis. Eqns 33-34 have already been cast in non-dimensional form using characteristic length, velocity and temperature scales. The strain rate tensor and the Kroenecker delta tensor are given in Equations 35 and 36, respectively.

$$x_{i=1,2,3} = \vec{x} = \langle x, y, z \rangle \qquad \text{Eq. (30)}$$

$$u_{i=1,2,3} = \vec{u} = \langle u, v, w \rangle \qquad \text{Eq. (31)}$$

$$\phi_1 = f \qquad \text{Eq. (32)}$$
$$\phi_2 = h$$

$$\frac{\partial \rho}{\partial t} + \frac{\partial}{\partial x_i}\left(\rho u_i\right) = 0,\ i = 1..3 \qquad \text{Eq. (33)}$$

$$\frac{\partial \rho u_i}{\partial t} + \frac{\partial}{\partial x_j}\left(\rho u_i u_j\right) = -\frac{\partial p}{\partial x_i} + \frac{1}{\mathrm{Re}}\frac{\partial}{\partial x_j}\left(2\mu S_{ij}\right),\ i = 1..3,\ j = 1..3 \qquad \text{Eq. (34)}$$

$$S_{ij} = \frac{1}{2}\left(\frac{\partial u_i}{\partial x_j} + \frac{\partial u_j}{\partial x_i}\right) - \frac{1}{3}\frac{\partial u_k}{\partial x_k}\delta_{ij},\ i = 1..3,\ j = 1..3,\ k = 1..3 \qquad \text{Eq. (35)}$$

$$\delta_{ij} = \begin{cases} 1\ if\ i = j \\ 0\ if\ i \neq j \end{cases},\ i = 1..3,\ j = 1..3 \qquad \text{Eq. (36)}$$

The enthalpy and mixture fraction equations are written in Equation 37, while the equation of state is represented in Equation 38. Due to the low-Mach number assumption,

terms such as viscous dissipation have been neglected from the enthalpy equation, as it has Mach number dependence. Thermal radiation in the gas phase is also ignored in the energy equation because in the current experimental regime, air is not radiatively participating. The pressure term is similarly absent from the enthalpy equation because the acoustic physics are being neglected. By ignoring compressibility and acoustics, i.e. the low-Mach number assumption, the pressure fluctuations are assumed to be decoupled from thermodynamic fluctuations, such as changes in density, enthalpy and entropy. This assumption implies the speed of sound is infinite. With an infinite speed of sound, pressure gradients cannot cause density variations. The pressure can then be decoupled into a perturbation pressure (also called the dynamic pressure), p, and a thermodynamic, or background, pressure, p_o, as is seen in Equation 39. The thermodynamic pressure does not appear in the momentum equation because its spatial derivative is zero under the low-Mach assumption, due to the infinite speed of sound. The dynamic pressure, p, is therefore the highest order pressure term that appears in the momentum equation, while the thermodynamic pressure is used in the equation of state. The thermodynamic pressure can only change in time due to a pressure change at an open boundary. However the thermodynamic pressure in this work is held constant in time, which is why it was not included in the enthalpy equation. It should be noted, that cast with Mach number scaling, the pressure gradient term in the momentum equation is divided by γM^2, which is why the perturbation pressure gradient in Equation 34 does not have a coefficient in front of it.

$$\frac{\partial \rho \phi_k}{\partial t} + \frac{\partial}{\partial x_j}\left(\rho \phi_k u_j\right) = \frac{1}{\mathrm{Re}\,\mathrm{Pr}_k}\frac{\partial}{\partial x_j}\left(\rho \alpha_k \frac{\partial \phi_k}{\partial x_j}\right) + \rho \omega_k \ , \ i = 1..3, \ k = 1..2 \qquad \text{Eq. (37)}$$

$$\rho = g(\phi_k),\ k = 1..2 \qquad \text{Eq. (38)}$$

$$P = p_o(t) + \gamma M^2 p(x_i, t) + O\left((\gamma M^2)^2\right) \qquad \text{Eq. (39)}$$

The ideal gas law is used as the equation of state in this work. In order to solve for the density, using the ideal gas law and low-Mach number assumption, the molecular weight, thermodynamic pressure and flow temperature must be known. The temperature is calculated from the scalar fields; in this case, the only scalar necessary is the enthalpy given that air is the sole gas species. Chemkin polynomials are used to write the enthalpy and heat capacity of air in terms of temperature. A Newton-Raphson iterative solver is then employed to reconstruct temperature from the enthalpy. Once the temperature is known, the density can then be calculated. Similarly the variations in viscosity and diffusivity due to temperature changes can be calculated through the use of Sutherland's Law.

2.2.2 LES Equations

In an LES approach, the Navier-Stokes equations are not directly solved, as that would require grid and time resolution on the order of the Kolmogorov scales, representing a massive cost for flows of engineering interest. Rather the Navier-Stokes equations are filtered, which can be thought of as a type of spatial and temporal average. Variables can then be represented as the sum of the filtered variable and a fluctuation. Density for example is written in Equation 40, where an overbar denotes a filtered quantity and a prime denotes a fluctuating quantity. The term fluctuating may be misleading as the filtered quantity can vary in both space and time. The fluctuating

component relates the unfiltered and filtered quantities, or is a fluctuation off of the filtered quantity. A mathematical representation of a filtering operation is shown in Equation 41. A filtered variable is the integral of the unfiltered variable times a given filter. In finite-difference codes, like LES BLAC, a top-hat filter is normally used, the equation for which is shown in Equation 42. Plugging in the filter definition, the filtered quantity is similar to the average of the unfiltered quantity over some filter width, Δ.

$$\rho = \overline{\rho} + \rho' \qquad \text{Eq. (40)}$$

$$\overline{g}(x) = \int g(x')G(x',x,\Delta)dx' \qquad \text{Eq. (41)}$$

$$G(x_0,x) = \begin{cases} 1/\Delta \ \ if \ \ |x - x_0| \le \Delta/2 \\ 0 \qquad otherwise \end{cases} \qquad \text{Eq. (42)}$$

For variable-density LES flows, the primary variables are Favre-averaged, or weighted by density in order to make the Navier Stokes equations more tractable. The Favre-averaged velocity for example, is the filtered quantity of the product of density and velocity divided by the filtered density, as is seen in Equation 43. The unfiltered velocity can then be decomposed into its Favre-averaged component and a Favre-Averaged fluctuating component denoted by a double-prime. Filtering the governing equations presented in §2.2.1 (Eqns. 33-35, 37, 38), in tandem with the use of Favre-averaged quantities, results in the filtered Navier-Stokes, scalar and state equations, shown in Equations 43-49.

$$\tilde{u} = \frac{\overline{\rho u}}{\overline{\rho}} \qquad \text{Eq. (43)}$$

$$u = \tilde{u} + u'' \qquad \text{Eq. (44)}$$

$$\frac{\partial \overline{\rho}}{\partial t} + \frac{\partial}{\partial x_i}\left(\overline{\rho}\tilde{u}_i\right) = 0, \ i = 1..3 \qquad \text{Eq. (45)}$$

$$\frac{\partial \overline{\rho}\tilde{u}_i}{\partial t} + \frac{\partial}{\partial x_j}\left(\overline{\rho}\tilde{u}_i\tilde{u}_j\right) = -\frac{\partial \overline{p}}{\partial x_i} + \frac{1}{\mathrm{Re}}\frac{\partial}{\partial x_j}\left(2\overline{\mu}\tilde{S}_{ij}\right) + \frac{\partial t_{ij}}{\partial x_j},\ i = 1..3,\ j = 1..3 \quad \text{Eq. (46)}$$

$$\tilde{S}_{ij} = \frac{1}{2}\left(\frac{\partial \tilde{u}_i}{\partial x_j} + \frac{\partial \tilde{u}_j}{\partial x_i}\right) - \frac{1}{3}\frac{\partial \tilde{u}_k}{\partial x_k}\delta_{ij},\ i = 1..3,\ j = 1..3,\ k = 1..3 \quad \text{Eq. (47)}$$

$$\frac{\partial \overline{\rho}\tilde{\phi}_k}{\partial t} + \frac{\partial}{\partial x_i}\left(\overline{\rho}\tilde{\phi}_k\tilde{u}_i\right) = \frac{1}{\mathrm{Re}\,\mathrm{Pr}_k}\frac{\partial}{\partial x_i}\left(\overline{\rho}\tilde{\alpha}_k\frac{\partial \tilde{\phi}_k}{\partial x_i}\right) + \frac{\partial q_{ik}}{\partial x_i} + \overline{\rho}\tilde{\omega}_k,\ i = 1..3,\ k = 1..2 \quad \text{Eq. (48)}$$

$$\overline{\rho} = g\left(\tilde{\phi}_k\right),\ k = 1..2 \quad \text{Eq. (49)}$$

A few standard LES assumptions should be noted here. First the filtered viscosity and diffusivity are assumed to be functions of the Favre-Averaged temperature only. Similarly the filtered density also relies on the Favre-Averaged temperature, calculated from the Favre-Averaged enthalpy. The terms t and q represent the subgrid-scale shear stress tensor (analogous to the Reynolds stresses in RANS modeling) and subgrid-scale heat flux vector, respectively. In LES approaches, these terms need to be modeled or closed. These subgrid-scale terms represent the effect of the unresolved scales on the filtered or resolved scales. The pressure is solved via a Poisson equation that acts to conserve mass.

2.2.3 Subgrid-scale Turbulence Modeling

Many subgrid-scale LES models, including the ones used in this study, are based on the eddy-diffusion hypothesis, where the subgrid-scales act as enhanced diffusion and dissipation on the filtered variables through a turbulent, or eddy, viscosity and diffusivity. This assumption holds well for Kolmogorov turbulence in which the turbulence cascade and separation of turbulent scales exist. In this type of turbulence, the small scale motion is more uniform, diffusive and dissipative in nature, supporting the use of the eddy-diffusion hypothesis. The eddy-diffusion, subgrid-scale shear stress tensor and the

subgrid-scale heat flux are seen in Equations 50 and 51, respectively. Here μ_t and α_t represent the subgrid-scale eddy viscosity and diffusivity, respectively.

$$t_{ij} = -\overline{\rho}\widetilde{u_i u_j} + \overline{\rho}\tilde{u}_i\tilde{u}_j = 2\mu_t\tilde{S}_{ij},\ i = 1..3,\ j = 1..3 \qquad \text{Eq. (50)}$$

$$q_{ik} = -\overline{\rho}\widetilde{u_i\phi_k} + \overline{\rho}\tilde{u}_i\tilde{\phi}_k = \overline{\rho}\alpha_t\frac{\partial\tilde{\phi}_k}{\partial x_i},\ i = 1..3,\ k = 1..2 \qquad \text{Eq. (51)}$$

Most LES subgrid-scale models use a form of the dynamic procedure [75] to calculate the eddy viscosity and diffusivity. In essence, the dynamic procedure uses resolved information on the scales just larger than the filter width to model the subgrid-scale motions. According to the turbulent cascade, the smallest scales of the flow behave similarly. Therefore if the grid filter is appropriately small (i.e. in the inertial range), the scales just larger than the filter length should behave similar to the scales smaller than the filter length. In practice, variables are filtered over both the standard filter width and a larger test filter width (normally twice the filter width). These filtered and test filtered quantities are used to calculate the modeled coefficients in the eddy-diffusion model. If the grid is not carefully selected and the grid filter is outside the intertial range then the scale similarity breaks down and the justification for the LES approach becomes suspect.

Next the development of the dynamic procedure will be described more specifically to derive the relationships for the subgrid-scale shear stress tensor and heat flux. The subgrid-scale shear stress tensor is dependent on velocity. Shown in Eq. 52, the filtered subgrid-scale shear stress tensor can be decomposed into two components: 1. the regular subgrid-scale shear stress tensor based on the filtered velocity, and 2. A modeled term based on the filtered velocity. A test filtered quantity is denoted as a hat or using the notation in Equation 53. If a test filter is applied to this filtered subgrid-scale shear stress

tensor, the regular and modeled terms are based off of the test filtered velocity as is seen in Equation 54. Subtracting a test-filtered, subgrid-scale shear stress tensor from the

$$\widehat{\overline{t(u)}} = t(\widehat{\overline{u}}) + m(\widehat{\overline{u}}) \qquad \text{Eq. (52)}$$

$$[ab]^* = \widehat{ab} \qquad \text{Eq. (53)}$$

$$\overline{t(u)} = t(\overline{u}) + m(\overline{u}) \qquad \text{Eq. (54)}$$

regular subgrid-scale shear stress tensor (based on the test-filtered velocity) results in Equation 55. As can be seen in Equation 56, the modeled term is normally some coefficient, c, multiplied by some gradient term, s, that is dependent on the filter width and the filtered velocity. Using Equation 56, Equation 55 is rewritten in terms of c and s to form Equation 57.

$$\widehat{t(\overline{u})} - t(\widehat{\overline{u}}) = m(\widehat{\overline{u}}) - \widehat{m(\overline{u})} \qquad \text{Eq. (55)}$$

$$m(\overline{u}) = c\, s(\overline{u}, \Delta) \qquad \text{Eq. (56)}$$

$$\widehat{t(\overline{u})} - t(\widehat{\overline{u}}) = [c]^* s(\widehat{\overline{u}}, \widehat{\Delta}) - [cs(\overline{u}, \Delta)]^* \qquad \text{Eq. (57)}$$

Since the grid filter and test filter scales behave similarly, the coefficient c and $[c]^*$ are assumed to be constant. This equation is known as Germano's identity [75], which allows for the calculation of the modeled coefficient. Prior to this identity, this coefficient was specified or modeled, involving a bit of empiricism and making the coefficient unresponsive to local changes in the flow. Germano's identity can be rewritten as

$$L = c\, M \qquad L = \widehat{t(\overline{u})} - t(\widehat{\overline{u}}) \qquad M = s(\widehat{\overline{u}}, \widehat{\Delta}) - \widehat{s(\overline{u}, \Delta)} \qquad \text{Eq. (58)}$$

where L and M are referred to as the Leonard Stress Tensor and the Modeled Stress Tensor, respectively. Now it should be noted that since L and M are tensors, there are a number of solutions for the coefficient c. c is normally averaged as shown in Equation 59.

$$c = \frac{\langle L \cdot M \rangle}{\langle M \cdot M \rangle} \qquad \text{Eq. (59)}$$

In this work, Lagrangian averaging is used, which was introduced originally by Meneveau et al. [76]. This type of averaging is based upon averaging over a given fluid parcel's motion and was shown to remove sharp fluctuations in the eddy viscosity that can cause simulations to become unstable.

The dynamic smagorinsky model is used for the calculation of the turbulent subgrid-scaled viscosity. The Smagorinsky equation for the eddy viscosity is shown in Equation 60 and is

$$\mu_t = C_s \bar{\rho} \Delta^2 \left|\tilde{S}\right| \qquad \text{where} \qquad \left|\tilde{S}\right| = \sqrt{\tilde{S}_{ij}\tilde{S}_{ij}} \qquad \text{Eq. (60)}$$

written in terms of the Smagorinsky coefficient, the filter size and the magnitude of the shear stress tensor. In the dynamic procedure for the momentum equation, the Leonard Stress, L, and Model Stress, M, can be calculated based on the resolved flow field properties. They are reproduced below in Equations 61 and 62.

$$L_{ij} = -\widehat{\bar{\rho}\tilde{u}_i\tilde{u}_j} + \hat{\bar{\rho}}\frac{\widehat{\bar{\rho}\tilde{u}_i}}{\hat{\bar{\rho}}}\frac{\widehat{\bar{\rho}\tilde{u}_j}}{\hat{\bar{\rho}}} \qquad \text{Eq. (61)}$$

$$M_{ij} = \hat{\bar{\rho}}(\hat{\Delta}^2)\frac{\widehat{\bar{\rho}\left|\tilde{S}\right|}}{\hat{\bar{\rho}}}\frac{\widehat{\bar{\rho}\tilde{S}_{ij}}}{\hat{\bar{\rho}}} - [\bar{\rho}\Delta^2\left|\tilde{S}\right|\tilde{S}_{ij}]^* \qquad \text{Eq. (62)}$$

The turbulent subgrid-scale eddy diffusivity is also calculated using a form of the dynamic smagorinsky model and is shown in Equation 63. The coefficient, C_A, is analogous to the momentum coefficient, C_s. The analogous Leonard stress term, denoted F, and Modeled stress term, denoted K, are shown in Equations 64 and 65, respectively. This results in the dynamic coefficient reported in Equation 66, which was first done by Moin et al. [77].

$$\alpha_t = C_A \Delta^2 \left| \tilde{S} \right| \qquad \text{Eq. (63)}$$

$$F_i = -[\bar{\rho}\tilde{u}_i\tilde{\phi}]^* + \hat{\bar{\rho}}\frac{\widehat{\bar{\rho}\tilde{u}_i}}{\hat{\bar{\rho}}}\frac{\widehat{\bar{\rho}\tilde{\phi}}}{\hat{\bar{\rho}}} \qquad \text{Eq. (64)}$$

$$K_i = \hat{\bar{\rho}}(\hat{\Delta}^2)\frac{\widehat{\bar{\rho}\left|\tilde{S}\right|}}{\hat{\bar{\rho}}}\frac{\widehat{\bar{\rho}\frac{\partial\tilde{\phi}}{\partial x_i}}}{\hat{\bar{\rho}}} - [\bar{\rho}\Delta^2\left|\tilde{S}\right|\frac{\partial\tilde{\phi}}{\partial x_i}]^* \qquad \text{Eq. (65)}$$

$$c_A = \frac{\langle F_{ij} \cdot K_{ij} \rangle}{\langle K_{ij} \cdot K_{ij} \rangle} \qquad \text{Eq. (66)}$$

2.2.4 Numerical Algorithms and Implementation of the LES Equations

LES BLAC is a second-order accurate in space and time, finite-difference CFD code that solves the filtered Navier-Stokes Equations using a low-Mach number assumption and is based largely on the works of Keating [74] and Pierce [78]. All tildas and overbars from the governing equations have been dropped as the LES filtering is now implied. Before presenting the fully discrete equations, a compact notation will be introduced to make the discrete equations tractable. Since some of the variables are staggered with respect to other variables, it is helpful to define an interpolation operator, as is seen in Equation 67. In this equation, the u velocity interpolated in x and y are shown. When stretched grids are used, it becomes possible to write alternate forms of interpolation. However in the present work, grid stretching was achieved gradually thus making the interpolation error a higher order effect. Also it was found that while a more accurate interpolation scheme could be devised, in terms of non-linear stability, the interpolation operators defined in Equation 67 work well [78]. A discrete finite-difference operator is defined in Equation 68 for both streamwise and wall-normal derivatives. Note that both the interpolation and the finite-difference operators calculate values that are

somewhere in between the velocity locations involved in the operation. The indexing notation was carefully selected here because of the staggered mesh that is featured in LES BLAC.

$$\overline{u}^{x}\Big]_{l,m} = \frac{u_{l+1/2,m} + u_{l-1/2,m}}{2}; \qquad \overline{u}^{y}\Big]_{l,m} = \frac{u_{l,m+1/2} + u_{l,m-1/2}}{2} \qquad \text{Eq. (67)}$$

$$\delta_x(u)\Big]_{l,m} = \frac{u_{l+1/2,m} - u_{l-1/2,m}}{\Delta x}; \qquad \delta_y(u)\Big]_{l,m} = \frac{u_{l,m+1/2} - u_{l,m-1/2}}{\Delta y} \qquad \text{Eq. (68)}$$

Introduced originally by Harlow and Welsh [79], velocity components are staggered both in space and time with respect to scalars like pressure, density, temperature and enthalpy. This staggering is set up to avoid the common "checkerboarding" error when evaluating derivatives in pressure in the momentum equations. Also evaluating the continuity equation without interpolation becomes easy. In fact, the derivatives in the continuity equation are all second order accurate because of the staggering used. A schematic of the space and time discretization is shown in Figure 9. When variables are multiplied or added, they must be located at the same location and instant in time to make sense, which necessitates interpolation on the staggered mesh. Before presenting the discrete LES equations, it is helpful to define a mass flux operator as is shown in Equation 69.

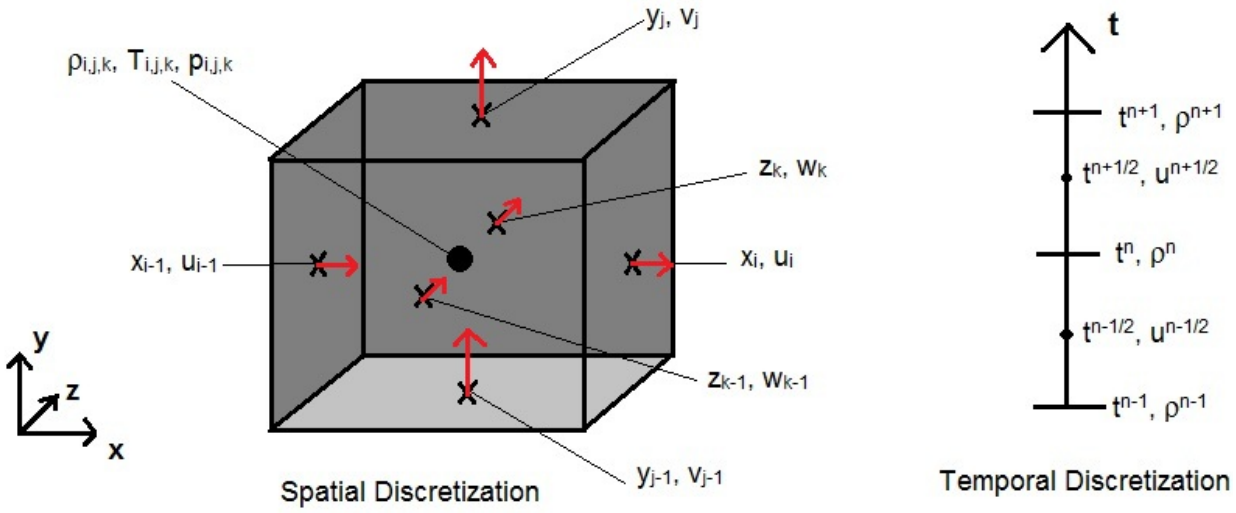

Figure 9. Schematic of the spatial and temporal discretization in LES BLAC.

$$r_j = \overline{\overline{\rho}^{x_j}}^{t} u_j \qquad \text{Eq. (69)}$$

Notice that this mass flux is a vector and is collocated with velocity in both space and time. Using this notation, the discrete LES equations are shown in Eqns. 70-72. Overbars, which denote interpolation, do not follow the summation rules of indicial notation. As an example, the continuity equation shown in Eqn. 70 is expanded and written in discrete form in Equation 74.

$$\delta_t(\rho) + \delta_{x_j}(r_j) = 0 \qquad \text{Eq. (70)}$$

$$\delta_t(r_j) + \delta_{x_j}\left(\overline{\overline{r}_j^{x_i}}^{t}\,\overline{\overline{u}_i^{x_j}}^{t}\right) = -\delta_{x_i}(p) + \delta_{x_j}(\tau_{ij}) \qquad \text{Eq. (71)}$$

$$\tau_{ij} = \begin{cases} 2\mu\left[\delta_{x_j}(\overline{u}_i^{t}) - \frac{1}{3}\delta_{x_k}(\overline{u}_k^{t})\delta_{ij}\right] & if\ i = j \\ \overline{\overline{\mu}^{x_i}}^{x_j}\left[\delta_{x_j}(\overline{u}_i^{t}) + \delta_{x_i}(\overline{u}_j^{t})\right] & if\ i \neq j \end{cases} \qquad \text{Eq. (72)}$$

$$\delta_t(\rho\phi) + \delta_{x_j}\left(r_j\,\overline{\overline{\phi}^{x_j}}^{t}\right) = \delta_{x_j}\left(\overline{\overline{\rho\alpha}^{x_j}}^{t}\,\delta_{x_j}(\overline{\phi}^{t})\right) \qquad \text{Eq. (73)}$$

$$\frac{\rho_{i,j,k}^{n+1} - \rho_{i,j,k}^{n}}{\Delta t} + \left[\frac{\left(\rho_{i+1,j,k}^{n+1} + \rho_{i,j,k}^{n+1} + \rho_{i+1,j,k}^{n} + \rho_{i,j,k}^{n}\right)u_{i,j,k}^{n+1/2} - \left(\rho_{i,j,k}^{n+1} + \rho_{i-1,j,k}^{n+1} + \rho_{i,j,k}^{n} + \rho_{i-1,j,k}^{n}\right)u_{i-1,j,k}^{n+1/2}}{4\Delta x}\right] +$$
$$\left[\frac{\left(\rho_{i,j+1,k}^{n+1} + \rho_{i,j,k}^{n+1} + \rho_{i,j+1,k}^{n} + \rho_{i,j,k}^{n}\right)v_{i,j,k}^{n+1/2} - \left(\rho_{i,j,k}^{n+1} + \rho_{i,j-1,k}^{n+1} + \rho_{i,j,k}^{n} + \rho_{i,j-1,k}^{n}\right)v_{i,j-1,k}^{n+1/2}}{4\Delta y}\right] + \qquad \text{Eq. (74)}$$
$$\left[\frac{\left(\rho_{i,j,k+1}^{n+1} + \rho_{i,j,k}^{n+1} + \rho_{i,j,k+1}^{n} + \rho_{i,j,k}^{n}\right)w_{i,j,k}^{n+1/2} - \left(\rho_{i,j,k}^{n+1} + \rho_{i,j,k-1}^{n+1} + \rho_{i,j,k}^{n} + \rho_{i,j,k-1}^{n}\right)w_{i,j,k-1}^{n+1/2}}{4\Delta z}\right] = 0$$

2.2.4.1 Time Integration

The discretized equations shown in Eq. 70-74 are fully implicit in time. Implicitness is desirable because of the stability of the regime. However implicit systems

are stable at the cost of becoming very stiff. Therefore, it is desirable normally to use some implicitness to retain stability but avoid the direct inversion of matrices, which is computationally demanding. Following the analysis of Pierce [78], the general form for a differential equation is seen in Equation 75. The temporal evaluation of the right hand side determines if the discrete method is implicit, explicit or semi-implicit. An implicit discretization, for the approach shown in Equation 76, will involve the discrete solution at time step n+1. When g is non-linear, an iterative scheme is often used to solve the equation. A Newton-Raphson iteration is one such iterative scheme that is used to solve this equation. When applying a Newton-Raphson technique, where k denotes the current iteration, Equation 76 can be manipulated into the form of Equation 77 ignoring higher order terms. Equation 77 written in delta form is shown in Equation 78. If the Jacobian, $\partial\square/\partial u$, is set to zero then the iterative scheme is explicit, while the entire time-integration scheme is said to be implicit [78]. The explicitness refers to whether the right hand side of Equation 76, is evaluated at the k or k+1 iteration, while the implicitness refers to whether the right hand side is evaluated at time step n or n+1 or some combination therein. Pierce [78] showed that this approach is non-linearly stable and the linear stability has limits similar to RK-3 methods, when three iterations are used and an Euler explicit iteration is used for the first iteration. This means the initial guess for the new solution at time n+1 and iteration 1 is the value of the old solution at time n, as is seen in Equation 79.

The stiffest terms are treated using implicit iterations due to the small time step required for stability (for example the wall-normal diffusion terms). In fact, in this work only the wall-normal diffusion terms and the pressure terms are treated implicit iterations,

making the iterative semi-implicit, with implicit time integration. The pressure term is solved implicitly via a Poisson equation used to enforce mass conservation. This approach is common to low-Mach number CFD techniques involving the solutions of perturbation pressures. In this method, a predictor-corrector method is used to incorporate the pressure term into the momentum equation. The momentum equation is initially solved for without the pressure flux. The predicted velocity is then corrected for the pressure flux coming from a Poisson equation used to enforce mass conservation and will be derived later in this section. More information on this technique can be found in Kim and Moin [80].

$$\frac{du}{dt} = g(u) \qquad \text{Eq. (75)}$$

$$\frac{u^{n+1} - u^n}{\Delta t} = g\left(\overline{u}^t\right) = g\left[\tfrac{1}{2}\left(u^{n+1} + u^n\right)\right] \qquad \text{Eq. (76)}$$

$$u^{n+1,it+1} = u^n + \Delta t\ g\left[\tfrac{1}{2}\left(u^{n+1,it} + u^n\right)\right] + \tfrac{1}{2}\Delta t\left[\frac{\partial g}{\partial u}\right]\left(u^{n+1,it+1} - u^{n+1,it}\right) \qquad \text{Eq. (77)}$$

$$\left[1 - \tfrac{1}{2}\Delta t\frac{\partial g}{\partial u}\right]\left(u^{n+1,it+1} - u^{n+1,it}\right) = u^n + \Delta t\ g\left[\tfrac{1}{2}\left(u^{n+1,it} + u^n\right)\right] - u^{n+1,it} \qquad \text{Eq. (78)}$$

$$u^{n+1,it=0} = u^n \qquad \text{Eq. (79)}$$

Charles Pierce's time integration scheme [78] was used in LES BLAC and will be reviewed below. Once again the time advancement occurs from time step *n* to time step *n+1* (or from *n - 1/2* to *n + 1/2* for the velocity field) and from iteration *it* to iteration *it+1*. The initial guesses occur when *it* is equal to zero. The CFL condition is shown in Equation 80. While the time integration scheme is non-linearly stable for CFL numbers greater than 0.5, this non-linear stability limit is not well-defined. Therefore 0.5 is chosen as an upperbound of the allowable CFL condition. Notice that wall-normal diffusion is

neglected from the CFL condition since these terms are treated implicitly. Additionally the viscosity, υ, here is the summation of the laminar and subgrid-scale eddy viscosities.

$$CFL = \Delta t\left(\frac{|u|}{\Delta x}+\frac{|v|}{\Delta y}+\frac{|w|}{\Delta z}+\frac{\nu}{\Delta x^2}+\frac{\nu}{\Delta z^2}\right) \qquad \text{Eq. (80)}$$

Step 1

The predicted values or guesses are set at iteration zero. In this work, these predicted values are set to the values from the previous time step, which translates to Euler explicit for the first iteration. The only variable not set to the previous value is the density, which is extrapolated, using the continuity equation. This choice for density was found to speed convergence and has beneficial conservation properties. These initial guesses may be seen in Equation 81. It should be noted other initial guesses are possible, as the initial guess will primarily affect the number of iterations required for convergence. Not enforcing the continuity equation with the initial condition has from experience slowed convergence and can theoretically create stability issues, especially at extreme conditions. Additional variables such as temperature, viscosity and diffusivity are also initialized as the value at the last time step.

$$u_i^{n+1/2,it=0} = u_i^{n-1/2};\ \phi^{n+1,it=0} = \phi^n;\ p^{n+1,it=0} = p^n;\ \rho^{n+1,it=0} = \rho^n - \Delta t\delta_{x_j}\left(g_j^0\right) = 2\rho^n - \rho^{n-1}$$

Eq. (81)

Step 2

This step is the start of the iterative loop that will yield quantities at time n+1 once iterations converge. Each scalar equation is implicit for wall-normal diffusion, meaning a separate tri-diagonal matrix for each scalar is formed and solved using approximate factorization and the Thomas algorithm. In this step the scalar equations are solved to yield estimates for the scalar field. It should be noted that this approximate

factorization is second order accurate in time [80]. In this implementation the values of $(\rho\phi)^{n+1,it+1}$ are solved. Combined with the density from the previous iteration (or the initial guess), a provisional estimate of the scalar field can be made. This provisional estimate ϕ^* is shown in Eq. 83. Boundary conditions can then be applied to the provisional scalar field. The advection terms in the scalar field were solved using either the Quadratic Upstream Interpolation for Convective Kinematics (QUICK) [81] or a modified QUICK scheme called Bounded QUICK (BQUICK) [82]. These two techniques will be detailed and jusitified in §2.4.2.3.

$$\phi^* = \left(\rho\phi\right)^{n+1,it+1} / \rho^{n+1,it} \qquad \text{Eq. (83)}$$

The diffusivity term can be decomposed into a laminar diffusivity, α_L, and a subgrid-scale diffusivity, α_T. The laminar diffusivity is a function of temperature based on Sutherland's law and therefore is temporally located at the same time as the other scalar variables, e.g., n or n+1. The turbulent subgrid-scale diffusivity is primarily a function of the velocity field and therefore is spatially cell-centered and temporally collocated with the velocity field, e.g. n-1/2 or n+1/2. The actual term used for the diffusivity in the energy equation is shown in Eq. 84. For convenience, the discretized scalar equation using a central differencing approach is written in 2D in Appendix A.

$$\overline{\overline{\rho\alpha}^{x_j}}^{t} = \tfrac{1}{4}\left(\rho_{j+1}^{n+1,it}\alpha_{L,j+1}^{n+1,it} + \rho_{j}^{n+1,it}\alpha_{L,j}^{n+1,it} + \rho_{j+1}^{n}\alpha_{L,j+1}^{n} + \rho_{j}^{n}\alpha_{L,j}^{n}\right) + \tfrac{1}{2}\left[\tfrac{1}{2}\left(\rho_{j+1}^{n+1,it} + \rho_{j+1}^{n}\right)\alpha_{T,j+1}^{n+1/2,it} + \tfrac{1}{2}\left(\rho_{j}^{n+1,it} + \rho_{j}^{n}\right)\alpha_{T,j}^{n+1/2,it}\right] \qquad \text{Eq. (84)}$$

Step 3

Here the provisional estimates of the scalar field are used to calculate an updated density field using the equation of state, as is seen in Equation 85. More specifically, the ideal gas law is used to update the density based on the provisional temperature field.

$$\rho^{n+1,it+1} = g\left(\phi^{*}\right) \qquad \text{Eq. (85)}$$

Step 4

The updated density field is used to calculate finalized values of the scalar field as is seen in Equation 86. In our own experience, this step was not necessary for stability or accuracy for the problems considered, as subsequent iterations will improve the guess for density. However Pierce [78] states this step is required for scalar conservation and was therefore included in this work. Boundary conditions are then applied again on the updated scalar field.

$$\phi^{n+1,it+1} = \left(\rho\phi\right)^{n+1,it+1} / \rho^{n+1,it+1} \qquad \text{Eq. (86)}$$

Step 5

Next the momentum equations are solved to calculate provisional estimates for the mass flux vector. As was stated previously, the pressure is implicit in time and therefore the current estimate for pressure is used in the pressure gradient terms. It is also possible to make the pressure collocated with the velocity in time (i.e., the pressure gradient terms is calculated from an average of p^{n+1} and p^{n}) as well but since the pressure is a perturbation pressure, it acts to enforce continuity. Averaging it with the old value of pressure will only serve to decrease this correction and will slow convergence. Since acoustics are ignored, this implicitness in pressure does not adversely affect the scheme. Each component of velocity in the momentum equations forms a tri-diagonal matrix in the wall-normal direction that is solved using approximate factorization and the Thomas algorithm. From the provisional mass flux vector, r_i^{*}, a provisional estimate for the velocity vector, u_i^{*}, is made, according to Equation 87. Boundary conditions are then applied to this provisional velocity field. The density term involves an average in time,

where the current best estimate of density and the density from the previous time step are used.

$$u_i^* = r_i^* / \overline{\overline{\rho}^x}^t \qquad \text{Eq. (87)}$$

It should be noted that the viscosity is decomposed in a similar manner as the diffusivity. The viscosity can also be divided into a laminar, μ_L, and turbulent subgrid-scale part, μ_T; the laminar part is collocated in time with the scalar fields and the turbulent part is collocated in time with the velocity field. The viscosity discretized in time that appears in the momentum equation is shown in Equation 88. The discretized streamwise momentum equation is provided in Appendix A.

$$\mu = \mu_L^n + \tfrac{1}{2}\left(\mu_T^{n+1/2,it} + \mu_T^{n-1/2}\right) \qquad \text{Eq. (88)}$$

Step 6

In this step a Poisson equation is used to update the pressure and velocity required to satisfy the continuity equation. To derive this equation following the analysis of Pierce [78], consider the pressure and mass flux vector at the current iteration as being decomposed into two parts: the provisional estimate and a correction to this estimate as is seen in Equation 89. Rewriting the discrete momentum equation, using this

$$p^{n+1,it+1} = p^* + \delta p \qquad r_i^{n+1/2,it+1} = r_i^* + \delta r_i \qquad \text{Eq. (89)}$$

decomposition for the temporal flux and the pressure gradient flux, results in Equation 90, with all other terms lumped into the RHS term. Using a predictor-corrector method,

$$\frac{r_i^* + \delta r_i - r_i^{n-1/2}}{\Delta t} = -\delta_{x_i}\left(p^* + \delta p\right) + RHS_i \qquad \text{Eq. (90)}$$

where the provisional values are calculated first and then updated with corrector value, makes the momentum equation become Equations 91 and 92.

$$\frac{r_i^* - r_i^{n-1/2}}{\Delta t} = -\delta_{x_i}\left(p^*\right) + RHS_i \qquad \text{Eq. (91)}$$

$$\delta r_i = -\Delta t\ \delta_{x_i}\left(\delta p\right) \qquad \text{Eq. (92)}$$

Eq 91 was already solved in Step 4. Equation 92 can be made into a Poisson equation by taking the derivate with respect to x_i and substituting in the conservation of mass equation. This Poisson equation can then be simplified into a constraint on the conservation of mass for the current iteration as is seen in Eq. 93. This Poisson equation can then be solved to find the corrector pressure. This predictor-corrector method that splits the pressure flux common to many low-Mach number LES codes has been found to be second-order in time, consistent with the time-integration technique [80].

$$\delta_{x_i}\left(\delta_{x_i}\left(\delta p\right)\right) = -\delta_{x_i}\left(\delta r_i\right)/\Delta t = -\delta_{x_i}\left(r_i^{n+1/2,it+1} - r_i^*\right)/\Delta t = \delta_{x_i}\left(r_i^*\right)/\Delta t + \left(\frac{\rho^{n+1,it+1} - \rho^n}{\Delta t}\right)/\Delta t \qquad \text{Eq. (93)}$$

The boundary conditions for the perturbation pressure solver are all zero-gradient Neumann boundary conditions. Since the gradient of δp constrains mass flux in order to ensure mass conservation, this Neumann boundary condition is equivalent to zero mass entering the domain. As Pierce [78] mentions as the iterations converge δp gets smaller and smaller, meaning the continuity equation becomes better enforced, avoiding some of the errors associated with fractional step methods and time splitting.

Step 7

The velocity, mass flux and pressure must be corrected using the values of the corrector pressure. The conditions for velocity, mass flux and pressure are shown in Eqn.

94 a-c, respectively. After these values are updated, the iterative process is completed for one iteration. If the iterations have not converged the process would repeat starting at Step 2. If the iterations have converged, the process would start over at Step 1 and would advance the next time step. Typically the convergence criteria used in this work is that the non-dimensional density did not change by more than 10^{-6}, while the right hand side of the Poisson equation was less than $10^{-3}/\Delta t$.

$$\begin{aligned} &a) \quad r_i^{n+1/2,it+1} = r_i^* - \Delta t \delta_{x_i}(\delta p) \\ &b) \quad u_i^{n+1/2,it+1} = r_i^{n+1/2,it+1} / \overline{\overline{\rho}^x}^t \\ &c) \quad p^{n+1,it+1} = p^* + \delta p \end{aligned} \qquad \text{Eq. (94)}$$

2.4.2.2 Ghost Cells

Due to the staggered spatial grid, seen in Figure 9, Dirichilet boundary conditions can become difficult to enforce for the variables not spatially located at the boundary. One can remove the staggering at the wall and place all the variables directly at the boundary degrading the accuracy to first order. Another option is to create "ghost cells" that are fake fluid cells that are embedded in the wall. A schematic of the ghost cells at the wall are shown in Figure 10. The only purpose of ghost cells is to properly enforce the boundary conditions when gradient terms are required for the first fluid cell above the wall. The values at the wall in this arrangement simply need to be interpolated between the first fluid cell and the first ghost cell. As an example, both the velocity and scalar ghost cells are written for both a Dirichilet and Neumann boundary condition in Equations 95a and 95b, respectively, where bc denotes the desired boundary value and the indexing refers to Figure 10. It should be noted all these boundary conditions are either exact or second order except for the Neumann boundary condition for v velocity,

which is first order. More terms could be incorporated to make this condition second order as well.

$$\begin{aligned} u_{j=0} &= 2u_{bc} - u_{j=1} \\ v_{j=0} &= 0 \\ w_{j=0} &= 2w_{bc} - w_{j=1} \\ \phi_{j=0} &= 2\phi_{bc} - \phi_{j=1} \end{aligned} \quad (a) \qquad \begin{aligned} u_{j=0} &= u_{j=1} - \Delta y \frac{\partial u}{\partial y}\Big]_{bc}; \quad w_{j=0} = w_{j=1} - \Delta y \frac{\partial w}{\partial y}\Big]_{bc} \\ v_{j=0} &= v_{j=1} - \Delta y \frac{\partial v}{\partial y}\Big]_{bc}; \quad \phi_{j=0} = \phi_{j=1} - \Delta y \frac{\partial \phi}{\partial y}\Big]_{bc} \end{aligned} \quad (b) \quad \text{Eq. (95)}$$

2.4.2.3 QUICK and BQUICK

As was mentioned previously, QUICK and BQUICK are used to calculate the convective flux terms in the scalar equations. Using the ubiquitous central differencing creates unphysical dispersion of gradients. Consider the 1D wave equation where a top hat wave is advected at constant speed as is seen in Equation 96. As the wave moves, in finite difference approaches, the hat shape is distorted and experiences unphysical

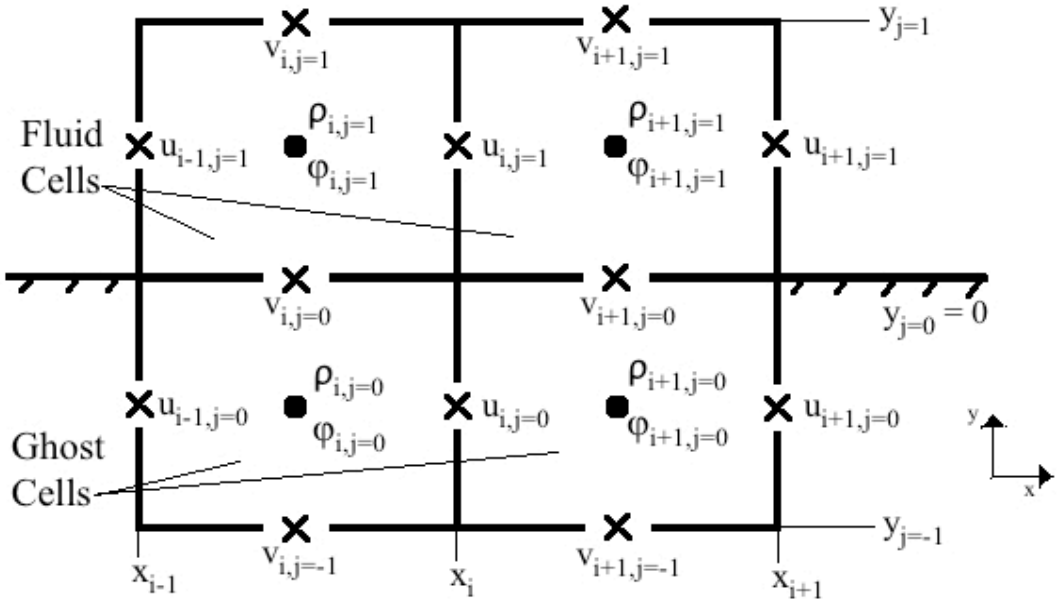

Figure 10. Schematic depicting ghost cell locations for boundary conditions.

oscillations at the edges of the wave, due to dispersion errors in the specific finite difference scheme. Using central differencing, these oscillations grow to quickly distort

$$\frac{\partial \phi}{\partial t} + u_{const} \frac{\partial \phi}{\partial x} = 0 \qquad \text{Eq. (96)}$$

the original signal, as can be seen in Pierce [78]. It should be noted that these oscillations occur even if they violate physical bounds, for example negative species concentrations might be observed. In fact, in pure convection, a 2nd order central differencing explicit technique is unconditionally unstable. QUICK involves a finite difference stencil that is upstream biased. These upstream differencing schemes have much smaller dispersion errors than their central differencing counterparts and are stable for the simple 1D wave equation. The oscillations created at the discontinuity are dissipated and smoothed. While in LES added dissipation removes some of the important scalar physics and reduces the order of accuracy, the uncontrolled oscillations created at sharp gradients due to advection are generally more destructive to the order of accuracy. The interpolation stencil used for the convection terms is seen in Equation 97. Herrmann et al. [82] found that the QUICK scheme, while decreasing the large oscillations near sharp gradients, still violated physical bounds of problems; for example if a mixture fraction gradient is convected, QUICK schemes still might predict negative mixture fractions. Hermann et al. modified QUICK to a 1st order upwind when such physical violations occurred. 1st order upwinding has the fortunate property of smoothing out sharp gradients and generates no oscillations. However this scheme is very dissipative and not appropriate for entire domains of LES flows. Instead a blended approach is preferred. First QUICK is used in the advancement of the scalar field. The out of bounds scalar locations are then identified. The scalar advancement is then redone with a QUICK stencil in all places where the

scalar is within physical bounds and a 1st order upwind stencil when out of physical bounds. This scheme, called BQUICK [82], does require some prior knowledge of physical bounds if temperature or enthalpy is used. Fortunately in adiabatic film cooling flows without radiation and compressibility, the flow temperature can never be greater than the mainstream temperature and can never be less than the coolant temperature.

$$\overline{\phi}^{x} = \begin{cases} -\frac{1}{8}\phi_{i-3/2} + \frac{3}{4}\phi_{i-1/2} + \frac{3}{8}\phi_{i+3/2} & if\ u_i > 0 \\ -\frac{1}{8}\phi_{i+3/2} + \frac{3}{4}\phi_{i+1/2} + \frac{3}{8}\phi_{i-1/2} & if\ u_i < 0 \end{cases} \qquad \text{Eq. (97)}$$

Figure 11 shows the finite difference solution of the 1D wave equation after one non-dimensional time unit. The exact solution is shown, along with the QUICK and BQUICK finite-difference solutions. Notice that the QUICK scheme violates the boundedness of the problem, namely, it predicts temperatures greater than two and less than one. Also the QUICK scheme generates small oscillations near the sharp gradients. The BQUICK solution meanwhile, effectively smoothes these oscillations and maintains physical boundedness; the top hat wave merely diffuses. It should be noted that BQUICK is not conservative due to the changing of operators near sharp gradients; however this lack of conservation is relatively minor since the stencil change only occurs near sharp gradients that violate physical bounds and smoothes these gradients.

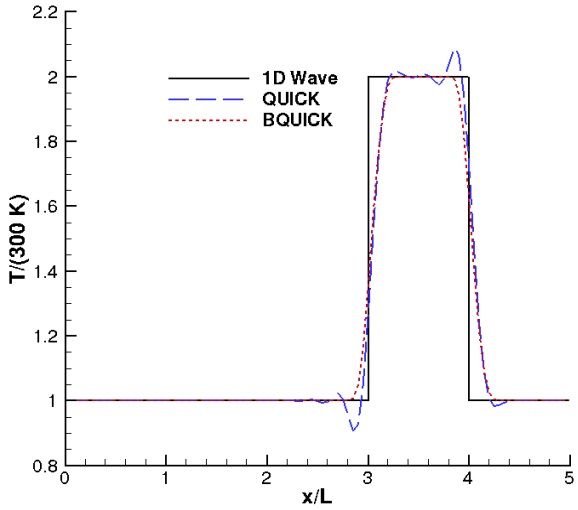

Figure 11. Temperature profiles showing the 1D convection of a scalar field.

2.2.5. LES Grid Design Criteria

Proper grid discretization is required for both accuracy and stability in CFD calculations. Stability and cost restrictions often favor larger grid spacing, while accuracy depends on finer spacing. Therefore a grid size tradeoff exists between these two conflicting requirements, meaning

careful selection of grid spacing is necessary. Normally grid spacing is selected to adequately resolve flow physics with a high degree of fidelity and the time step is adjusted to account for stability. In LES, grid selection is even more vital as the grid size determines the size of turbulent eddies that can be resolved. In order for an LES to be accurate in Kolmogorov flows, the grid spacing must be in the inertial subrange. This guideline is due to the assumption that the smaller, more dissipative structures are isotropic and can be easily modeled, while the larger turbulent structures are highly dependent on the geometry. Therefore if the grid spacing is too large, the energy carrying eddies will not be resolved and will most likely be inadequately modeled by the subgrid-

scale model. As a rule of thumb, 10 points are needed to accurately resolve the integral length scale of the flow. In the film cooling domain, this length scale is largely determined by the slot height and the incoming boundary layer thicknesses, which are on the order of the slot height. Therefore as a first-order estimate, at least 10 points are required over one slot height.

In the wall region, a different grid density is needed as the eddy sizes scale with the proximity to the wall. To make this more apparent, consider the length and velocity scale in the near-wall region for turbulent flows, which are often called the frictional length and frictional velocity. The quantities are shown in Equation 98 a and b. Note, here that τ is the wall-normal shear stress and w subscript refers to the fact that the parameters are at the wall. The convection in the near-wall region is minimal in comparison to the wall-normal diffusion, meaning that the important parameters in this region are the wall-normal shear stress and the momentum diffusion coefficient (the viscosity). Using these scales, the coordinate direction and velocity vector can be formed in wall units, denoted by +, and are presented in Equation 99.

The LES literature [54, 83] has shown that wall-normal grid spacing must be less than one frictional length. LES guidelines on the spacing in the other directions are less stringent; the streamwise spacing must be less than 50 wall units (or frictional lengths), while the spanwise spacing should be approximately 20 wall units [54]. The sharp gradients in the near wall region, specifically in the wall-normal direction, requires fine grid resolution in order to accurately resolve the wall shear stress and important near-wall, shear physics. Turbulent flow observation shows that the turbulent structures responsible for the majority of turbulent kinetic energy generation comes from long,

slow-moving, streamwise roller structures, very close to wall that are ejected into the boundary layer [84, 85]. The suqsequent mixing of these structures with the faster moving fluid creates large amounts of shear and turbulent energy. These roller structures are on the order of 100 wall units in the streamwise direction and approximately 5 wall-normal units in height, which also gives some justification why the wall-normal grid spacing is much more stringent than the streamwise grid spacing. For film cooling flows, both the near wall physics, governed by the wall scaling, and the shear layer mixing, governed by the integral length scaling, are important. Both sets of grid design guidelines are relevant depending on the region in the flow.

$$\delta_v = \sqrt{\frac{\nu_w^2 \rho_w}{\tau_w}} \quad (a) \qquad u_\tau = \sqrt{\frac{\tau_w}{\rho_w}} \quad (b) \qquad \text{Eq. (98)}$$

$$\vec{x}^+ = \vec{x}/\delta_v \quad (a) \qquad \vec{u}^+ = \vec{u}/u_\tau \quad (b) \qquad \text{Eq. (99)}$$

2.2.6 LES Validation

To ensure that LES BLAC is capable of solving an LES of film cooling with reasonable accuracy, it must first be validated for flows with heat transfer and turbulence. For the full verification and validation studies of LES BLAC, see Bravo [86]. The first test case is a DNS of fully developed channel flow without heat transfer done by Moser et al. [87]. The second test case is a DNS of fully developed channel flow with heat transfer done by Nicoud [88]. These cases involve both turbulent momentum and heat transport and therefore should serve as validation studies containing the important flow physics of film cooling flows. Additionally, the second validation test case with heat transfer will form the basis of the inflow generation technique described in the §2.2.8.

The computational schematic with boundary conditions for fully developed channel flow is shown in Figure 12. The wall-normal boundary features Dirichlet boundary conditions, with zero velocity and constant temperature at the walls. For the channel without heat transfer, both walls are set to the same non-dimensional wall temperature of one. In the case of heat transfer, the top and bottom walls have non-dimensional temperatures of two and one, respectively. The streamwise and spanwise planes feature periodic boundary conditions. Spanwise periodicity essentially mimics an infinitely wide 2D slot. The streamwise periodicity is allowed because of a numerical trick. A source term is added to the momentum equation to create a mean pressure gradient, which acts to keep the mass flux constant. In this way, one can imagine the whole control volume moving with the fluid as the fluid develops and eventually reaches a fully developed state, where turbulent statistics are stationary in the streamwise direction.

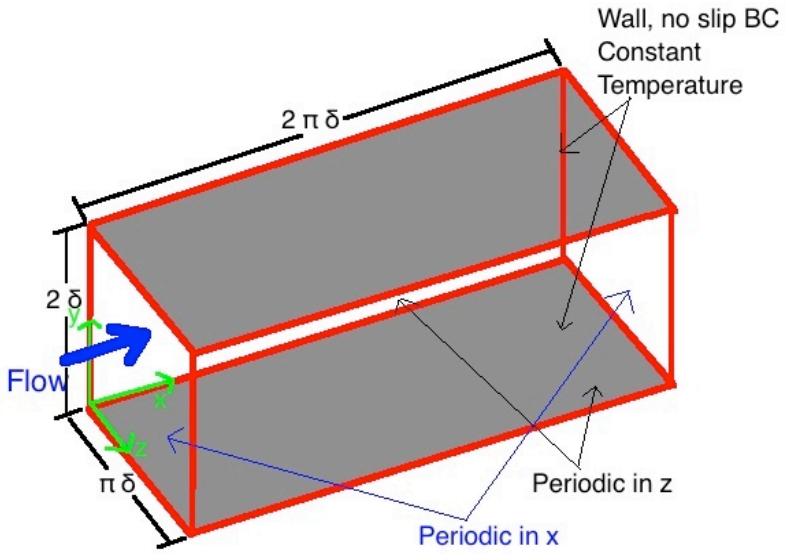

Figure 12. Schematic of Computational Domain for Fully Developed Channel Flow.

2.2.6.1 Fully Developed Channel Flow Without Heat Transfer

The computational grid details of the present LES and the DNS of Moser et al. [87] are shown in Table 5. The domain extents are identical between the two simulations but the grid density is between three and five times coarser in each coordinate direction for the LES simulation; the DNS calculates approximately 47 times the grid points being solved. Considering the time step must also be smaller for the DNS, this calculation is even more than 47 times more expensive than the LES calculation. The current LES grid fulfills all the LES grid criteria discussed previously. Even though it is not listed in the table, the first grid cell spacing in the wall-normal direction is less than one wall unit, which ensures the wall shear stress is adequately captured. The streamwise and spanwise spacings are uniform in the current LES calculations. It should be noted that the Δy_{CL} refers to the wall-normal spacing at the centerline. Equation 100 gives the wall-normal grid distribution. Also, it should be noted that Moser et al. [87] do not report a bulk Reynolds number but rather report the frictional Reynolds number. In LES BLAC, the bulk Reynolds number is an input and the relationship between Reynolds number and frictional Reynolds number is a non-linear function involving the shear stress. Therefore the bulk Reynolds number was iterated to get approximately the same frictional Reynolds number. The final LES frictional Reynolds number is within 1.7 % of the DNS value.

$$y_j = \tanh(5*(j/N_Y - 0.5)/\tanh(2.5) + 1 \qquad \text{Eq. (100)}$$

Table 5. Comparison of LES grid conditions with those of Moser et al. [87]

	L_X, L_Y, L_Z	N_X, N_Y, N_Z	Δx^+	Δz^+	Δy_{CL}^+	Re_τ	Re
DNS	2πδ, 2δ, πδ	256, 193, 192	10	6.5	6.5	392.24	N/A
Current LES	2πδ, 2δ, πδ	48, 65, 64	51.6	19.3	30.6	385.79	6600

The mean, fully-developed, streamwise velocity profile is shown using frictional scaling in Figure 13. Since the flow is only fully-developed in a statistical sense, a large number of flow samples were required to ensure statistics were relatively converged. An estimate of the resolved turbulent kinetic energy time history was monitored until a quasi-steady state was reached. Flow realizations were recorded every five non-dimensional time units for over 300 non-dimensional time units. Also plotted are the well-known log-law and the relationship between velocity and friction very close to the wall in the viscous sub-layer. Very close to the wall, the LES curves overlaps the DNS very well. The good agreement remains through the transition region and starts diverting from the DNS curve near the channel centerline. The LES underpredicts the DNS velocity by less than 5% at the channel centerline.

The normal and shear Reynold Stresses in frictional units are shown in Figure 14a and 14b, respectively. The peak streamwise Reynolds stress is overpredicted by over 26%. The overall normal Reynolds stresses are predicted very well, giving some confidence that the LES solution is adequately resolving the important turbulent flow features. Similarly, one of the most important turbulent values, the peak streamwise, wall-normal Reynolds cross stress, R_{uv}, responsible for much of the turbulent energy generation, is predicted very well to within 0.5 %. The other Reynolds stresses are also predicted reasonably well, validating the LES's ability to resolve the turbulent statistics of this flow. These trends are consistent with the LES findings of Keating [74]; more specifically the good agreement overall along with the overprediction of the streamwise normal Reynolds stress, R_{uu}^{+}.

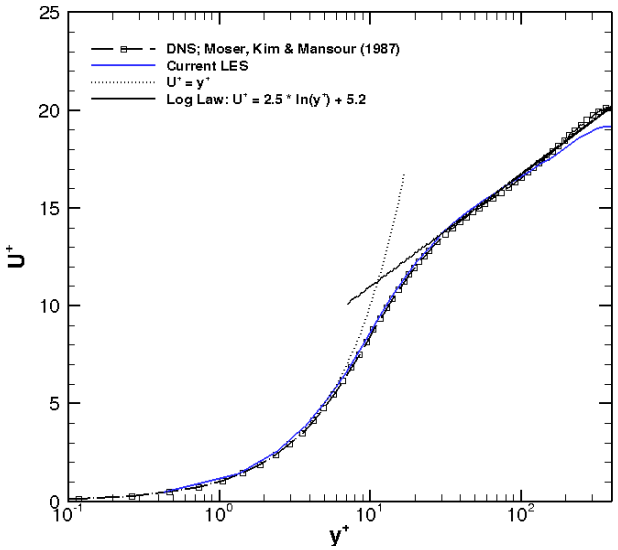

Figure 13. Log linear profile of velocity in wall units. LES is compared to DNS [87] and log law.

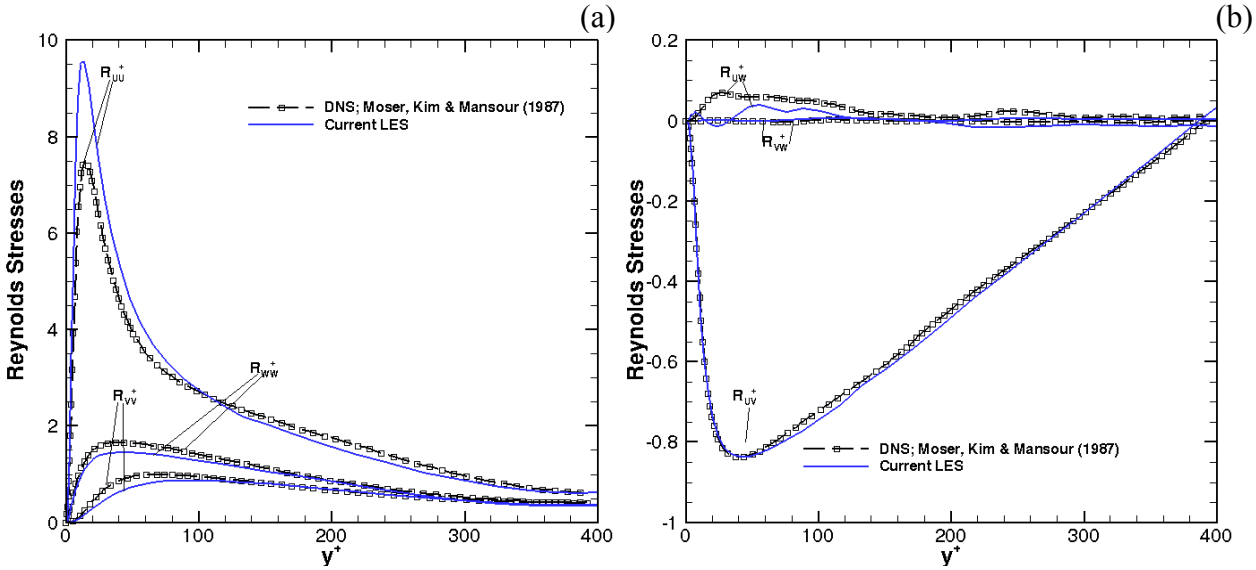

Figure 14. (a) Normal and (b) cross Reynolds stresses in wall units compared to DNS [87].

2.2.6.2 Fully Developed Channel Flow With Heat Transfer

In order to validate turbulent heat transfer physics, the DNS of Nicoud [88] was simulated using LES BLAC. In this simulation, air is simulated flowing through a channel with an upper wall temperature of 600 K and a lower wall temperature of 300 K.

The Prandtl number is 0.76 and Sutherland's law (for the dynamic viscosity and thermal conductivity as described in Nicoud [88]) was used. Table 6 shows grid information and the simulation parameters. Once again, Nicoud [88] did not provide a bulk Reynolds number so this value was iterated until relatively close agreement was found; in this case the Reynolds number based on the friction velocity was within 1.2% and 3.5% of the DNS values for the top and bottom walls respectively. The domain of Nicoud [88] is larger than that currently simulated in the LES. Also Nicoud's grid spacing represents a coarse DNS. The LES grid spacing are within a factor of two of the DNS spacings of Nicoud [88] and can be considered a very fine LES study. Once again the first grid cell size in the wall normal direction was less than one wall unit at both walls to ensure proper resolution of the wall shear stress. The streamwise and spanwise grid spacings are uniform, while the wall-normal grid distribution is shown in Equation 101.

Table 6. Comparison of LES grid criteria to the DNS data of Nicoud [88].

	L_X, L_Y, L_Z	N_X, N_Y, N_Z	Δx^+	Δz^+	$\Delta y_{CL}{}^+{}_{MAX}$	T_2/T_1	$Re_{\tau 1}$	$Re_{\tau 2}$	Re
DNS	4πδ, 2δ, 4πδ/3	120, 100, 120	8.4-21.5	2.8-7.2	9	2	200	82	N/A
Current LES	2πδ, 2δ, πδ	48, 75, 64	10.6-27.1	4.0-10.2	11.4	2	207	81	2455

$$y_j = \tanh(4*(j/N_Y - 0.5)/\tanh(2) + 1 \qquad \text{Eq. (101)}$$

Figure 15 compares the LES mean velocity and temperature profiles in frictional units with those of Nicoud's DNS [88]. As shown in Equation 102, the temperature field is normalized by the heat transfer at the wall, similar to how the velocity is normalized by the wall shear stress. Here w denotes that values are taken at the wall, while $c_{p,w}$ and $\dot{q}''_w$ refer to the heat capacity and wall heat flux, respectively. The mean velocity field is captured better at the hot upper wall than at the lower wall but excellent agreement is nonetheless found in both cases. Similarly in the mean temperature field, the upper wall

is predicted better than the lower wall with a slight underprediction of the cold wall temperature curve. In both cases, this may be due to a friction velocity that is too high as is indicated by the larger Reynolds number near the lower wall when based on friction velocity. Despite these minor discrepancies, the overall mean velocity and temperature fields are captured quite well.

$$T^+ = \frac{(T_w - T)\rho_w c_{p,w} u_\tau}{\dot{q}''_w} \qquad \text{Eq. (102)}$$

Figure 16 shows the mean velocity and temperature using different scalings. Instead of using the gradient information at the wall (i.e., the friction velocity and the heat flux), the maximum velocity and wall temperatures are used to non-dimensionalize the velocity and temperature, respectively. This figure gives some sense of how the velocity and temperature varies in physical space (or using typical engineering non-dimensionalization), which is needed because the prior curves in Figures 14 and 15 are non-dimensionalized using wall scaling, which according to turbulent boundary layer theory can collapse a wide variety of turbulent flows. The agreement is once again excellent with only minor differences between the DNS and LES datasets. It can be noted both for the velocity and temperature fields that the profiles near the upper wall match the DNS data better than at the lower wall.

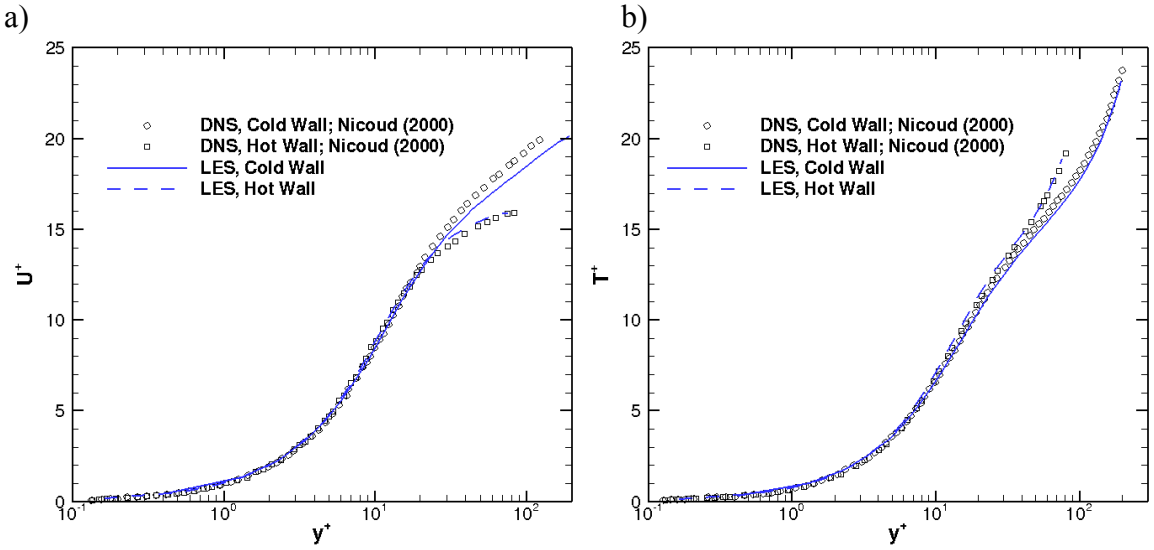

Figure 15. Mean velocity and temperature profiles in wall units compared to DNS data [88]

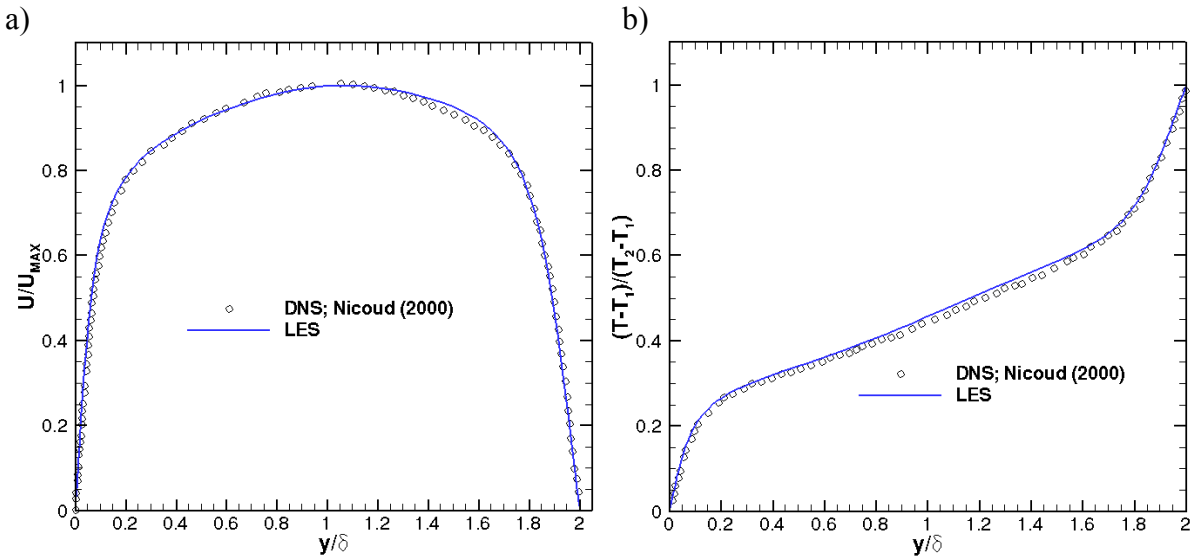

Figure 16. Velocity and Temperature profiles in regular units compared to DNS data [88].

To better quantify these mean differences, especially near the lower wall, the gradient information for both the kinematic and thermal fields are compared to the DNS data [88]. Table 7 shows the ratio of the friction velocity at each wall divided by the mean friction velocity. Also a non-dimensional heat flux parameter, B_q, is used to characterize the wall heat transfer. The definition of B_q is given in Equation 103. As can be seen, there is a minor discrepancy in the wall shear stress, as is evidenced by the friction velocity. Similarly, the non-dimensional heat flux parameter matches the DNS slightly better at the upper wall than at the lower wall but the differences are small.

Table 7. LES BLAC wall results compared to DNS data of Nicoud [88].

	T_2/T_1	$u_{\tau 1}/u_{\tau,avg}$	$u_{\tau 2}/u_{\tau,avg}$	B_{q1}	B_{q2}
DNS	2	0.87	1.13	-0.018	0.014
Current LES	2	0.88	1.12	-0.019	0.014

$$B_q = \frac{\dot{q}''_w}{T_w \rho_w c_{p,w} u_\tau} \qquad \text{Eq. (103)}$$

The mean information, while the most important, is not sufficient to determine whether the turbulent mixing mechanisms are faithfully simulated. Therefore high order statistics are needed to determine the level of agreement between the DNS and LES simulations. To ensure that the turbulent heat transfer physics and flow kinematics are adequately captured, the second order root mean squared (RMS) statistics of the present LES are compared to the data of Nicoud [88]. Figure 17 compare some of these turbulent statistics. Figure 17a shows the streamwise, wall-normal and spanwise RMS velocities in wall units. The overall agreement is excellent between the LES and DNS simulations with the largest discrepancy occurring now near the upper wall in the streamwise RMS velocity peak. This finding is consistent with the LES streamwise normal Reynolds stress disagreement with the DNS of Moser et al. [87] This overprediction of the DNS curve is not seen at the lower wall but this could be because the wall shear stress is overpredicted and is used to non-dimensionalize the RMS velocity curves. Figure 17b shows the streamwise, wall-normal component of the Reynolds stress, R_{uv}. Similar to the LES simulations of Moser et. al [87], the cold wall Reynold stress is predicted very well with minor disagreement occurring towards the channel center line. The hot wall LES curve, however, underpredicts the DNS Reynolds cross stress, which is responsible for much of the turbulent heat transport. The RMS of temperature, shown in Figure 17c, compares very well to the DNS data. The best agreement is found near the cold wall, while the hot wall shows minor discrepancies in magnitude but overall follows the same trends as the DNS. Overall the second order LES statistics compare very well to the DNS data of Nicoud [88], thus validating the current CFD code's ability to predict canonical, turbulent fluid dynamic and convective heat transfer problems.

2.2.7 Inflow Generation

As described in §1.4.2.2, the kinematic mixing in film cooling flows is highly dependent on the fluid dynamic state of the coolant and mainstream flows. For example, turbulent streams mix dramatically faster than laminar streams because turbulent structures transport fluid between the streams on a variety of different length scales via advection. This advection is in sharp contrast to the diffusion limited process of laminar streams where mixing occurs only on the small diffusion length scales. Since the downstream mixing is dependent on the fluid dynamic states of the two streams, it follows that the specification of the inflow boundary condition is critically important. In LES, the large scale geometry-dependent flow structures are resolved; therefore if mixing occurs close to the inflow injection-plane realistic LES turbulent structures must convect into the domain so physical mixing will be simulated.

As a result of the LES inflow generation literature survey, the precursor simulation technique was selected as the ideal film cooling inflow technique. In this technique, separate simulations modeling the coolant and mainstream are performed prior to the film cooling simulation. These "precursor" simulations are then used to extract realistic LES structures and provide profiles of kinematic and thermal data that can be specified at the LES inflow plane. A fully developed turbulent channel simulation is used to simulate the coolant channel. Two different precursor simulations are tested for the mainstream flow. The first technique, developed by Cruz [7], also features the use of the fully developed turbulent channel simulation. The second technique simulates a developing boundary layer over a flat plate, which consequently mimics the experiment

downstream of the turbulent grid prior to injection; the experimental set-up is described in §2.1.1 and in Cruz [7] and Raffan [60].

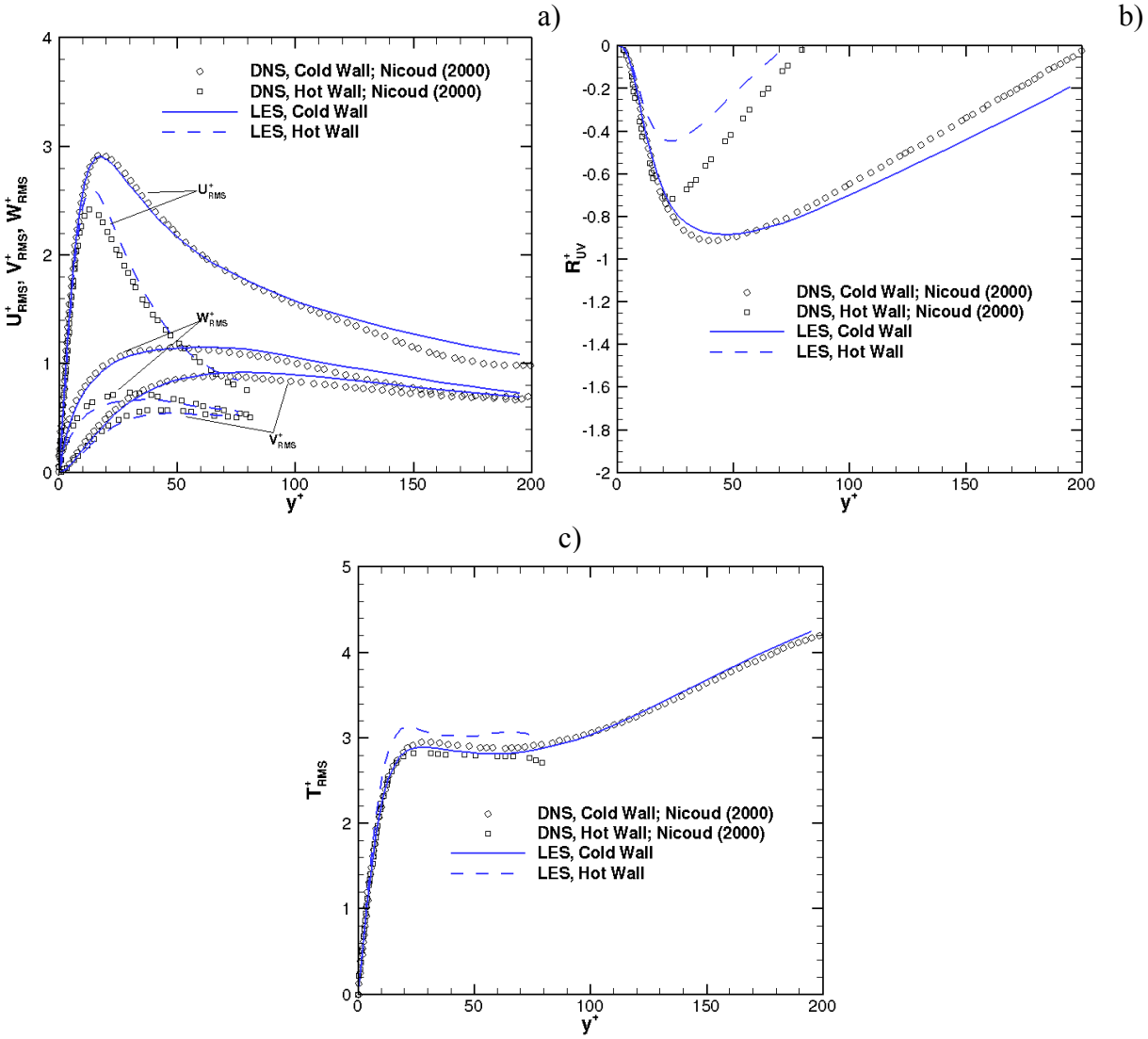

Figure 17 a) Wall normal and b) cross Reynolds stresses in wall units. c) RMS of temperature in wall units. Compared to DNS data of Nicoud [88].

2.2.7.1 Coolant Precursor Simulation

The coolant precursor technique employs the fully developed turbulent channel simulation. The domain schematic is the same as in §2.2.6 and is seen in Figure 12; here the channel half height, δ, is equal to half the slot height. Since the LES code is non-

dimensional, all lengths are normalized by the slot height. Similarly the velocities are normalized by the coolant bulk velocity reported in Table 3; all temperature and scalars are normalized by air with properties at 300K. Dirichlet constant temperature boundary conditions are enforced on the upper and lower wall. The upper and lower wall temperatures are extracted from the first experimental film cooling temperature profile, which is measured very near the film cooling inlet. The mass flux for this simulation is also prescribed from experimental data. After fully developed turbulence is reached, wall-normal, spanwise planes at a constant streamwise position are extracted. All the fully developed turbulent channel simulations employ the same grid resolution as the Nicoud validation case. The precursor simulation uses a non-dimensional time step of 0.003. This specific time step was selected *a posteriori* to ensure that the CFL condition was met for the film cooling simulations.

2.2.7.2 Mainstream Fully Developed Turbulent Channel Simulation

As was briefly mentioned in §1.4.2.2, one mainstream precursor simulation technique employs a fully developed turbulent channel assumption to simulate the mainstream mixing physics. In this approach, the mean experimental profiles of velocity and temperature will be imposed for the film cooling inflow boundary condition. However, generating fluctuations that correspond to physical fluid dynamic structures is extremely challenging. Instead, a simulation can be used to simulate the fluctuating information, which is then superimposed on top of the mean profiles.

The schematic for this mainstream fully developed turbulent channel simulation is shown in Figure 12. Here, however, the channel half height corresponds to the

experimental mainstream boundary layer thickness; the boundary layer thickness is defined as the wall-normal distance above the wall where the streamwise velocity is 99 % of the mainstream velocity. The lower channel wall temperature is specified as the upper louver wall temperature, which is extracted from experimental data. Due to the presence of the upper wall, this simulation unfortunately does not capture the kinematic and thermal physics of the mainstream. However the turbulent dynamics of a flat plate boundary layer and a channel flow boundary layer are similar, especially for the near-wall turbulent structures. Once again, this simulation is used only to capture fluctuating information (corresponding to turbulent structures), which is superimposed on top of mean experimental data in the mainstream. The fluctuations like the mean profiles must be filtered, rescaled and forced to asymptote to the experimental mainstream values at the edge of the mainstream boundary layer. It is desirable to have roughly the correct mean velocity and thermal mean profiles, especially near the lower channel wall. A first order approach that approximately enforces the correct temperature at the channel centerline (corresponding to the boundary layer edge) occurs when specifying an upper wall temperature that is the sum of the louver temperature and twice the difference of the mainstream and louver temperatures, i.e., $T_{upperwall}=T_{louver}+2(T_{\infty}-T_{louver})$. This upperwall temperature will approximately result in a channel centerline temperature of T_{∞}.

Examples of typical mainstream profiles before filtering are shown in Figure 18. A solid black line denotes wall-normal location of the upper wall in the channel flow simulation, while the dashed black line corresponds to the channel half-height. As can be seen, the channel flow velocity profile closely resembles the mainstream velocity profile up until the channel centerline, wherein the velocity starts decreasing due to the upper

wall no-slip condition. The channel flow temperature profile deviates farther typically from the mainstream temperature profile even below the channel half height. Above the channel half height, the channel flow temperature profile starts increasing past the mainstream temperature due to the high upper wall temperature specified there. Just as the mean channel flow profiles of velocity and temperature need to be filtered to resemble the mean mainstream profiles, any fluctuating profiles also need to be filtered. Since the mean profiles remain close below the channel half height, the filter only slightly modifies the mean channel flow structures. However above the channel half height, the channel flow turbulent structures are dampened out to zero by the filter, as no physical analogy to the mainstream flat plate boundary layer exists in this region. A sample filter that is multiplied by the fluctuating velocity is $f = 1 - tanh(y^*)$, which takes values of one near the wall and zero far away from it.

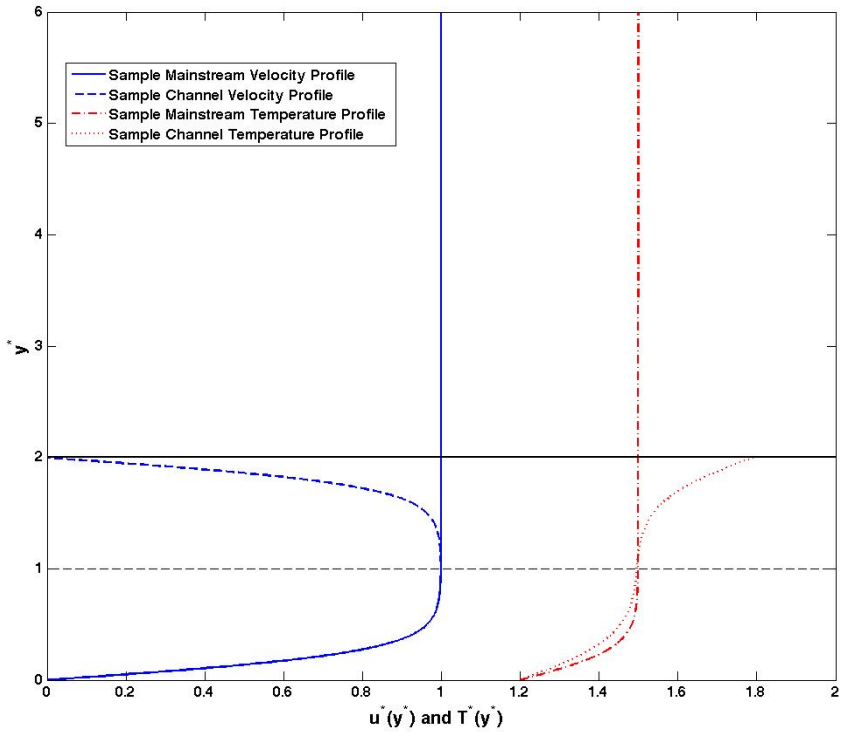

Figure 18. Sample profiles of velocity and temperature for a fully developed turbulent channel.

2.2.7.3 Mainstream Flat Plate Turbulent Boundary Layer Simulation

A more physically based precursor technique that mimics the mainstream flow is a zero-pressure gradient, boundary layer developing over a flat plate. A schematic for this simulation is shown in Figure 19. In this technique, flow is injected into the domain and the boundary layer develops as the fluid convects downstream. At a certain point, the thermal and momentum boundary layer will resemble that of the experimental mainstream boundary layer. At this location, flow profiles can be extracted to feed into a film cooling domain.

If a uniform inflow boundary condition were used, the flow would eventually trip to turbulence, once the critical Reynolds number is met. Unfortunately, this most likely would occur far downstream, such that it would be infeasible to calculate the entire transition to turbulence. Additionally the uniform inlet cannot account for turbulent flow structures in the core of the mainstream (away from the wall) created by a grid. To solve these problems, the inflow technique of Batten et al. [89] was adopted. In this technique, semi-physical fluctuations are created at the inlet that obey specified profiles of mean and second-order statistics profiles. Batten et al.'s [89] technique also conserves mass so no unphysical pressure oscillations will form. In an LES study of turbulent boundary layers, Keating and Piomelli [53] showed that turbulent boundary layers with appropriate statistics are recovered after about 15-20 boundary layer thicknesses downstream of the inlet when using the technique of Batten et al. [89]. The turbulent development of the boundary layer may now be simulated due to the reduced computational domain. Plug flow for the mean streamwise velocity is enforced, along with zero wall-normal and spanwise velocity. The inflow temperature is constant and equal to the mainstream

temperature. Isotropic turbulent fluctations profiles for the velocity field are imposed to generate grid turbulence, using the technique of Batten et al. [89]. The scaling laws of Pope [90] were used to set the initial turbulence levels and dissipation to achieve the experimental turbulence intensity at the extraction plane.

The grid for this simulation is based on the film cooling mainstream spacing in the mixing layer, which will be discussed in §4. The bottom wall features a no-slip boundary condition held at the louver upper wall temperature. The top wall boundary condition enforces zero wall-normal gradients, which is approximately true in the freestream. The spanwise plane features periodic boundary conditions, while the outflow uses a simple, 1D Orlansky convection boundary condition that scales the outflow to globally conserve mass. The equation solved at the outflow plane is shown in Equation 104 for a generic scalar, ϕ. The convection speed, c, is set to the maximum streamwise velocity along the outflow plane. This velocity was selected according the guidance of Pierce [78]. If this velocity is too low, flow structures will not convect out of the domain fast enough and a build up a fluid will occur. If this convection velocity is too high, flow structures will stretch and accelerate at the boundary. In the limit of infinite convection velocity, this boundary condition reverts to a zero gradient condition, which can create instability problems [78].

$$\frac{\partial \phi}{\partial t} + c\frac{\partial \phi}{\partial x} = 0 \qquad \text{Eq. (104)}$$

2.2.7.4 Inflow Processing

The results of the precursor simulation are processed to create a temporal database of inflow slices that vary in the wall-normal and spanwise directions. All precursor simulations were normalized using the coolant velocity and a reference

temperature of 300K and used the same constant time step. Each slice is filtered to preserve the mean statistics of the experimental data and interpolated to match the film cooling inflow plane. If the mainstream fully developed turbulent channel is used, the slices are further filtered to remove the influence of the upper wall boundary condition. Zero velocity and a linear temperature profile are assumed across the louver lip, consistent with steady, 1D conduction in a solid. A database of 4500 slices, each separated by a constant non-dimensional time step of 0.003, is created after post processing. The slices are recycled to essentially create an infinitely long temporal database. The total time from the first slice to the last is 13.5 non-dimensional units, which was deemed long enough to prevent unwanted periodicity.

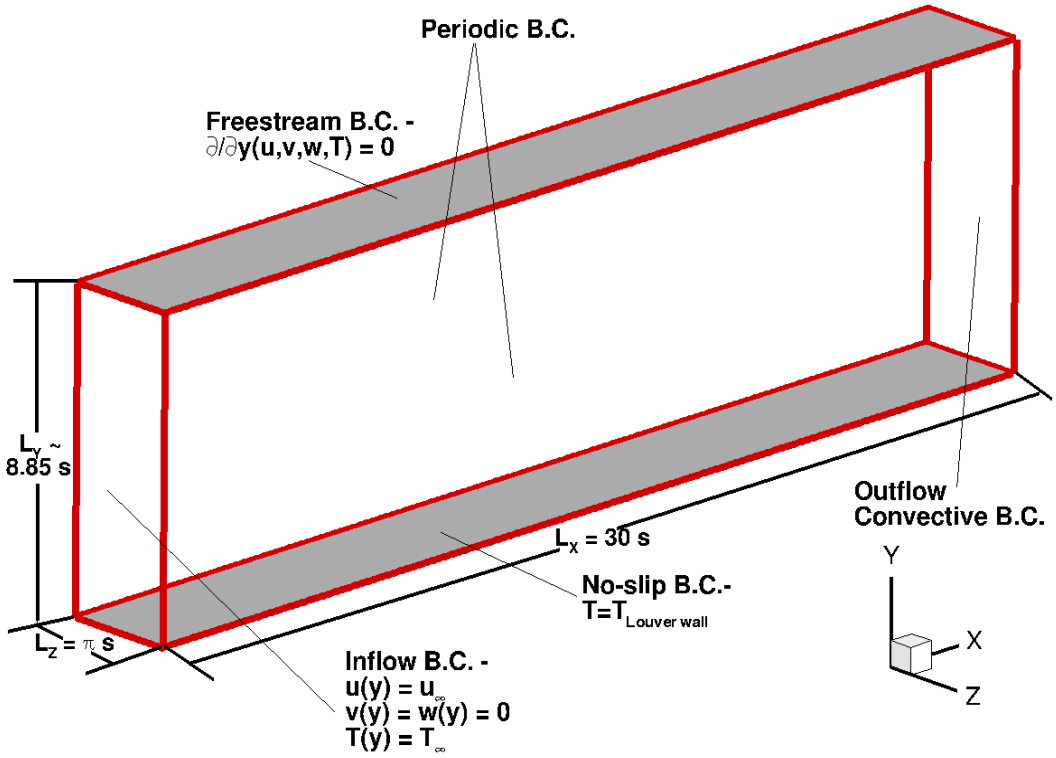

Figure 19. Schematic of the turbulent boundary layer developing over a flate plate.

Chapter 3: Experimental Results

In this chapter, the results of the adiabatic and non-adiabatic film cooling experiments will be detailed and analyzed. First the heat transfer characteristics at the wall will be described for the adiabatic and non-adiabatic cases. Next the kinematic and thermal mixing is characterized in an effort to explain and frame the heat transfer results. In each section, the major distinguishing characteristics between the different shear cases will be highlighted in an attempt to explain how the different film cooling regimes behave.

3.1 Wall Temperatures and Heat Transfer

As discussed previously, the wall temperature in engine applications needs to be kept at safe levels to avoid material failure, therefore the wall effectiveness, a non-dimensional wall temperature, is the primary metric of interest. Figure 20 shows the wall effectiveness for each of the three adiabatic wall shear cases. Error bars are drawn to denote the uncertainty in both the streamwise location of the measurement and the actual temperature measurement. Notice that the uncertainty remains very small, especially in terms of the wall effectiveness and temperature. In general the uncertainty is smaller than the symbol and therefore will be dropped in subsequent plots. Remember that a higher effectiveness translates to a cooler wall; therefore the minimum shear case in which the effectiveness remains higher for longer is the best performing case. The wall jet retains similar protection to the minimum shear, while the wall wake performs dramatically worse. Similar to Simon's [17] analysis, film cooling flows can be divided into distinct regions to aid the analysis and understanding of the flow. Take for example Figure 3; a dashed line is used to denote the mean extents of the mixing layer. Before

mixing layer impingement on the wall, the wall temperature is governed primarily by the coolant flow. After mixing layer impingement on the wall, the wall temperature is a much stronger function of the mainstream flow as well. In wall effectiveness space, this transition from one region to the next is characterized by a rapid change in slope, which occurs for all cases between 5 and 12 slot heights downstream. Before this impingement point, the decay in effectiveness occurs gradually and stays near the perfect film protection value of one. After the mixing layer strikes the wall, the wall effectiveness rapidly decays as the wall comes into contact with hot fluid from the mainstream, which can be seen in the effectiveness trends after 12 slot heights downstream.

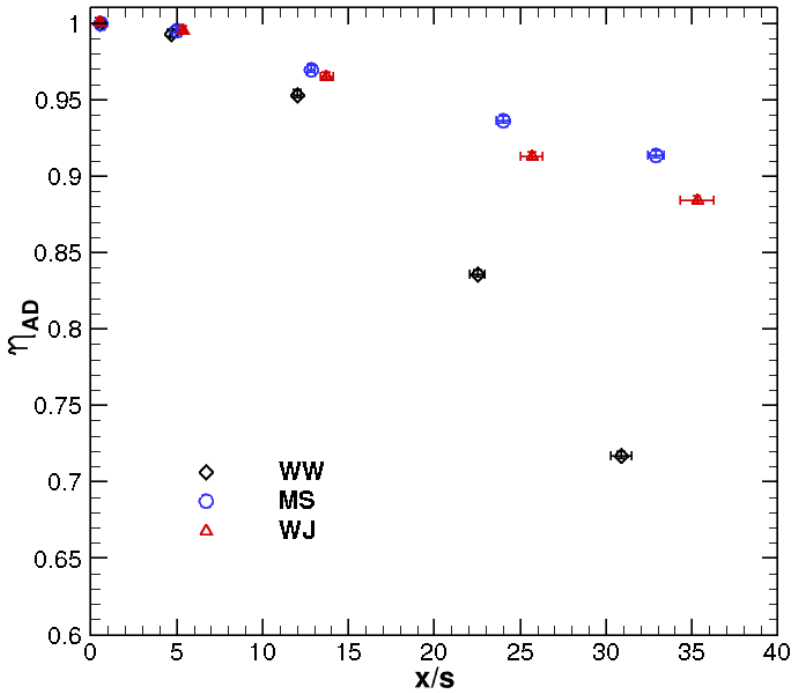

Figure 20 – Experimental adiabatic wall effectiveness for the Wall Wake (WW), Minimum Shear (MS) and Wall Jet (WJ) cases. Error bars are shown both for the streamwise location and the effectiveness.

As was shown earlier, the nominal failure value in effectiveness of a typical engine is approximately 0.8. In the adiabatic experiments, only the wall wake

experiments reach this critical value. The film protection length, or the length from the injection where the effectiveness remains above 0.8, cannot be determined from the wall jet and minimum shear cases. However this length is strongly dependent on the near-injection mixing and the location where the mixing layer impinges with the wall. It is this region of the flow that is of interest because this region is where the typical engineering correlations fail. In fact, farther downstream the thermal and kinematic profiles begin to resemble boundary layers over a flat plate and therefore assume some similarity as was shown by Weighardt [8]. The implication here is that far from the injection the film decay is much easier to predict and understand; therefore in the present study the importance of the decay in this far-field region was considered secondary.

A note should be made here about the radiation correction to the thermal flow field. In §2.1, it was shown that the radiative thermal error was always small in this experiment due to the small probe size. This analysis however does not preclude the possibility that the film-protected wall is not appreciably heated due to radiative interaction with the other walls; rather it showed that the thermal measurement would be accurate. This distinction is beneficial because the degree of radiative heating can be characterized. Additionally, air is a radiatively non-participating gas, meaning the radiative heat transfer is almost entirely between the wind tunnel walls and the test plate. A note on terminology used in this research is now in order. The heat transfer boundary condition for the experiments shown in Figure 20 has been described as adiabatic. This labeling is not strictly speaking correct. It has already been noted that a minor amount of thermal conduction occurs through the wall but it remains small due to the insulation and low-thermal conductivity of the wall. On another note, if radiation is present, further

heating occurs past the convective heating due to fluid flow. Most studies consider film cooling without the presence of radiation. The thermal mixing profiles are not dominated by radiation as will be shown in the thermal analysis section. Actual engines experience an appreciable amount of radiation, so understanding the influence of radiation on film cooling flows is quite important.

When radiative heating is present, an alternate form of the adiabatic wall effectiveness is possible. Since radiation increases the temperature of the wall past the temperature of the fluid adjacent to the wall, the minimum temperature now occurs in the flow field as opposed to at the wall in the true adiabatic scenario. Therefore the effectiveness can be cast using either the wall temperature or the minimum temperature, as is shown in Equation 105, the minimum temperature being effectively a correction of the film cooling effectiveness to remove the radiative heat flux occurring. Figure 21 shows the effectiveness of these two definitions. In the minimum shear and wall jet cases, the degree of radiative heating is minor, as essentially no difference between the two effectivenesses exist. However the wall wake shows more appreciable radiative heating effects in the near injector field; farther downstream convective heating dominates (or thermal mixing layer heat transfer with the wall) and the two effectivenesses begin to collapse. These assessments and observations will be further demonstrated and explained in the subsequent sections. It should be noted that Figure 20 shows the effectiveness based on the minimum fluid temperature and not the actual wall temperature.

$$\eta_{wall/\min} = \frac{\left(T_\infty - T_{wall/\min}\right)}{\left(T_\infty - T_C\right)} \qquad \text{Eq. (105)}$$

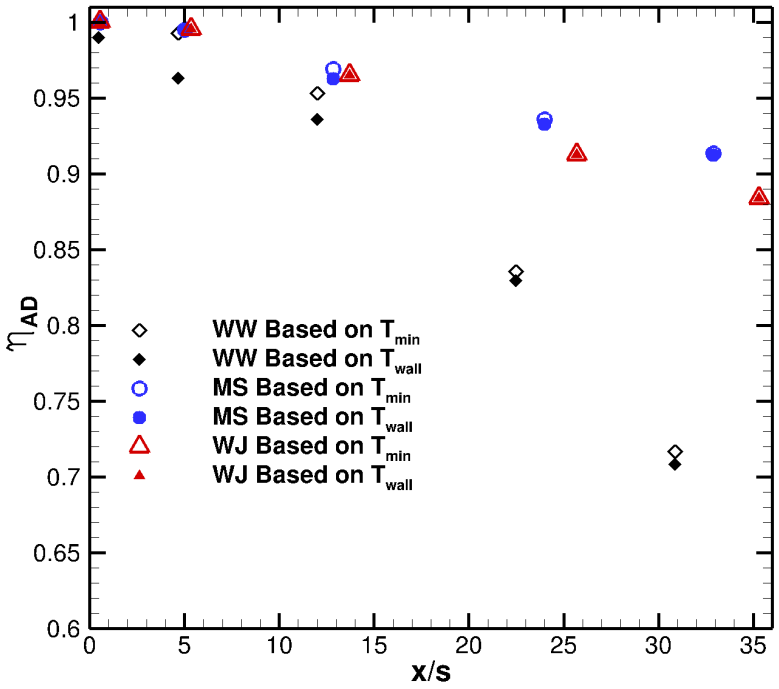

Figure 21 Experimental Adiabatic Effectiveness based on the minimum flow temperature and the wall temperature for the Wall Wake (WW), Minimum Shear (MS) and Wall Jet (WJ) cases.

Next consider the thermal wall characteristics of the non-adiabatic wall cases. Recall these cases occur when appreciable backside heat transfer is present, schematically shown in Figure 6. Now consider the non-adiabatic wall effectiveness shown in Figure 22. The convention for the effectiveness remains the same, i.e., the coolant, wall and mainstream temperatures are the only ones present in the effectiveness formulation. What is perhaps unusual is that the wall effectiveness can now take values greater than unity. This discrepancy is easily explained and is actually expected. Since the backside of the wall is significantly cooled, the wall actually becomes cooler than the coolant temperature. Stated another way, the backside cooling actually cools the coolant. Therefore if the wall is cooler than the coolant, the effectiveness must be greater than one. Also if the effectiveness is greater than one, it is most likely that the conductive load

is appreciably larger than the radiative heating load. In fact in these cases, the minimum temperature always occurs at the wall, further validating the relative strength of the backside cooling relative to the radiative wall heating. This statement will be further explored in the subsequent wall heat transfer rate discussion. Notice that once again the wall wake remains more susceptible to the thermal boundary condition change in the near-injector region. In this case, however the wall wake case cools in the near injector region more than the wall jet and minimum shear cases, as opposed to radiative heating sensitivity in the adiabatic experiments. While starting out cooler, eventually the wall wake film once again dramatically decays past the wall jet and minimum shear cases.

To further explore the various thermal boundary conditions, consider the effectiveness plots shown in Figure 23, for the wall wake (a), minimum shear (b) and wall jet cases (c). In each subfigure, three effectiveness curves are shown. One curve is for the adiabatic wall effectiveness, using the wall temperature. The other two curves are for the non-adiabatic cases, using effectivenesses based on the wall temperature or the backside water coolant temperature. The backside water temperature was plotted to effectively show the minimum wall temperature or highest effectiveness that is possible in the system. Therefore in the non-adiabatic cases the range of possible effectiveness range from zero to the effectiveness based on the backside water temperature; in contrast, the adiabatic effectiveness can range only from zero to one. The backside effectiveness essentially remains constant with only minor heating occurring in the streamwise direction. This constant temperature implies that the water (and accompanying chiller system) acts as a thermal reservoir that is unaffected by the heat transfer occurring above the test plate. Notice also that the streamwise distance is normalized by the blowing ratio,

BR, to effectively collapse the adiabatic and non-adiabatic curves downstream where convective heating dominates. The adiabatic and non-adiabatic curves are taken at slightly different kinematic conditions and slot heights, which can be accounted for by normalizing the streamwise distance by the blowing ratio. This type of scaling is extensively used in the literature to collapse film cooling data. Also in the interest of being explicit, notice that the limits of the effectiveness and streamwise axes for a, b and c are different so that the effectiveness decay trends can be highlighted.

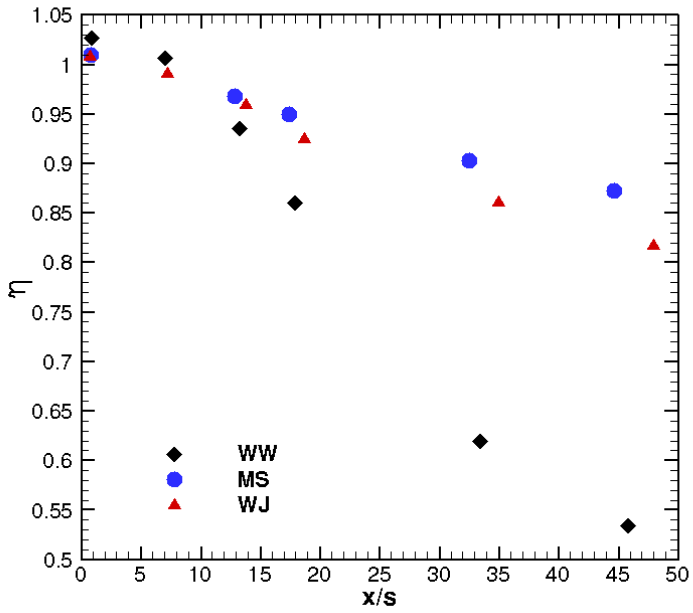

Figure 22 – Wall Effectiveness for the Non-Adibatic Cases.

a.

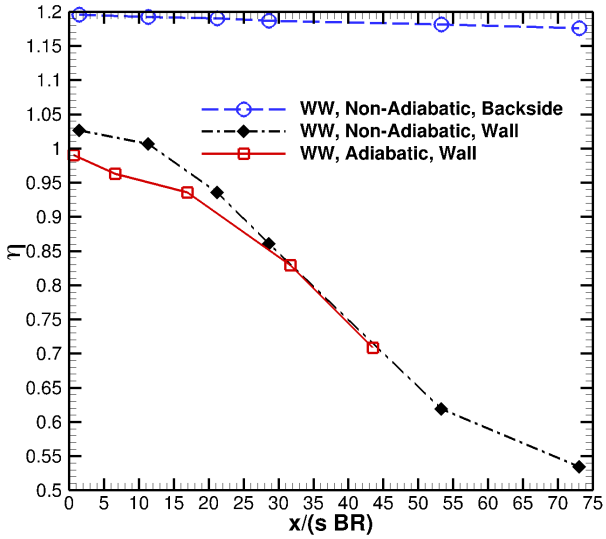

b.

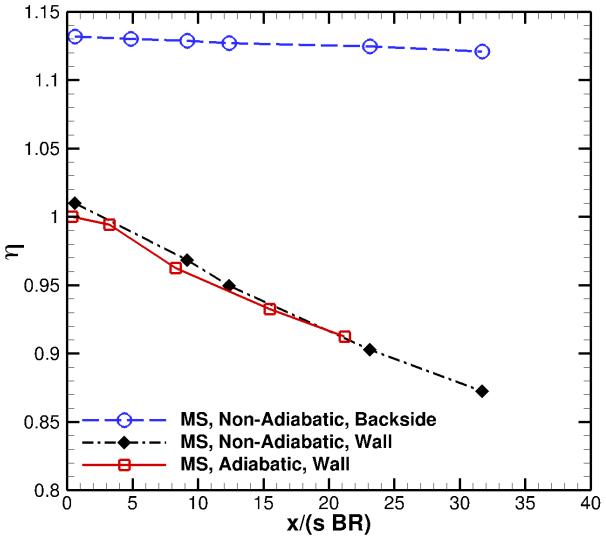

c.

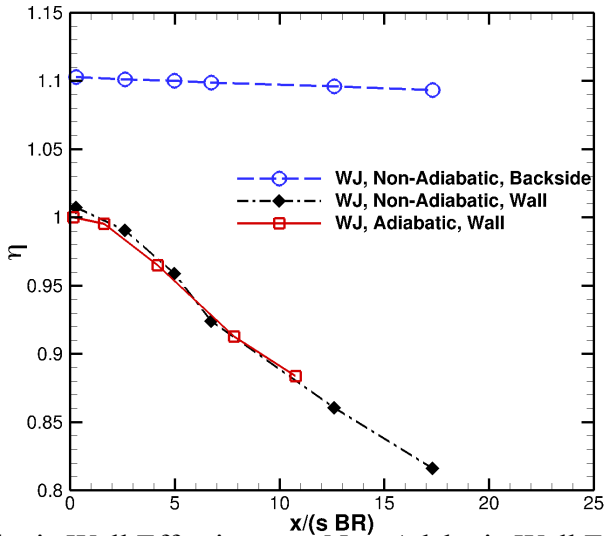

Figure 23 – Adiabatic Wall Effectiveness, Non-Adabatic Wall Effectiveness and Non-Adiabatic Backside Coolant Effectiveness as a function of downstream distance for a. the Wall Wake, b. the Minimum Shear and c. Wall Jet shear cases.

Firstly, due to environmental variability in the experimental lab, the coolant (room temperature air) was different for all three cases, leading to different T_C and therefore different effectivenesses for the water coolant channel. In all three cases, the backside coolant temperature, T_{back}, remained fairly consistent. Also, the non-adiabatic wall effectiveness starts out higher than the adiabatic case due to the backside cooling. Eventually at some downstream distance (which is strongly dependent on the mixing layer impingement location), the convective heat flux due to the presence of the hot fluid near the wall dominates over the conductive cooling through the wall and the two scenarios collapse into a similar film decay trend. The reason for this collapse will be explained further in the numerical results section. Once again the film decay of the wall wake is the most severe. The wall jet performs slightly worse than the minimum shear case, meaning the non-dimensional wall temperatures are higher, for both adiabatic and non-adiabatic boundary conditions.

Theoretically, the non-adiabatic case should always remain cooler than the adiabatic case given the strength of the conductive cooling relative to the radiative heating. However minor differences in kinematic conditions can prevent this from happening. It is natural to next wonder why backside cooling is useful and how to characterize its benefit. The area between the adiabatic and non-adiabatic effectiveness curves is related to the heat removed due to backside cooling. Backside cooling mitigates the effects of wall radiation, in addition to providing longer film protection lengths. It just so happens that the specific non-adiabatic regimes explored in this study did not appreciably increase the film protection length. Stated another way, the conductive cooling was not strong enough to balance the convective heating due to the film mixing

with the mainstream. However in engine applications, the backside cooling is designed to be stronger to remove relatively more heat from the wall.

As is shown in Figure 22 and Figure 23, the non-adiabatic wall wake case starts at a higher effectiveness than the other cases. One reason why this occurs is because the temperature difference between the backside coolant and the coolant air is largest for the wall wake case, as can be ascertained from Table 3, in addition to Figure 22 and Figure 23. This larger temperature difference means the wall wake film experiences a larger heat flux than the other two shear scenarios. Also it was claimed that the wall wake film seemed more susceptible to heating and cooling in the near-injection region, depending on the thermal loads present there. From Table 3, the mass flux in each scenario can be inferred. It can be seen that the mass flux of the wall wake film is approximately half the mass flux of the wall jet and minimum shear films. Therefore the lower amounts of mass in the coolant channel mean less heat flux is required to change the coolant temperature. Another way of thinking about this phenomenon is considering the residence time that the film is exposed to a heat flux. Given some fixed heating or cooling length, the wall wake film will have the longest residence time since it has the lowest velocity. This translates to the wall wake film being exposed to a given heat flux for a longer time, meaning more heat is transferred or extracted from the wall wake film than the other films. For these reasons, the wall wake experimental film is claimed to be more susceptible to the heat flux upstream of injection or in the near-injector region. These explanations also demonstrate why there is a larger separation or cooling effect in the wall wake case between the adiabatic and non-adiabatic curves.

The magnitudes of the heat fluxes at the wall are shown for the (a) wall wake case, (b) minimum shear case and the (c) wall jet case in Figure 24. The heat flux is subdivided into three different sources: the conductive heat flux, the convective heat flux and the radiative heat flux. The conductive heat flux is the heat flux occurring through the test plate due to backside cooling. The radiative heat flux is the radiation at the test plate on the flow side due to radiative exchange with the hot wind tunnel walls. The convective heat flux is the heat flux due to the turbulent mixing occurring over the test plate and is the difference of the conductive and radiative heat fluxes. The axes of the plots are consistent so comparisons can be made more easily. For example, it is immediately apparent that the conductive heat flux load is largest for the wall wake case, especially far from injection. The reason for this large heat flux can be seen when considering Equation 25, reproduced here for convenience.

$$\vec{q}''_{conduction} = -k_{wall}\nabla T_{solid} \approx -k_{wall}\frac{\partial T_{solid}}{\partial y} \approx -k_{wall}\frac{\left(T_{wall} - T_{back}\right)}{t_{wall}} \qquad \text{Eq. (25)}$$

As can be seen the conductive heat flux is largely

dependent on the flow side wall temperature, because the other variables remain relatively constant. For the wall wake case, the film degrades much more rapidly than the other cases; therefore the wall temperature and the associated heat flux through the wall are larger. Another important observation is that the radiative heat flux remains small compared to the conductive heat flux, meaning that the flow is not radiatively dominated, which is also experimentally observed in the other wall effectiveness plots. The radiative heat flux is largest in the near injector region primarily because the wall temperature is the lowest in this area and the radiative heat flux has a power four dependence on the

wall temperature. Therefore it is in this region, in both the adiabatic and non-adiabatic cases, that radiative effects would be most prominent. This point is also evidenced by the fact that the largest separation between the adiabatic effectiveness based on wall and minimum temperatures (Figure 21) occurs in the near injector fields, due to this larger relative importance of radiative heating (compared to convective heating) in this region. Overall however the convective heat flux is primarily a function of the conductive heat flux and is stronger than the radiative heat flux. It is also interesting to note that the conductive and convective heat fluxes mimic the effectiveness trends. As the mixing layer impinges on the wall, nominally between the second and third experimental data points, the heat flux slope increases, which is both sensible and physical.

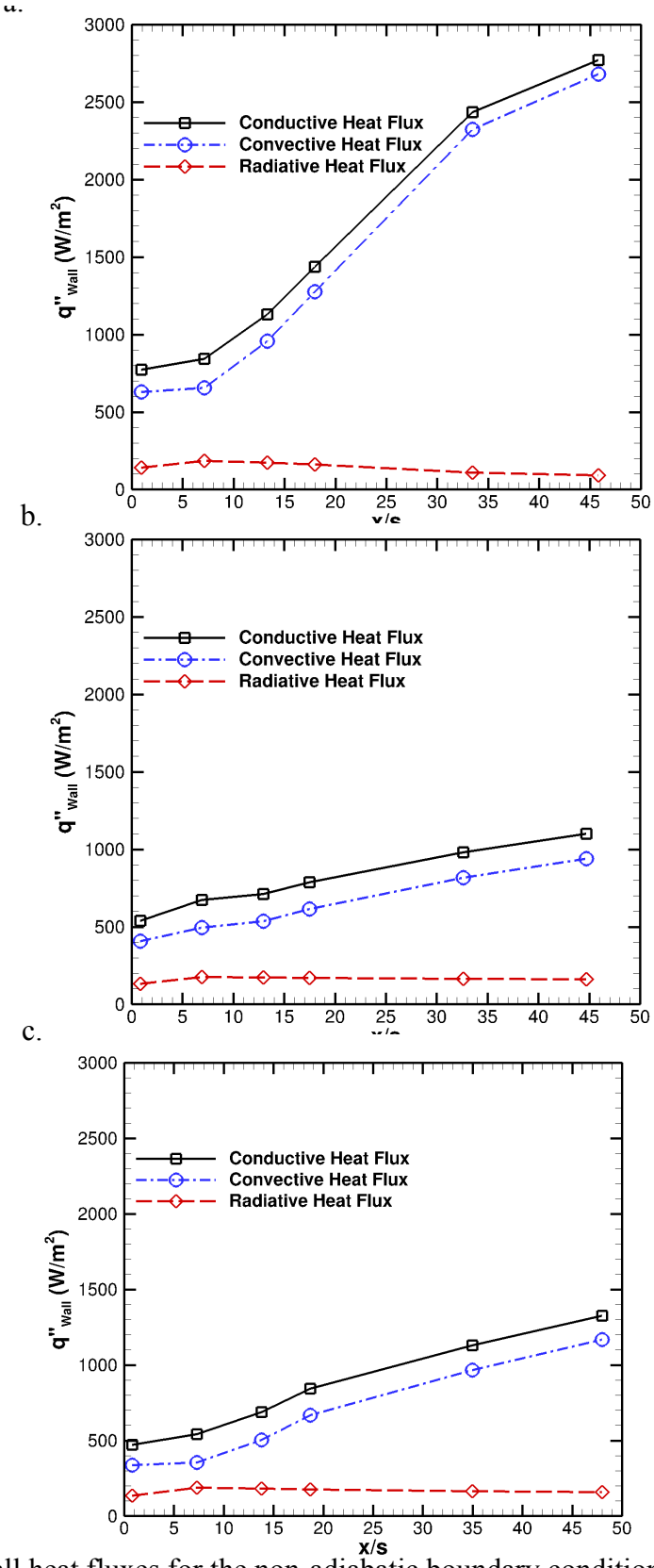

Figure 24 – Wall heat fluxes for the non-adiabatic boundary condition experiments. (a) Wall Wake, (b) Minimum Shear, (c) Wall Jet shear scenarios.

3.2 Mean Kinematic and Thermal Flow Fields

In the last section, some of the wall thermal characteristics of the experimental film cooling flows were observed. The purpose of this section is to present the flow field measurements and physics, using them to explain and understand the wall measurements. The wall measurements in these experiments are strongly governed by the flow field mixing occurring over the wall and therefore the kinematic and thermal fields are responsible for the film decay trends at the wall.

One way of characterizing the film cooling experiments is to observe the degree to which they follow Weidghardt's scaling [9]. As was mentioned in §1, Weidghardt [9] developed a self-similarity expression for film cooling flows of the form shown in Eqns. 8 and 9, reproduced below. To confirm the degree to which these experiments follow this similarity, the mean temperature profiles for the adiabatic experiments are plotted in Figure 25 using the Weidghardt scaling. This scaling is derived using an energy balance, boundary layer assumptions and a turbulent power law velocity field. Notice that in general the first two streamwise experimental measurement stations do not follow Weidghardt's scaling, whereas further downstream the thermal profiles collapse for each case to a similar profile. As was stated in §1, Weidghardt's scaling should only hold in the far field of the injector (or the far-injector field), where the rapid streamwise variations and mixing in the near-injection region do not violate the boundary layer assumptions. Therefore it is not surprising that the first two streamwise measurements are not similar. Nevertheless, at first glance, these experiments follow typical film cooling scaling, especially in the far-injector field.

$$\theta = \frac{T - T_\infty}{T_{ad,W} - T_\infty} \approx e^{-0.768\left(\frac{y}{\delta_T}\right)^{\frac{13}{6}}} \qquad \text{Eq. (8)}$$

$$\delta_T = \int_0^\infty \left(\frac{T - T_\infty}{T_{ad,W} - T_\infty} \right) dy = \int_0^\infty \theta dy \qquad \text{Eq. (9)}$$

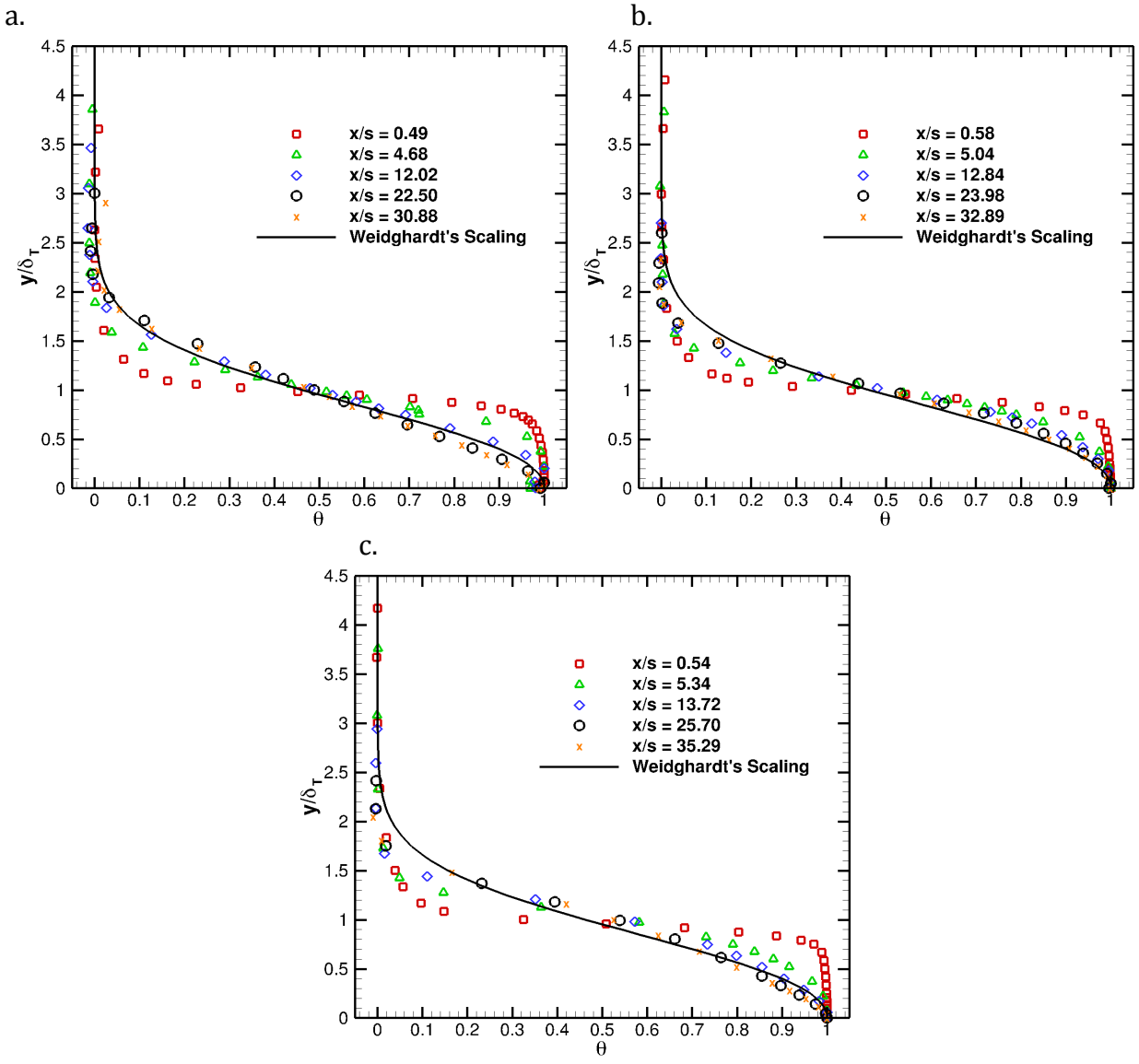

Figure 25 – Normalized mean temperature profiles using Weighardt Scaling for the adiabatic a. Wall Wake, b. Minimum Shear and c. Wall Jet cases. Weighardt's correlation is also plotted.

To really understand the way the film mixes and breaks down, the kinematic field must be analyzed. The mean streamwise velocity for each adiabatic case is shown in Figure 26. Notice that similar to Table 3, the velocity is normalized by the peak velocity

a.

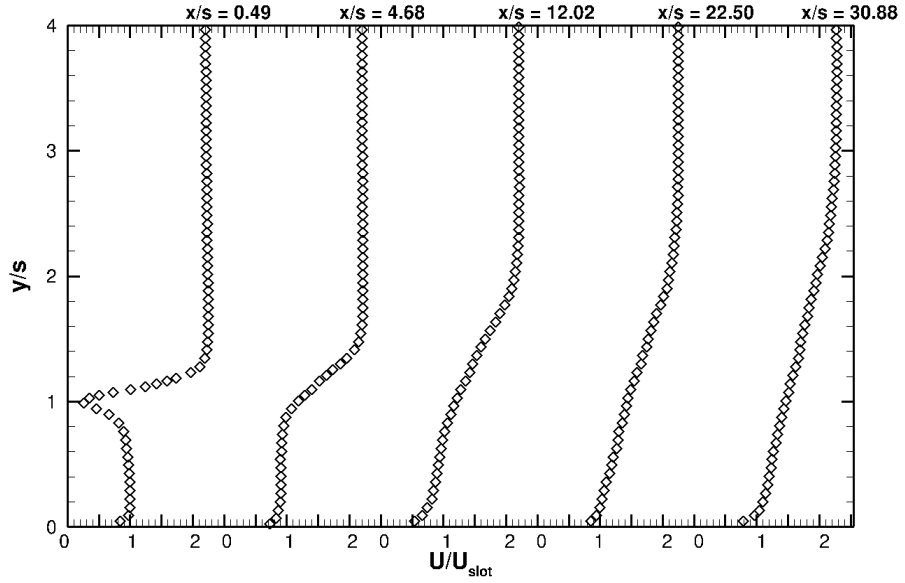

b.

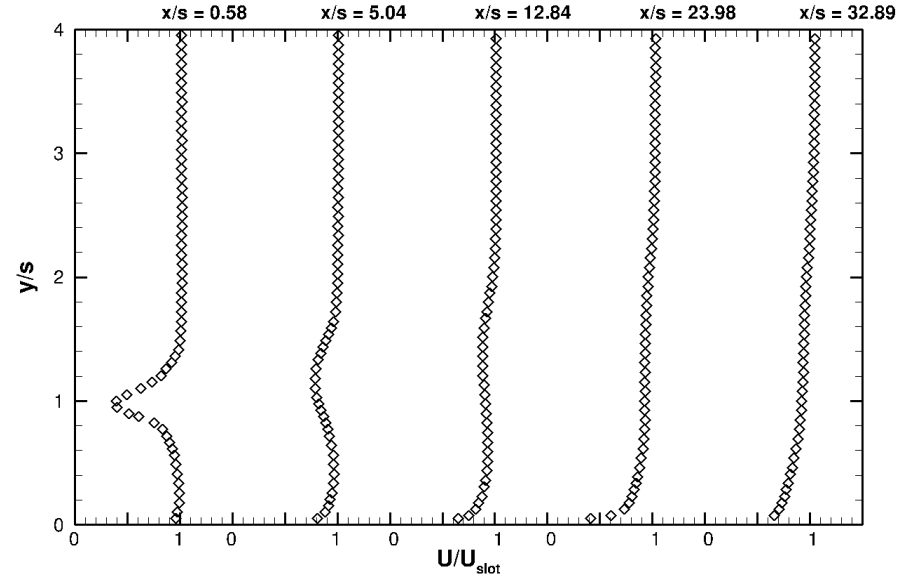

c.

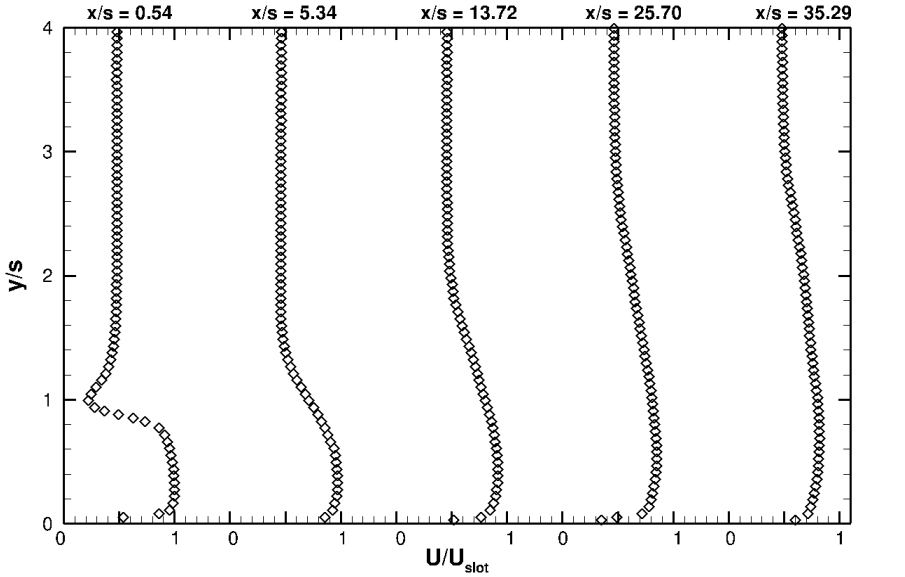

Figure 26 – Mean streamwise velocity profiles at different streamwise stations for the adiabatic a. wall wake, b. minimum shear and c. wall jet cases.

in the coolant slot at the first streamwise measurement location. This normalization is used instead of the bulk coolant velocity due to the uncertainty in this quantity. As can be observed in the experimental data, the velocity cannot be measured very close to the wall due to laser noise reflections. In this region and also in the vicinity of the louver splitter plate the velocity profile would need to be reconstructed and then integrated. The variations in the bulk coolant velocity, which depend on choices of integration techniques and velocity reconstruction methods near the wall, was on the order of two meters per second, which corresponds to an uncertainty on the order of 10%. This uncertainty is in addition to the experimental velocity uncertainty that is less than 2% for the PIV system and approach used in this flow. Therefore the peak coolant velocity, which can be directly measured, was chosen as the normalizing parameter. A coolant velocity and not a mainstream velocity is chosen for normalization because the near-wall region, the region of interest in this study, should collapse better than most other possible normalizations, especially for the turbulent profiles. One useful normalization often considered is the wall friction velocity, but this characteristic velocity is dependent on the velocity gradient at the wall, which is not captured in the present velocity measurement technique and thus not used.

From the mean velocity profiles, the major defining features of the wall wake, minimum shear and wall jet cases become apparent. Much insight can be gained into the mixing features of the flow just from the analysis of the mean velocity profiles. Starting with the basics, the wall wake has a coolant velocity that is less than the mainstream, while the wall jet is the reverse of this scenario. The minimum shear case has coolant and mainstream velocities that are approximately the same. Large velocity differences can be

seen from the first experimental profile between the coolant and mainstream velocities for the wall wake and wall jet experiments resulting in a large amount of turbulent shear mixing. In fact due to this large amount of shear, the turbulent mixing layers grow faster, as will be shown later. Some remarks on the general features of the three shear cases should also be made.

The wall jet resembles a jet being injected into a boundary layer. In a mean sense there will be a negative gradient of streamwise velocity in the cross-stream direction. Also the jet, due to larger relative amounts of momentum, will spread into the mainstream. Described another way, due to the wall boundary and the slower moving mainstream fluid, the coolant flow will in the mean decelerate. According to conservation of mass, this deceleration for incompressible fluids will lead to a positive vertical velocity and therefore the jet spreads into the mainstream. This spreading effect leads to a decrease in the maximum jet velocity as a function of streamwise distance.

The wall wake on the other hand more closely resembles flow over a backward facing step, with a positive cross-stream gradient of streamwise velocity in the mixing layer. Due to the fast moving mainstream and viscosity, the coolant fluid near the louver splitter plate accelerates. Once again, using the conservation of mass for an incompressible fluid, this acceleration in the streamwise direction leads to a negative vertical velocity. This effect translates to the mainstream in a mean sense spreading into the coolant flow for the wall wake case. The peak velocity in the wall wake should similarly increase as a function of streamwise distance until boundary layer effects take over far downstream. As a note, the minimum shear has a minimal average cross-stream

gradient of streamwise velocity; spreading will be controlled primarily by the blowing ratio, BR, which is greater than unity.

The upper extent of the mixing layer can be also visualized in the velocity data, even though better methods exist to visualize the mixing layer as will be shown later. The location where the velocity gradient returns to a zero wall-normal gradient occurs approximately at the upper extent of the mixing layer. Looking at the last streamwise station, it can be discerned that the wall jet spreads the furthest from the wall, followed by the minimum shear and then the wall wake.

The mean thermal profiles at distinct downstream distances for the adiabatic cases are shown in Figure 27. It is often easier to see the mixing trends in scalar mixing profiles or temperature profiles. Each velocity ratio case has a nearly isothermal coolant up until ¾ of a slot height at which thermal mixing is apparent, most likely due to coolant heating through the louver wall. As was stated for the kinematic section, each velocity ratio case exhibits different mean mixing trends, which upon careful observation can be discerned from the mean temperature profiles. In the mean temperature profiles, the upper and lower extent of the thermal mixing layers can be visualized by the wall normal gradient of the temperature returning to zero. Once again the wall jet has spreading occur farthest from the wall, in agreement with the kinematic findings discussed earlier. The wall wake shows the lower boundary of the mixing layer penetrating into the film the fastest. Not surprisingly, the wall temperature increases the most for the wall wake, which is due to the wall wake spreading in a mean sense towards the wall. The minimum shear and wall jet scenarios show less thermal degradation at the wall due to their mixing layers spreading preferentially away from the wall.

To understand what these thermal mixing trends correlate to in wall effectiveness space, the flow effectiveness, or non-dimensional temperature is provided in Figure 28. The flow effectiveness follows the same definition as the wall effectiveness, except that the wall temperature is replaced with the flow temperature. At the wall, the flow effectiveness and wall effectiveness revert to the same value, allowing for better visualization of the thermal mixing layer and its impact on the wall effectiveness. In effectiveness space, it is easier to see that the wall heats up the most for the wall wake case, followed by the wall jet and then the minimum shear. This finding is perhaps somewhat remarkable in the sense that the wall jet actually utilizes more relative mass to cool the wall than the minimum shear, as evidenced by its larger blowing ratio shown in Table 3. However due to the larger shear between the two streams in this case, the wall jet film actually degrades faster than the minimum shear. This finding implies that there is some optimal velocity and blowing ratio that corresponds to the best film protection.

Some discussion of the adiabaticity of the experiment is in order. The way this evaluation is accomplished is by determining the near wall temperature gradient. In a purely adiabatic experiment with no radiation, the near-wall, wall-normal gradient of temperature should be zero. Examining the temperature profiles, this adiabaticity is very nearly met. However as was noted earlier, there is a small level of radiation, which actually heats the wall; this in turn means that in certain regions of the flow, the fluid above the wall is actually cooler than the wall itself. Although difficult to see in Figure 27 and Figure 28, the temperature profiles show a negative wall-normal gradient, meaning radiation effects are apparent. Unfortunately, the resolution of the temperature measurements do not allow for direct quantification of the heat flux at the wall. However,

using the non-adiabatic cases, the wall heat fluxes can be attained through use of the wall temperature and the backside wall coolant temperature, thus providing some estimation for the gradients very close to the wall, not afforded in the adiabatic measurements. Further quantification and discussion of this near wall temperature profile will be reserved for §4 when numerical comparisons to experimental data are made.

To further aid visualization of the mean thermal spreading, contour lines of constant effectiveness are drawn for the wall wake, minimum shear and wall jet scenarios in Figure **29**. Effectiveness of 0.1 and 0.9 were selected to visualize the upper and lower extents of the thermal mixing layer, respectively. The 0.5 effectiveness line meanwhile is used to show the direction and asymmetry of mean spreading. The wall jet once again is shown to spread the furthest from the wall, while the wall wake spreads preferentially towards the wall. The 0.9 effectiveness contour impinges with the wall at around 16 and 30 slot heights for the wall wake and wall jet cases, respectively. The minimum shear line interestingly does not impinge with the wall, which is perhaps unsurprising since the wall effectiveness for the minimum shear shown earlier does not degrade past 0.91. The strength of shear can also be qualitatively determined from this visualization by considering the distance between the 0.1 and 0.9 effectiveness lines. The wall wake and wall jet both exhibit large amounts of shear since these two lines spread apart the fastest. This finding is consistent with film cooling understanding; the absolute velocity differences between the coolant and mainstreams for the wall wake and wall jet are much larger than for the minimum shear. Since the shearing rate is primarily a function of this velocity difference, the wall wake and wall jet spread the most. The minimum shear shows the least amount of mixing, reemphasizing the function of turbulent shear as the

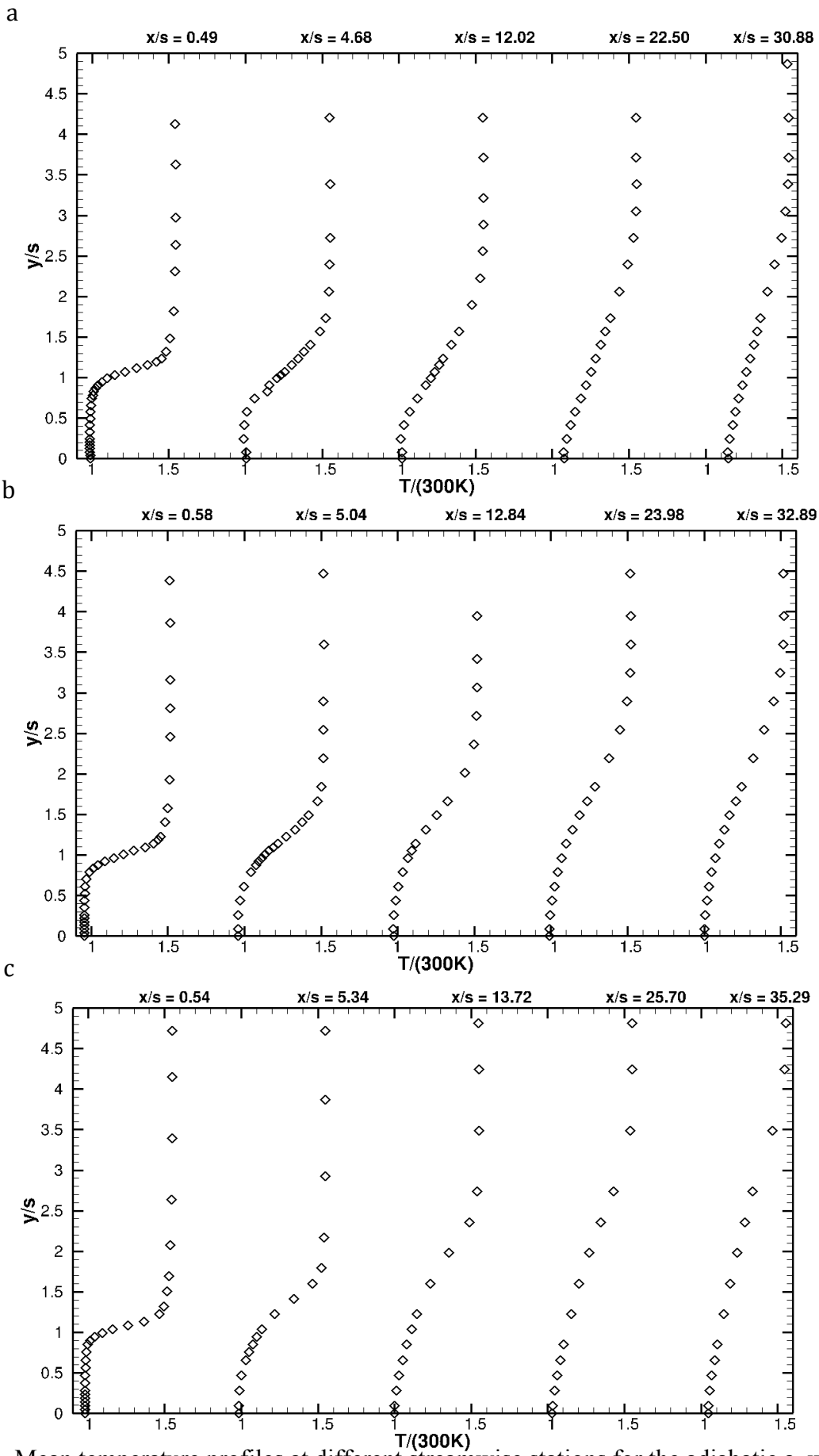

Figure 27 - Mean temperature profiles at different streamwise stations for the adiabatic a. wall wake, b. minimum shear and c. wall jet cases.

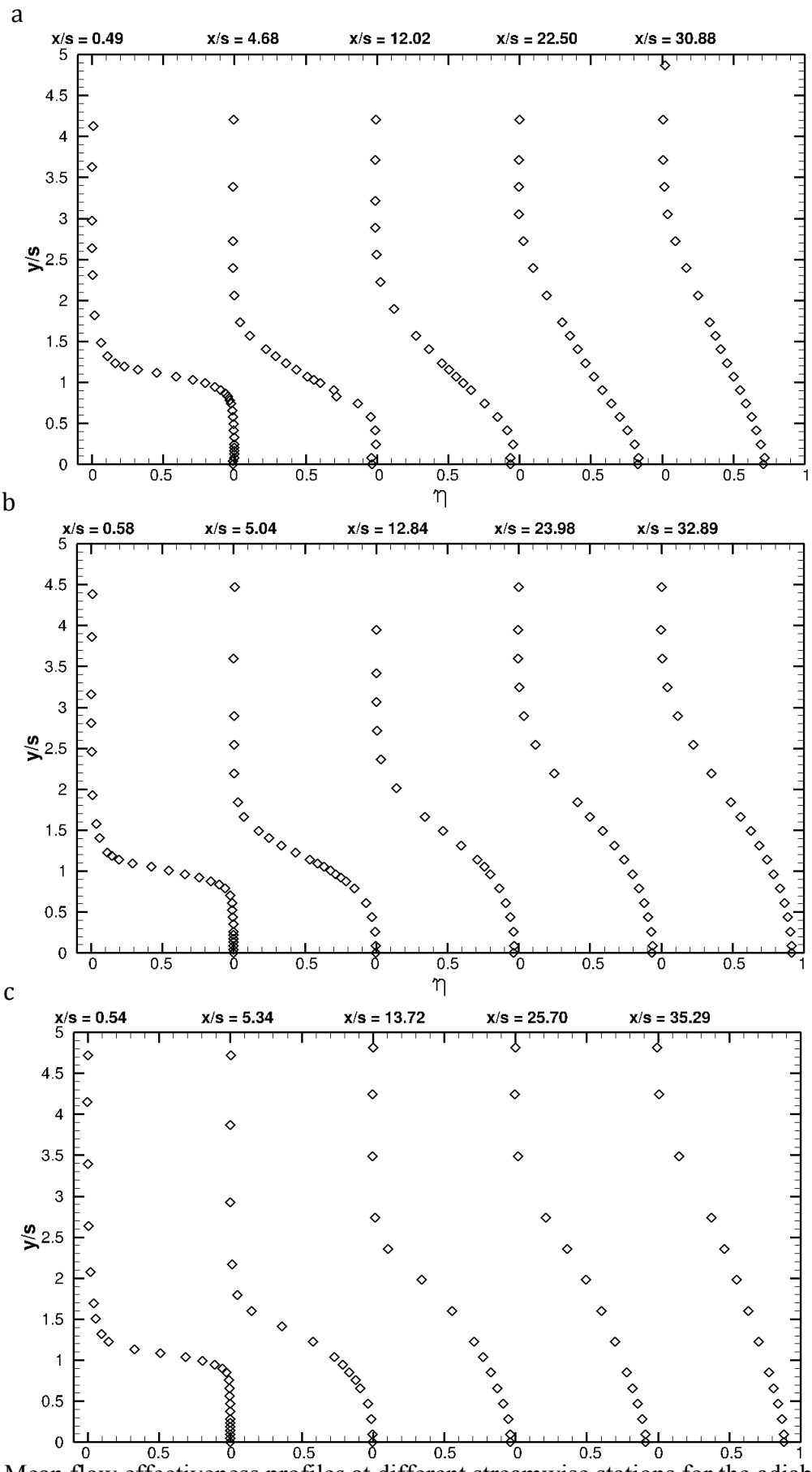

Figure 28 - Mean flow effectiveness profiles at different streamwise stations for the adiabatic a. wall wake, b. minimum shear and c. wall jet cases.

primary mechanism for film mixing. The wall jet and minimum shear in a mean sense spread away from the wall as is demonstrated through the 0.5 effectiveness contour line relative to the other contour lines. In contrast, the wall wake spreads preferentially towards the wall. Lastly, from free-shear layer mixing theory, the mixing layer spread rate is constant, meaning lines of constant effectiveness are linear. In the near injector region, this finding does not hold as there are rapid streamwise gradients disrupting the balance between spread rate, advection and wall-normal turbulent diffusion. However after the third experimental station, the contour lines of effectiveness are very nearly linear, except near the wall, where this time, the presence of the wall disrupts this balance.

Another observation can be made here concerning the blowing ratio. In turbulent regimes like the minimum shear case, where the velocity ratio is approximately unity, the blowing ratio can become the dominant term governing film cooling performance. While

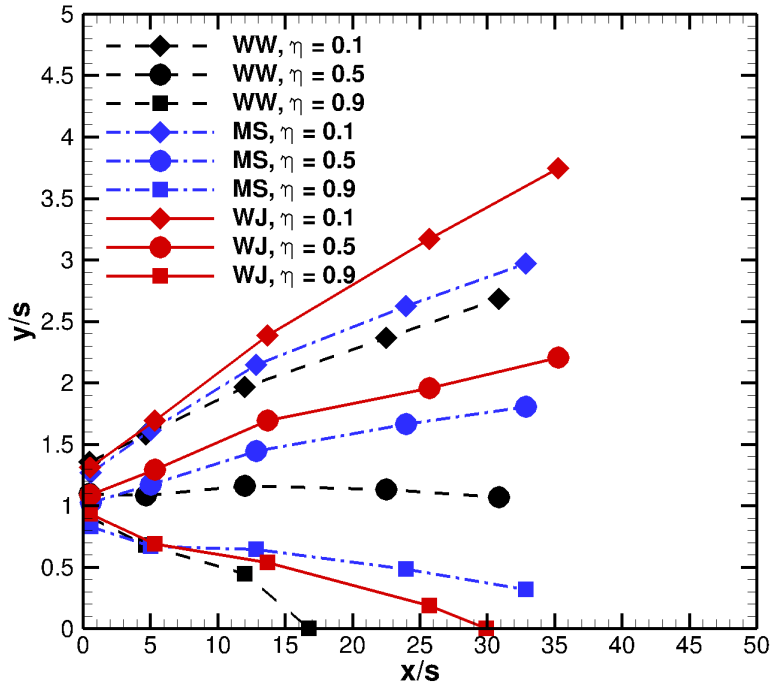

Figure 29 – Lines of constant flow effectiveness for the adiabatic wall wake, minimum shear and wall jet cases.

in a purely laminar sense, the shear layer instability is purely governed by velocity ratio, which characterizes the velocity differences of the two streams, the blowing ratio can be important for mixing layers with turbulent boundary layers upstream. To understand why, consider a parcel of fluid from the hot mainstream and a parcel of fluid from the coolant stream for the minimum shear case. In this case, the velocity of the two parcels are approximately the same, however the momentum of the coolant is higher. Imagine these two parcels collide. The coolant parcel will tend to dominate and move into the mainstream, allowing hot mainstream fluid to move in its wake, thus setting up and generating further turbulent motion.

For the sake of completeness the temperature and effectiveness profiles of the non-adiabatic case are given in Figure **30** and Figure **31**, respectively. Similar observations can be made about the thermal spreading rates as were made for the adiabatic cases. Non-adiabatic mean velocities and plots of lines of constant flow effectiveness will be reserved for Appendix B, along with other experimental data, as the trends are not overly different from the adiabatic cases. The non-adiabatic thermal experimental data exhibits signs of heat flux at the wall, as is expected. In all the profiles near the wall, a positive temperature gradient in the wall normal direction can be discerned. The implications of this fact are that conduction is stronger than radiation throughout the flow domain as was already apparent from Figure **24**. The direction of heat transfer is always the same in the non-adiabatic cases, i.e. the wall-normal gradient of temperature is always positive. The largest gradients at the wall occur for the wall wake case, once again confirming the heat transfer is the largest for this case.

a

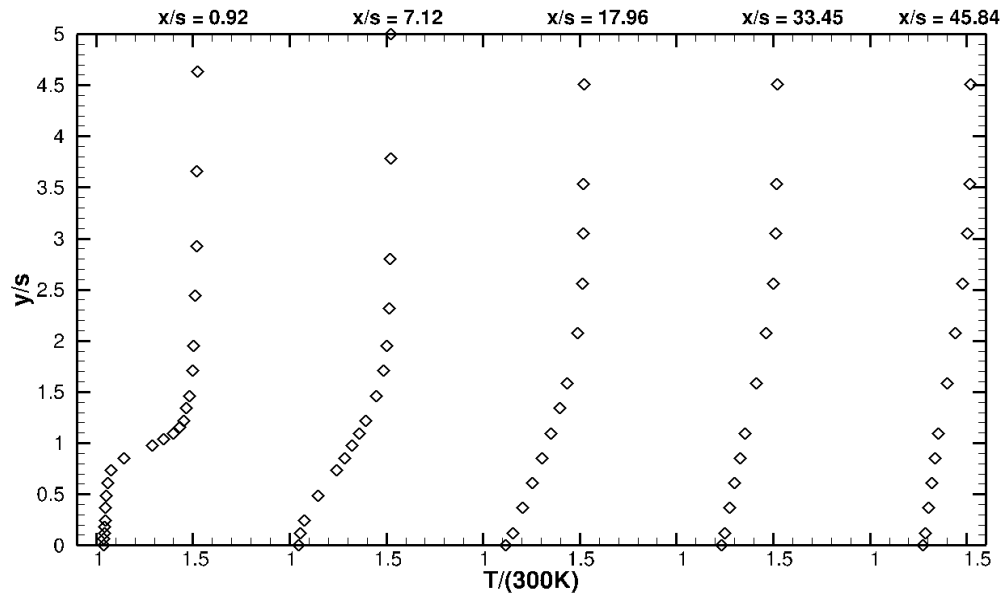

b

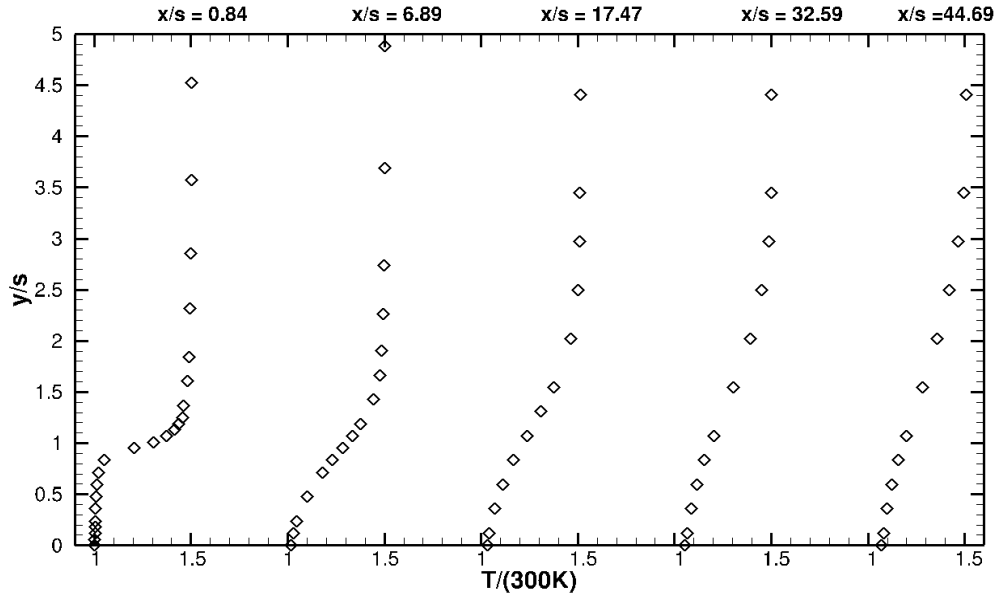

c

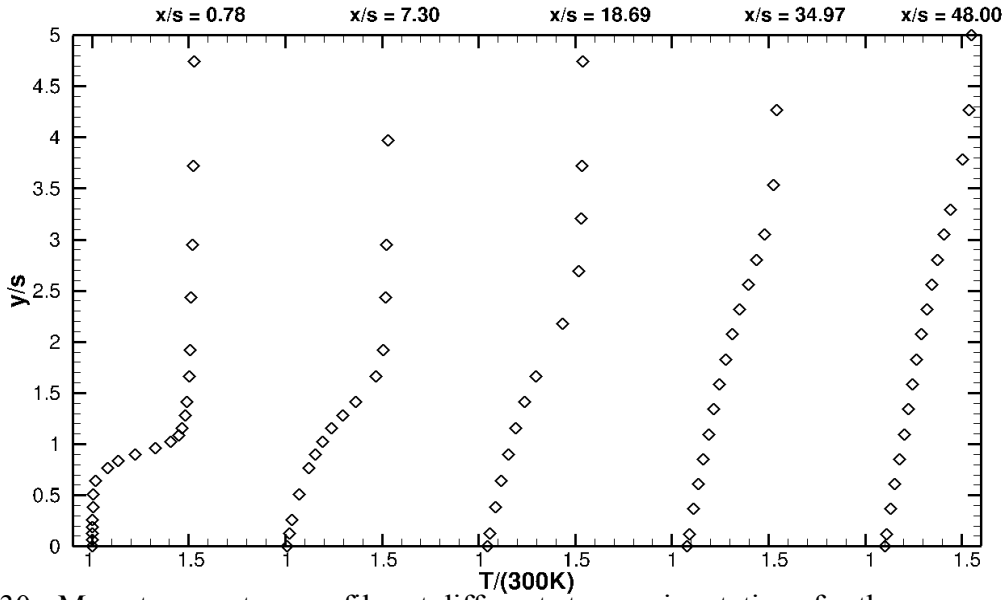

Figure 30 - Mean temperature profiles at different streamwise stations for the non-adiabatic a. wall wake, b. minimum shear and c. wall jet cases.

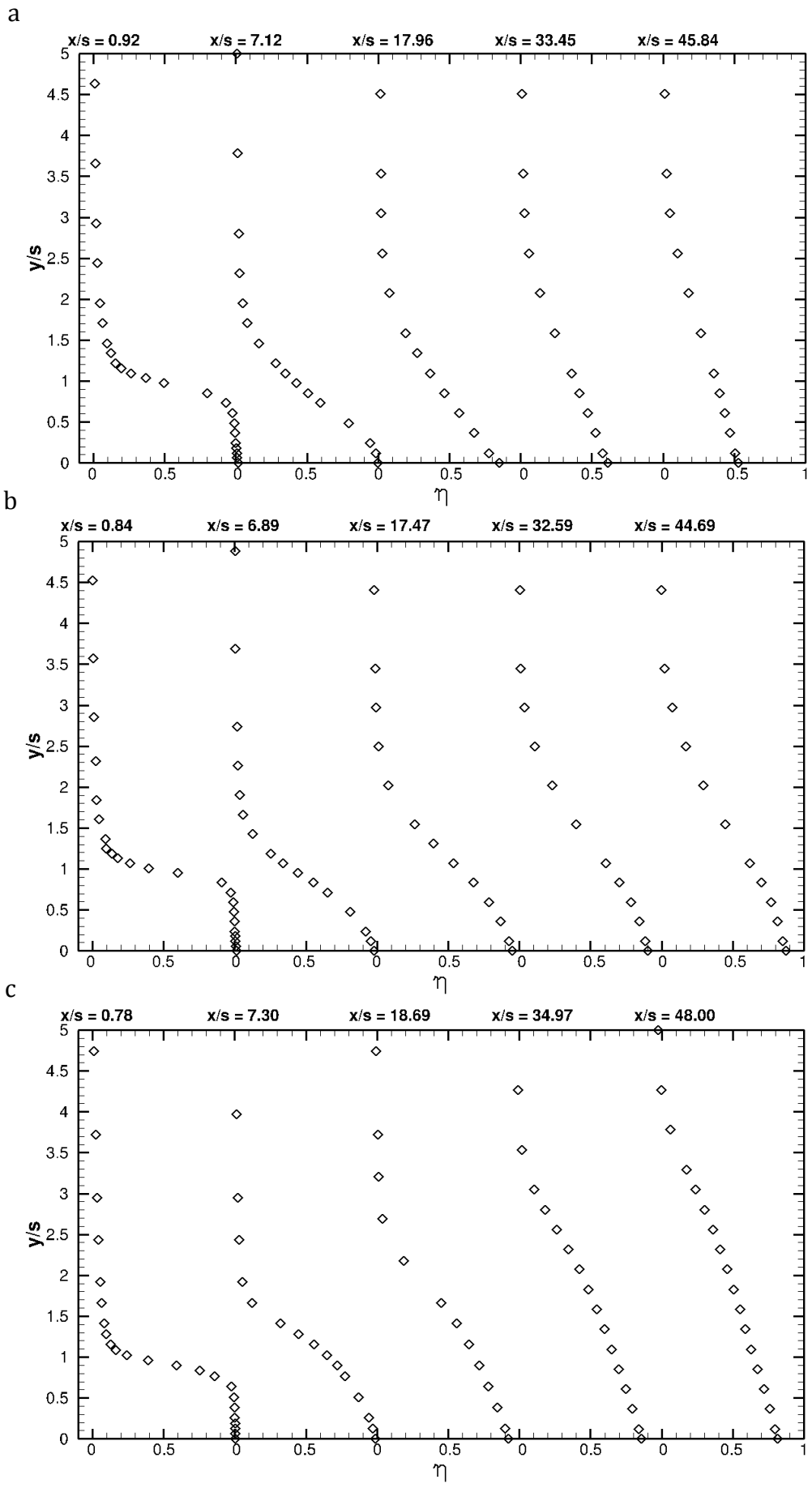

Figure 31 - Mean flow effectiveness profiles at different streamwise stations for the adiabatic a. wall wake, b. minimum shear and c. wall jet cases.

3.3 Fluctuating Kinematic and Thermal Flow Fields

In this section, the fluctuating flow fields are presented with the view of trying to analyze the turbulent, unsteady mixing, primarily responsible for film cooling mixing. As has been discussed, the experiments and real-world engine applications are turbulent and therefore mean statistics do not provide an adequate, stand-alone perspective of the film cooling mixing. Fluctuating information, more specifically second order statistics, are presented in an attempt to quantify the mixing flow fields. Consider an actual engine, where the mean effectiveness at the wall is approximately 0.82 and the failure effectiveness is 0.80. Using mean criteria, the wall should be safe; however if the wall effectiveness has a root mean squared (RMS) fluctuation of about 0.10 around the mean, for example, the engine may still fail because for extended times the wall is exposed to effectivenesses below 0.80, e.g., 0.72.

Figure 32 shows flow visualization, or instantaneous realizations, of the turbulent shear structures existing for each velocity ratio case. The mainstream and coolant are each visualized in different images to give an idea of the spread of the film into the mainstream and vice-versa. The shear structures, shown for the wall wake case and wall jet case, are predominantly clockwise and counterclockwise, respectively, in the orientation shown. It should be noted that the flow goes left to right in the images. A white line is drawn to denote a slot height for each case. To explain these orientations, first consider the wall jet case. The coolant is moving faster than the mainstream; through viscosity the mainstream acts to decelerate the coolant and vice-versa. From the definition of vorticity, if the wall-normal gradient of the streamwise velocity is negative (as it is at the interface between the coolant and mainstream) positive spanwise vorticity

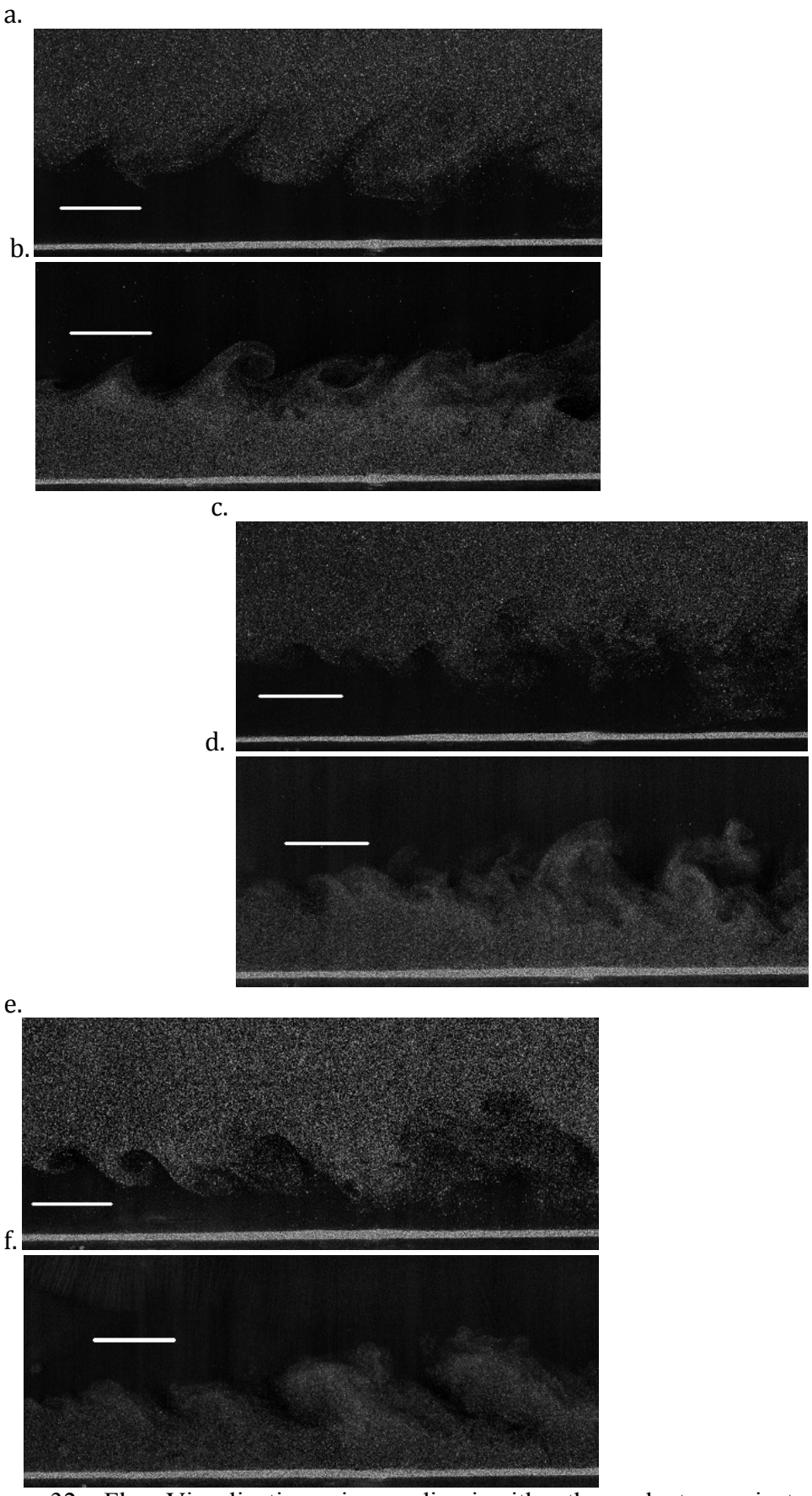

Figure 32 – Flow Visualization using seeding in either the coolant or mainstream. a-b. Wall Wake, c-d. Minimum Shear, e-f. Wall Jet. a., c., e. use mainstream seeding. b., d., f. use coolant seeding.

is created, meaning the fluid structures will spin in a counter-clockwise direction. For the wall wake case, examining the spanwise component of vorticity, the positive wall-normal gradient of streamwise velocity will create a negative vorticity, meaning the shear structures must have a clockwise orientation. Another way of analyzing the transport would be to perform a force balance. For the wall jet case, a positive streamwise shear force is imparted on the mainstream, which is counter balanced by a positive advection term, comprised of the product of a negative vertical velocity and a negative wall-normal derivative of streamwise velocity. This negative vertical velocity along with the higher momentum of the coolant fluid sets up the counter-clockwise motion. For the wall wake case, a negative streamwise shear force is enacted on the mainstream fluid, which is counterbalanced by an advection term that is the product of a negative wall-normal velocity and a positive wall-normal streamwise velocity gradient. This negative vertical velocity combined with higher momentum of the mainstream fluid creates the clockwise shear structure. The minimum shear case has structures of both orientations, clockwise and counter-clockwise, meaning the coherence and the bulk fluid transport, via turbulent structures, is not predominantly in one direction, nor is it as strong as the other cases. It is the strength of the shear that generates this turbulent fluid mixing.

Turbulence in general and these structures in particular, are adept at enhancing mixing. This turbulence acts to mix the initial mean fields, which have sharp gradients across the louver splitter plate, until the mean flow fields are relatively smooth and continuous in the far-field. Notice from the flow visualization that upstream, these structures are very well defined and coherent but downstream they begin to deform and

break down, generating turbulent activities at a variety of scales other than the size of the initial turbulent shear eddies, which also enhances the local mixing.

Another way to visualize the turbulent fluid structures is by analyzing the instantaneous fluctuating components of velocity, as is shown in Figure 33 for the adiabatic cases. The instantaneous fluctuating components give a good indication of relative motion of the turbulent structures, that may be embedded into the mean velocity field, and therefore difficult to visualize otherwise. In Figure 33, the shear structures in the mixing layer very close to the injection plane are shown. The boxes with black dashed lines highlight the dominant shear structures for each case. For example in the wall wake case, the strong shear structures are clockwise. In wake problems, like the ones generated behind the louver lip, vortices are generated in pairs, with each vortex spinning in opposite directions. This vortex pairing is once again evident in the experimental velocity data and therefore the weak vortices are highlighted with a box with white dotted lines. In the minimum shear case, since there is no dominant shear direction, all the fluid structures are highlighted with a box with black dashed lines. In general, the turbulent vortical structures interact to both constructively and destructively interfere with each other in different regions of the flow. For example, between two counter-rotating vortices, a large amount of velocity tangent to the vortices is generated; in other regions, say very far away from each vortex core, the vortices destructively interfere. This vortex interaction of constructive interference is one prime example of how a bulk amount of coolant fluid is ejected into the mainstream, or how a bulk of mainstream fluid can be swept into the coolant stream.

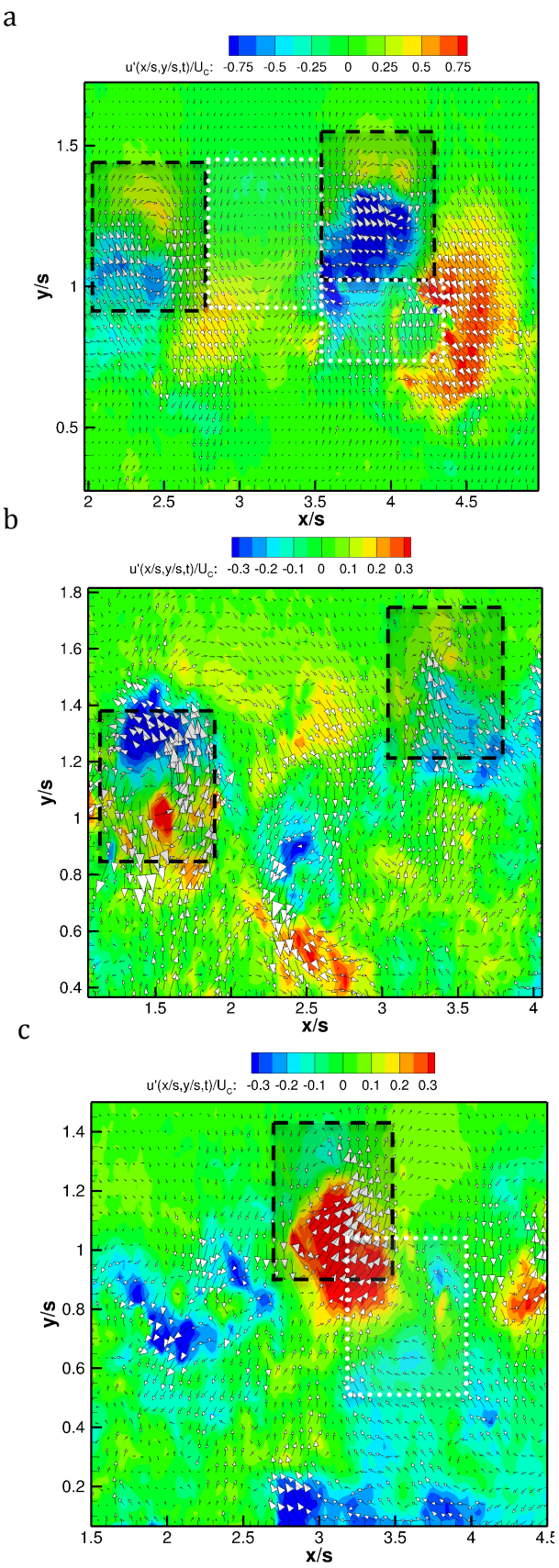

Figure 33 – Vector maps of fluctuating velocity components for the adiabatic: a. wall wake, b. minimum shear and c. wall jet cases. Contours of the streamwise fluctuating component are also shown.

To get a better understanding of the kinetic energy of turbulent motions, the fluctuating components of streamwise and wall-normal velocity should be shown. Figure 34 and Figure 35 show the RMS components of streamwise and wall-normal velocities, respectively. The turbulent kinetic energy, tke, is defined in Equation 106, below, and gives a representation for the strength of the fluctuations, or the amount of energy contained in turbulent motions. Since a two-dimensional PIV system is used, only streamwise and wall-normal components of velocity can be measured, meaning the turbulent kinetic energy cannot be fully resolved. Additionally the turbulent kinetic energy is derived from the turbulent motion of all the turbulent fluid structures, meaning scales below the resolution of the measurements are not incorporated into the fluctuating velocity measurements. Fortunately from Kolmogorov turbulent theory, an energy cascade exists, where turbulent kinetic energy is generated by the large scales and is transferred to the smaller scales where it is finally dissipated. The actual kinetic energy resides primarily in the larger scales, meaning if the large-scale structures are resolved, the majority of the motions responsible for turbulent kinetic energy are also resolved. To give an idea of scale, the spatial resolution of the PIV measurements in this experiment is approximately 0.15 mm, which corresponds to approximately 0.03 slot heights. This resolution translates to about 35 velocity vectors per slot height. The most energetic shear structures have sizes on the order of the slot height meaning these eddies should be adequately resolved. The mainstream turbulence has an integral streamwise turbulent length scale of about 0.2 slot heights in all the cases, meaning this resolution only barely

$$tke = \frac{1}{2}\left(\left\langle u'^2 \right\rangle + \left\langle v'^2 \right\rangle + \left\langle w'^2 \right\rangle\right) = \frac{1}{2}\left(u_{RMS}^2 + v_{RMS}^2 + w_{RMS}^2\right) \qquad \text{Eq. (106)}$$

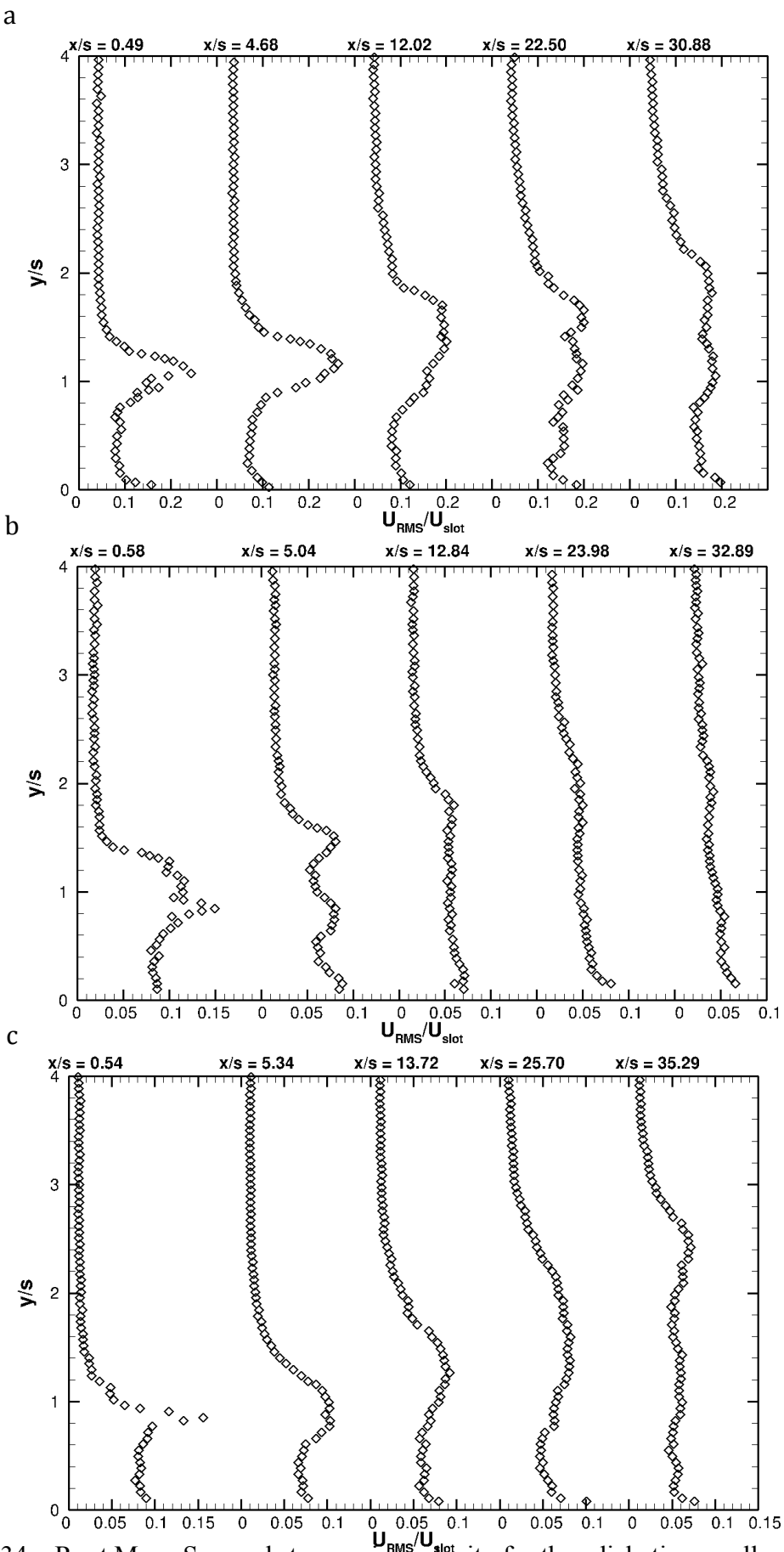

Figure 34 – Root Mean Squared streamwise velocity for the adiabatic a. wall wake, b. minimum shear, c. wall jet cases.

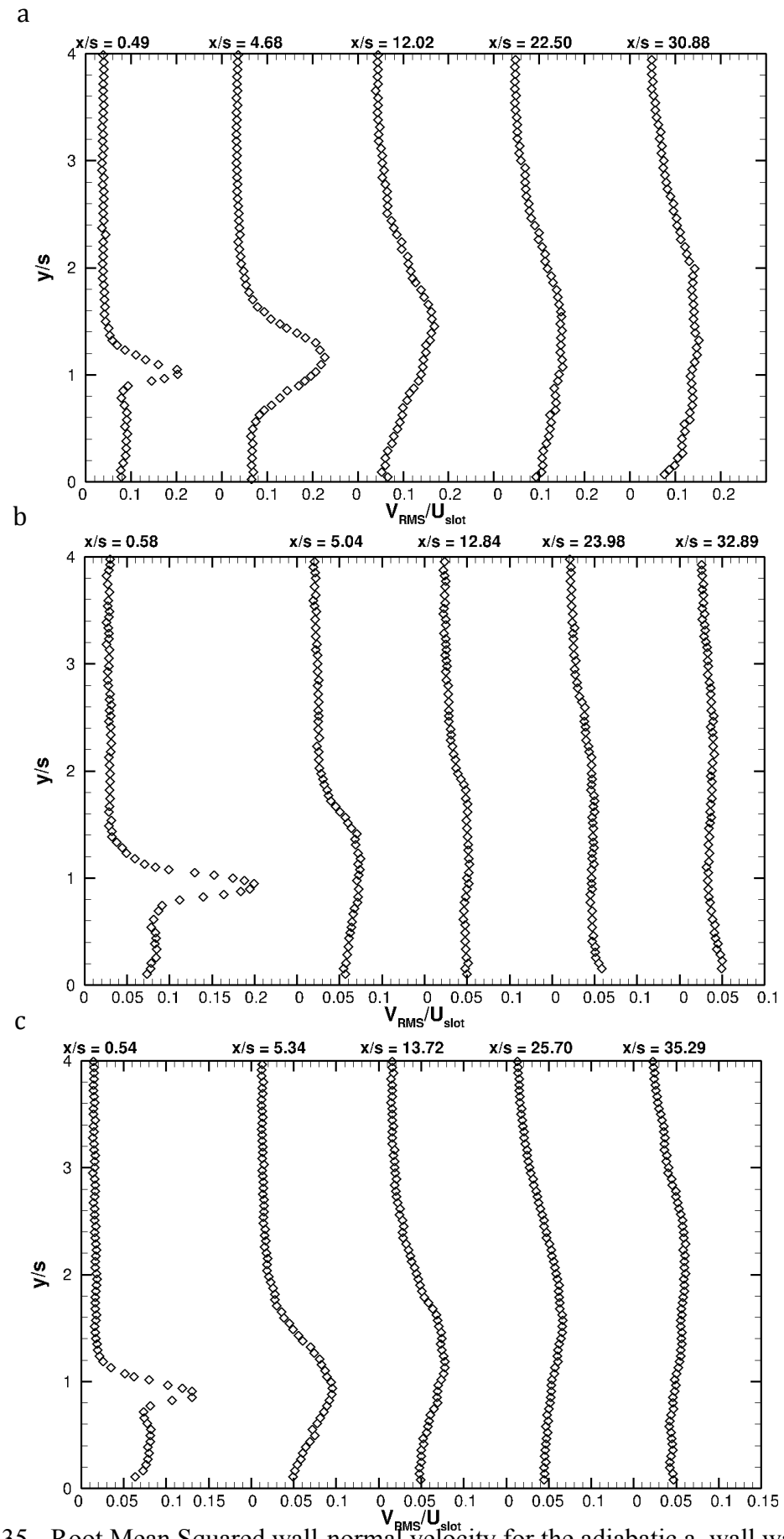

Figure 35 - Root Mean Squared wall-normal velocity for the adiabatic a. wall wake, b. minimum shear, c. wall jet cases.

captures the turbulent eddies of this scale. As a quick note, the most energetic eddies are larger than the integral turbulent length scale, by some factor. For isotropic turbulence (a good representation of grid turbulence), this factor is on the order of 5 [90]. Fortunately the turbulent kinetic energy is contained primarily in the boundary layer and shear layer, meaning that the turbulence in the mainstream is of secondary importance. The peak dissipation scales are dramatically smaller, on the order of $1/25^{th}$ of the characteristic turbulent scales, meaning that these structures, associated with turbulent kinetic energy dissipation, are not adequately resolved by the current PIV measurements [90].

The RMS of streamwise velocity has at least two different peaks, one near the wall and one associated with the turbulent mixing layer. As the flow moves downstream, the peak RMS in the mixing layer decreases through turbulent diffusion. Eventually the turbulence in the mixing layer interacts with boundary layer turbulence in some complicated way. The wall-normal component of RMS velocity shows less of a trace near the wall but remains large in the mixing layer. From turbulent data for boundary layers, the turbulent RMS peak of the wall-normal component is much smaller than the streamwise component (on the order of 3 times smaller from the turbulent validation studies in §2). Next consider the RMS components of velocity downstream of the first measurement station. The RMS peaks are largest in the wall wake and wall jet case. This fact is somewhat obscured by the normalizing slot velocity. However considering the wall-wake velocity has a normalizing velocity, U_{slot}, that is about one-half the normalizing velocities of the wall jet and minimum shear, it can be shown that the wall wake and wall jet have fluctuating velocities of approximately the same intensity. An alternate normalization would be to use the convective velocity, which is defined as the

average of the coolant and mainstream velocities. This scaling was not chosen since it is a derived measurement. Keeping in mind that the wall wake and wall jet have convective velocities smaller than the minimum shear, it becomes easier to see that the relative turbulence of the wall wake and wall jet is stronger than that of the minimum shear. Another trend that can be discerned from the turbulent velocity data is the upper extent of the mixing layer, which once again confirms that the wall jet spreads the furthest from the wall. Another interesting phenomenon that should be noted is the double-peak in the mixing layer of the streamwise RMS velocity, which is only seen in the minimum shear data near the inlet. Most likely this fact is because the turbulence associated with shear is relatively weak, meaning the RMS peaks from the upstream boundary layers are still evident. For example in Gharib and Williams's study [91] on free shear layers, this double peak indicates the shear layer has not fully developed into turbulence, where one peak will occur in the mixing layer. Notice also that downstream the turbulent profiles are all relatively flat outside of the near-wall region, similar to boundary layers, where the modeling of turbulent flows becomes simpler.

The kinetic energy of the turbulence has already been discussed and quantified. However a discussion of how exactly these turbulent fields affect the mean-field, fluid mixing is now necessary. This analysis is most easily accomplished by reviewing the simplified form of the Reynolds Averaged incompressible boundary layer equation for the streamwise velocity shown in Equation 107. While this equation does not exactly hold for the current case, as the density changes, the form is similar to the full Navier-Stokes and sheds light on the kinematic mixing mechanisms in this flow. As can be seen from Equation 107, the Reynolds Averaged boundary layer equation contains only one

fluctuating term in the form of a turbulent flux, called the Reynolds stress. The dominant Reynolds stress is the wall-normal derivative of the streamwise, wall-normal velocity fluctuations, which is responsible for mixing, or enhanced diffusion of the mean velocity field. In fact, in the eddy-diffusion hypothesis, the correlation of the wall-normal and streamwise components of fluctuating velocity are related to an eddy viscosity multiplied by the velocity gradient, thus further emphasizing that this "stress" acts to mix and diffuse the flow, like the shear stress tensor.

$$\rho\left[\frac{\partial \overline{u}}{\partial t}+\overline{u}\frac{\partial \overline{u}}{\partial x}+\overline{v}\frac{\partial \overline{u}}{\partial u}\right]=-\frac{\partial \overline{P}}{\partial x}+\frac{\partial \overline{\tau}_{xy}}{\partial y}-\frac{\partial}{\partial y}\left(\rho\left\langle u'v'\right\rangle\right) \qquad \text{Eqn. (107)}$$

Next consider the equations for the mean kinetic energy and the turbulent kinetic energy in Equations 108 and 109 [92]. The mean kinetic energy, KE, and turbulent kinetic energy equations have several terms in them (most of which are analogous to each other); the left hand side are the typical advection terms. The first three terms on the right hand side are transport terms in the presence of inhomogeneties. The last terms in each equations are viscous and eddy dissipation terms. Most importantly, the second to last term on the right hand side of each equation involves the Reynolds Stress multiplied by the mean velocity gradient. Notice that in the mean kinetic energy equation this term is a positive value on the right hand side meaning it is a loss of mean kinetic energy, since the velocity gradient and the Reynolds stress have opposite signs in a mixing layer. The same exact term appears in the turbulent kinetic energy equation, except with the opposite sign. This difference is striking and particularly revealing. The Reynolds stress acts to remove mean kinetic energy in the presence of a velocity gradient; this Reynolds stress term then acts a production term in the turbulent kinetic energy equation. Therefore, the Reynolds stress in the presence of a mean velocity gradient acts to remove kinetic energy from the

mean fields and give that energy to the turbulent motions. Therefore the Reynolds stress is of crucial importance to turbulence generation and turbulent mixing.

$$\frac{\partial(KE)}{\partial t}+\overline{u}_i\frac{\partial(KE)}{\partial x_i}=\frac{\partial}{\partial x_j}\left\{\frac{-1}{\rho}\left\langle P\overline{u}_i\right\rangle\delta_{ij}-\frac{1}{2}\left\langle u'_i u'_j\right\rangle\overline{u}_i+2\nu\left\langle S_{ij}\overline{u}_i\right\rangle\right\}+\left\langle u'_i u'_j\right\rangle\frac{\partial(\overline{u}_i)}{\partial x_j}-2\nu\left\langle S_{ij}S_{ij}\right\rangle \quad \text{Eqn. (108)}$$

$$\frac{\partial(tke)}{\partial t}+\overline{u}_i\frac{\partial(tke)}{\partial x_i}=\frac{\partial}{\partial x_j}\left\{\frac{-1}{\rho}\left\langle p'u'_i\right\rangle\delta_{ij}-\frac{1}{2}\left\langle u'_k u'_k u'_j\right\rangle+\nu\frac{\partial(tke)}{\partial x_j}\right\}-\left\langle u'_i u'_j\right\rangle\frac{\partial(\overline{u}_i)}{\partial x_j}-\nu\left\langle\frac{\partial(u'_i)}{\partial x_j}\frac{\partial(u'_i)}{\partial x_j}\right\rangle \quad \text{Eqn. (109)}$$

The Reynolds stress, more specifically the streamwise, wall-normal Reynolds stress, has been identified as the mechanism of both generating turbulence but also mixing the mean momentum. Through use of the Reynolds Analogy, the mechanisms of fluid mixing and thermal mixing occur through the same fluid processes, e.g., momentum is mixed through turbulent shear structures, which is also responsible for thermal mixing. Therefore capturing this Reynolds stress provides a great deal of information and insight into the turbulent mixing of film cooling flows.

The streamwise, wall-normal Reynolds stress is shown for the wall wake, minimum shear and wall jet cases in Figure 36. Notice that the relative magnitudes of the Reynolds stress are largest for the wall jet and wall wake case, emphasizing that the mixing layer instability, or Kelvin-Helmholtz instability, is a result of the shear between the two streams. Unlike the RMS velocities that are positive by definition, the Reynolds stresses carry sign information that reflect the nature of the turbulent structures. As will be shown shortly, a negative Reynolds cross stress corresponds to turbulent mixing layer structures that are clockwise in the orientations shown earlier. These turbulent structures correspond to a wall wake case. The converse is also true; positive Reynolds cross stress in a mixing layer mean that counter-clockwise turbulent shear structures are dominant, which occurs in the wall jet scenario. The fact that the minimum shear has regions where

the Reynolds cross stress is both positive and negative further indicates that neither turbulent mixing layer eddy orientation dominates. Near the wall, boundary layer flows have a negative Reynolds cross stress, meaning that with the positive velocity gradient existing here, turbulence is generated near the wall and is then convected away from the wall.

Figure 37 shows a hodograph plane of the fluctuating velocity vector. There are four quadrants, referring to different combinations of positive and negative streamwise and wall-normal velocity fluctuations. Consider first quadrant 1 of the hodograph plane, where both the streamwise and wall-normal components of fluctuating velocity are positive. When the streamwise component is drawn first and then the wall-normal component is added to it, a rotation can be assigned; in this case the rotation is counter-clockwise, as occurs in the wall jet. Consider quadrant 3, where both components of velocity are negative. Once again drawing the streamwise component and then adding the wall-normal component, the rotational direction is again counter-clockwise. Following the same analysis as previously, it can be seen than quadrant 2 and 4 refer to clockwise roller structures, as exists predominantly for the wall wake case. Therefore the sign of the Reynolds cross stress gives information on the orientation of the turbulent mixing layer structures. Similar analysis and plots can be given for the non-adiabatic cases; however since there are no profound differences in the kinematics of these cases, their plots are given in the Appendix. Also the casing temperatures and the backside wall temperature distribution is also given in the Appendix, for the sake of completeness.

a

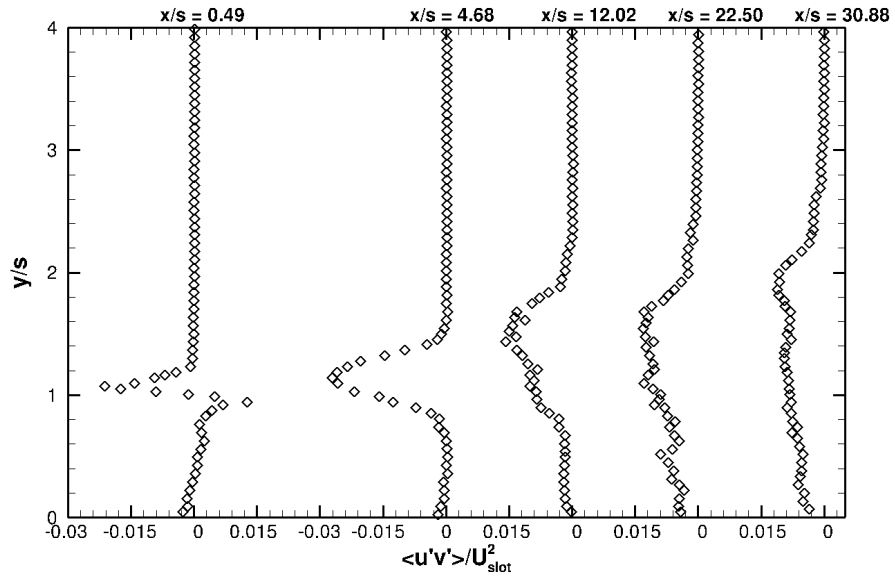

b

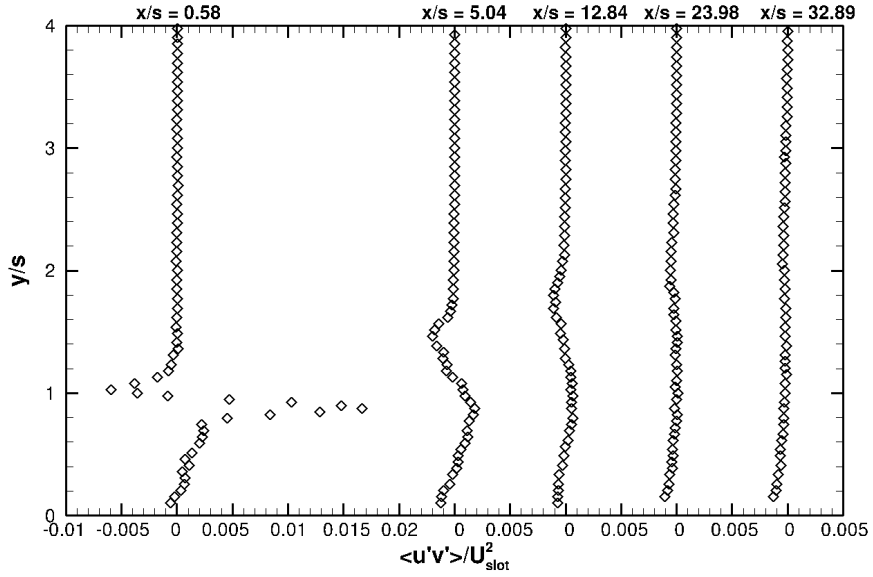

c

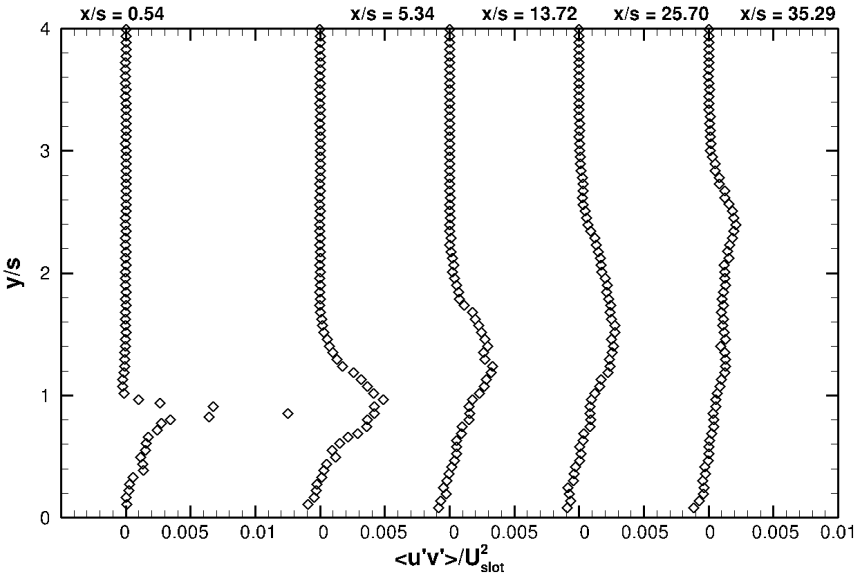

Figure 36 – Reynold's cross stress for the streamwise, wall-normal direction for the adiabatic a. wall wake, b. minimum shear, and c. wall jet cases.

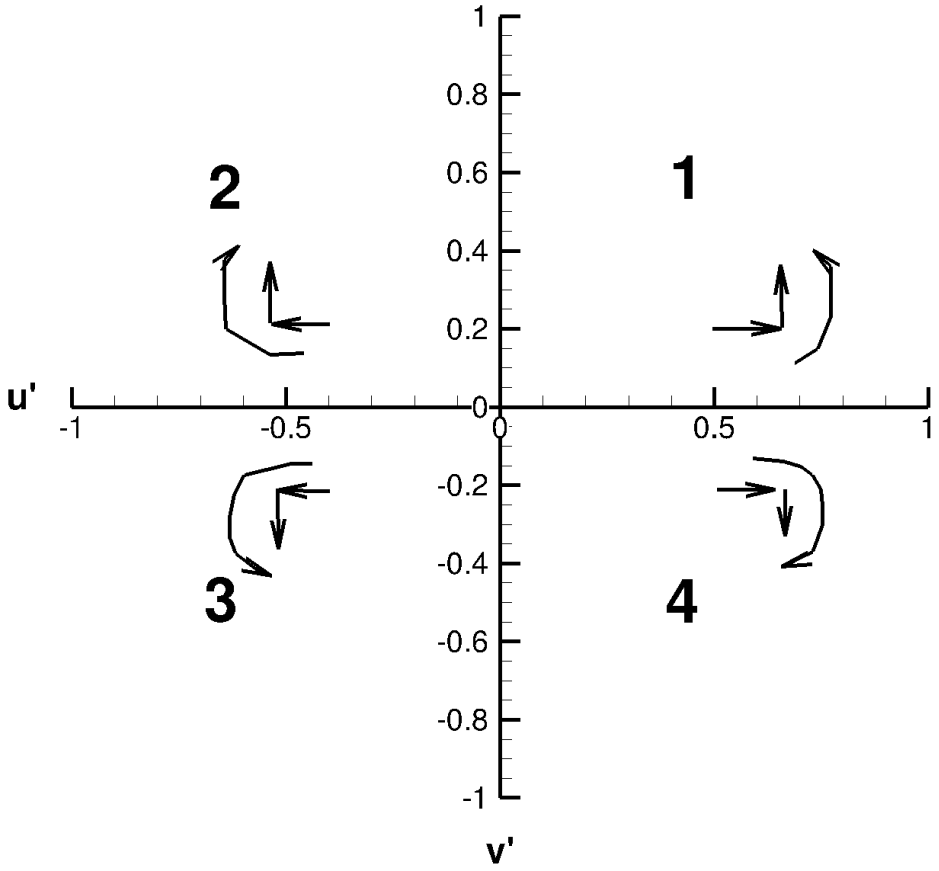

Figure 37 – Schematic of fluctuating hodograph plane.

Chapter 4: Numerical Results

Previously, the adiabatic and non-adiabatic film cooling experiments were described and reviewed. In this chapter, these experiments are simulated using the high-fidelity CFD code, LES BLAC, described in §2.2. First the domain and grid will be described, along with a discussion of the boundary conditions. Next the LES results of the adiabatic film cooling simulations will be detailed, followed by a description of the non-adiabatic film cooling simulations.

4.1 Film Cooling Domain, Grid & Boundary Conditions

A schematic of the simulated 3D film cooling domain with boundary conditions is shown in Figure 38. Even though the film cooling geometry has primarily 2D features, the turbulent phenomena are inherently three dimensional and therefore a technique that attempts to resolve these features, e.g. LES of film cooling, also needs to be 3D. Table 8 shows the size of the domain for each case along with pertinent grid spacing information. The streamwise size of the domain varies because each experimental case has slightly different measuring extents and therefore the simulated volume is different. In general,

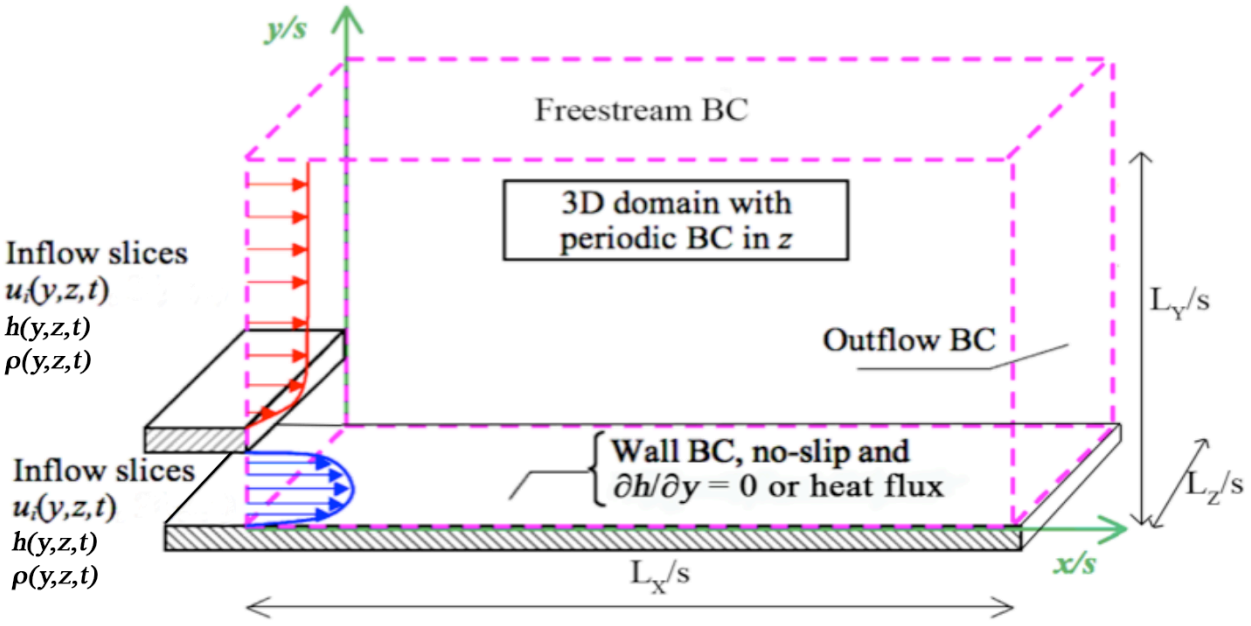

Figure 38 – Schematic of the Film Cooling Domain with boundary conditions shown. Adapted from Cruz [7].

the same streamwise domain size, whereas the non-adiabatic domain extents are exactly the same. The wall-normal length is 10 slot heights, which was found to remove the boundary far enough from the region of interest and prevent boundary perturbations to affect the important flow physics. Similarly the spanwise length has to be several times larger than the largest important flow features, which are on the order of half a slot height. To confirm this, the spanwise length was doubled; increasing the spanwise length had a negligible effect on the solution. In Table 8, the thermal boundary condition for the test plate is either adiabatic (AD) or non-adiabatic (NA). WW, MS and WJ refer to the wall wake, minimum shear and wall jet cases, respectively.

Table 8 – List of the CFD domain and grid information for all the cases.

Case	Thermal BC	L_X/s	L_Y/s	L_Z/s	$\Delta x/s$	$\Delta y_{MIN}/s$	$\Delta y_{MIX}/s$	$\Delta z/s$	Δx^+	Δy^+_{MIN}	Δz^+	N_X	N_Y	N_Z
WW	AD	32	10	π	0.06202	0.00112	0.0418	0.06545	7.8-11.1	0.14-0.2	8.2-11.7	516	144	48
MS	AD	35	10	π	0.06076	0.00112	0.04444	0.06545	8.1-13.0	0.15-0.24	8.8-14.0	576	141	48
WJ	AD	36	10	π	0.0625	0.00112	0.0478	0.06545	8.4-12.8	0.15-0.23	8.8-13.4	576	135	48
WW	NA	49	10	π	0.0638	0.00123	0.04634	0.06545	3.1-5.7	0.06-0.11	3.2-5.9	768	143	48
MS	NA	49	10	π	0.0638	0.00123	0.04524	0.06545	6.2-9.9	0.12-0.19	6.4-10.1	768	144	48
WJ	NA	49	10	π	0.0638	0.00123	0.04872	0.06545	5.2-9.3	0.10-0.18	5.3-9.6	768	135	48

As is shown in Figure 38, the film cooling boundary condition features a time-varying inlet where velocity, enthalpy and density are specified along the inflow plane. The precursor techniques discussed in §2 were used to generate a temporal database of flow slices, which are supplied to the film cooling domain. The test plate features a no-slip, wall boundary condition with a zero wall-normal enthalpy gradient for the adiabatic cases; for the non-adiabatic cases the enthalpy gradient is related to the heat flux. The latter thermal boundary condition will be discussed in more detail later. The upper, cross-stream boundary uses zero wall-normal gradient assumptions mimicking far-field assumptions, commonly used for boundary layers. This type of boundary condition

violates the flow physics near rapid cross-stream variations, which is why this boundary is so far removed from the region of interest. The outflow boundary features use of the traditional convection boundary condition described in §2. The spanwise planes use periodic boundary conditions, which simulates an infinitely long, two-dimensional slot.

For all CFD flows, and LES in particular, the grid spacings must be carefully selected so as to make simulations affordable, while also resolving the important flow length scales. First a generic discussion of grid spacing requirements is performed. A more detailed and thorough study will then follow. In any LES study, some knowledge of the flow is needed prior to CFD grid design. As a rule of thumb, approximately 10 grid points are needed to adequately and accurately resolve a particular length scale. In the mixing layer, turbulent structures are fairly isotropic and scale with the slot height. Therefore streamwise, spanwise and wall-normal spacings should also be relatively uniform with grid spacings less than one-tenth of a slot height. Near the wall the turbulent dynamics are vastly different, requiring a different set of grid criteria there. To simulate turbulent near wall physics, the necessary grid spacings scale with the shear stress at the wall. The streamwise and spanwise grid spacings should be on the order of 50 and 20 wall units (the concept of a wall unit was discussed in §2), respectively [54]. The first wall-normal, grid spacing, meanwhile, should be less than one wall unit [54]. Grid stretching is used in the wall-normal direction to smoothly take the spacings from the near-wall spacing to the mixing layer spacings. Away from the mixing layer, near the upper grid boundary, stretching is also used to reduce the grid requirements in this far-field region.

From Table 8, it can be seen that the streamwise and spanwise spacings, which are both constant, are governed by the mixing layer spacings. Both spacings are less than their required wall spacing and are approximately the same size. The wall-normal spacing, however, is still governed by the fine requirements near the wall; therefore the first grid spacing, Δy_{MIN}, and the mixing layer grid spacing, Δy_{MIX}, are both reported. The wall unit scalings are not known *a priori* and must be verified after a calculation is performed. Minor grid spacing changes are made from case to case in order to better align the grid with boundaries, for example the splitter plate in the near-injection region.

To actually verify that the selected grid spacings from Table 8 are adequate a grid sensitivity analysis is performed. In such an approach, at least three grid densities are selected ranging from coarse to fine. Going from one grid to the next, each direction is consistently varied by some constant factor. The flow results on each grid are then compared. If the results do not change appreciably from one grid density to the next, the solutions are often said to be grid insensitive, or grid independent, depending on the type of simulations being performed. For LES flows that model subgrid-scales, the terminology grid-insensitive is used, as different flow scales are resolved, meaning the results will always change with different grid densities, until DNS resolutions are met. These changes can be relatively minor, however, and therefore results are not sensitive to grid spacings.

Such an analysis was performed for the wall jet case on a shortened domain; the most dynamic and stringent requirements are needed near the injector after all. These grid spacing guidelines were then applied to all other cases to form the grid spacings seen in Table 8. Table 9 shows three sets of grid resolutions for the coarse, medium and fine wall

jet film cooling case. The coarse spacings are approximately 4/3 the medium spacings, while the fine grid is approximately 1.5 times finer than the medium grid. Notice the near-wall spacing stays fixed in order to ensure the wall-normal grid requirement in that region.

Table 9 – List of grid spacings for the CFD grid sensitivity analysis.

Case	$\Delta x/s$	$\Delta y_{MIN}/s$	$\Delta y_{MIX}/s$	$\Delta z/s$
Coarse	0.089	0.0011	0.072	0.098
Medium	0.066	0.0011	0.048	0.065
Fine	0.049	0.0011	0.036	0.049

d fine wall jet film cooling grids. As can be seen, there is a noteable discrepancy between the coarse and medium grids. The medium and fine grids provide essentially the same answer, even though the relative refinement from the medium to the fine is greater than from the coarse to the medium. The effectiveness is the parameter of interest; hence this plot is the most important in determining film cooling grid sensitivity. As a brief aside, the LES simulations of Cruz [7] and Voegele [42] used even coarser grid spacings than the coarse grid.

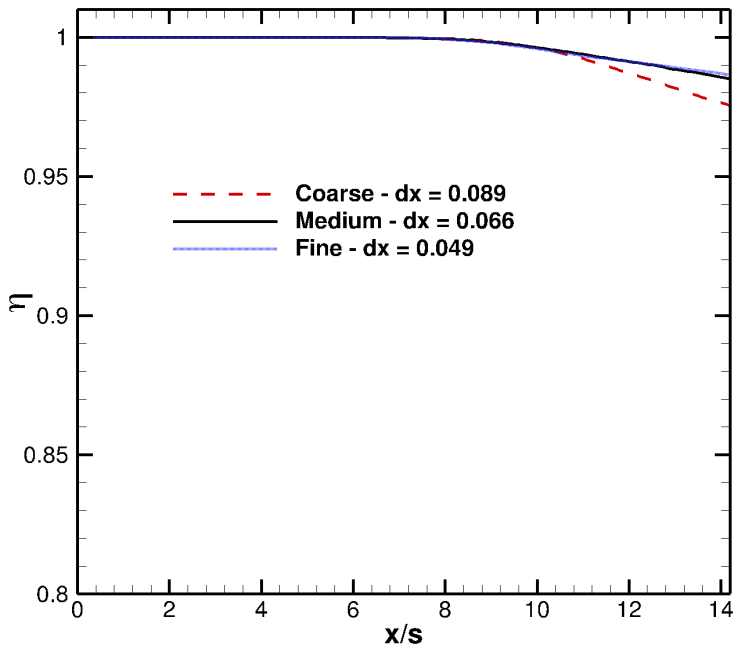

Figure 39 – Effectiveness for the wall jet grid sensitivity study.

Figure 40 and Figure 41 show mean velocity and temperature profiles at different downstream stations in the grid sensitivity study. At these resolutions, very little discernible differences between the cases are noticeable. This trait emphasizes the sensitivity of the wall effectiveness. Together with the effectiveness results, the medium grid is insensitive to grid spacing, meaning that further refinement will not dramatically change the simulated result. Therefore these grid spacings were selected as the basis of the grid design shown in Table 8.

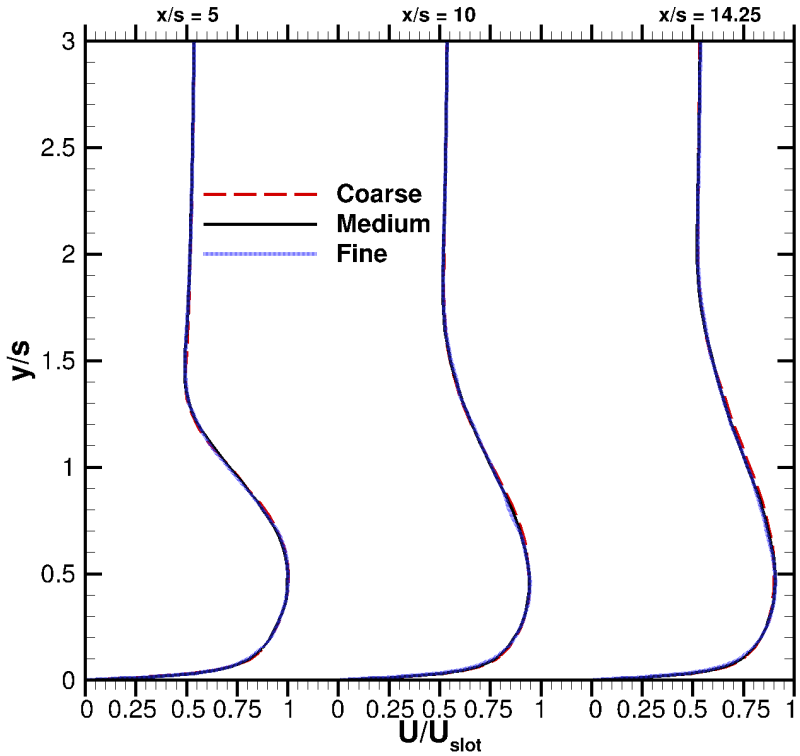

Figure 40 – Velocity profiles for the wall jet grid sensitivity study at different downstream streamwise stations.

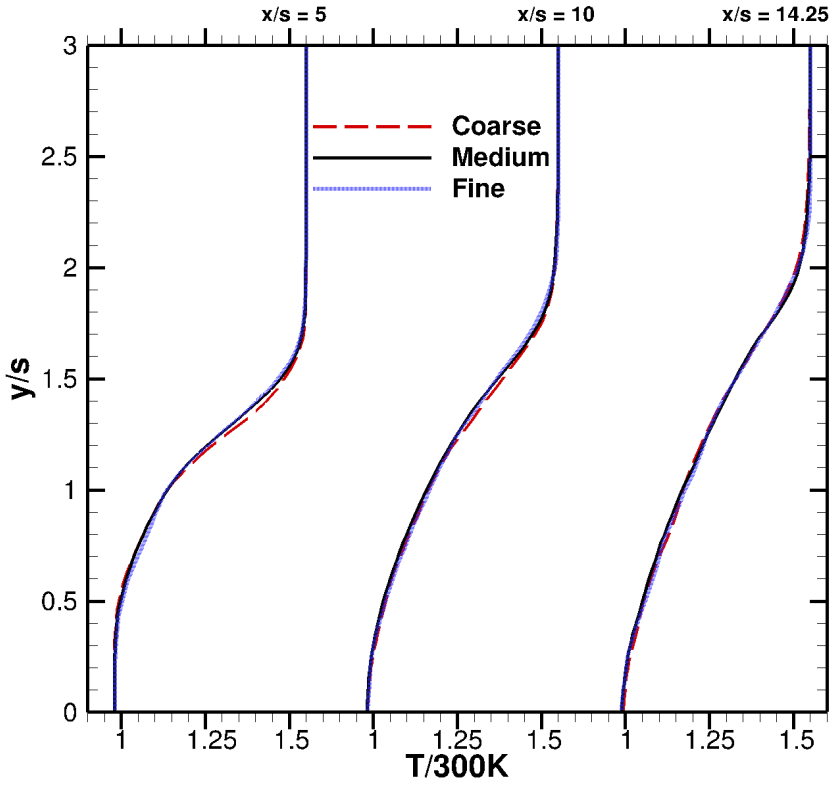

Figure 41 - Temperature profiles for the wall jet grid sensitivity study at different downstream streamwise stations.

4.2 Adiabatic Film Cooling Simulations

In this section, the general features of the adiabatic LES of film cooling will be presented and reviewed. In Figure 42, the adiabatic wall effectiveness for the film cooling experiment, LES simulation and RANS simulations from Voegele [42] are compared for the wall wake, minimum shear and wall jet cases. The LES and RANS simulations use the same precursor inflow techniques and wall boundary conditions, so a more consistent comparison can be made.

In each case, the LES wall effectiveness more accurately predicts the experimental effectiveness, but since LES is generally considered a higher fidelity technique in which more of the flow physics are resolved, this is perhaps not surprising. Of particular note is the near-injector mixing and the length of the potential core. As a reminder, the potential core length is the streamwise location where the mean mixing layer impinges with the wall. This length can be approximated in this scenario by the location where the effectiveness is 0.99. As can be seen, the potential core length is over predicted by both the RANS and LES solutions, with the LES providing a better prediction of this potential core length. To remind the reader, at the end of the potential core, the film begins to rapidly breakdown and the mixing physics near the wall change as is evidenced by the slope change in effectiveness in this region. The far-field decay rate is also of interest. For the wall jet and minimum shear cases, the LES underpredicts the near wall mixing resulting in a higher effectiveness, whereas for the wall wake case the LES overpredicts the film mixing but appears to be following the film decay trends. The maximum effectiveness error for the LES simulations is approximately 4%, 5% and 5% for the wall wake, minimum shear and wall jet cases, respectively.

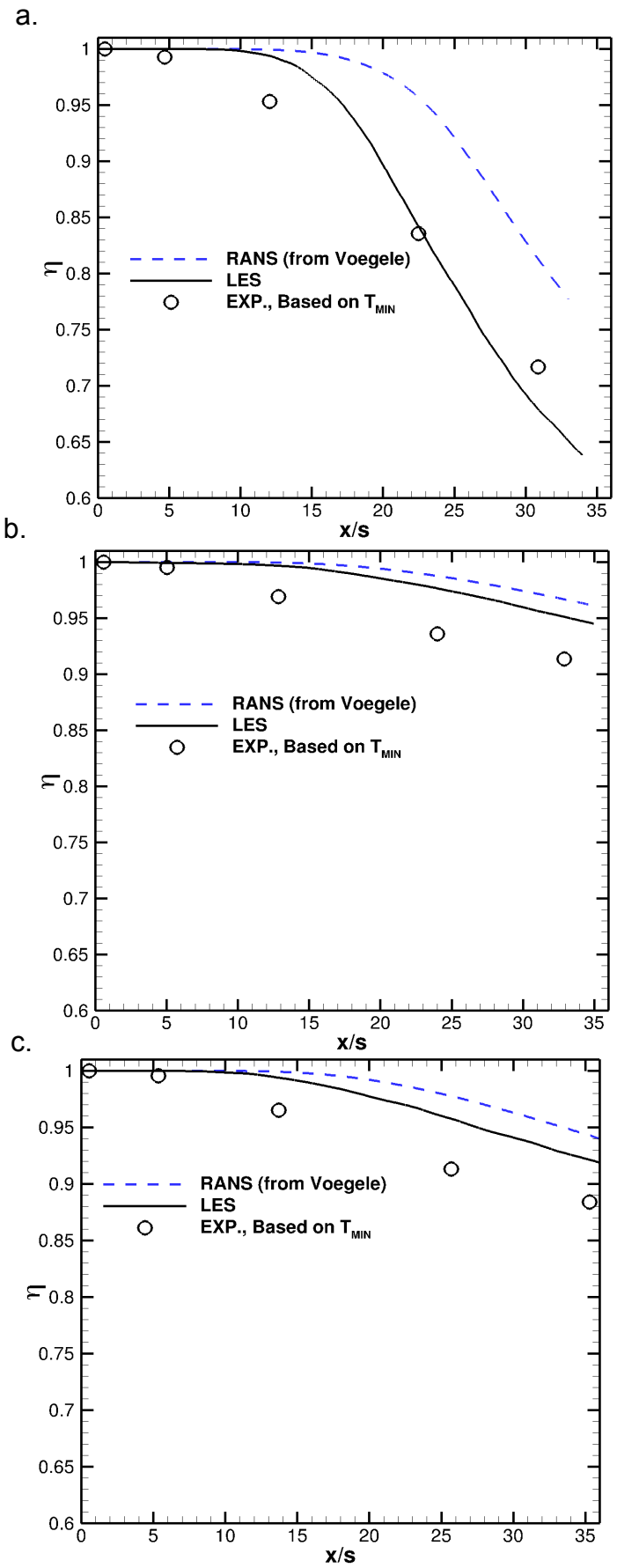

Figure 42 Comparison of the LES, RANS and experimental adiabatic wall effectiveness for the a. wall wake, b. minimum shear and c. wall jet cases. RANS data from Voegele [41].

As a final comparison between the RANS and LES solutions, consider the flow effectiveness profiles for all the adiabatic film cooling cases shown in Figure 43. The inlet temperature for the RANS and LES profiles are slightly different however the effect seems to be minimal on the downstream flow solutions. For example, in each case, the LES solutions better predict the upper extent of the mixing layer than the RANS solutions even though the thermal mixing layer starts off higher in the RANS inlet solution, which is evident from the profiles at the first streamwise station. Overall the LES and RANS thermal profiles are similar, with the LES providing slightly better predictions of the experimental thermal mixing.

The general features of the LES solutions for the wall wake (WW), minimum shear (MS) and wall jet (WJ) adiabatic cases can be ascertained from the mean contours of streamwise velocity and temperature shown in Figure 44 and Figure 45, respectively. The contours for the minimum shear and wall jet cases have been shifted to allow for adequate visualization in the same figure. Kinematically, the mean flow behavior agrees with the qualitative description of the different shear mixing cases provided in §3. For example, the peak wall jet velocity in the coolant continuously decelerates, while the wall jet momentum spreads away from the wall. Conversely the wall wake accelerates, with the momentum spread primarily towards the wall. The temperature contours, meanwhile, show the mean mixing of interest for film cooling designers, namely how hot the wall region is and how mixed the film is. As observed earlier, the wall wake film degrades the fastest, whereas the wall jet and minimum shear have comparable film temperatures. As can be seen from the temperature contours, the wall jet spreads away from the wall the

most, followed by the minimum shear and then the wall wake. Also the minimum shear has the thinnest mixing layer as was found in the experimental flow solutions.

a.

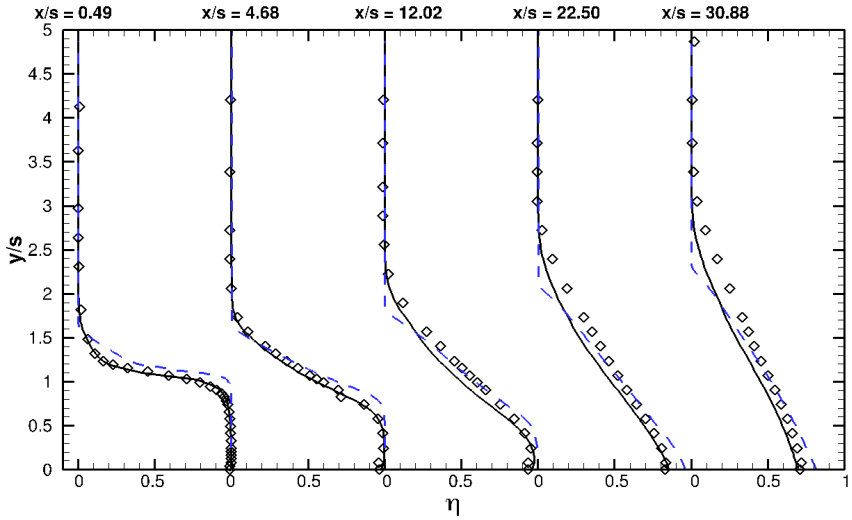

b.

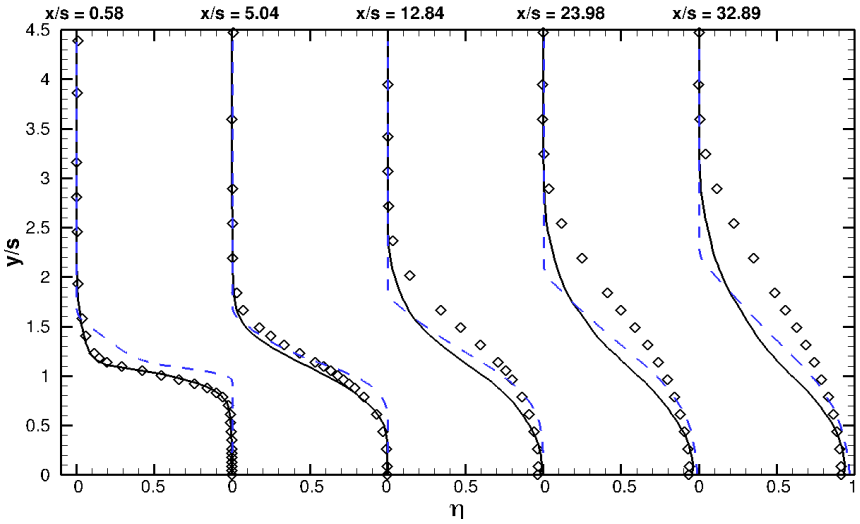

c.

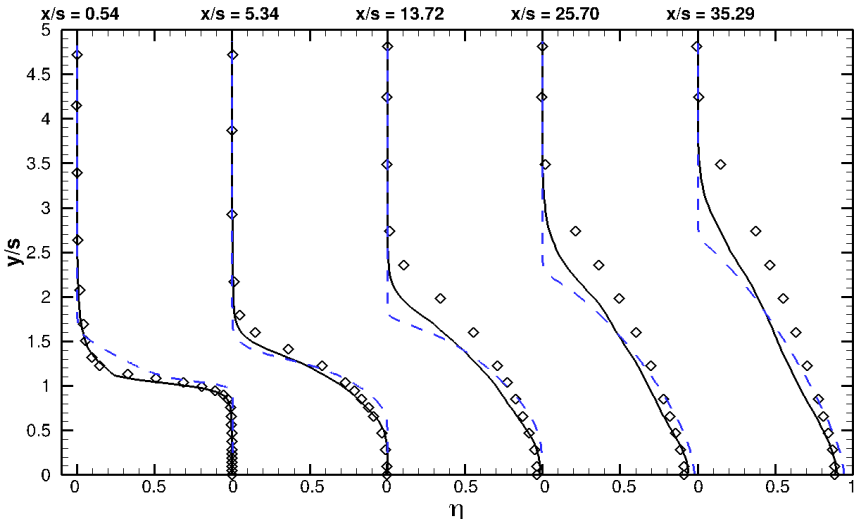

Figure 43 - Comparison of the flow effectiveness contours for the RANS (dashed lines), LES (solid lines) and experimental (symbols) adiabatic a. wall wake, b. minimum shear and c. wall jet film cooling cases.

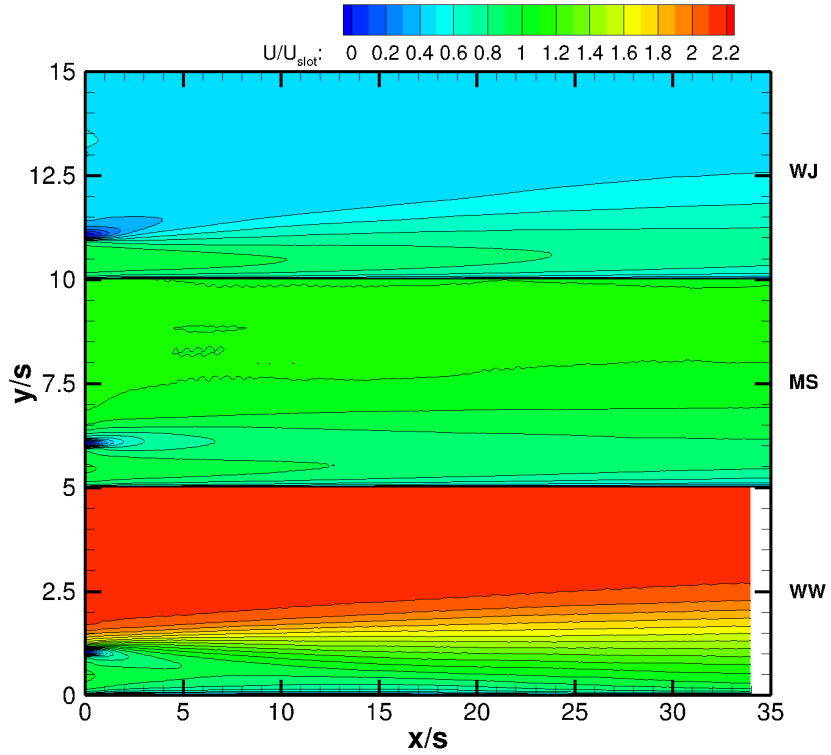

Figure 44 – Mean velocity contours for the adiabatic wall jet (WJ), minimum shear (MS), and wall wake (WW) cases.

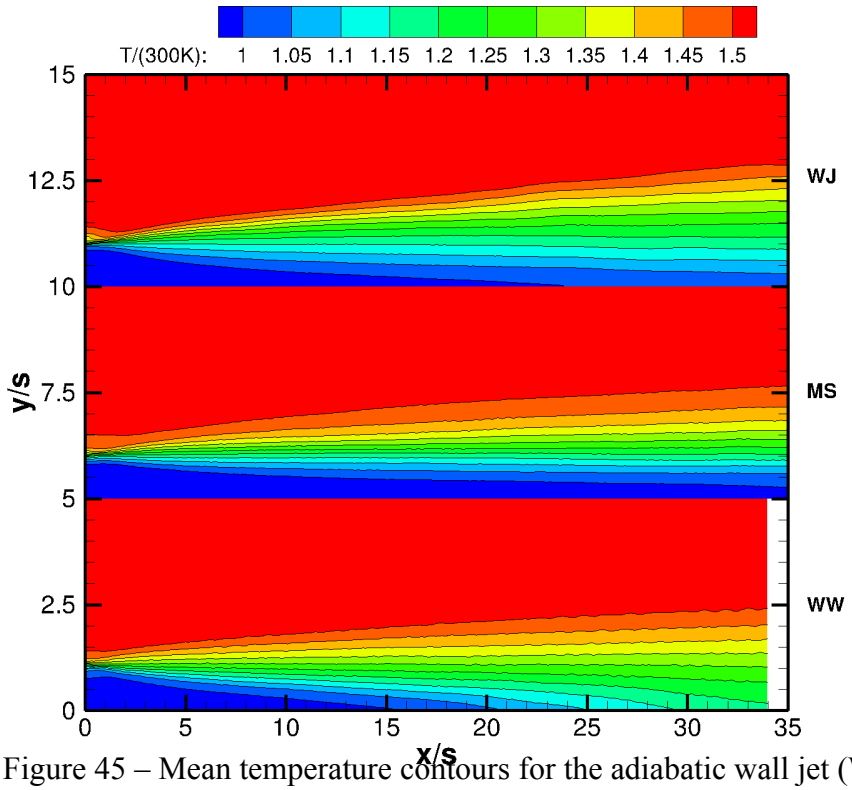

Figure 45 – Mean temperature contours for the adiabatic wall jet (WJ), minimum shear (MS), and wall wake cases (WW).

Figure 46 and Figure 47 show the mean subgrid scale viscosity and thermal diffusivity, respectively, for each adiabatic case. The subgrid-scale viscosity and thermal diffusivity plays a role similar to the turbulent eddy viscosity and diffusivity in RANS calculations. However they represent the effect of the unresolved motions (or motions smaller than the grid scale) on the mean solution rather than the effect of all turbulent motions on the mean field. Therefore the magnitude of the subgrid-scale viscosity gives a measure of how much of the flow field is resolved. The maximum subgrid-scale viscosity always occurs very near the splitter plate, indicating that the resolution is coarsest here relative to the flow structures. This finding is not surprising because the mixing layer turbulent shear structures can be on the order of the thin splitter plate in this region before rapidly growing in size downstream. Considering that in general the turbulent viscosity is much higher than the laminar viscosity (by at least an order of magnitude), each simulation is very well resolved, since the subgrid-scale viscosity is on the same order as the laminar viscosity at 300K. The subgrid-scale diffusivity is three times higher than the laminar diffusivity at 300K, indicating that the thermal structures contain features that are finer than the kinematic features and therefore more of the thermal flow field must be modeled through the subgrid-scale diffusivity. In all the LES simulations, the laminar viscosity and diffusivities vary according to Sutherland's law, the exact form of which is given in Nicoud [88]. Hence, the maximum magnitude of these ratios in Figure 46 and Figure 47 are actually smaller when compared to the laminar viscosity in that same location; this is due to the fact that the subgrid-scale viscosity and diffusivity maximums are located in regions where the temperature is greater than 300K and the laminar diffusivities increase with increasing temperature. Nevertheless, Figure 46 and Figure 47

show that a large amount of the flow-field is resolved but the simulation is too coarse to constitute a DNS calculation, which would occur if the ratio of these viscosities was very small.

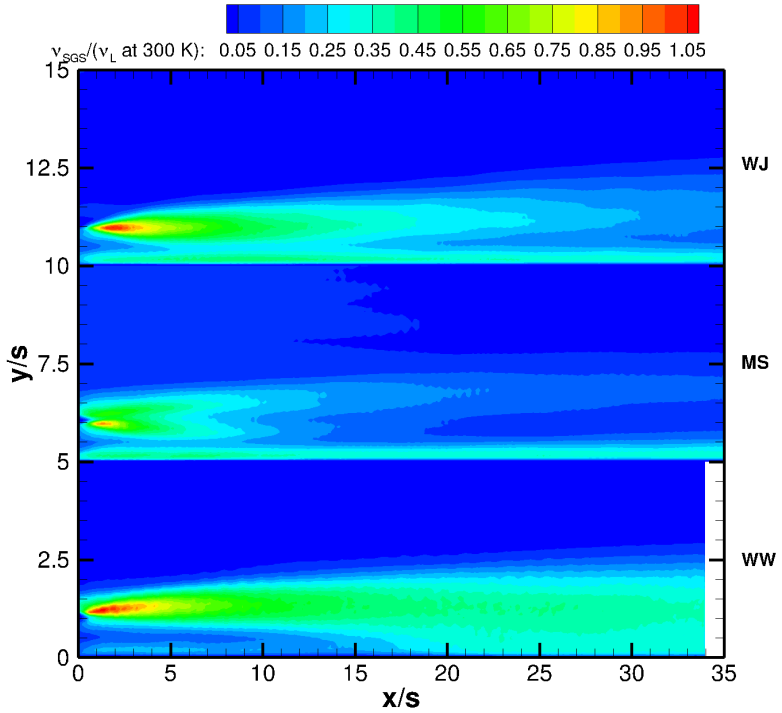

Figure 46 – Mean contours of the subgrid-scale viscosity for the adiabatic wall jet (WJ), minimum shear (MS) and wall wake (WW) cases.

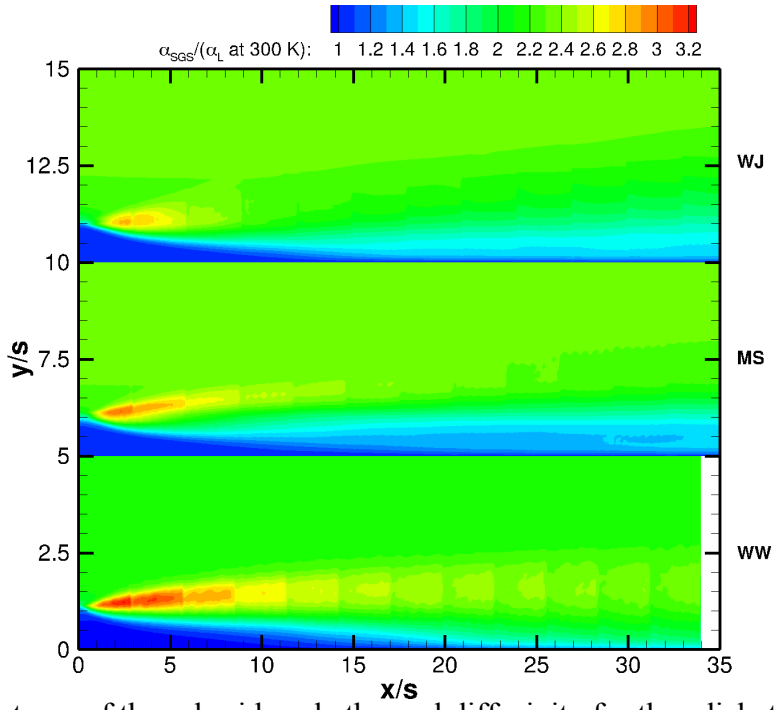

Figure 47 Mean contours of the subgrid-scale thermal diffusivity for the adiabatic wall jet (WJ), minimum shear (MS) and wall wake (WW) cases.

4.3 Adiabatic Film Cooling Simulations – Inlet Study & Convection Scheme

Now that the qualitative features of the LES film cooling solutions have been demonstrated, a more thorough look into the film cooling features compared to the experiment is needed; this more comprehensive analysis will occur while also performing different LES film cooling parametric studies. In this section, the effect of inlet specification, crucial for LES flows, is explored.

Figure 48 compares the experimental and LES adiabatic wall effectiveness for each of the shear cases with three different inflow techniques; the three inlet treatments are the FDTC, FPS (described in §2) and an inflow technique with no fluctuating information provided at the inlet, referred to from here on out as the Mean Only treatment. The most striking feature of these plots is the poor performance by the Mean Only cases. In each shear scenario, the film decay rate is grossly underpredicted. The Mean Only cases were run not in the expectation of an accurate answer, but rather to highlight the importance of providing realistic turbulent information at the inlet plane. In the wall wake case, the FPS simulation performs the best in terms of the far-field decay, even though it still overpredicts the mixing; the FDTC approach simulates the near-injector mixing and subsequent film breakdown best. For the other two cases the FDTC simulation provides an improvement relative to the FPS adiabatic simulations both in terms of near and far-field adiabatic effectiveness decay. The maximum effectiveness error for the FDTC is less than 8%, 2% and 3%, for the wall wake, minimum shear and

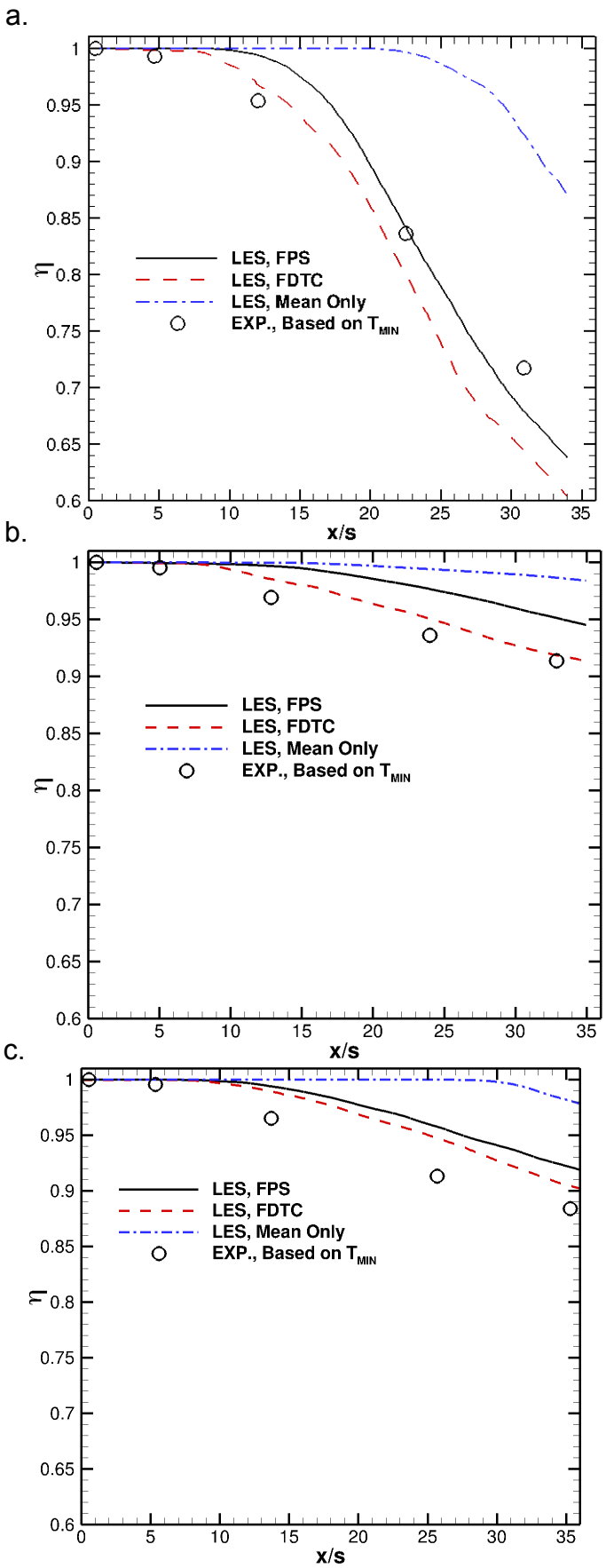

Figure 48 – Comparison of the experimental adiabatic film cooling effectiveness with LES film cooling simulations with different inlet treatments.

wall jet cases. The FPS's effectivenesses have maximum errors less than 4%, 4%, and 5% for the wall wake, minimum shear and wall jet cases, respectively.

To better understand the LES mixing trends, especially those of the Mean Only cases, consider instantaneous temperature contours for the wall jet case shown in Figure 49. In general, the mean mixing trends will not be discussed as the simulations and experiments generally capture the same physics. The exception is when explaining differences between the experiments and simulations or to aid understanding of the simulation trends. In the temperature contours, the FDTC and FPS techniques provide qualitatively similar features, namely a seemingly "noisy" mixing process with a variety of different "random" length scales. The fields are not actually noisy or random in a mathematical sense but have a variety of time and length scales in the turbulent regions, which is true of turbulent flows. These two contours are in sharp contrast to the Mean Only temperature contour, where the flow structures do not even form until 5 slot heights downstream. For this case, the delay could be affected by inadequate grid spacing, since the size of the structure in the near-injector region is almost entirely controlled by the splitter plate thickness which is not properly resolved. After five slot heights, the classical, laminar vortex shedding problem in a wake flow is observed, in which a pair of counter rotating vortices are shed. These vortices grow as they convect downstream. However notice the fine delineation between cold regions and warm regions in these vortices. Also take note that at each downstream location only one structure is observed, not a cascade of structures ranging from large to small. Since turbulent mixing has not onset for this case, the film decay occurs very slowly, which is unsurprising. According to turbulent stability theory, with these Reynolds numbers, the different shear cases

should eventually trip to turbulence; unfortunately, this theory does not prescribe when, only that it will occur.

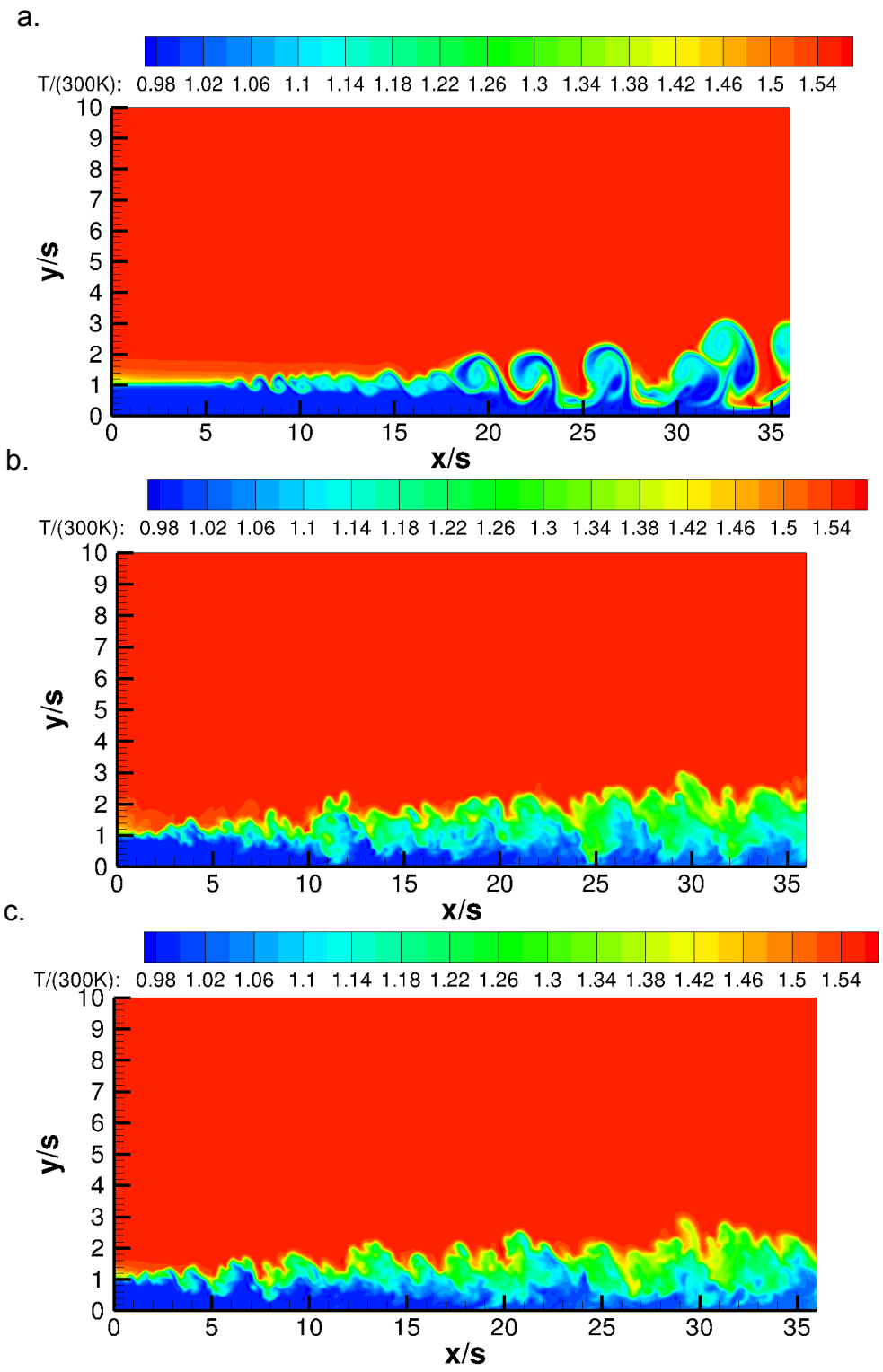

Figure 49 – Instantaneous temperature contours for the LES of adiabatic wall jet case using a. Mean only, b. FPS, and c. FDTC as the inlet treatment.

The mean flow effectiveness profiles are provided in Figure 50. It should be noted that the Mean Only case was dropped from these plots as they provided unrealistic predictions of the turbulent mixing trends. Generally speaking, both the FDTC and FPS provide good agreement with experimental mixing. However far-field injector mixing away from the wall is underpredicted by both LES techniques, especially in the minimum shear and wall jet cases. The exact cause of this inaccuracy is not known except that the experiment seemingly has an enhanced transport away from the wall. As will be shown, this could be in part due to increased mean velocity in the cross-stream direction for the experiments relative to the LES data. The FDTC performs nominally better in that it mirrors the wall effectiveness trends. In fact, the near wall mixing seems to be accurately captured by the different LES techniques, which should be the most difficult region to predict due to the presence of the mixing layer and the wall. For the FPS technique, the maximum near wall effectiveness error ($y/s < 0.7$) is 5%, 5% and 5% for the wall wake, minimum shear and wall jet cases. Farther from the wall, the maximum effectiveness errors of the FPS are 12%, 25% and 24% for the wall wake, minimum shear and wall jet cases. The near wall error for the FDTC are 8%, 11% and 4%, while the far-field errors are 7%, 25% and 24% for the wall wake, minimum shear and wall jet cases, respectively. These larger errors primarily arise due to the thermal mixing layers spreading faster experimentally than they do numerically. In the experiment, a point may still be in the mixing layer while in the simulation it is not, leading to a large discrepancy. These discrepancies are largest for the minimum shear and wall jet cases.

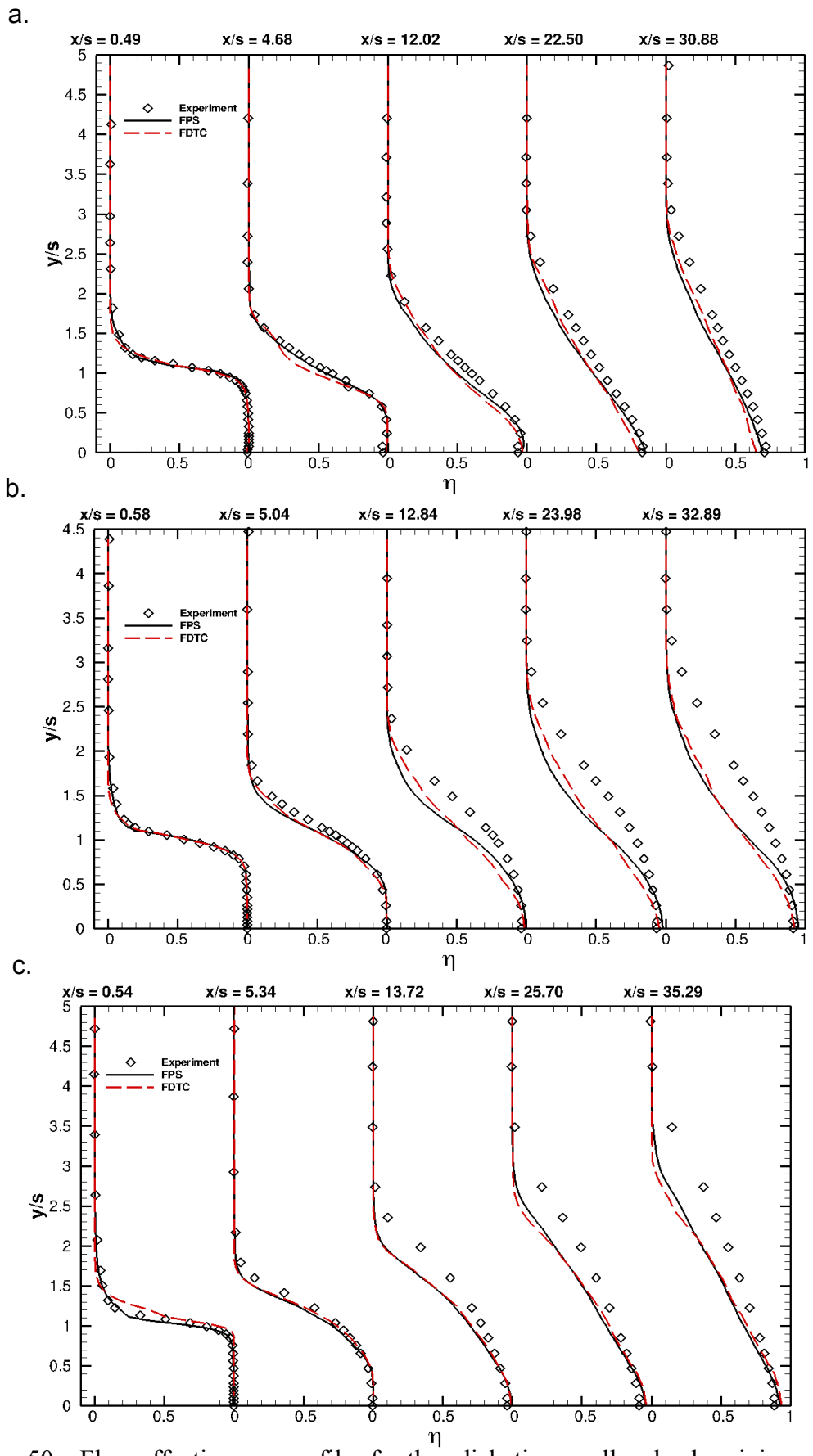

Figure 50 – Flow effectiveness profiles for the adiabatic a. wall wake, b. minimum shear, c. wall jet cases, comparing the experimental data with the LES simulations using the FPS or FDTC inlet treatment.

The mean streamwise velocity profiles, meanwhile, are shown in Figure 51 for the LES inlet parametric simulations and the experimental data. Here the numerical solutions match the experiments very well. The peak experimental velocity in the near wall region is always slightly underpredicted in the far-field. However the mixing layer spread is in general matched very well. In fact the maximum velocity errors for the FPS are 16%, 8% and 11% for the wall wake, minimum shear and wall jet cases. The FDTC has errors of 22%, 5% and 9% for these same cases. A brief note is needed on the inlet discrepancy in the mean velocity profiles for the wall wake FDTC and FPS simulations. The kinematic boundary layer thickness was specified as being slightly too large, with a slight error in the mean velocity in the wall wake mainstream for the FDTC simulation. Their effects are relatively minor, however, and in the interest of time were not updated, as the effectiveness results would not change significantly. The large velocity error, in fact, is due to this discrepancy.

The wall-normal velocity profiles for the LES inlet simulations and the experiments are shown in Figure 52. Near the inlet, at the first streamwise station, the wall-normal component of velocity have similar trends in the mixing layer; namely the coolant velocity takes positive values, while the mainstream takes negative values, showing the mean spread of these two fields very near the inlet. This spreading occurs due to the low pressure region existing behind the louver splitter plate. The LES simulations underpredict the peaks of this mean spreading in the near-injector regions. Experimentally the wall wake and minimum shear have relatively significant positive wall-normal velocities away from the wall, while the wall jet has initially negative wall-

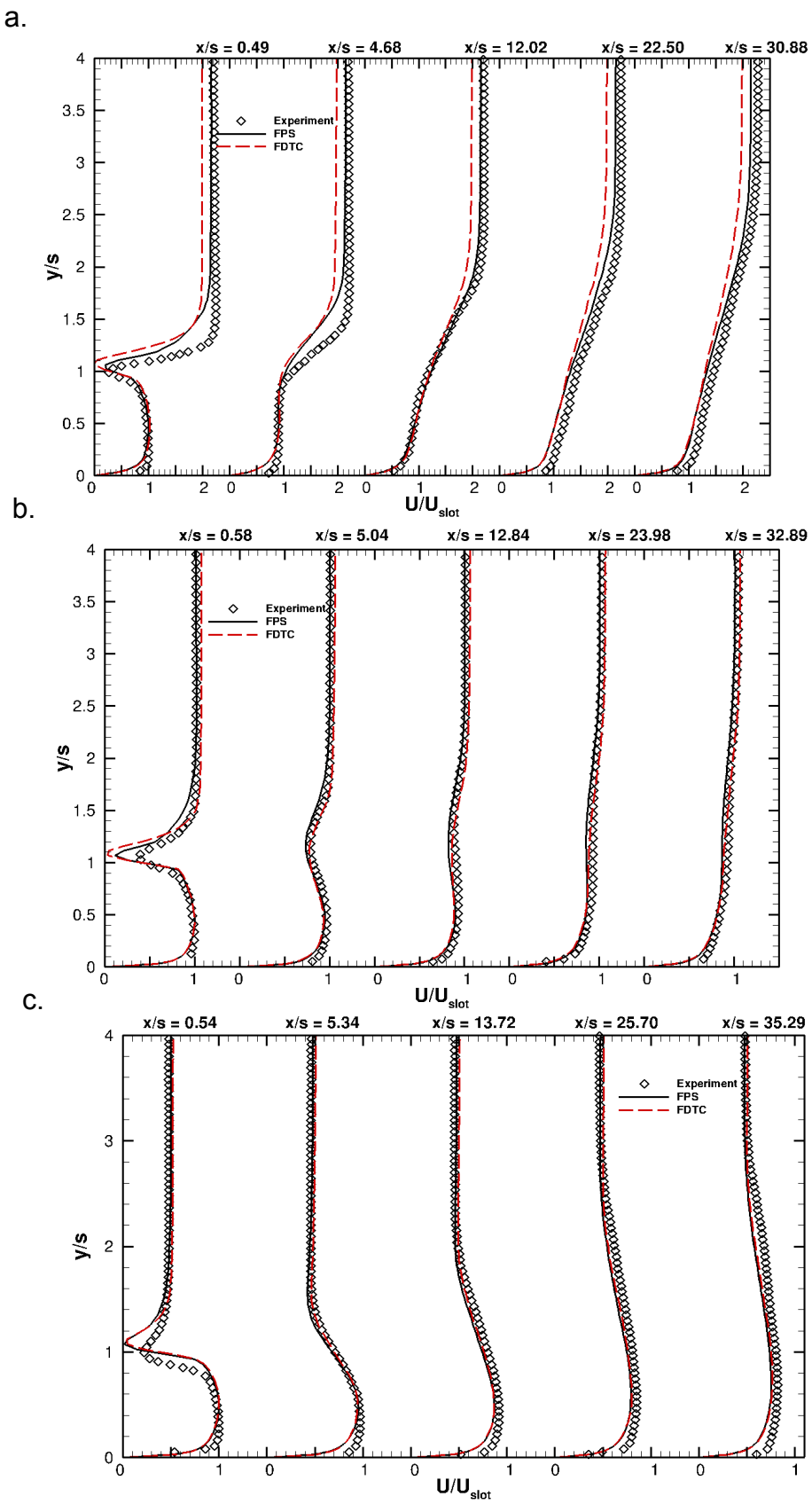

Figure 51 – Mean streamwise velocity profiles for the adiabatic a. wall wake, b. minimum shear, c. wall jet cases, comparing the experimental data with the LES simulations using the FPS or FDTC inlet treatment.

normal velocities that switch to being positive far from injection. Away from the wall, the wall jet should initially have a negative velocity since there is strong fluid entrainment from the mixing layer; the mainstream fluid is accelerated meaning fluid must be entrained to conserve mass. If the mainstream fluid is not being accelerated, the wall-normal velocity profile from a boundary layer developing over a flat-plate will cause a small, positive, vertical velocity for flows that have a zero-mean pressure gradient. Therefore, far from injection, even the wall jet will have positive, vertical velocity, both experimentally and numerically. Unfortunately the magnitude of the vertical-velocity is significantly underpredicted by the numerical simulations. Whether this occurs due to upper wall effects or other uncontrolled wind tunnel variations is unclear. However, it is clear that the experiment in general has a larger positive vertical velocity across all the cases than the simulations, which results in enhanced spreading of the thermal field, especially outside of the mixing layer. In fact, the case for which the simulation predicts the vertical velocity best, the wall wake case, the LES also best predicts the thermal mixing layer away from the wall. One numerical technique that attempts to compensate for such effects would be to impose the experimental vertical wall-normal velocity as a boundary condition; however this technique was beyond the scope of the current work as the near-wall region is the primary region of interest. The near-injector regions being considered in this study are relatively unaffected by vertical spreading far from the wall. As a matter of note, very little differences exist between the two inlet techniques with respect to wall-normal velocity, at least on the scale of the numerical variations with experiments. Additionally RANS simulations of these same experimental flows

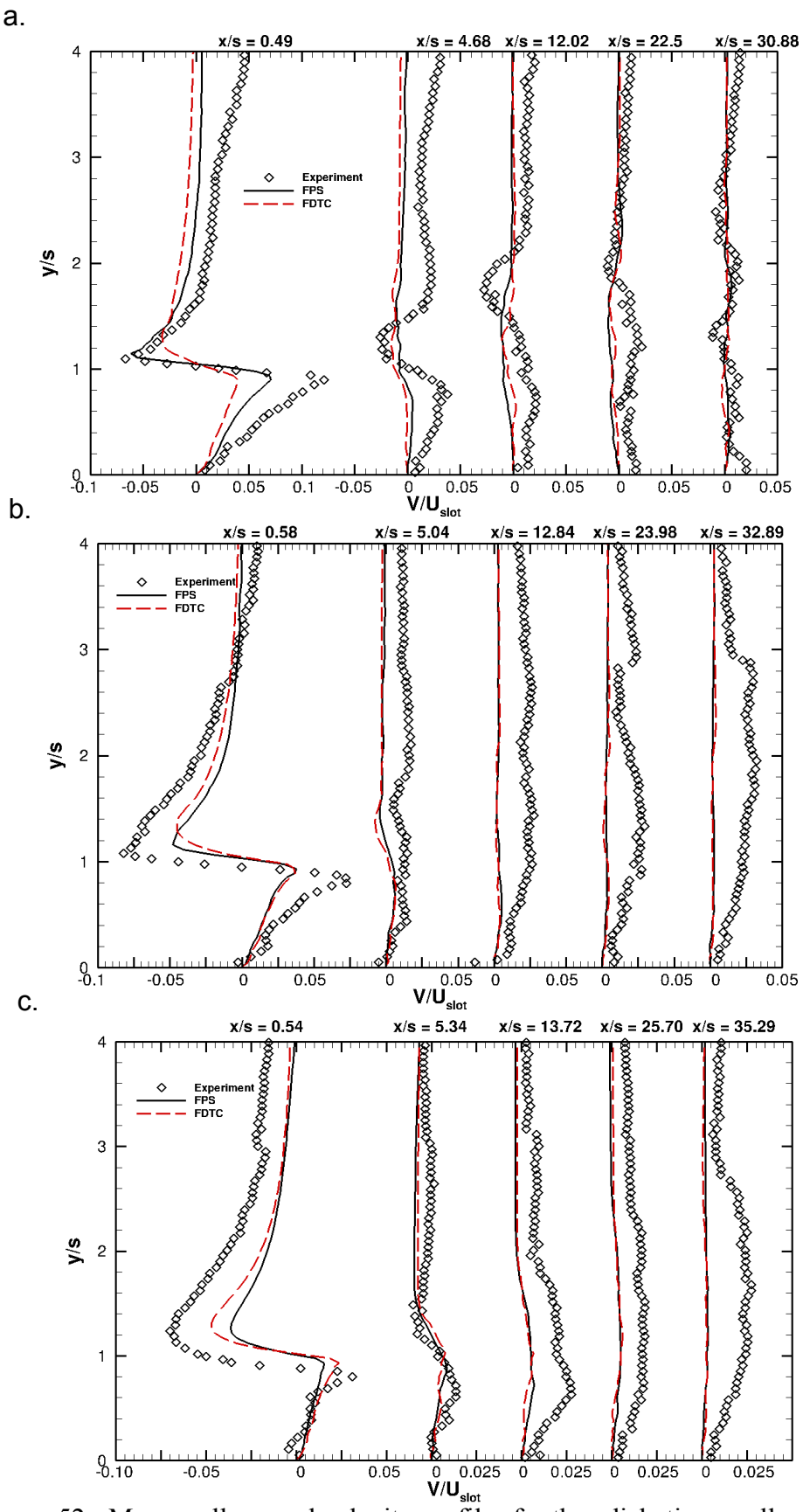

Figure 52 - Mean wall-normal velocity profiles for the adiabatic a. wall wake, b. minimum shear, c. wall jet cases, comparing the experimental data with the LES simulations using the FPS or FDTC inlet treatment.

performed using a different flow solver (i.e, the study of Voegele [41]) also predict similar wall-normal velocities.

Now that the mean experimental and numerical solutions have been compared, the fluctuating turbulent fields will be examined to evaluate the LES's capability in capturing the turbulent mixing mechanisms. The streamwise and wall-normal RMS velocity profiles are shown for the adiabatic experimental and numerical cases in Figure 53 and Figure 54, respectively. As discussed in §3, the RMS of fluctuating velocity gives an indication of the strength of turbulent motion, while the sum of squares of multiple components give an idea of the energy contained in turbulent motions. Regarding the streamwise RMS velocity profiles, the LES overall does a very good job at predicting the mixing trends, especially after the first experimental streamwise station. The main differences between the FPS and FDTC can be seen from these two figures. Where the FPS always asymptotes to the experimental mainstream turbulence levels away from the splitter plate, the FDTC asymptotes to zero, which is due to the inherent assumption of only resolving the splitter plate boundary layer. In the FDTC approach uniform flow is prescribed away from the boundary layer, whereas experimentally there is turbulence in the mainstream coming from the wall and the turbulent grid upstream. One benefit of the LES technique is that the RMS peaks near the wall can be resolved, where experimentally, laser noise affects the turbulent signal. The peak RMS velocities are resolved very well downstream of the first streamwise station; the spread of RMS velocity in the mixing layer is also well predicted. In the cases of extreme shear mixing (i.e. the wall wake and wall jet cases), the RMS trends have a single mixing layer peak that spreads and reduces in magnitude as the flow progresses downstream. In the

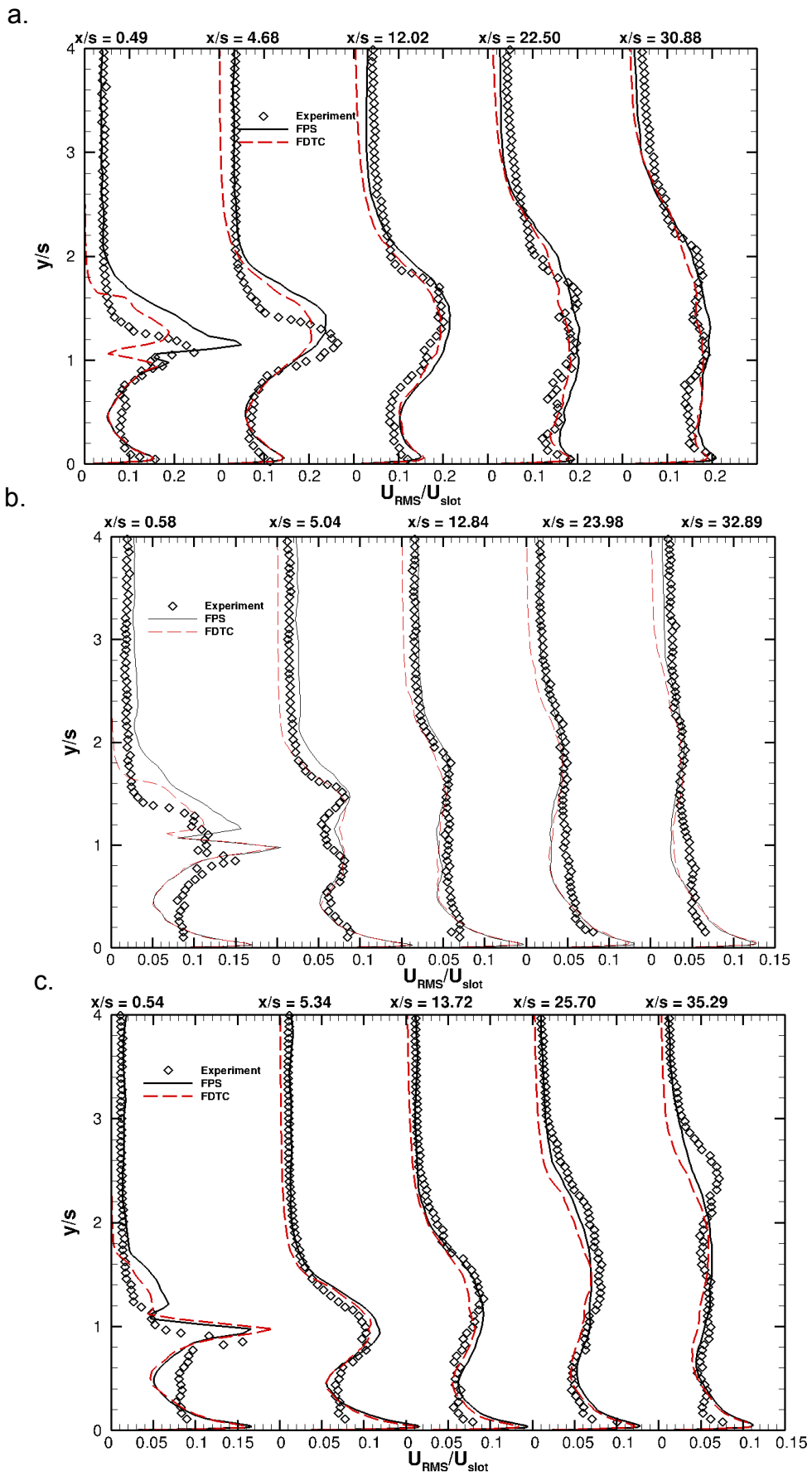

Figure 53 – Profiles of the RMS of streamwise velocity for the a. wall wake, b. minimum shear and c. wall jet adiabatic cases.

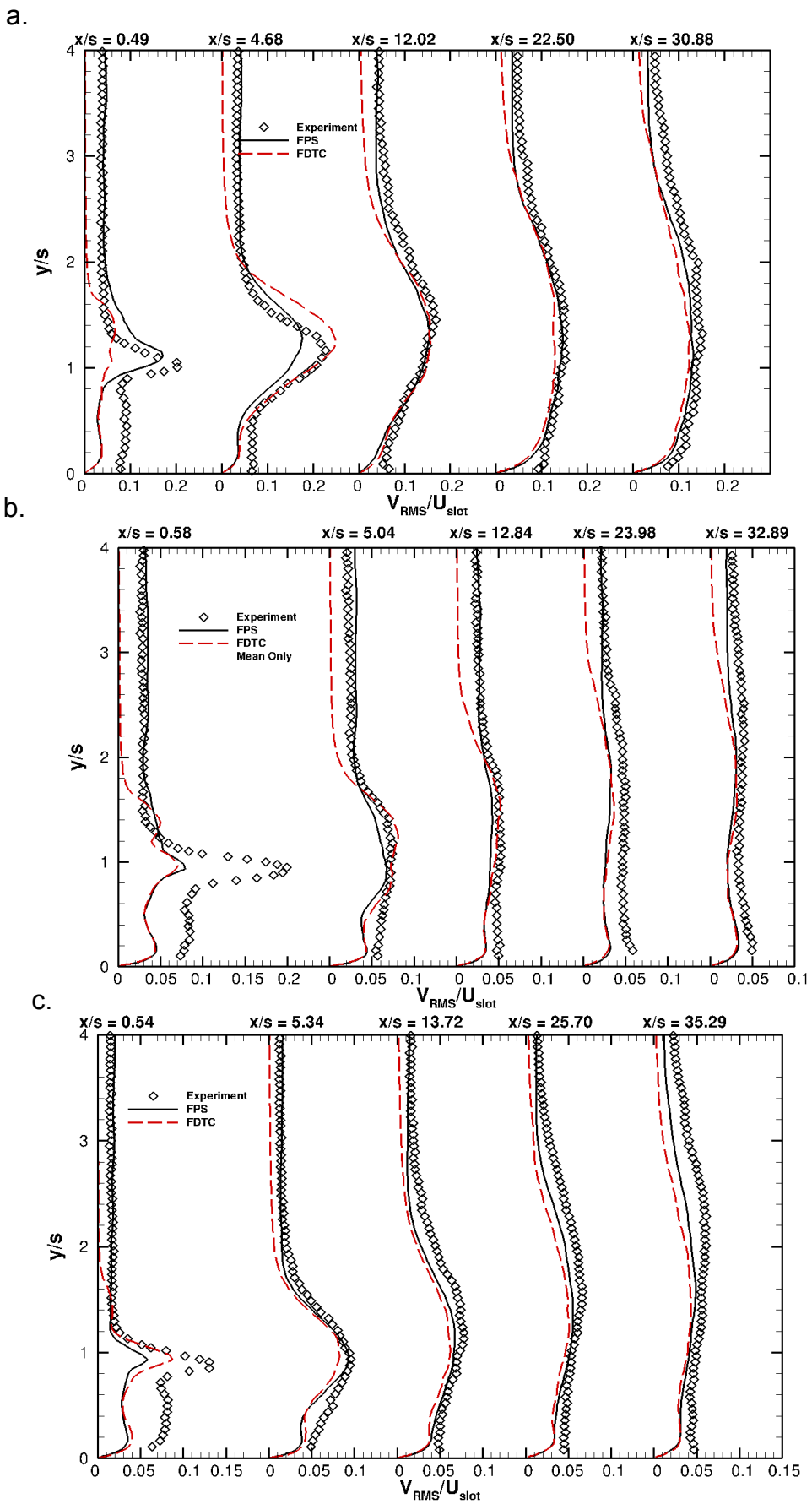

Figure 54 - Profiles of the RMS of wall-normal velocity for the a. wall wake, b. minimum shear and c. wall jet adiabatic cases.

minimum shear case, the streamwise RMS velocity retains two peaks from the boundary layers on either side of the splitter plate, which the LES also predicts. Eventually these peaks combine to create a region of constant RMS velocity. While very little overall difference between the FPS and FDTC in the RMS mixing solution exists, the FPS does better represent the experimental turbulent kinematic mixing physics because the grid turbulence is simulated.

A little more analysis is needed to understand the relatively poor turbulent agreement in the near-injector field. The streamwise RMS is overpredicted by the LES techniques while the wall-normal component is underpredicted. Downstream the wall-normal RMS velocity recovers and the streamwise overpredictions reduce in magnitude and follow the experimental data well. To understand these trends consider Equation 110 [92], which is the transport equation for each component of the incompressible, turbulent kinetic energy, shown in Equation 109. As before, the incompressible assumption is not true but makes the equations more straight-forward and understandable, which will serve for the present purpose. Notice that each term in the component form of the turbulent kinetic energy has an analogous term in the turbulent kinetic energy equation, except for the first term on the right hand side involving the fluctuating pressure and

$$\left[\frac{\partial}{\partial t}+\overline{u}_j\frac{\partial}{\partial x_j}\right]\frac{1}{2}\left\langle u_i'^2\right\rangle=\left\langle p'\frac{\partial u_i'}{\partial x_i}\right\rangle+\frac{\partial}{\partial x_j}\left\{-\frac{1}{\rho}\left\langle p'u_i'\right\rangle\delta_{ij}-\frac{1}{2}\left\langle u_j'u_i'^2\right\rangle+2\nu\left\langle\frac{1}{2}\left(\frac{\partial u_i'}{\partial x_j}+\frac{\partial u_j'}{\partial x_i}\right)u_i'\right\rangle\right\}$$
$$-\left\langle u_i'u_j'\right\rangle\frac{\partial\overline{u}_i}{\partial x_j}-2\nu\left\langle\frac{1}{2}\left(\frac{\partial u_i'}{\partial x_j}+\frac{\partial u_j'}{\partial x_i}\right)\frac{1}{2}\left(\frac{\partial u_i'}{\partial x_j}+\frac{\partial u_j'}{\partial x_i}\right)\right\rangle \qquad \text{Eqn. (110)}$$

the gradient of fluctuating velocity. Adding up the equations and using incompressible continuity, this first term will go to zero in the turbulent kinetic energy equation. The

presence of this pressure-strain rate term is particularly illuminating. This term is responsible for intercomponent transfer of turbulent kinetic energy, or moving turbulent kinetic energy from one direction into the other directions. In turbulent 2D, free shear flows, the turbulent kinetic energy enters into the streamwise component via the turbulent streamwise, wall-normal Reynolds stress. The turbulent kinetic energy is then transferred from the streamwise component to the cross-stream and spanwise components through this pressure strain-rate term. When using LES with inadequate grid resolution to resolve the gradients in a given region, the turbulent kinetic energy will not transfer properly into the other components. Hence in the near-injector region, where the fine structures are not adequately resolved, the streamwise component of turbulent kinetic energy will be large because its energy cannot be transmitted to the other components, which are underpredicted. Downstream, the flow structures are resolved very well and therefore the intercomponent transfer physics are better represented and match experimental data better.

Next consider the streamwise, wall-normal Reynolds stress profiles for the experiment and the LES solutions shown in Figure 55. Here as in Figure 53 and Figure 54, the agreement in the Reynolds stress at the first streamwise station is only modest with the peak often being under resolved. Once again in this region the FPS performs better than the FDTC for the wall wake case, but performs worse for the wall jet case. Overall the FPS better predicts the experimental trends, even though both techniques closely approximate the experiments away from the first streamwise measuring station. The wall wake simulations, due to the thicker boundary layer imposed there, do not agree as well as the other cases at the second streamwise location but the agreement recovers

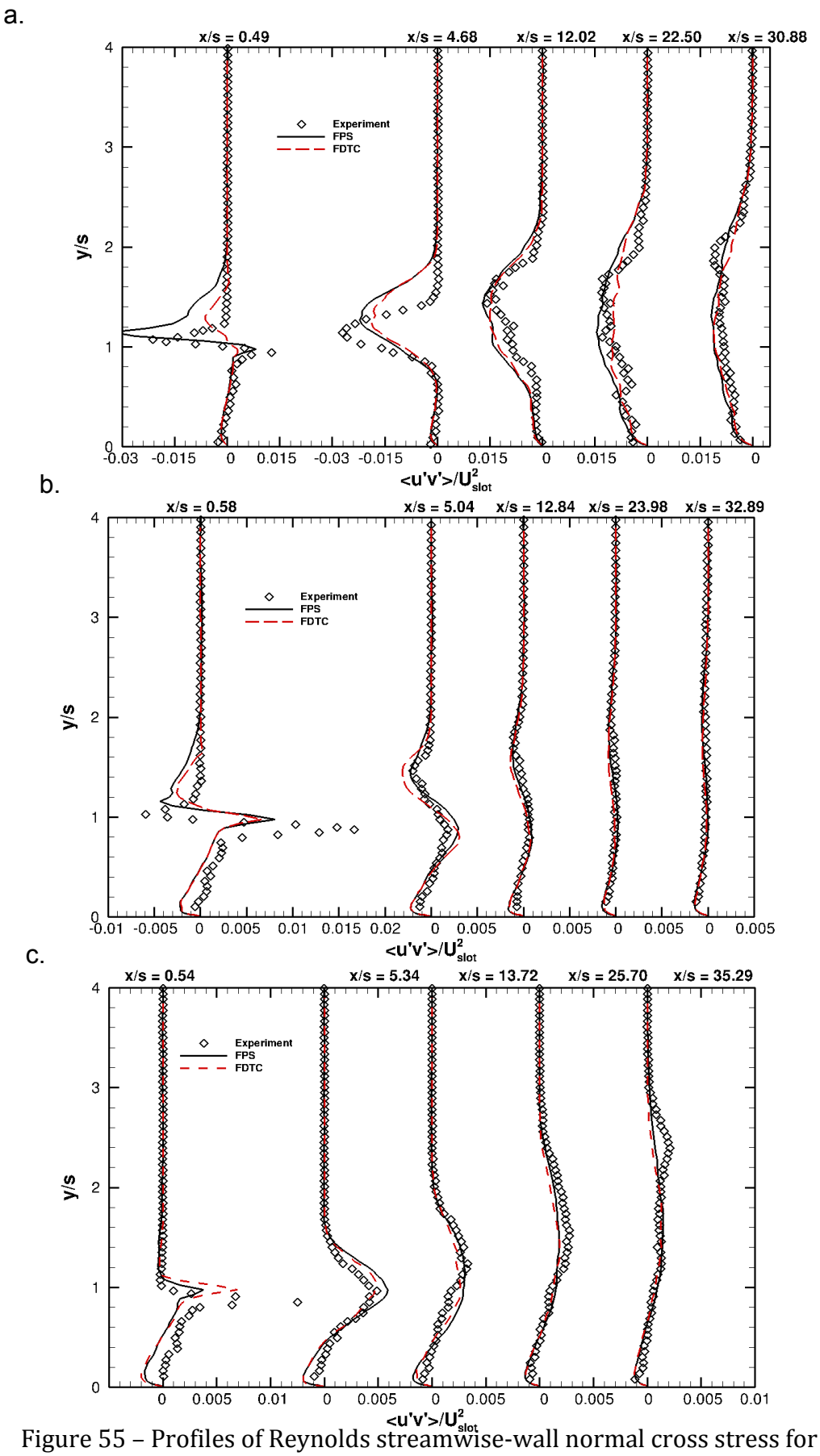

Figure 55 – Profiles of Reynolds streamwise-wall normal cross stress for the a. wall wake, b. minimum shear and c. wall jet cases.

soon after that. It should be emphasized that this turbulent mixing is the primary driver in film cooling and these plots show that LES techniques accurately resolve this type of shear mixing. More qualitatively, the LES solutions correctly predict that the wall wake has largely negative Reynolds stress, while the wall jet has largely positive Reynolds stress in the mixing layer. The flow solutions also correctly predict the double peak occurring in the minimum shear case, as was discussed earlier.

Now that the LES techniques have been shown to simulate the turbulent mixing physics well, the actual turbulent structures analyzed in §3 will also be numerically visualized. Turbulent flow structure visualizations in the mixing layer near the second experimental measuring station are shown in Figure 56, Figure 57 and Figure 58 for the wall wake, minimum shear and wall jet cases, respectively. In a. of each plot, the fluctuating velocity vectors are drawn on top of contours of instantaneous pressure, where blue represents low pressure and red represents high pressure. These contours and vectors occur on a streamwise, wall-normal plane with flow moving from left to right. The fluctuating vector fields are useful for identifying turbulent flow structures, which are identified by finding regions of circulating vectors. Notice that in the dark blue regions there are strong vortical structures, especially for the wall wake and wall jet cases. Notice that these structures are clockwise for the wall wake and counter-clockwise for the wall jet, which was also shown in §3. The minimum shear contains strong structures of both orientations. Actually, all the LES solutions show structures of both orientations, with large fluctuating velocities in between these counter-rotating vortices occuring due to constructive intereference of the vortices. Oftentimes at the center of vortices a low pressure region is present, making iso-surfaces of pressure a tool for

visualizing vortices in a mixing layer. Similarly the Q-criterion is often used in turbulent research to visualize near-wall structures. Therefore in b. of each plot, the fluctuating

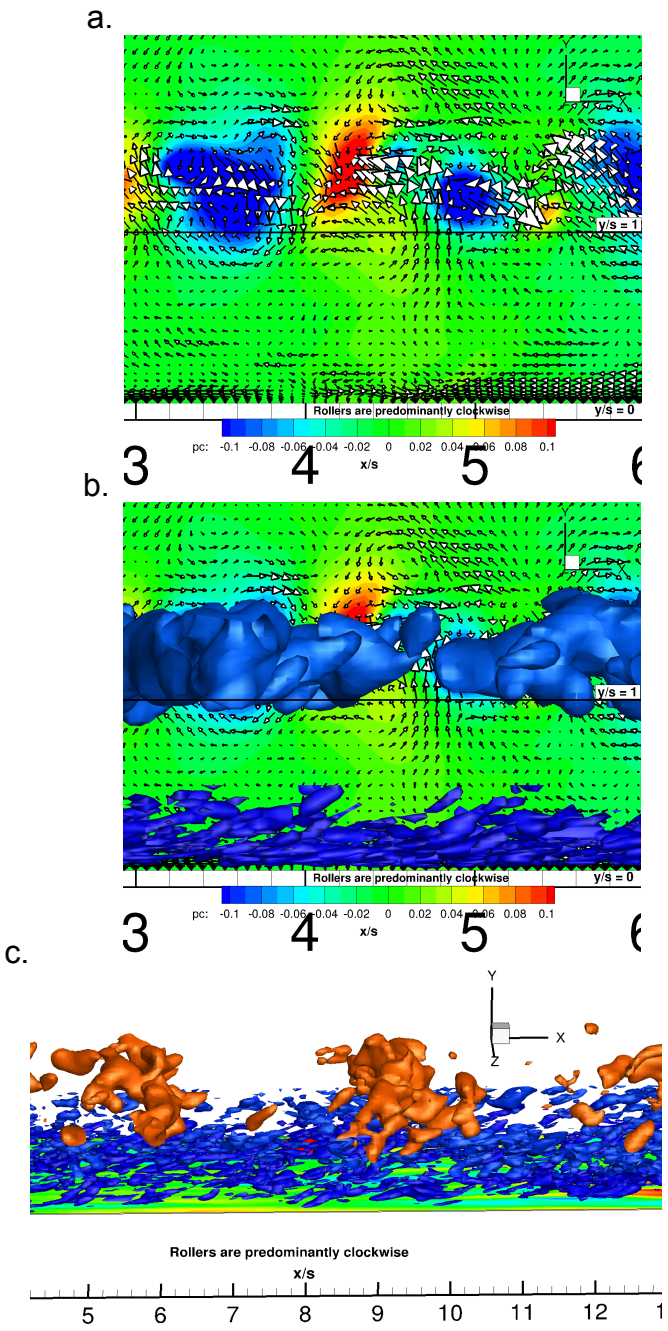

Figure 56 – Flow visualization of the wall wake turbulent shear structures. a. streamwise and cross-stream fluctuating vector fields on top of instantaneous pressure contours. b. streamwise and cross-stream fluctuating vector fields on top of instantaneous pressure contours, along with iso-surfaces of pressure and the Q-criterion near the wall, c. iso-surfaces of pressure and the Q-criterion.

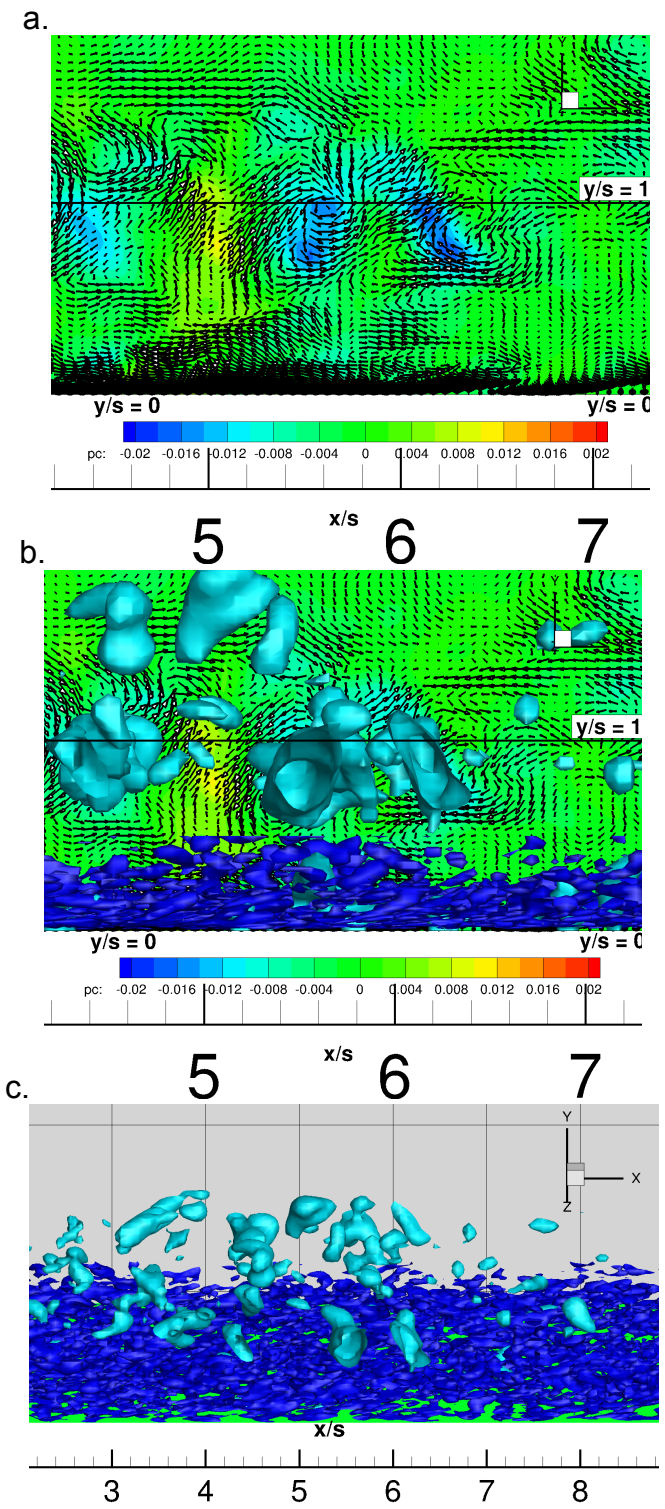

Figure 57 - Flow visualization of the minimum shear turbulent shear structures. a. streamwise and cross-stream fluctuating vector fields on top of instantaneous pressure contours. b. streamwise and cross-stream fluctuating vector fields on top of instantaneous pressure contours, along with iso-surfaces of pressure and the Q-criterion near the wall, c. iso-surfaces of pressure and the Q criterion.

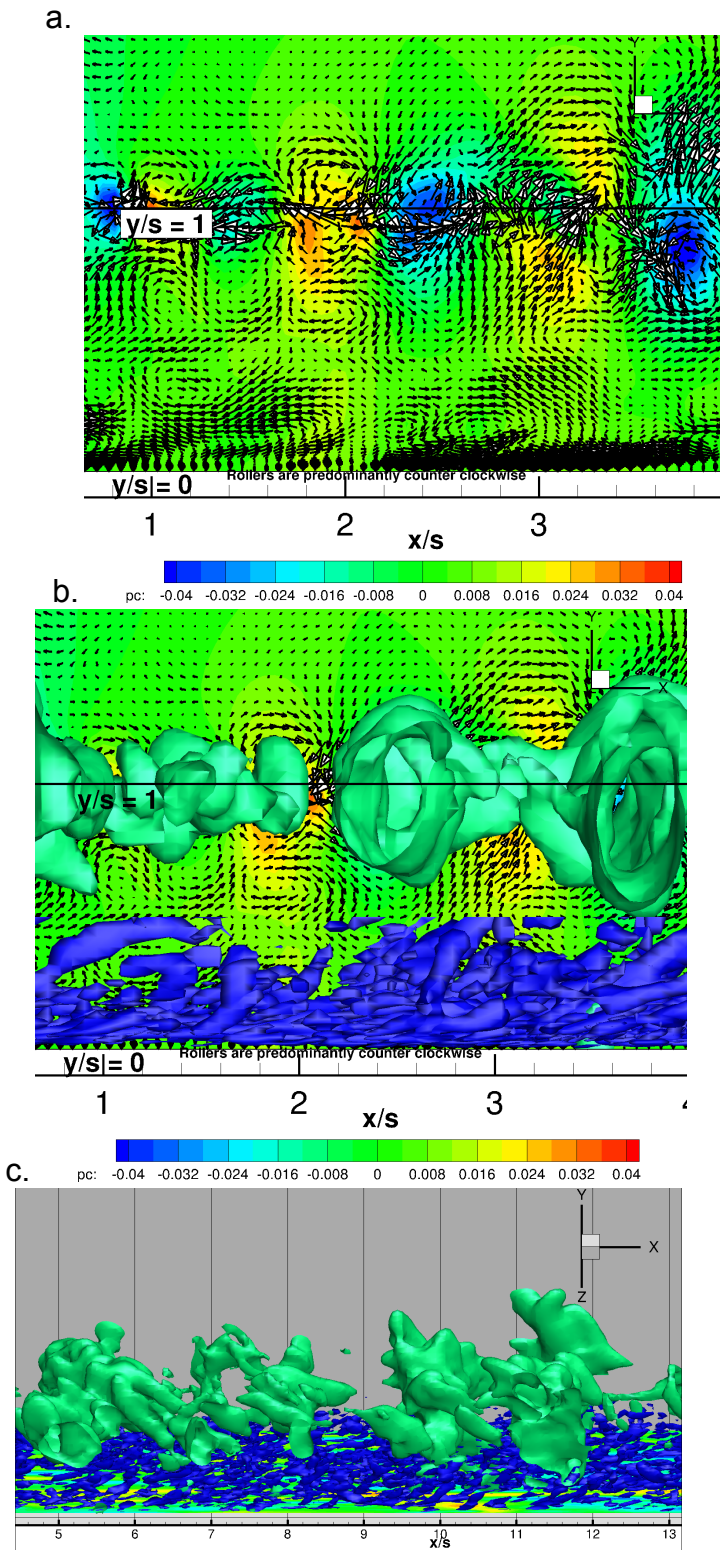

Figure 58 - Flow visualization of the wall jet turbulent shear structures. a. streamwise and cross-stream fluctuating vector fields on top of instantaneous pressure contours. b. streamwise and cross-stream fluctuating vector fields on top of instantaneous pressure contours, along with iso-surfaces of pressure and the Q-criterion near the wall, c. iso-surfaces of pressure and the Q-criterion.

vectors and pressure contours are drawn but superimposed on top of them are iso-surfaces of low pressure in the mixing layer and iso-surfaces of the Q-criterion near the wall. Notice that these low pressure iso-surfaces correspond very well to the turbulent shear structures visualized in a. It can also be seen that both the Q-criterion and pressure iso-surfaces are three-dimensional in nature. This is emphasized even further in c. where a three-dimensional, isometric view of the pressure iso-surfaces and Q-criterion are drawn. The plots in c. are drawn slightly downstream of a. and b. to show the complex interaction of the wall structures with the turbulent shear structures. As the series of roller structures, or turbulent shear vortices, move downstream, they grow in size and eventually interact with the wall in some complicated way, causing both sets of structures to deform. The numerical description for these interactions is partially, although not entirely, described by the series of mean and fluctuating plots presented previously. The purpose of Figure 56, Figure 57 and Figure 58 is to qualitatively, not quantitatively, visualize the three-dimensional turbulent structures and reemphasize the complexity of the turbulent interactions inherent in film cooling flows.

Figure 59 and Figure 60 show the LES RMS profiles of temperature and density, respectively, for the wall wake, minimum shear and wall jet cases. The streamwise stations in these plots are not given explicit values, as the exact location of the streamwise station differs between the shear cases. These locations are the same as shown previously and are similar, therefore the profiles are shown together in the interest of brevity. Also only the FPS is shown since experimental data were not available to compare against. Since FPS and FDTC LES solutions provide similar results, the trends are therefore set forth using only the FPS solutions. As is expected, the temperature and

density fields mirror each other, even though their magnitudes differ. Notice once again that the spread of the thermal mixing layer shows that the wall jet spreads away from the

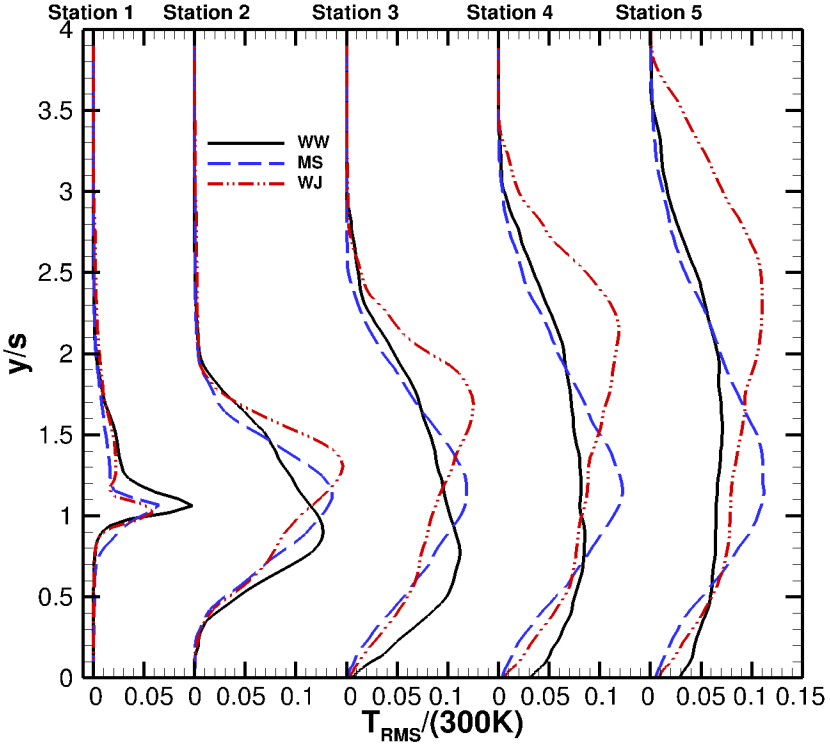

Figure 59 - Profiles of the RMS of temperature at different streamwise stations for the LES FPS simulation.

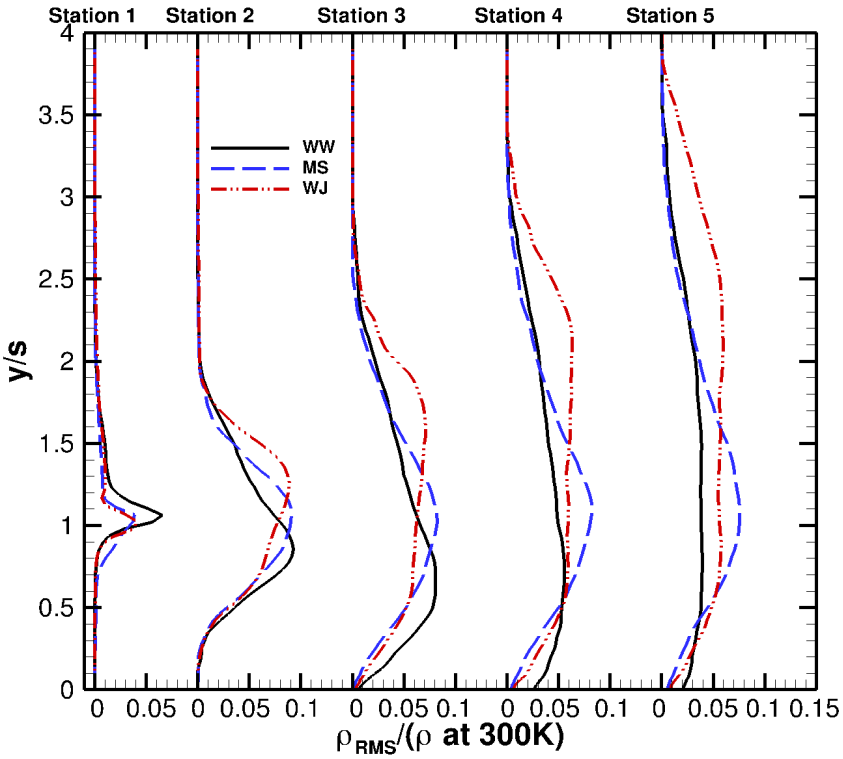

Figure 60 - Profiles of the RMS of temperature at different streamwise stations for the LES FPS simulation.

wall, with the wall wake spreading towards the wall. Notice also that as the mixing layer impinges on the wall for the wall wake case, the wall no longer retains a zero value of RMS temperature or density. It is also interesting to note that while the wall jet has the largest fluctuations of temperature, the wall wake has the largest fluctuations of density.

CFD simulations have the advantage that three-dimensional information can be easily extracted. Additionally correlations of velocity and temperature are relatively simple to calculate from CFD solutions; calculations that are experimentally extremely challenging to perform. In Figure 61, one such important correlation, the correlation of wall-normal velocity fluctation and temperature fluctation, from the LES simulations are shown at the different experimental streamwise stations for the wall wake, minimum shear and wall jet cases. To examine the importance of this quantity, consider the transport equation for the incompressible, mean flow temperature using the boundary layer assumptions; this is given in Equation 111. Just like the Reynolds stress acts to spread and mix the momentum, the fluctuations of wall-normal velocity and temperature act to spread and mix the mean thermal energy. This term is responsible for fluid transport of hot fluid from the mainstream into the coolant stream and cool fluid from the coolant stream into the mainstream. Notice that this correlation is always negative meaning that the fluctuations of wall-normal velocity and temperature take opposite signs. If hot fluid is brought into the mainstream, the temperature fluctuation will be positive since the coolant fluid there is heated, but the motion to bring it downward creates a negative wall-normal velocity fluctuation. Meanwhile the reverse scenario of cold fluid transport via a structure into the mainstream causes a negative temperature fluctuation, along with a positive wall-normal velocity fluctuation. In a mean sense,

therefore, the correlation of the fluctuations of wall-normal velocity and temperature is negative, for film cooling flows of this orientation. Keeping in mind that the coolant velocity of the wall wake is half that of the wall jet and minimum shear cases, the wall wake and wall jet have the strongest relative thermal turbulent transport.

$$\rho\left[\frac{\partial \overline{T}}{\partial t}+\overline{u}\frac{\partial \overline{T}}{\partial x}+\overline{v}\frac{\partial \overline{T}}{\partial y}\right]=\frac{\partial \overline{q}}{\partial y}-\frac{\partial}{\partial y}\left(\rho\left\langle v'T'\right\rangle\right) \qquad \text{Eqn. (111)}$$

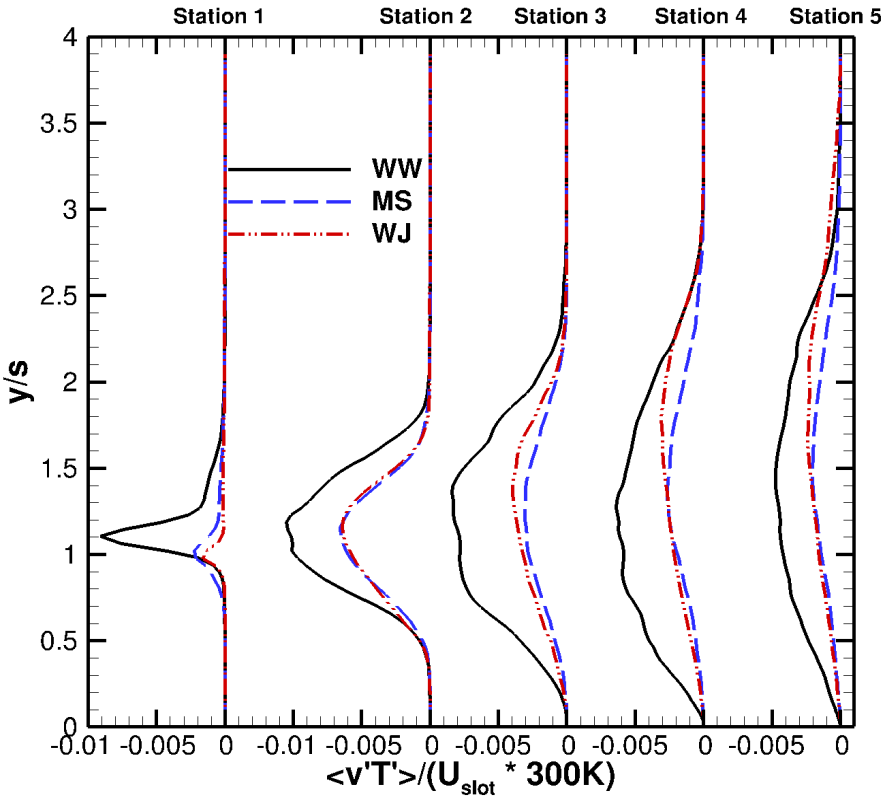

Figure 61 – Correlation of the wall-normal velocity and temperature fluctuations at different downstream stations for the LES solutions.

Another advantage of the LES solutions is that different scalings can be easily extracted. For example, wall scaling can be performed, which is often used in wall models and classical turbulent boundary layer scaling. Figure 62 shows the mean streamwise profiles of velocity using this wall scaling for the adiabatic film cooling

cases. From turbulent theory, classic, turbulent, equilibrium boundary layers collapse when using this wall scaling. A near-wall, viscous sublayer forms for y^+ less than about five and a log-linear region forms above y^+ of about thirty. From this figure, it can be seen that the minimum shear and wall jet cases approximately collapse for y^+ less than 100, confirming the possibility that wall models can capture the near-wall dynamics for these flows. The wall wake meanwhile does not collapse in this scaling. Accelerating flows do not generally follow the typical logarithmic law scaling, which occurs strongly for the wall wake case. Additionally the wall wake coolant is only weakly turbulent, which has the added effect of reducing the logarithmic region. Therefore more complex wall modeling that incorporates acceleration effects would be needed for a wall wake type flow with a weakly turbulent, Reynolds number. Additional plots of the LES velocities using wall scaling are provided in the Appendix.

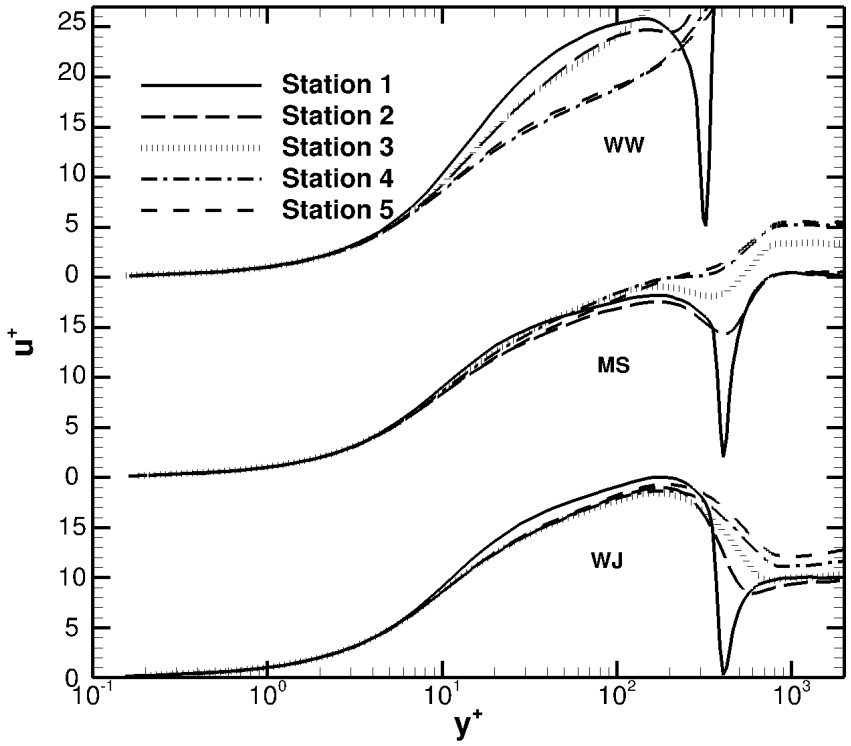

Figure 62 – Profiles of adiabatic velocity profiles for the wall wake, minimum shear and wall jet cases using wall scaling.

Another point of interest not previously noted for the adiabatic cases involves the convection scheme. As was mentioned earlier in §2, overshoots of temperature out of physical bounds can occur near the convection of sharp gradients in finite difference schemes. Two convective schemes were tested for the wall jet case: QUICK and BQUICK (Bounded QUICK). The adiabatic wall effectiveness and mean temperatures between these two cases were nearly identical and therefore are not reported. However there are noticeable differences in the fluctuating information involving the temperature. In a mean sense, BQUICK and QUICK do not dramatically alter thermal convection physics, but rather when sharp gradients occur, BQUICK will keep the magnitude of the temperature within the physical bounds of the problem, namely the mainstream and coolant temperatures. When the temperature violates this bound in a fluctuation of temperature, the RMS is overestimated. The RMS of temperature is indeed larger for QUICK, especially downstream, as is evidenced by Figure 63, which shows profiles of RMS temperature for the wall jet case when using QUICK and BQUICK. In the near-field the RMS of temperature are nearly identical. It is only downstream towards the upper edges of the mixing layer that the differences between QUICK and BQUICK are most apparent. The violation of physical bounds is most likely to occur in regions of hot fluid near the mainstream temperature, which defines the upper boundary. In the interior of the mixing layer, QUICK and BQUICK should revert to the same scheme as long as fluctations stay below the mainstream temperature and above the minimum coolant temperature. Similar differences can be seen in the far-field for the correlations of the fluctuations of temperature and wall-normal velocity, shown in Figure 64 for the LES adiabatic wall jet case. Over the first four experimental stations, the profiles of these

correlations are approximately the same; differences arise in the last station, especially near the upper extent of the mixing layer. BQUICK shows promise as an LES scheme for film cooling flows when defined physical bounds exist, especially when boundedness is important, for example in combustion problems.

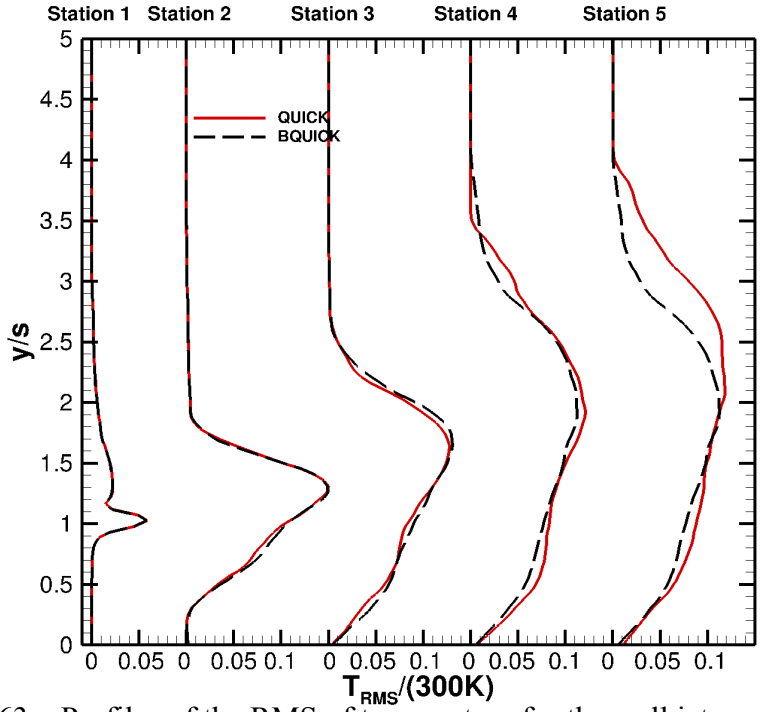

Figure 63 – Profiles of the RMS of temperature for the wall jet case using QUICK and BQUICK.

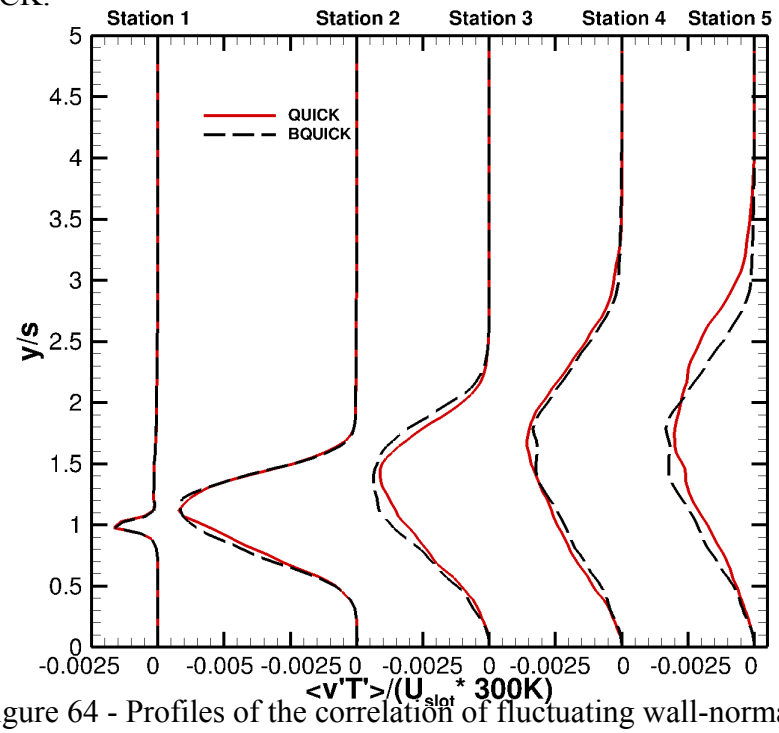

Figure 64 - Profiles of the correlation of fluctuating wall-normal velocity and temperature for the wall jet case using QUICK and BQUICK.

4.4 Adiabatic Film Cooling Simulations – Radiative Boundary Condition

Experimentally, radiation at the wall was shown to have an influence on the wall temperature and the near-wall region. Normally numerical simulations of radiative flows involve complex schemes to respect the radiation physics; these schemes involve the radiative transfer equation, while also taking into account scattering and absorption by the working gas. Fortunately in this problem with temperature ranging from 300K to 460K, air can be considered as a non-participating gas, meaning only walls radiatively interact. Radiation may be incorporated into the thermal boundary condition without adding extra complexity due to radiation physics. In §2, the radiation heat flux in the experimental wind tunnel was described, while the experimental radiation was characterized in §3. The radiation boundary condition uses a heat balance of convection and radiation at the wall to write the enthalpy gradient at the wall. This enthalpy gradient is given in Equation 111 below. Remember that the 0 subscript denotes the parameters used to non-dimensionalize LES BLAC, while fluid represents the fluid properties at the wall. Also * denotes non-dimensionalized parameters. The experimental casing temperatures were nominally 423K, 416K and 420K for the wall wake, minimum shear and wall jet cases, respectively.

$$\left.\frac{\partial h^*_{fluid}}{\partial y^*}\right|_{y^*=wall} = -\frac{\sigma\varepsilon_{wall}\varepsilon_{SS}VF\left(T^{*\,4}_{casing} - T^{*\,4}_{wall}\right)T_0^4\,\mathrm{Pr}\,\mathrm{Re}}{\rho_0 U_{slot} h_0 \alpha^*_{fluid}\rho^*_{fluid}} \qquad \text{Eqn. (111)}$$

The effectiveness based on minimum temperature is shown for the different shear cases with and without radiation at the wall in Figure 65. Note that the different turbulent

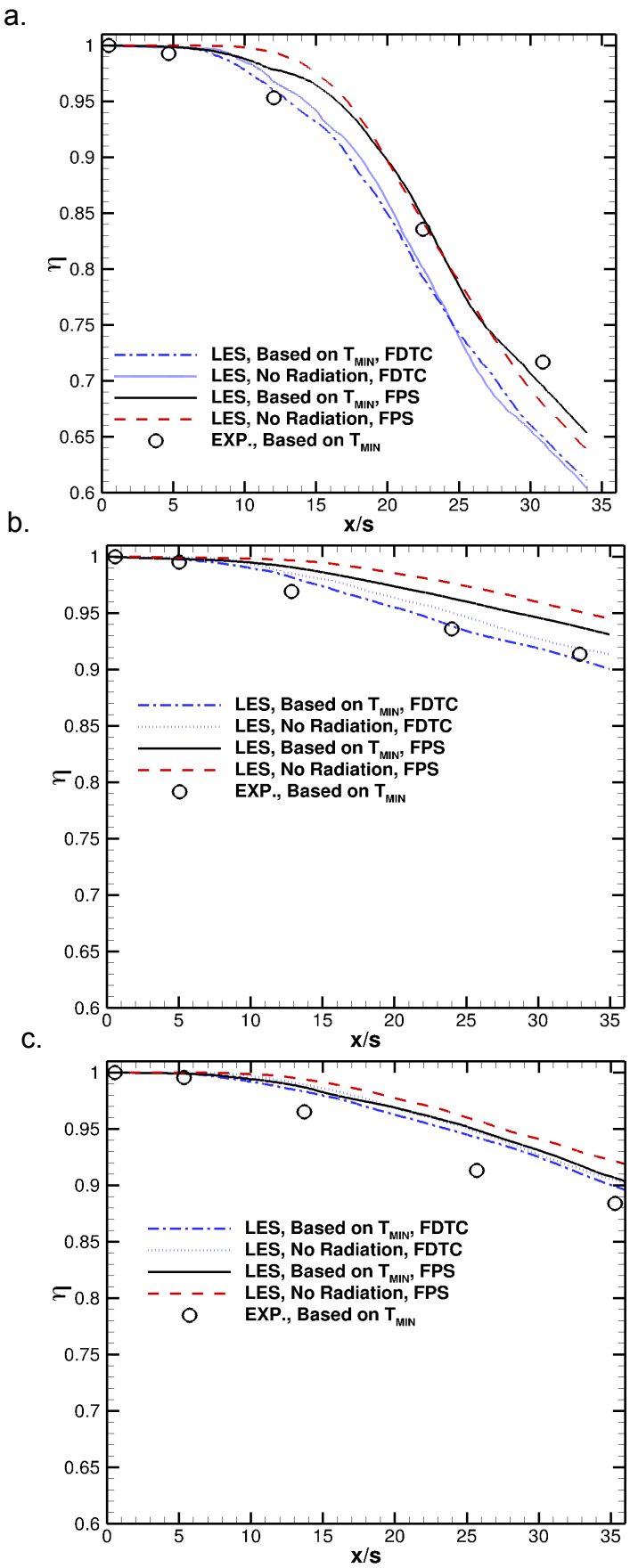

Figure 65 – Adiabatic effectiveness with and without radiation at the wall for the LES FPS and FDTC simulations and experimental data for the a. wall wake, b. minimum shear and c. wall jet shear cases.

inlets are also explored in this plot. The effect of radiation is largest in the wall wake case, which experimentally is also found to be most sensitive to radiation, due to the relative amount mass near the wall. This effect is seen best in the near-injector region and is best understood by considering the separation between the curves with and without radiation. Far from the injector in the wall wake case, the cases with and without radiation at the wall collapse, demonstrating that the heat flux downstream is dominated by the thermal mixing layer and not the radiative interactions between the test plate and the wind tunnel walls. The strength of the numerical heat fluxes will be explored more in depth for the non-adiabatic cases in the next section. As occurred in the cases with no radiation, the FPS outperformed the FDTC simulations for the wall wake case. Similarly, the FDTC better simulated the adiabatic effectiveness for the minimum shear and wall jet cases. With radiation effects, the FDTC predicted the adiabatic effectiveness within 8%, 2% and 3% for the wall wake, minimum shear and wall jet cases, respectively; meanwhile the FPS predicted the adiabatic effectiveness within 3%, 3% and 4% for the wall wake, minimum shear and wall jet cases, respectively. Overall the radiation at the wall does not dramatically affect the effectiveness results but does provide a mechanism for increased wall heating that is found in the experiments.

A better way to explore the fidelity of the LES radiation physics is to compare the effectiveness based on wall temperature with the effectiveness based on minimum temperature (which was already shown in Figure 65). These effectivenesses based on either wall or minimum temperature for the different LES radiation cases and the experiments are shown in Figure 66. Notice the strong effect of radiation on the wall wake case is immediately recognizable by comparing the separation between the

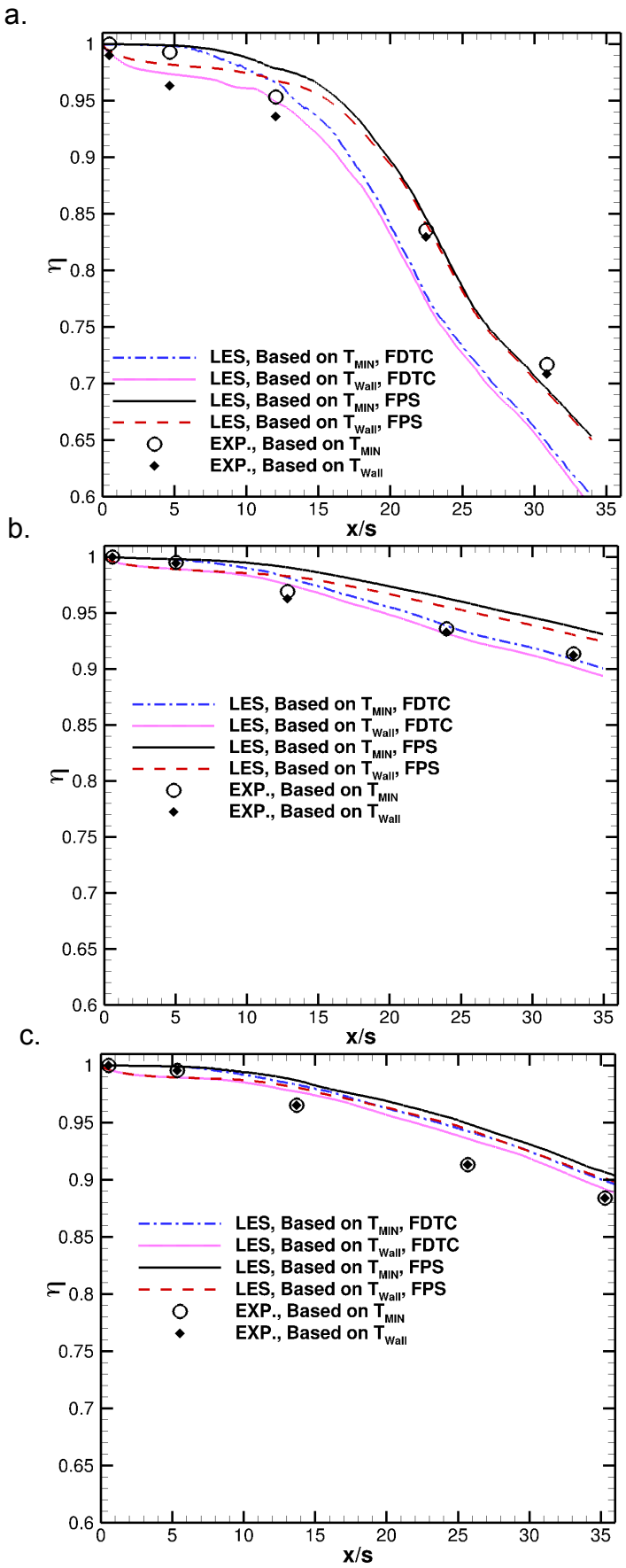

Figure 66 – Adiabatic Effectiveness based on either wall or minimum temperature for the FPS and FDTC LES simulations with radiation for the a. wall wake, b. minimum shear and c. wall jet cases. The LES data is compared to experimental data for the same shear conditions.

effectivnesses based on the wall temperature and the minimum temperature. This separation is much less noticeable in the wall jet and minimum shear cases both experimentally and numerically. In the near injector region, the FDTC better predicts the trends and decay of the effectivenesses for all the cases. At some downstream location, normally around the third measurement station, the adiabatic effectivenesses based on wall and minimum flow temperatures collapse. In this series of plots, the relative strength of the radiation, both numerically and experimentally, are nominally the same. However, without radiation effects, there is no mechanism in this flow to make the mean minimum temperature occur away from the wall.

The kinematic transport is not significantly affected by the radiation at the wall since the radiation is not very strong. The thermal fields show some minor sensitivity to the radiation but only near the wall. Consider Figure 67, where the adiabatic temperature profiles are shown for the LES FPS simulations both with and without radiation. The LES profiles are compared to the experimental temperature. In a mean sense, no discernible distinction can be made between the LES results with and without radiation. The near-wall region, however, is isolated in Figure 68, so that radiation effects can be more easily visualized. Once again the temperature profiles for the LES FPS both with and without radiation are compared to experimental data. The main differences between the radiative and non-radiative cases occur very close to the wall, less than a tenth of a slot height away. Keep in mind that this region consists of slow-moving fluid, and therefore the near wall fluid is susceptible to heating due to contact with the wall. This figure shows that the film acts as a heat sink for the wall in cases with radiation, with heat being transported from the wall to the fluid. In each case, it can be seen that the minimum

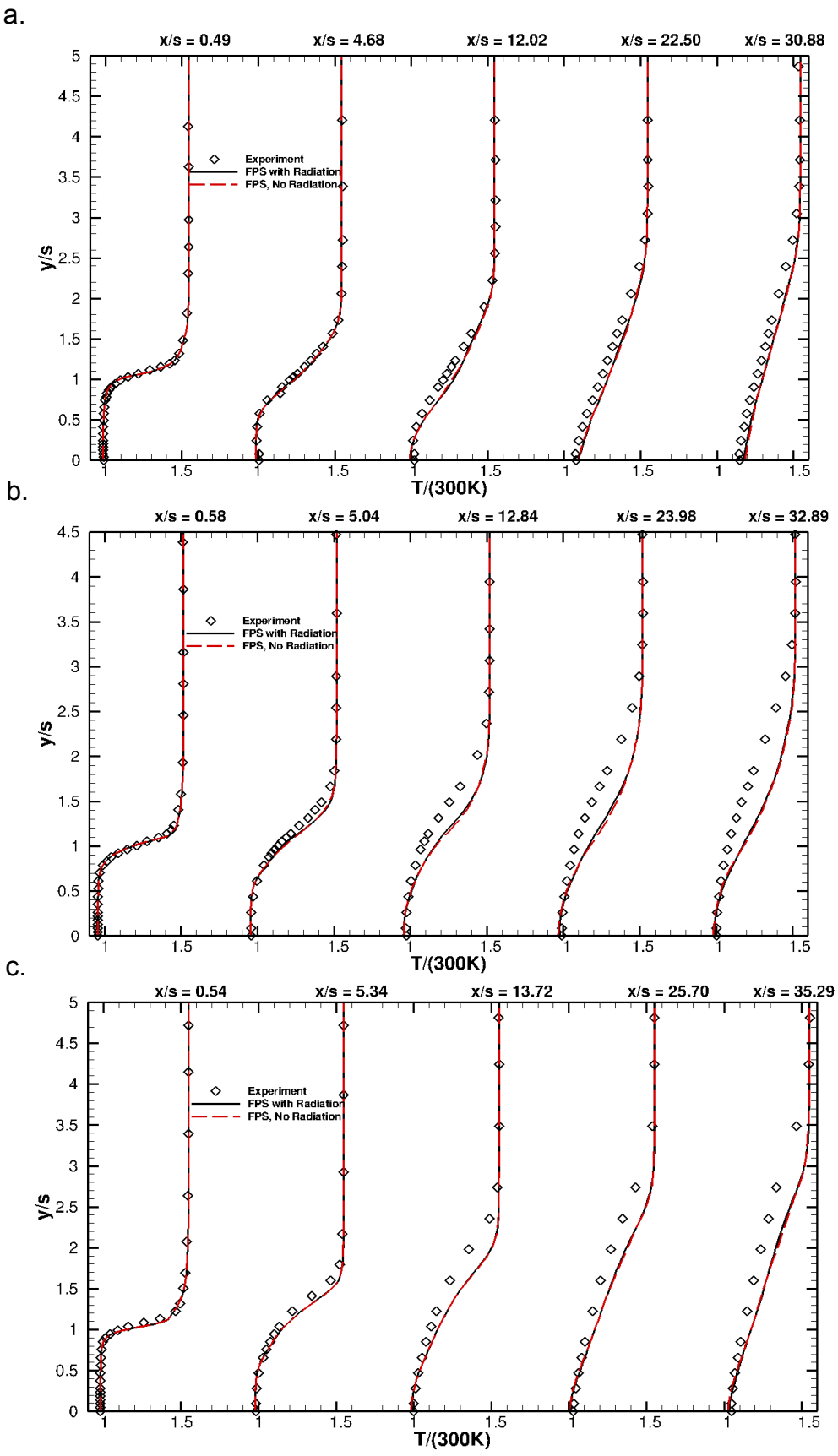

Figure 67 – Adiabatic temperature profiles for the LES FPS simulations with and without radiation at the wall for the a. wall wake, b. minimum shear and c. wall jet shear cases.

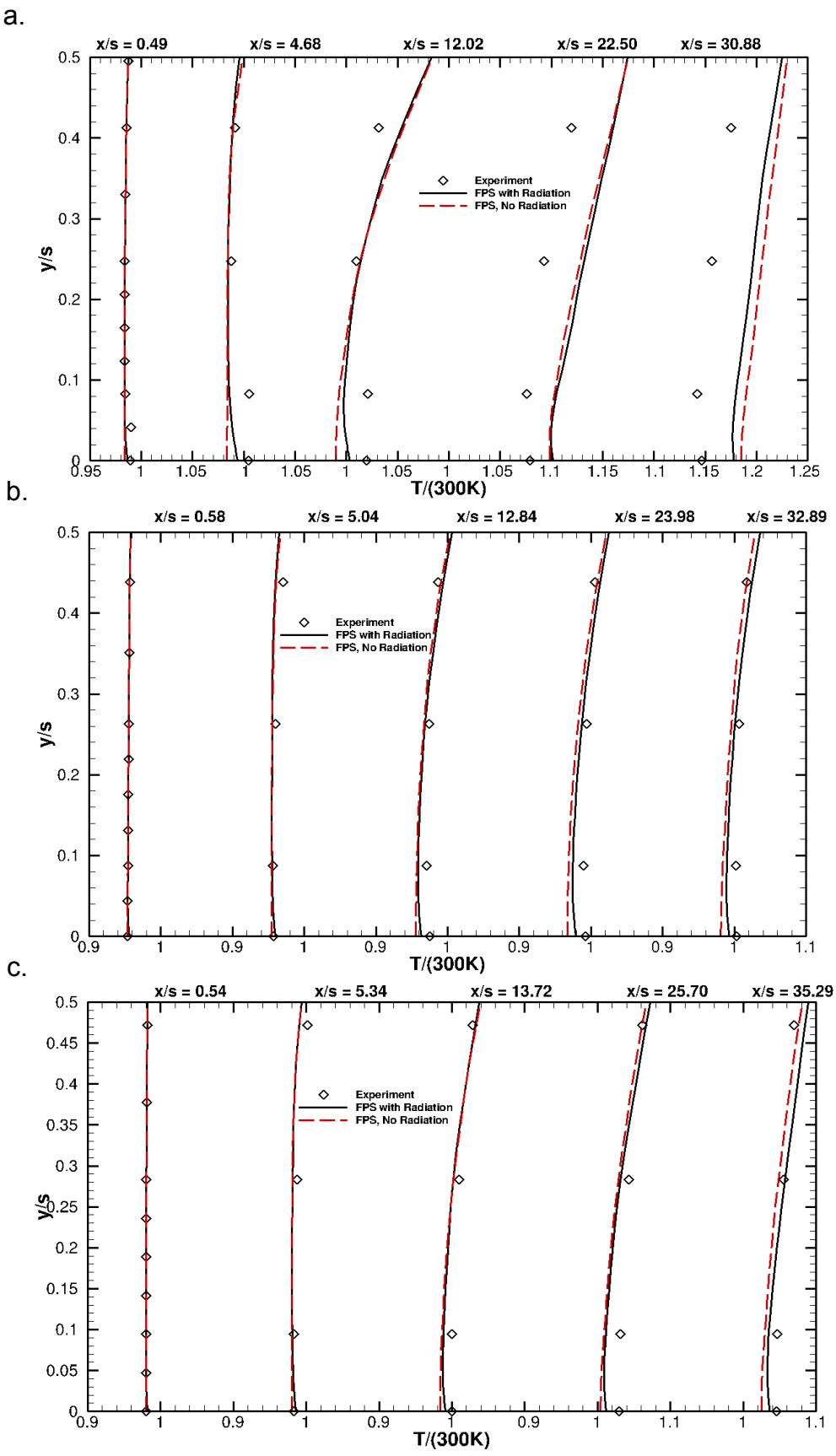

Figure 68 - Near-wall adiabatic temperature profiles for the LES FPS simulations with and without radiation at the wall for the a. wall wake, b. minimum shear and c. wall jet shear cases.

temperature occurs in the flow and not at the wall. Unfortunately, following the analysis in §2, the first experimental data point is the most susceptible to radiation errors due to the slow velocity and low convection of the probe in this region. Not that the radiative error is large, but the temperature at the first data point would be even less than what is indicated in Figure 68. This type of error is easiest to see for the wall wake case in the first experimental profile. Notice how the first data point off the wall is seemingly not following the trends of the data. This error is primarily occurring due to radiation, which is the largest across all the experimental data in this location for this shear case. Fortunately due to thermal contact with the wall, the radiative error is relatively minor for the experimental wall temperature. As a point of note, numerically the minimum temperature occurs between $1/20^{th}$ and $1/10^{th}$ of a slot height away from the wall; the first experimental measurement is about $1/10^{th}$ of a slot height off the wall.

4.5 Non-Adiabatic Film Cooling Simulations

In this section, the non-adiabatic film cooling cases are simulated using LES BLAC. The purpose is to further test the numerical ability to resolve problems with conjugate heat transfer and to assess the capability of LES techniques in providing predictions of different heat transfer physics that are representative of actual engines. In the regimes considered in this study, the kinematics are not significantly altered due to the presence of backside wall cooling and therefore not much attention will be paid here to the kinematics. For now, it suffices to say that the kinematic agreement between the LES simulations and the experimental measurements is comparable to the adiabatic cases. More attention is given to the thermal flow field, since it is primarily these measurements that change between the adiabatic and non-adiabatic cases. Once again the actual inlet techniques were not dramatically altered and therefore will not be presented either.

The boundary condition for enthalpy is given in Equation 112 and is once again an extension of the heat balance presented in Equation 111. The convective heat flux in the fluid is equal to the conduction heat flux through the wall minus the incident net radiative heat flux. The enthalpy terms in the fluid can be isolated to derive a boundary condition for the enthalpy at the wall. Note that the gradient of temperature through the wall can be solved in a variety of ways. The most physical of these is to solve the transient, solid heat conduction equation in multi-dimensions to track how the heat moves through the solid from the fluid. Fortunately, since the test plate has low thermal conductivity, the time scales associated with solid heat conduction is several orders of magnitude larger than the fluid time scales. This scaling allows for simplifying steady-

state assumptions to be made, where the transient effects can be ignored. Locally the steady-state assumption distorts the actual physical, thermal inertia effects that actually occur in the wall. However in a mean sense the steady-state assumption should be accurate. The wall-normal gradient term in the wall is just the difference in the wall temperature and the backside wall temperature, divided by the wall thickness; the latter temperature term remains fixed in the experiment and simulation. Already implicit in this form of the heat conduction equation is that the heat flows only in the wall-normal direction. As was discussed in §2 and §3, the test-plate is thin compared to the other directions, the temperature differential primarily occurs in the wall-normal direction and the thermal conductivity is very small, all of which support this one-dimensional conduction assumption. For one-dimensional conduction, along with constant thermal wall properties, the temperature in a mean sense is linear. While there are non-linearities, associated with temporal fluctuations at the boundary conditions, overall, in a mean sense, the temperature profiles in a solid are fairly linear.

$$\left.\frac{\partial h^*_{fluid}}{\partial y^*}\right|_{y^*=wall} = \frac{k^*_{wall}}{\alpha^*_{fluid}\rho^*_{fluid}}\frac{\partial T^*_{wall}}{\partial y^*} - \frac{\sigma\varepsilon_{wall}\varepsilon_{SS}VF\left(T^{*\,4}_{casing} - T^{*\,4}_{wall}\right)T_0^4\,\mathrm{Pr}\,\mathrm{Re}}{\rho_0 U_{slot} h_0 \alpha^*_{fluid}\rho^*_{fluid}} \qquad \text{Eqn. (112)}$$

First the non-dimensional wall temperatures are examined just as they were for the adiabatic cases. Figure 69 shows the effectiveness at the wall for the non-adiabatic experiments and the LES simulations using the FPS technique in the mainstream. The scaling between the adiabatic and non-adiabatic experimental effectivenesses was already explored in §3 and therefore will not be examined further here. The LES simulations follow the experimental effectiveness trends relatively well. The non-adiabatic cases

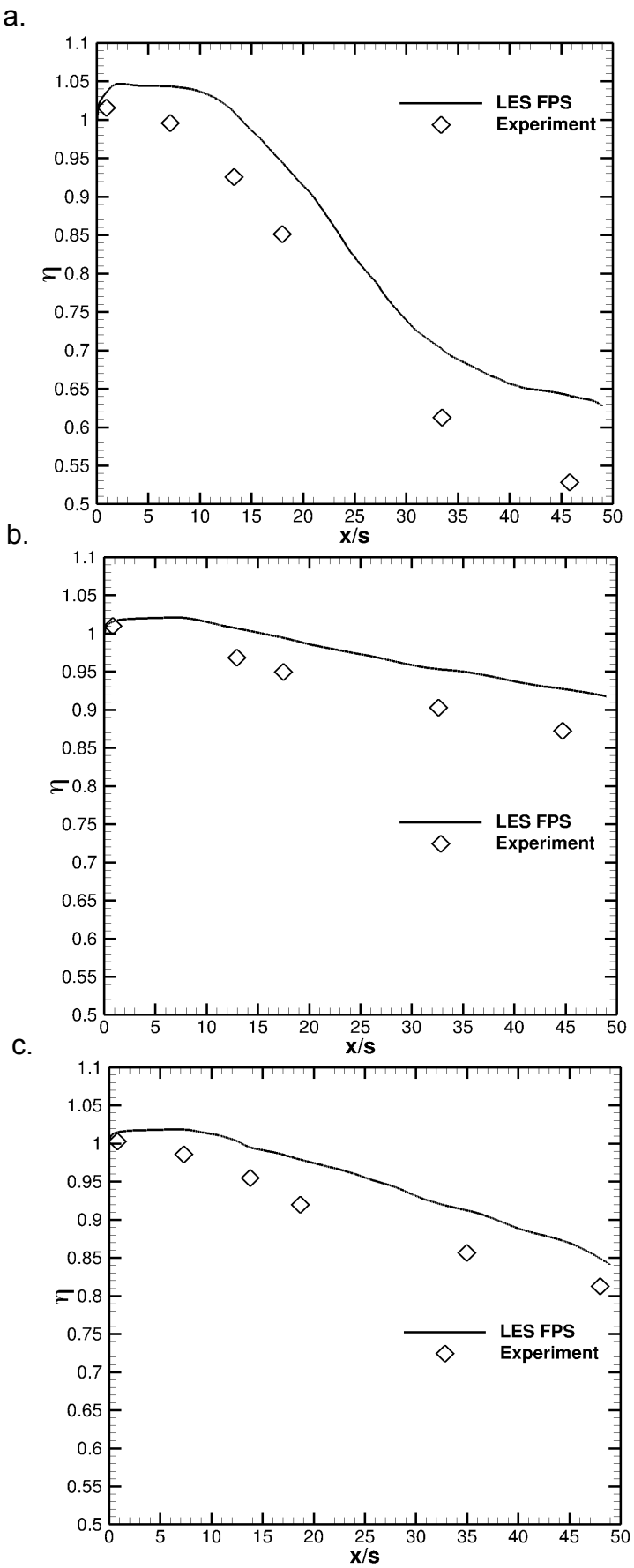

Figure 69 – Effectiveness at the wall for the LES simulations and the experiment for the a. wall wake, b. minimum shear and c. wall jet shear cases.

differ from the adiabatic cases because the minimum temperature always occurs at the wall and not in the fluid; this fact is one indication that the conductive heat flux dominates over the radiation. Therefore the effectiveness based on wall temperature also is the effectiveness based on minimum fluid temperature. The effectiveness error is less than 6% for both the minimum shear and wall jet non-adiabatic cases and in general is less than 9% for the wall wake case. The exception is far from the injection at the last two experimental stations in the wall wake case, where the deviation is 11%. The reasons for this deviation in the wall wake case only will be further examined, but overall the LES is shown to capture the modified fluid physics created by the wall conduction in the non-adiabatic cases, with relatively minor discrepancies occurring. Note that the heat balance in the near-injector seems to be predicted differently than what occurs experimentally. The magnitude of the errors in this region are on the order of 3% for the minimum shear and wall jet cases, while it is approximately 5% for the wall wake case. Unfortunately, this is in part due to incomplete knowledge of the temperature profile near the wall at the injector plane. If this near-injector imbalance did not exist, the effectiveness errors would be on the order of 3%, for the wall jet and minimum shear cases, and on the order of 6% for the wall wake case. These numbers are much more in-line with the adiabatic wall findings. Very near to the injection, the simulations predict that the film will cool more than is experimentally observed. Both experimentally and numerically, this cooling effect in the near-injector region manifests itself in the form of wall effectivenesses taking values greater than unity. As was experimentally observed, the LES non-adiabatic wall wake case shows the greatest cooling near the injector of all

the cases explored. Similarly both numerically and experimentally, the wall wake was found to have the worst wall performance, while the minimum shear performs the best.

To further explore these effectiveness findings, the heat fluxes at the wall need to be examined. Figure 70 shows the non-dimensional conductive, radiative and convective heat fluxes of both the LES simulations and the experiments for the non-adiabatic wall wake, minimum shear and wall jet cases. Each non-dimensional heat flux is created by dividing the dimensional heat flux with the product of the thermal conductivity and temperature difference between the two streams divided by the slot height as is shown in Equation 113. Otherwise the heat fluxes are defined in §2 and §3. For convenience, these heat fluxes are also presented in dimensional form in Figure 71. Notice that the conductive heat flux is always underpredicted by the LES simulations, indicating that the heat balance between the numerics and the experiments is slightly incorrect. To help determine why, consider Figure 69 again. From this plot, it can be seen that the effectiveness is always over-predicted relative to the experiment. A higher effectiveness corresponds to a lower wall temperature, which in turn means a lower conductive heat flux. Ultimately a heat flux condition is imposed at the wall, meaning the film decay will therefore not be as strong. Also keep in mind that the experimental conduction uncertainty varies between 3 and 9%, meaning that except for the wall wake case, the predicted conductive heat fluxes are approximately within the experimental uncertainty. The wall wake is the most sensitive to heat flux effects at the wall, so it is therefore unsurprising that the agreement in this case is the worst. Figure 70 does show that the LES correctly predicts the wall heat flux trends regardless of the case.

$$\dot{q}''_{wall}{}^{*} = \frac{\dot{q}''_{wall}}{\left(k_0 \Delta T / s\right)} \qquad \text{Eqn. (113)}$$

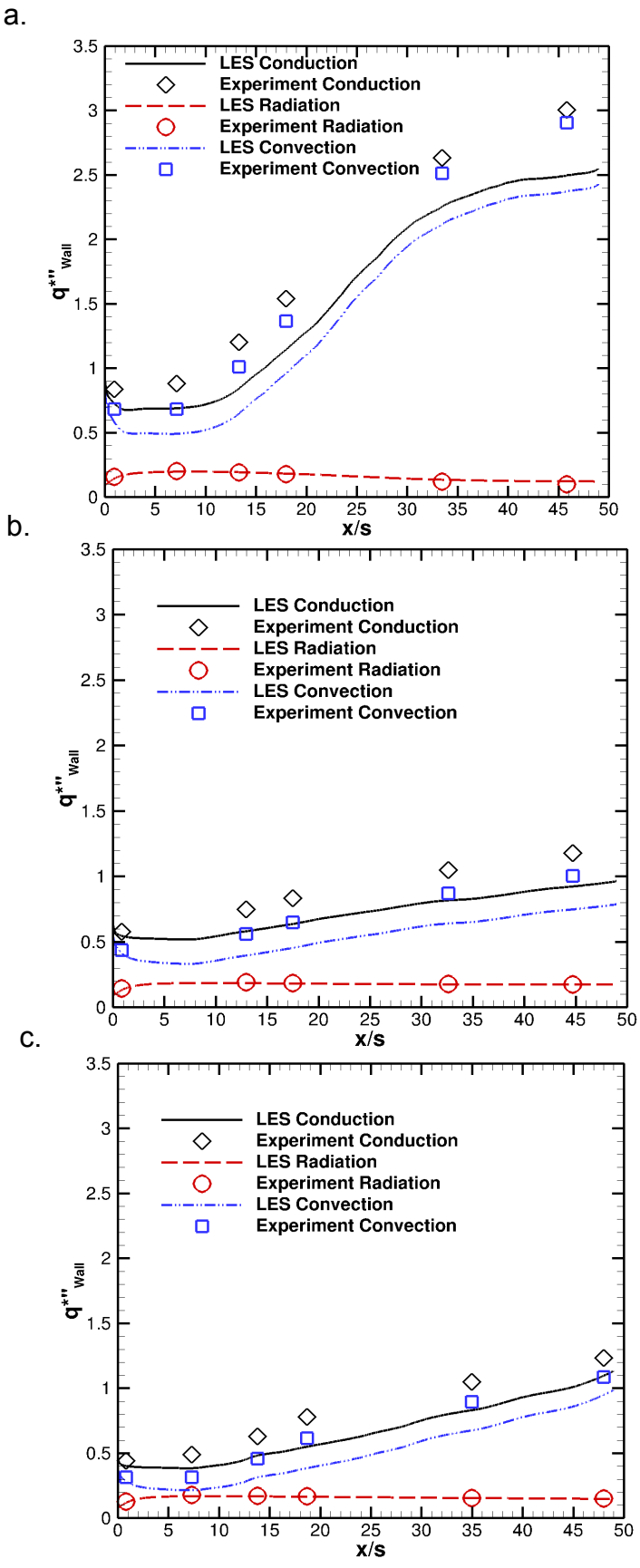

Figure 70 – Comparison of the non-dimensional experimental and LES non-adiabatic conductive, radiative and convective heat fluxes for the a. wall wake, b. minimum shear and c. wall jet cases.

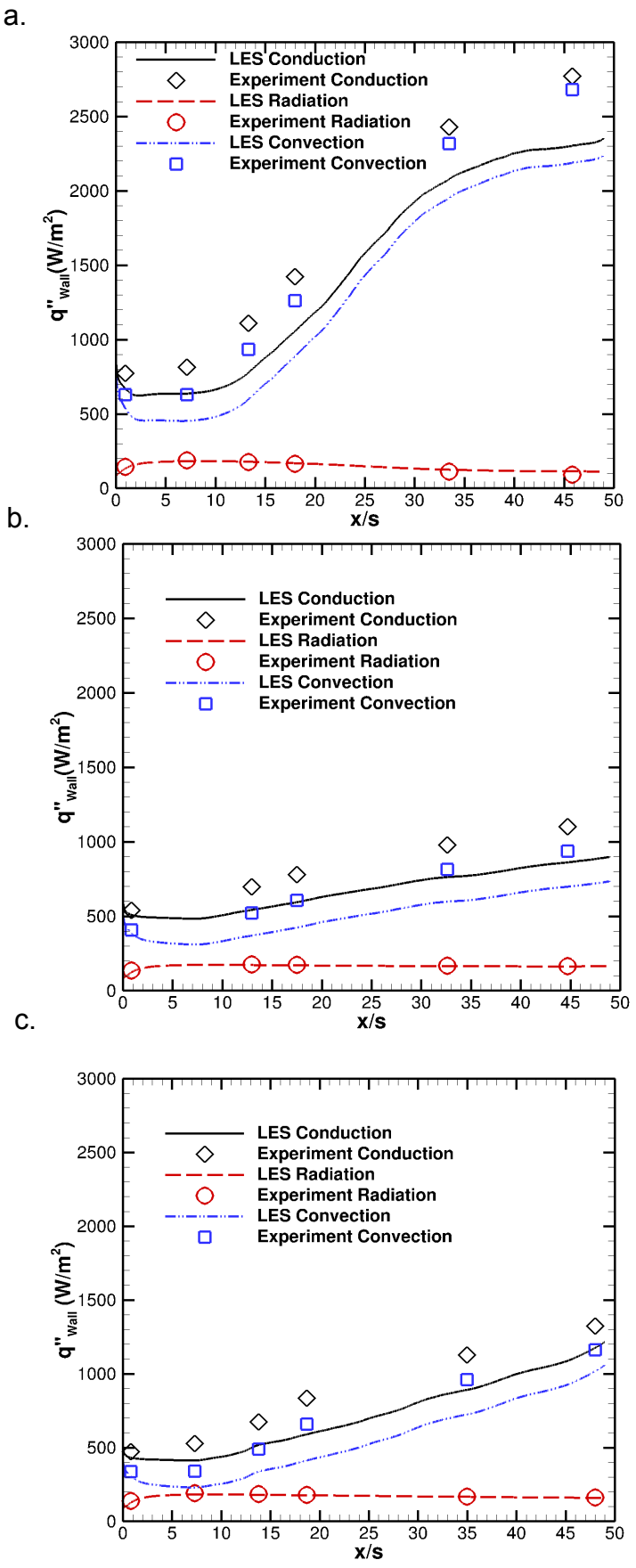

Figure 71- Comparison of the dimensional experimental and LES non-adiabatic conductive, radiative and convective heat fluxes for the a. wall wake, b. minimum shear and c. wall jet cases.

Further observations can be made on the heat flux trends. In the near injector region, the radiation represents a significant portion of the total heat flux, whereas far from injection the radiative heat flux becomes increasingly less important. The wall wake shows the highest non-dimensional heat flux, while the minimum shear once again shows the least. These trends mirror both the adiabatic and non-adiabatic effectiveness trends, where the minimum shear and wall jet cases vastly outperform the wall wake case.

In an attempt to further quantify the heat flux results, consider the dimensional heating rates of the LES simulations given in Table 10. The definitions of the heat rate in the slot (Inflow – Slot), the heat rate over the entire inflow plane (Inflow - Total) and the heat rate occurring through the test plate (Test Plate Wall) are given in Equations 114, 115 and 116, respectively. These heat rates are integral measures of the heat going into or leaving the domain. It is important to note that the sensible enthalpy in these equations is defined relative to 300K and thus affect the magnitude of the heat rates. The inflow heat flux occurs primarily through advection, whereas the heat leaving the wall occurs through conduction at the wall, both of which are reflected in the equations below. For the minimum shear and wall jet cases, the heat flux that occurs through the test plate is just a small portion of the total heat flux entering through the slot and is several orders of magnitude smaller than the total heat flux entering the numerical inflow boundary. The test plate heat rate represents a more significant fraction of the total heat rate entering via the slot advection; this once again confirms that the wall wake should be more affected by cooling and heating through the wall, especially in the near-injector region. In a control volume analysis, the net heating rates must be balanced by the total heat rate that is generated or consumed in the domain. In the near-injector region, due to proximity, the

heating rate of advection through the slot and the net conduction through the wall are dominant. Downstream when the mainstream fluid starts impacting the heat rate at the wall, it is not difficult to see that the wall heat flux will have a minimal impact on the coolant temperature relative to the mainstream advective heating; this finding is evidenced by the size of the total heat rate relative to the test plate heat rate. Hence the experimental findings in §3 show that the effectiveness results between the adiabatic and non-adiabatic cases collapse far from injection are physical because the relative fraction of heating occur from the test plate is a small proportion of the heat coming from the mainstream that will impinge on the wall.

Table 10 – LES non-adiabatic, integral heating rates at the simulated inflow plane and the test plate.

Non-Adiabatic, Integral Heat Rate (W)			
	WW	MS	WJ
Inflow - Slot	12.4	10.7	14.2
Inflow - Total	1320	1280	611
Test Plate Wall	3.41	1.35	1.26

$$\dot{Q}_{slot} = \left(\int_0^{\pi} \int_0^{1} h^*\left(x^* = 0, y^*, z^*\right) \rho^*\left(x^* = 0, y^*, z^*\right) u^*\left(x^* = 0, y^*, z^*\right) dy^* dz^* \right) \rho_0 h_0 U_{slot} s^2 \quad \text{Eqn. (114)}$$

$$\dot{Q}_{Total} = \left(\int_0^{\pi} \int_0^{10} h^*\left(x^* = 0, y^*, z^*\right) \rho^*\left(x^* = 0, y^*, z^*\right) u^*\left(x^* = 0, y^*, z^*\right) dy^* dz^* \right) \rho_0 h_0 U_{slot} s^2 \quad \text{Eqn. (115)}$$

$$\dot{Q}_{TestPlate} = \left(\int_0^{\pi} \int_0^{50} \frac{\partial}{\partial y^*} \left(h^*\left(x^*, y^* = 0, z^*\right) \right) \rho^*\left(x^*, y^* = 0, z^*\right) \alpha^*\left(x^*, y^* = 0, z^*\right) dx^* dz^* \right) \frac{\rho_0 h_0 U_{slot} s^2}{\mathrm{Re}\,\mathrm{Pr}} \quad \text{Eqn. (116)}$$

Finally, the experimental and LES profiles of effectiveness at several streamwise stations are given for the different non-adiabatic shear cases in Figure 72. The agreement between the experimental and LES thermal fields are in much better agreement than occurred for the adiabatic cases. The largest discrepancies occur in the wall wake case very near the wall, far away from injection. As a brief note, the second experimental thermal profile in the minimum shear case is incorrectly offset because the wall was not found correctly when running the experiment. However this offset is unknown and is therefore left unshifted. The excellent agreement between the simulations and the experiments confirm that the LES is capturing the important mixing mechanisms in the slot film cooling configuration. Overall there is some uncertainty associated with the transient interactions of the wall and the thermal flow field. For example, a hot turbulent structure impinging on a wall will cause heating of the wall. Meanwhile the wall, having a higher thermal inertia, reacts slowly to the structure and largely cools the structure. A more physical approach for both the adiabatic and non-adiabatic cases would be to solve the solid heat transfer equations and couple this solver to the LES flow solver. However this transient effect should not overly affect the mean mixing physics even in the near wall region.

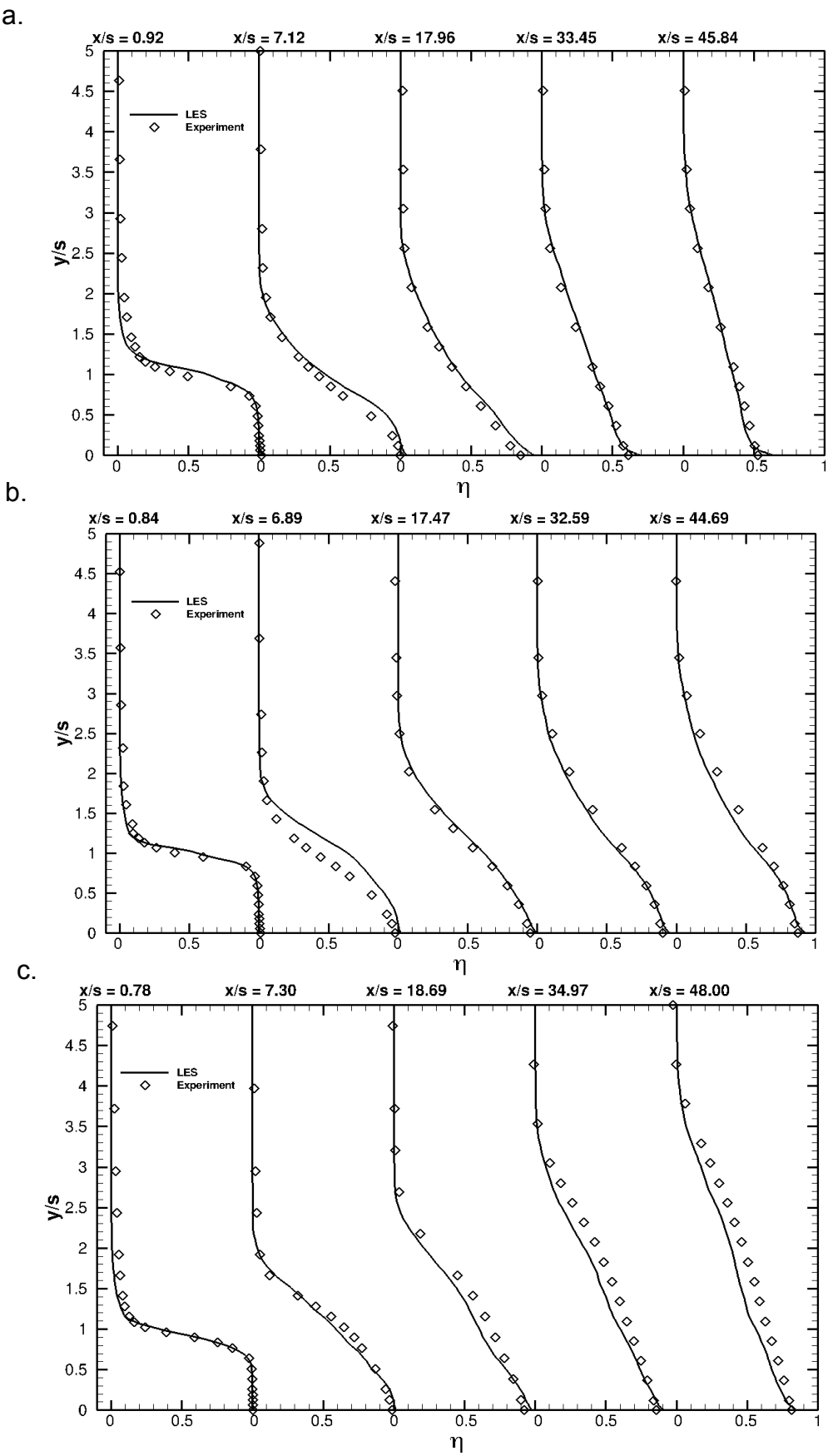

Figure 72 – Experimental and LES profiles of effectiveness for the non-adiabatic a. wall wake, b. minimum shear and c. wall jet cases.

Chapter 5: Conclusions

In this dissertation, tangentially-injected slot film cooling was examined at great length both experimentally and numerically. It was shown that experimentally there is a need for slot film cooling data that comprehensively characterizes the kinematic and thermal flow fields to allow for both detailed insight and CFD model validation. Very few studies provided detailed fluctuating velocity information in addition to mean kinematic and thermal data. These comprehensive experimental studies are not normally given across the three relevant, tangentially-injected slot film cooling shear regimes (VR < 1, VR ~ 1, VR > 1). Similarly heat transfer effects through the wall, involving conduction and radiation, are often neglected, even though adiabatic and non-adiabatic studies are relevant to practical film cooling flows. For example, the wall heat flux equation using the convection coefficient, involves both adiabatic and non-adiabatic temperatures. In this dissertation, experimental data were reported focusing on and measuring:

- Mean and fluctuating kinematic profiles at several streamwise stations for both adiabatic and non-adiabatic walls
- Mean thermal profiles at several streamwise stations for both adiabatic and non-adiabatic walls
- Flow visualization of the turbulent flow structures for adiabatic flows
- Adiabatic effectiveness across the three shear regimes (VR < 1, VR ~ 1, VR > 1)
- Non-adiabatic wall temperatures and heat fluxes across the three shear regimes (VR < 1, VR ~ 1, VR > 1)

- Mean and fluctuating conditions close to the injector plane to allow for CFD inflow generation
- Radiation effects in the adiabatic and non-adiabatic data in the near-wall temperature fields

This study should allow for film cooling engineers to design better correlations and understand film cooling mixing dynamics. A convenient dataset has been created for CFD modelers to validate their codes in a turbulent environment in the presence of strong thermal mixing.

Numerically, LES had yet to be studied in detail for subsonic, tangentially-injected slot film cooling flows. The film cooling literature for LES either focuses on: 1). hole film cooling [43-45, 57-59], which is not canonical, 2). constant density subsonic film cooling [7, 41, 42], which is not accurate in engineering applications or 3). supersonic slot film cooling [46, 48], where the intense, initial turbulent mixing is not nearly as dominant as in subsonic applications. In this dissertation, comprehensive LES parametric studies were performed. This PhD dissertation explored:

- LES wall-resolved, adiabatic simulations across the three shear regimes (VR < 1, VR ~ 1, VR > 1); the adiabatic wall effectiveness was found to agree within 3% of the experiments
- LES wall-resolved, non-adiabatic simulations across the three shear regimes (VR < 1, VR ~ 1, VR > 1); in general the wall effectiveness was found to be within 9% of the experimental data for the wall wake case and within 6% for the minimum shear and wall jet cases

- LES inlet generation parametrics studying inflow techniques and their importance for realistic flow solutions
- LES wall radiation effects for both adiabatic and non-adiabatic simulations; radiation can change the wall effectiveness by about 3% in the near-field for the adiabatic wall wake case
- LES validation against experimental data was presented in this dissertation

To this author's knowledge no LES non-adiabatic slot film cooling studies had been performed previously. Similarly no variable density, wall jet LES film cooling studies had been performed. Also, no studies have involved the prediction and study of LES film cooling in the presence of radiation at the wall. This research, which incorporates all of these studies, therefore, constitutes a major contribution to the film cooling and general LES literature.

Future Work

Overall much work potentially remains to fully study tangentially-injected slot film cooling. Experimentally, if radiation is present, more measurements can be made, including measurement of all the wind tunnel walls with high spatial fidelity. This would allow for a higher fidelity radiation solver to be implemented. In the non-adiabatic experiments, different heat flux strengths should be considered to examine the effect of radiatively, convectively and conductively dominated film cooling regimes. At the wall, fine resolution measurements in both temperature and velocity would also aid CFD validation and allow profiles to be cast using wall scaling. This type of scaling would

allow for the effects of the wall and mixing layer to be more easily examined. Another part of the experimental data that remains to be analyzed is the RMS of temperature fluctuations, which provides an estimate of the strength of thermal fluctuations. Additionally new PIV techniques involving phosphorescence are now capable of instantaneously measuring the temperature and velocity, allowing for turbulent cross stresses in the energy equation to be captured.

Numerically, DNS studies of slot film cooling would provide a budget of turbulent terms in the RANS equations, allowing RANS modelers to construct turbulence models for film cooling flows. The turbulent eddies near the splitter-plate, also, would be fully captured, leading to an even better prediction of the turbulent mixing in this region. An analysis of the sub-grid scale models could also be performed by comparing the full DNS, a filtered DNS and the wall-resolved LES solutions. In terms of LES simulations of film cooling, wall modeling should be performed for the adiabatic and non-adiabatic cases to determine the feasibility and the cost-savings of wall-modeled LES over wall-resolved LES simulations. This wall-modeling study of film cooling flows could examine the effect of using equilibrium models, or wall models that solve the spatially coupled boundary layer equations. In the non-adiabatic simulations, a transient, solid, conduction heat transfer solver coupled to the CFD solver could help simulate with higher-fidelity the physics in the near-wall region. This coupled solver would provide more realistic heat transfer measurements and thermal breakdown very close to the wall. Lastly, higher-fidelity radiation techniques that solve the radiative transfer equation could be implemented to examine film cooling in the presence of participating media.

Appendix A – Discretized LES BLAC Equations in 2D

Scalar Equation

$$\frac{\rho_{i,j}^{n+1,it+1}\phi_{i,j}^{n+1,it+1}-\rho_{i,j}^{n}\phi_{i,j}^{n}}{\Delta t}+\left[\begin{array}{l}\dfrac{\frac{1}{4}\left(\rho_{i+1,j}^{n+1,it}+\rho_{i,j}^{n+1,it}+\rho_{i+1,j}^{n}+\rho_{i,j}^{n}\right)u_{i,j}^{n+1/2,it}\,\frac{1}{4}\left(\phi_{i+1,j}^{n+1,it}+\phi_{i,j}^{n+1,it}+\phi_{i+1,j}^{n}+\phi_{i,j}^{n}\right)}{\Delta x}-\\ \dfrac{\frac{1}{4}\left(\rho_{i,j}^{n+1,it}+\rho_{i-1,j}^{n+1,it}+\rho_{i,j}^{n}+\rho_{i-1,j}^{n}\right)u_{i-1,j}^{n+1/2,it}\,\frac{1}{4}\left(\phi_{i,j}^{n+1,it}+\phi_{i-1,j}^{n+1,it}+\phi_{i,j}^{n}+\phi_{i-1,j}^{n}\right)}{\Delta x}\end{array}\right]$$

$$+\left[\begin{array}{l}\dfrac{\frac{1}{4}\left(\rho_{i,j+1}^{n+1,it}+\rho_{i,j}^{n+1,it}+\rho_{i,j+1}^{n}+\rho_{i,j}^{n}\right)v_{i,j}^{n+1/2,it}\,\frac{1}{4}\left(\phi_{i,j+1}^{n+1,it}+\phi_{i,j}^{n+1,it}+\phi_{i,j+1}^{n}+\phi_{i,j}^{n}\right)}{\Delta y}-\\ \dfrac{\frac{1}{4}\left(\rho_{i,j}^{n+1,it}+\rho_{i,j-1}^{n+1,it}+\rho_{i,j}^{n}+\rho_{i,j-1}^{n}\right)v_{i,j-1}^{n+1/2,it}\,\frac{1}{4}\left(\phi_{i,j}^{n+1,it}+\phi_{i,j-1}^{n+1,it}+\phi_{i,j}^{n}+\phi_{i,j-1}^{n}\right)}{\Delta y}\end{array}\right]$$

$$=\frac{1}{\Delta x}\left\{\begin{array}{l}\left[\begin{array}{l}\frac{1}{4}\left(\rho_{i+1,j}^{n+1,it}\alpha_{L,i+1,j}^{n+1,it}+\rho_{i,j}^{n+1,it}\alpha_{L,i,j}^{n+1,it}+\rho_{i+1,j}^{n}\alpha_{L,i+1,j}^{n}+\rho_{i,j}^{n}\alpha_{L,i,j}^{n}\right)+\\ \frac{1}{4}\left(\left(\rho_{i+1,j}^{n+1,it}+\rho_{i+1,j}^{n}\right)\alpha_{T,i+1,j}^{n+1/2,it}+\left(\rho_{i,j}^{n+1,it}+\rho_{i,j}^{n}\right)\alpha_{T,i,j}^{n+1/2,it}\right)\end{array}\right]\left[\dfrac{\frac{1}{2}\left(\phi_{i+1,j}^{n+1,it}+\phi_{i+1,j}^{n}\right)-\frac{1}{2}\left(\phi_{i,j}^{n+1,it}+\phi_{i,j}^{n}\right)}{\Delta x}\right]-\\ \left[\begin{array}{l}\frac{1}{4}\left(\rho_{i,j}^{n+1,it}\alpha_{L,i,j}^{n+1,it}+\rho_{i-1,j}^{n+1,it}\alpha_{L,i-1,j}^{n+1,it}+\rho_{i,j}^{n}\alpha_{L,i,j}^{n}+\rho_{i-1,j}^{n}\alpha_{L,i-1,j}^{n}\right)+\\ \frac{1}{4}\left(\left(\rho_{i,j}^{n+1,it}+\rho_{i,j}^{n}\right)\alpha_{T,i,j}^{n+1/2,it}+\left(\rho_{i-1,j}^{n+1,it}+\rho_{i-1,j}^{n}\right)\alpha_{T,i-1,j}^{n+1/2,it}\right)\end{array}\right]\left[\dfrac{\frac{1}{2}\left(\phi_{i,j}^{n+1,it}+\phi_{i,j}^{n}\right)-\frac{1}{2}\left(\phi_{i-1,j}^{n+1,it}+\phi_{i-1,j}^{n}\right)}{\Delta x}\right]\end{array}\right\}$$

$$+\frac{1}{\Delta y}\left\{\begin{array}{l}\left[\begin{array}{l}\frac{1}{4}\left(\rho_{i,j+1}^{n+1,it}\alpha_{L,i,j+1}^{n+1,it}+\rho_{i,j}^{n+1,it}\alpha_{L,i,j}^{n+1,it}+\rho_{i,j+1}^{n}\alpha_{L,i,j+1}^{n}+\rho_{i,j}^{n}\alpha_{L,i,j}^{n}\right)+\\ \frac{1}{4}\left(\left(\rho_{i,j+1}^{n+1,it}+\rho_{i,j+1}^{n}\right)\alpha_{T,i,j+1}^{n+1/2,it}+\left(\rho_{i,j}^{n+1,it}+\rho_{i,j}^{n}\right)\alpha_{T,i,j}^{n+1/2,it}\right)\end{array}\right]\left[\dfrac{\frac{1}{2}\left(\phi_{i,j+1}^{n+1,it+1}+\phi_{i,j+1}^{n}\right)-\frac{1}{2}\left(\phi_{i,j}^{n+1,it+1}+\phi_{i,j}^{n}\right)}{\Delta y}\right]-\\ \left[\begin{array}{l}\frac{1}{4}\left(\rho_{i,j}^{n+1,it}\alpha_{L,i,j}^{n+1,it}+\rho_{i,j-1}^{n+1,it}\alpha_{L,i,j-1}^{n+1,it}+\rho_{i,j}^{n}\alpha_{L,i,j}^{n}+\rho_{i,j-1}^{n}\alpha_{L,i,j-1}^{n}\right)+\\ \frac{1}{4}\left(\left(\rho_{i,j}^{n+1,it}+\rho_{i,j}^{n}\right)\alpha_{T,i,j}^{n+1/2,it}+\left(\rho_{i,j-1}^{n+1,it}+\rho_{i,j-1}^{n}\right)\alpha_{T,i,j-1}^{n+1/2,it}\right)\end{array}\right]\left[\dfrac{\frac{1}{2}\left(\phi_{i,j}^{n+1,it+1}+\phi_{i,j}^{n}\right)-\frac{1}{2}\left(\phi_{i,j-1}^{n+1,it+1}+\phi_{i,j-1}^{n}\right)}{\Delta y}\right]\end{array}\right\}$$

Streamwise Momentum Equation

$$\frac{r^{*}_{1,i,j}-r^{n-1/2}_{1,i,j}}{\Delta t}+\frac{1}{\Delta x}\left[\begin{array}{l}\frac{1}{4}\left(u^{n+1/2,it}_{i+1,j}+u^{n+1/2,it}_{i,j}+u^{n-1/2}_{i+1,j}+u^{n-1/2}_{i,j}\right)\frac{1}{4}\left(r^{n+1/2,it}_{1,i+1,j}+r^{n+1/2,it}_{1,i,j}+r^{n-1/2}_{1,i+1,j}+r^{n-1/2}_{1,i,j}\right)-\\ \frac{1}{4}\left(u^{n+1/2,it}_{i,j}+u^{n+1/2,it}_{i-1,j}+u^{n-1/2}_{i,j}+u^{n-1/2}_{i-1,j}\right)\frac{1}{4}\left(r^{n+1/2,it}_{1,i,j}+r^{n+1/2,it}_{1,i-1,j}+r^{n-1/2}_{1,i,j}+r^{n-1/2}_{1,i-1,j}\right)\end{array}\right]$$

$$+\frac{1}{\Delta y}\left[\begin{array}{l}\frac{1}{4}\left(u^{n+1/2,it}_{i,j+1}+u^{n+1/2,it}_{i,j}+u^{n-1/2}_{i,j+1}+u^{n-1/2}_{i,j}\right)\frac{1}{4}\left(r^{n+1/2,it}_{2,i+1,j}+r^{n+1/2,it}_{2,i,j}+r^{n-1/2}_{2,i+1,j}+r^{n-1/2}_{2,i,j}\right)-\\ \frac{1}{4}\left(u^{n+1/2,it}_{i,j}+u^{n+1/2,it}_{i,j-1}+u^{n-1/2}_{i,j}+u^{n-1/2}_{i,j-1}\right)\frac{1}{4}\left(r^{n+1/2,it}_{2,i+1,j-1}+r^{n+1/2,it}_{2,i,j-1}+r^{n-1/2}_{2,i+1,j-1}+r^{n-1/2}_{2,i,j-1}\right)\end{array}\right]=$$

$$-\frac{\left(p^{n+1/2,it}_{i+1,j}-p^{n+1/2,it}_{i,j}\right)}{\Delta x}+\frac{1}{\Delta x}\left\{\begin{array}{l}2\left(\mu^{n}_{L,i+1,j}+\frac{\mu^{n+1/2,it}_{T,i+1,j}+\mu^{n-1/2}_{T,i+1,j}}{2}\right)\\ \left[\begin{array}{l}\frac{\frac{1}{2}\left(u^{n+1/2,it}_{i+1,j}+u^{n-1/2}_{i+1,j}\right)-\frac{1}{2}\left(u^{n+1/2,it}_{i,j}+u^{n-1/2}_{i,j}\right)}{\Delta x}-\frac{1}{3}\left(\frac{\frac{1}{2}\left(u^{n+1/2,it}_{i+1,j}+u^{n-1/2}_{i+1,j}\right)-\frac{1}{2}\left(u^{n+1/2,it}_{i,j}+u^{n-1/2}_{i,j}\right)}{\Delta x}\right)\\ -\frac{1}{3}\left(\frac{\frac{1}{2}\left(v^{n+1/2,it}_{i+1,j}+v^{n-1/2}_{i+1,j}\right)-\frac{1}{2}\left(v^{n+1/2,it}_{i+1,j-1}+v^{n-1/2}_{i+1,j-1}\right)}{\Delta y}\right)\end{array}\right]\end{array}\right\}$$

$$-\frac{1}{\Delta x}\left\{\begin{array}{l}2\left(\mu^{n}_{L,i,j}+\frac{\mu^{n+1/2,it}_{T,i,j}+\mu^{n-1/2}_{T,i,j}}{2}\right)\\ \left[\begin{array}{l}\frac{\frac{1}{2}\left(u^{n+1/2,it}_{i,j}+u^{n-1/2}_{i,j}\right)-\frac{1}{2}\left(u^{n+1/2,it}_{i-1,j}+u^{n-1/2}_{i-1,j}\right)}{\Delta x}-\frac{1}{3}\left(\frac{\frac{1}{2}\left(u^{n+1/2,it}_{i,j}+u^{n-1/2}_{i,j}\right)-\frac{1}{2}\left(u^{n+1/2,it}_{i-1,j}+u^{n-1/2}_{i-1,j}\right)}{\Delta x}\right)\\ -\frac{1}{3}\left(\frac{\frac{1}{2}\left(v^{n+1/2,it}_{i,j}+v^{n-1/2}_{i,j}\right)-\frac{1}{2}\left(v^{n+1/2,it}_{i,j-1}+v^{n-1/2}_{i,j-1}\right)}{\Delta y}\right)\end{array}\right]\end{array}\right\}+$$

$$\frac{1}{\Delta y}\left\{\begin{array}{l}\left[\left(\frac{\mu^{n}_{L,i,j}+\mu^{n}_{L,i+1,j}+\mu^{n}_{L,i,j+1}+\mu^{n}_{L,i+1,j+1}}{4}\right)+\left(\frac{\mu^{n+1/2,it}_{T,i,j}+\mu^{n+1/2,it}_{T,i+1,j}+\mu^{n+1/2,it}_{T,i,j+1}+\mu^{n+1/2,it}_{T,i+1,j+1}+\mu^{n-1/2}_{T,i,j}+\mu^{n-1/2}_{T,i+1,j}+\mu^{n-1/2}_{T,i,j+1}+\mu^{n-1/2}_{T,i+1,j+1}}{8}\right)\right]\\ \left[\begin{array}{l}\frac{\frac{1}{2}\left(v^{n+1/2,it}_{i+1,j}+v^{n-1/2}_{i+1,j}\right)-\frac{1}{2}\left(v^{n+1/2,it}_{i,j}+v^{n-1/2}_{i,j}\right)}{\Delta x}+\frac{\frac{1}{2}\left(r^{*}_{1,i,j+1}\Big/\left(\rho^{A}\right)+u^{n-1/2}_{i,j+1}\right)-\frac{1}{2}\left(r^{*}_{1,i,j}\Big/\left(\rho^{B}\right)+u^{n-1/2}_{i,j}\right)}{\Delta y}\end{array}\right]\end{array}\right\}$$

$$-\frac{1}{\Delta y}\left\{\begin{array}{l}\left[\left(\frac{\mu^{n}_{L,i,j}+\mu^{n}_{L,i+1,j}+\mu^{n}_{L,i,j-1}+\mu^{n}_{L,i+1,j-1}}{4}\right)+\left(\frac{\mu^{n+1/2,it}_{T,i,j}+\mu^{n+1/2,it}_{T,i+1,j}+\mu^{n+1/2,it}_{T,i,j-1}+\mu^{n+1/2,it}_{T,i+1,j-1}+\mu^{n-1/2}_{T,i,j}+\mu^{n-1/2}_{T,i+1,j}+\mu^{n-1/2}_{T,i,j-1}+\mu^{n-1/2}_{T,i+1,j-1}}{8}\right)\right]\\ \left[\begin{array}{l}\frac{\frac{1}{2}\left(v^{n+1/2,it}_{i+1,j-1}+v^{n-1/2}_{i+1,j-1}\right)-\frac{1}{2}\left(v^{n+1/2,it}_{i,j-1}+v^{n-1/2}_{i,j-1}\right)}{\Delta x}+\frac{\frac{1}{2}\left(r^{*}_{1,i,j}\Big/\left(\rho^{B}\right)+u^{n-1/2}_{i,j}\right)-\frac{1}{2}\left(r^{*}_{1,i,j-1}\Big/\left(\rho^{C}\right)+u^{n-1/2}_{i,j-1}\right)}{\Delta y}\end{array}\right]\end{array}\right\}$$

$$\rho^{A}=\left(\frac{\rho^{n+1,it+1}_{i,j+1}+\rho^{n+1,it+1}_{i+1,j+1}+\rho^{n}_{i,j+1}+\rho^{n}_{i+1,j+1}}{4}\right)$$

$$\rho^{B}=\left(\frac{\rho^{n+1,it+1}_{i,j}+\rho^{n+1,it+1}_{i+1,j}+\rho^{n}_{i,j}+\rho^{n}_{i+1,j}}{4}\right)$$

$$\rho^{C}=\left(\frac{\rho^{n+1,it+1}_{i,j-1}+\rho^{n+1,it+1}_{i+1,j-1}+\rho^{n}_{i,j-1}+\rho^{n}_{i+1,j-1}}{4}\right)$$

Appendix B – Non Adiabatic Velocity and Temperatures

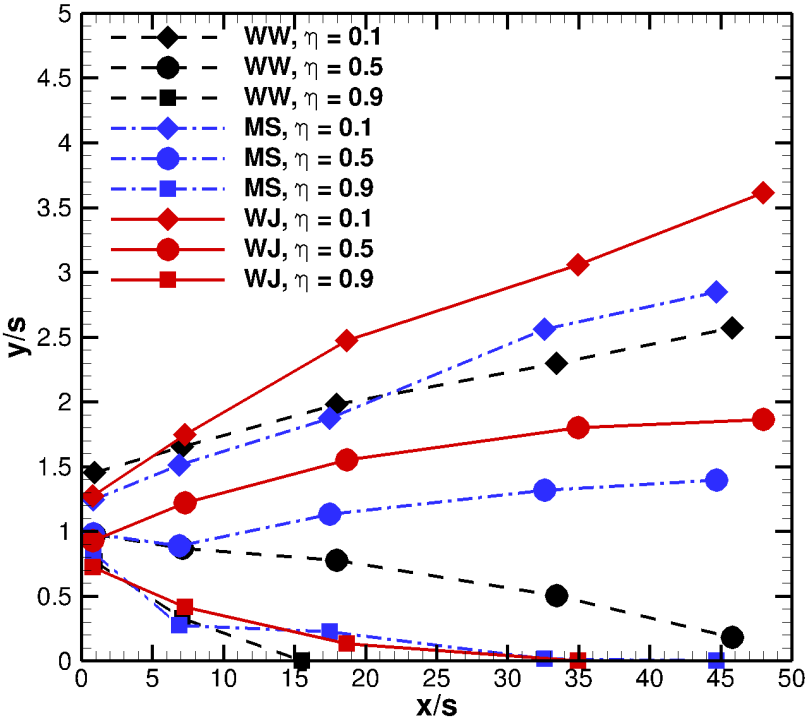

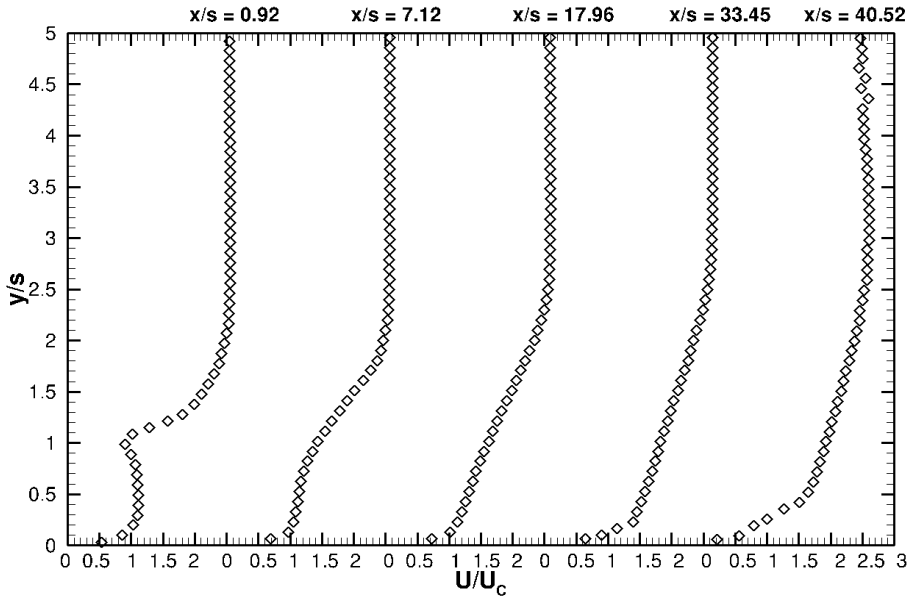
x/s = 0.92
x/s = 7.12
x/s = 17.96
x/s = 33.45
x/s = 40.52
y/s
U/U_C

WW

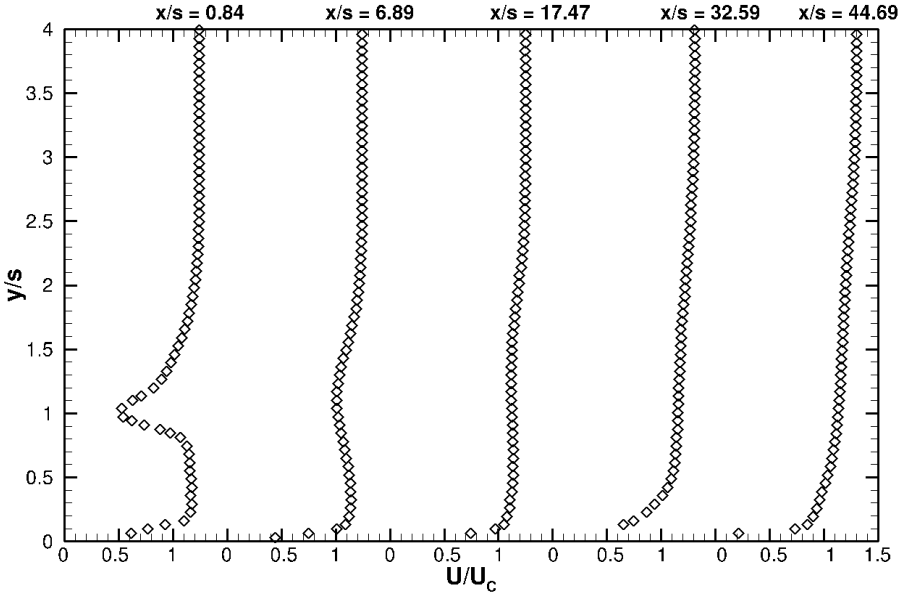
x/s = 0.84
x/s = 6.89
x/s = 17.47
x/s = 32.59
x/s = 44.69
y/s
U/U_C

MS

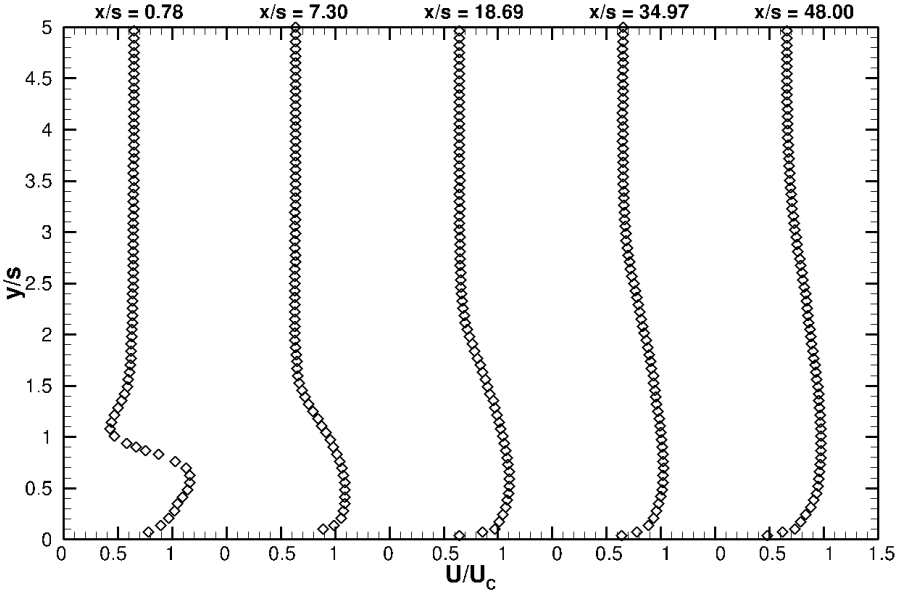
x/s = 0.78
x/s = 7.30
x/s = 18.69
x/s = 34.97
x/s = 48.00
y/s
U/U_C

WJ

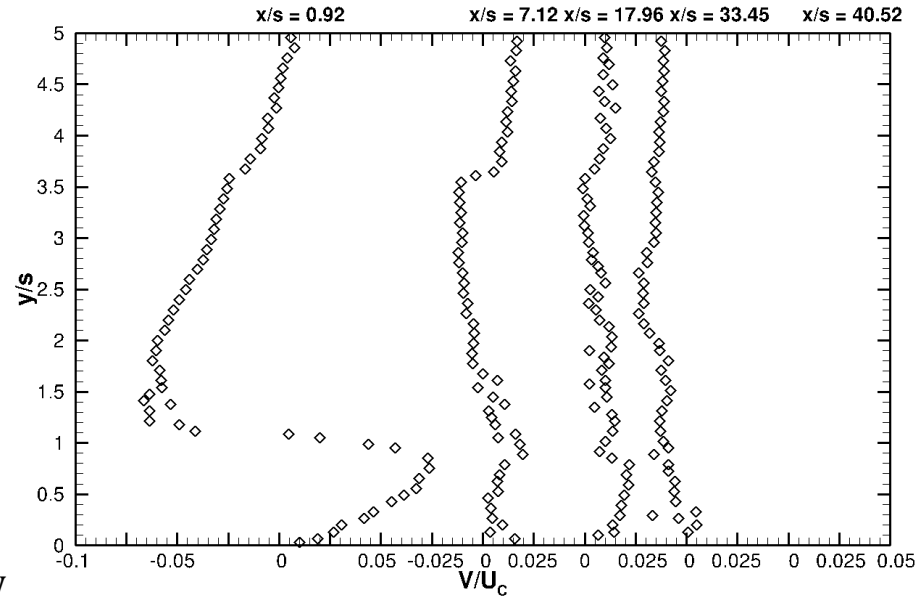
x/s = 0.92
x/s = 7.12 x/s = 17.96 x/s = 33.45
x/s = 40.52
y/s
V/U_c

WW

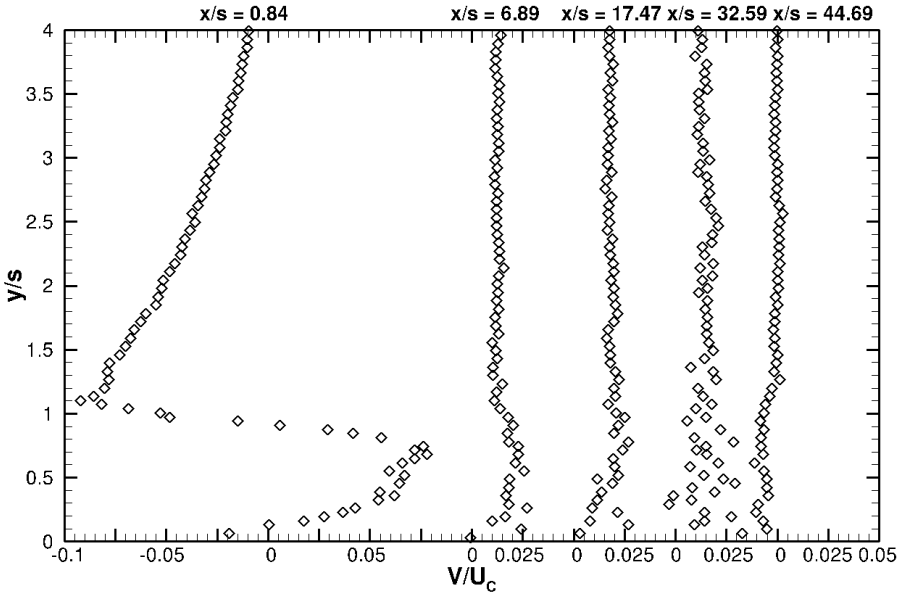
x/s = 0.84
x/s = 6.89
x/s = 17.47 x/s = 32.59 x/s = 44.69
y/s
V/U_c

MS

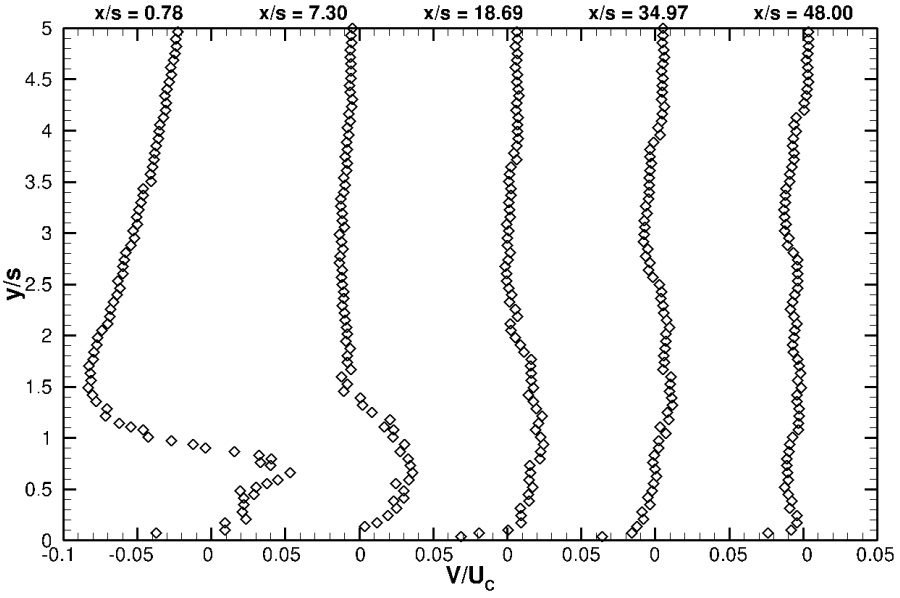
x/s = 0.78
x/s = 7.30
x/s = 18.69
x/s = 34.97
x/s = 48.00
y/s
V/U_c

WJ

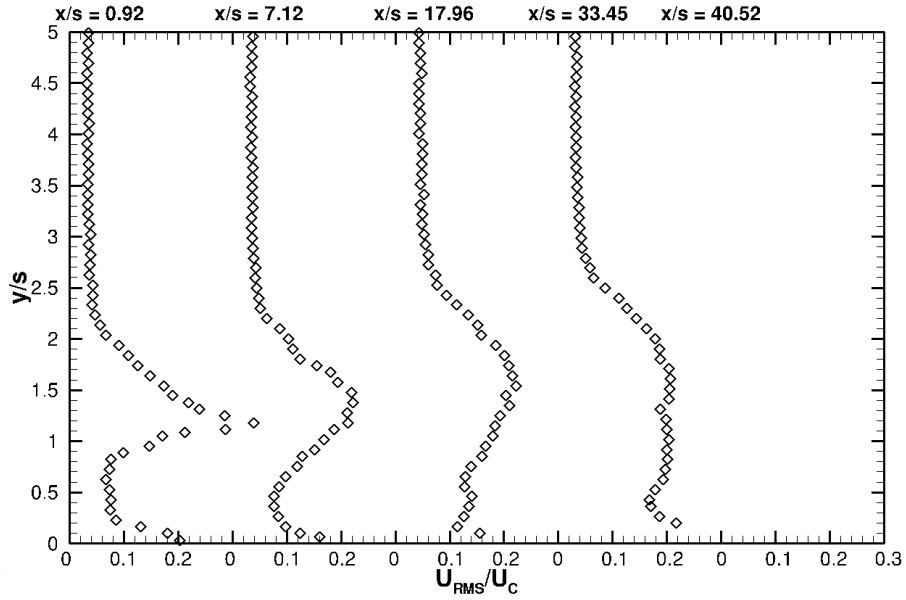
x/s = 0.92
x/s = 7.12
x/s = 17.96
x/s = 33.45
x/s = 40.52
y/s
U_{RMS}/U_C

WW

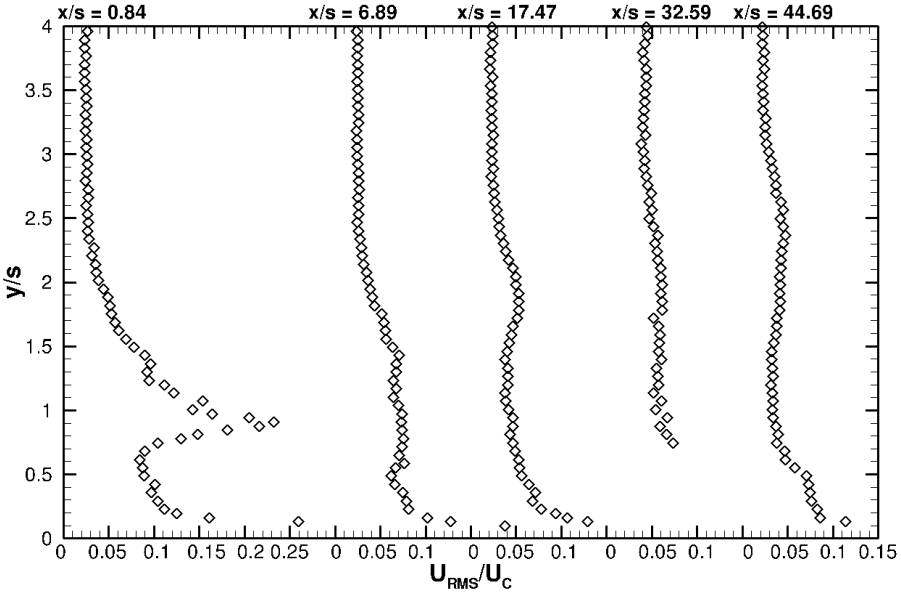
x/s = 0.84
x/s = 6.89
x/s = 17.47
x/s = 32.59
x/s = 44.69
y/s
U_{RMS}/U_C

MS

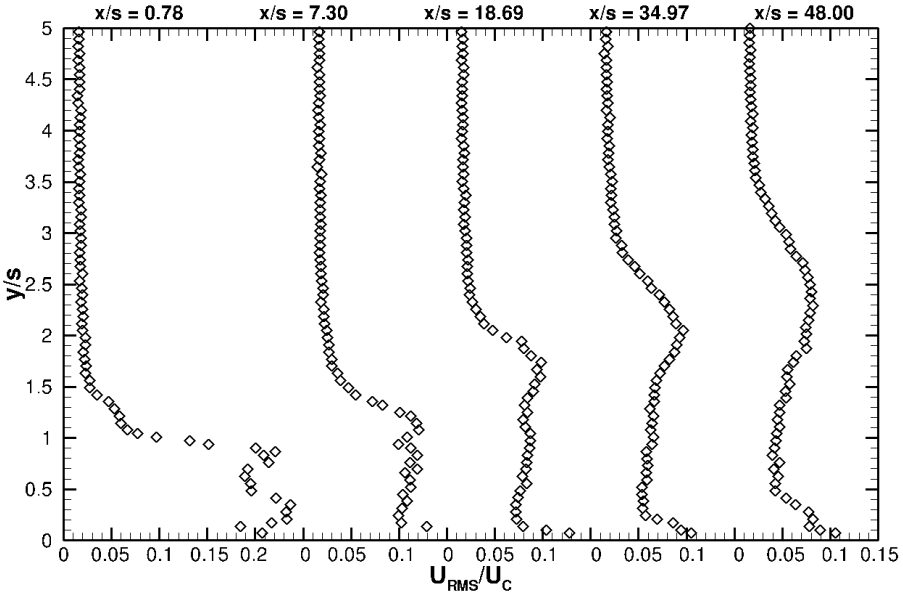
x/s = 0.78
x/s = 7.30
x/s = 18.69
x/s = 34.97
x/s = 48.00
y/s
U_{RMS}/U_C

WJ

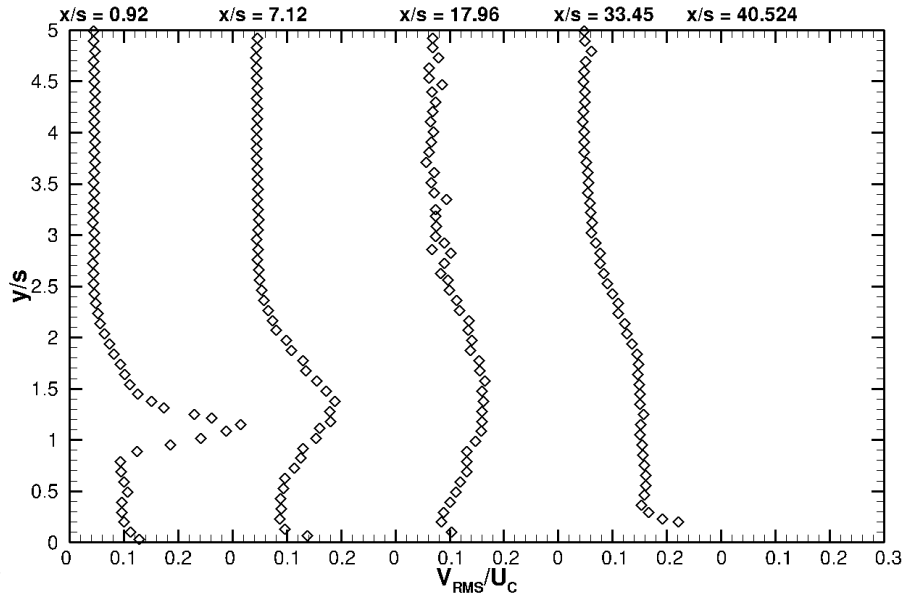
x/s = 0.92
x/s = 7.12
x/s = 17.96
x/s = 33.45
x/s = 40.524
y/s
V_{RMS}/U_C

WW

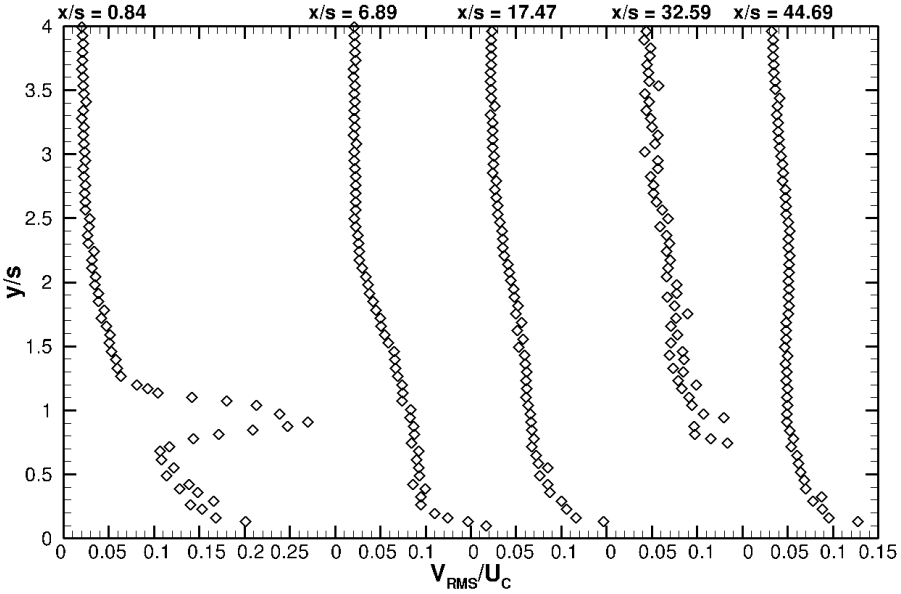
x/s = 0.84
x/s = 6.89
x/s = 17.47
x/s = 32.59
x/s = 44.69
y/s
V_{RMS}/U_C

MS

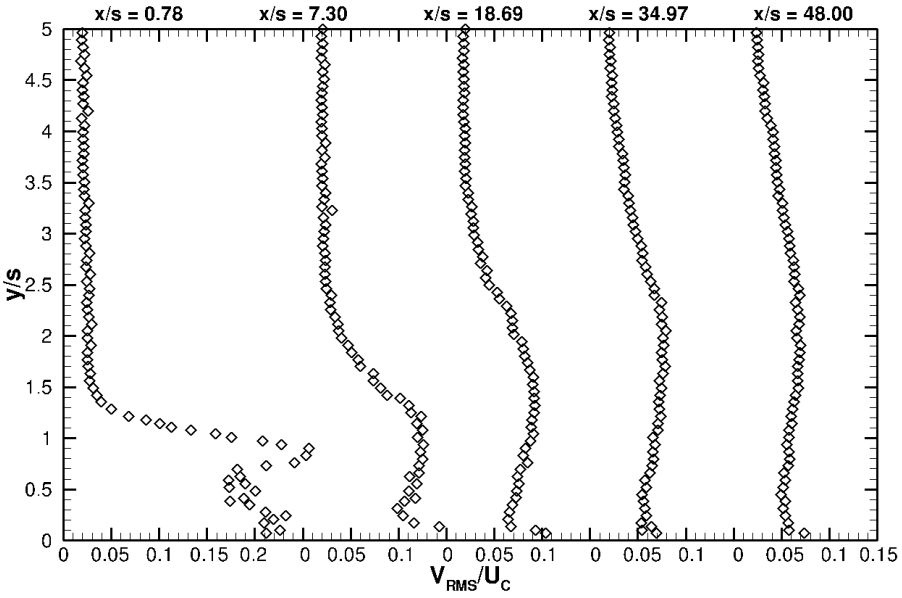
x/s = 0.78
x/s = 7.30
x/s = 18.69
x/s = 34.97
x/s = 48.00
y/s
V_{RMS}/U_C

WJ

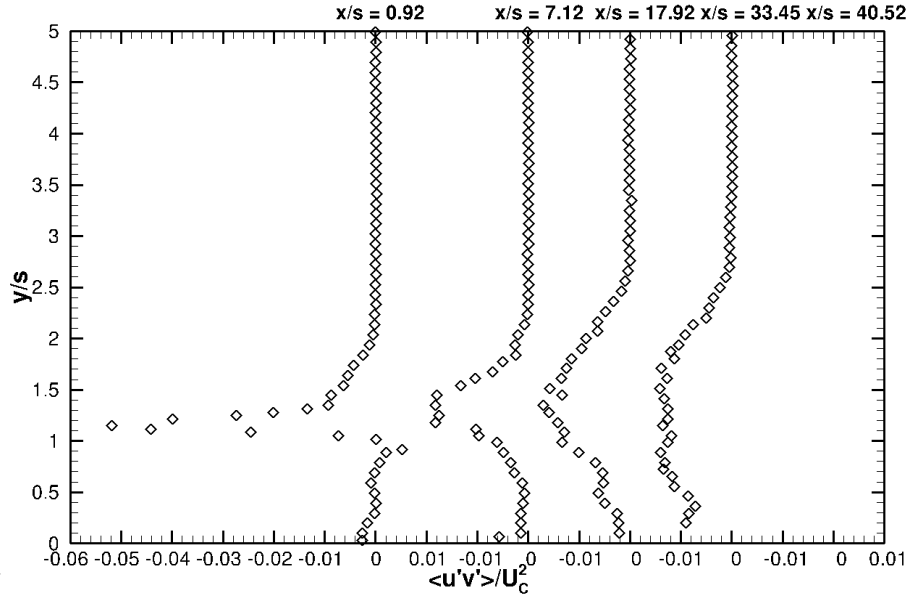
x/s = 0.92
x/s = 7.12
x/s = 17.92
x/s = 33.45
x/s = 40.52
y/s
<u'v'>/U_c^2

WW

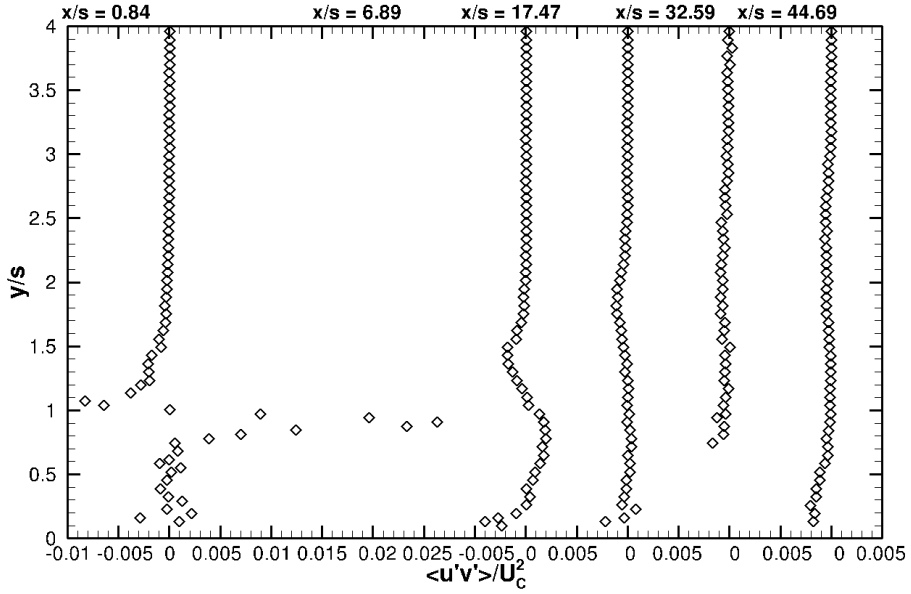
x/s = 0.84
x/s = 6.89
x/s = 17.47
x/s = 32.59
x/s = 44.69
y/s
<u'v'>/U_c^2

MS

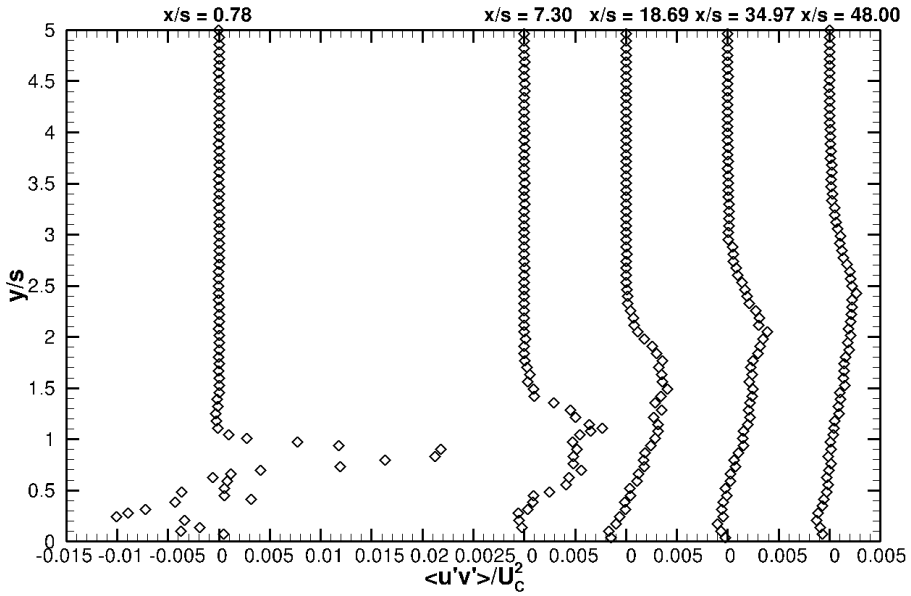
x/s = 0.78
x/s = 7.30
x/s = 18.69
x/s = 34.97
x/s = 48.00
y/s
<u'v'>/U_c^2

WJ

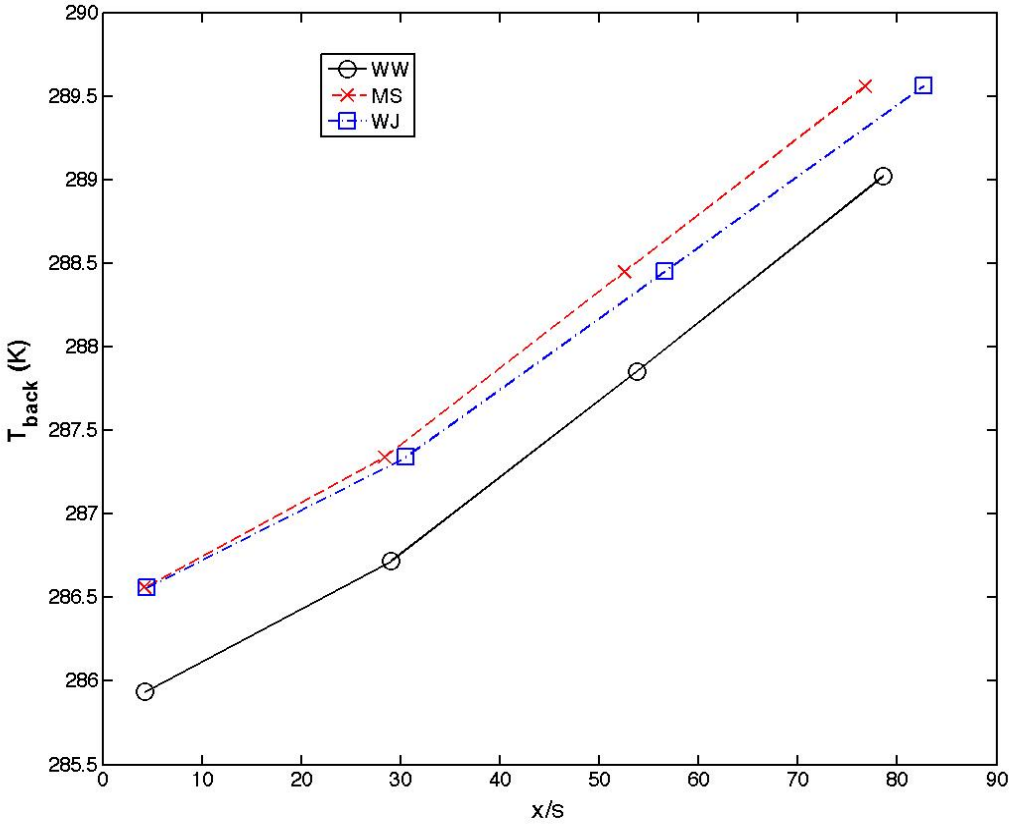
WW
MS
WJ
T_{back} (K)
x/s
290
289.5
289
288.5
288
287.5
287
286.5
286
285.5
0
10
20
30
40
50
60
70
80
90

Appendix C – Additional Adiabatic LES plots featuring wall scaling

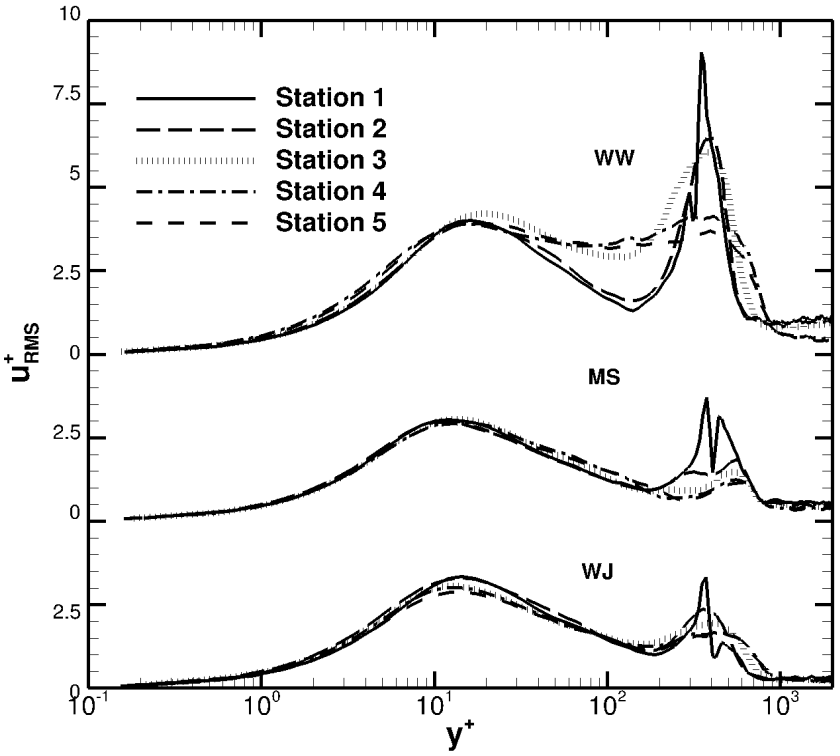

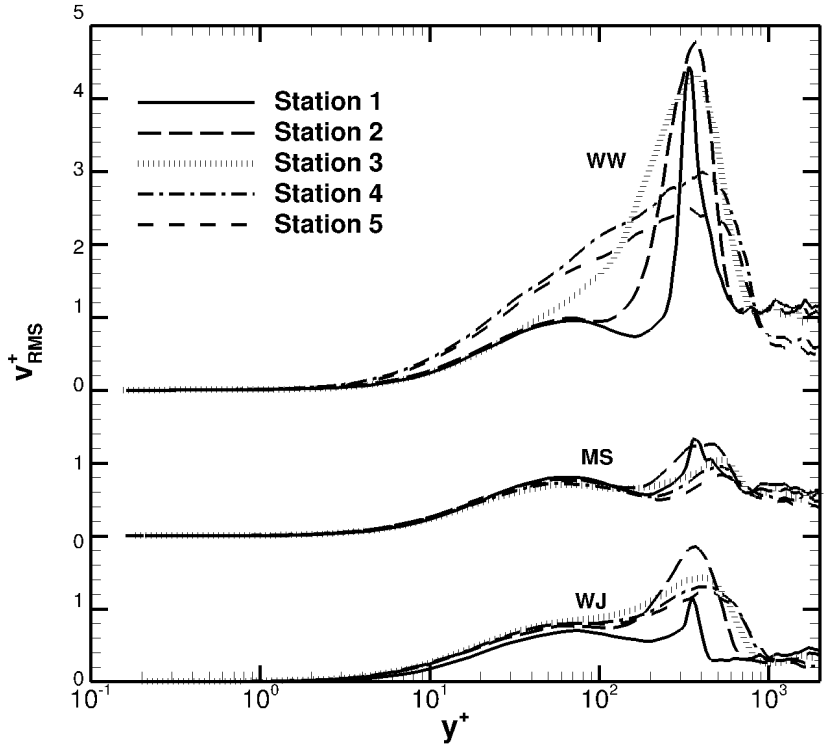

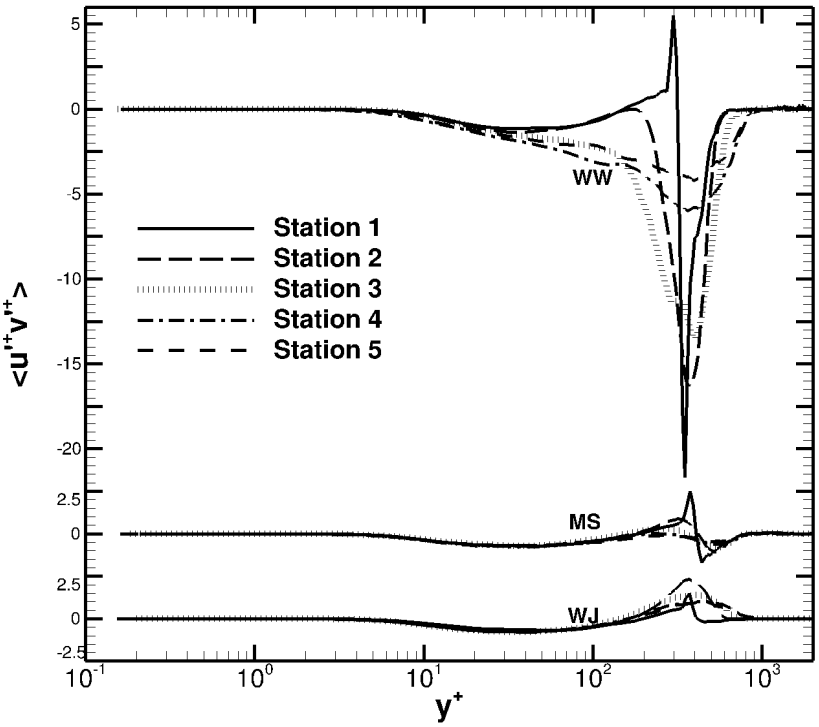
Station 1
Station 2
Station 3
Station 4
Station 5
WW
MS
WJ
<u'+v'+>
y+

References

[1] Research and Innovative Technology Administration "Airline Fuel Cost and Consumption (U.S. Carriers – Scheduled)" Bureau of Transportation Statistics. http://www.transtats.bts.gov/fuel.asp [retrieved 12/13/12]

[2]Lefebvre, A. H., *Gas Turbine Combustion*, Taylor & Francis, 1983

[3] Kaku, M. "The Cost of Space Exploration" Forbes.com LLC. Date of publication: 07-16-2009. http://www.forbes.com/2009/07/16/apollo-moon-landing-anniversary-opinions-contributors-cost-money.html [retrieved 12/13/12]

[4] Sutton , G.P., "Rocket Propulsion Elements," John Wiley and Sons, New York, 5th edition, 1986.

[5] Raffan, F., Experimental Characterization of Slot Film Cooling Flows With Minimally Intrusive Diagnostics, MS Thesis, University of Maryland at College Park, December 2008.

[6] NASA. "Constellation Program: America's Fleet of Next-Generation Launch Vehicles", FS-2006-07-84-MSFC Pub 8-40599 http://www.nasa.gov/pdf/151420main_aresV_factsheet.pdf [retrieved 12/13/12]

[7] Cruz, C., Experimental and Numerical Characterization of Turbulent Slot Film Cooling, PhD Dissertation, University of Maryland at College Park, May 2008.

[8] Wieghardt, K. "Hot Air Discharge for De-Icing", AAF Translation F-TS 919RE, 1946.

[9] Stollery, J. El-Ehwany, A. "A Note On The Use Of A Boundary-Layer Model For Correlating Film-Cooling Data". *Int. J. Heat Mass Transfer.* Vol. 8, pp. 55-65. 1965

[10] Stollery, J. El-Ehwany, A. "Shorter Communication: On The Use of a Boundary-Layer Model For Correlating Film Cooling Data*" Int. J. Heat Mass Transfer*. Vol. 10., pp. 101-105. 1967.

[11] Tribus, M.Klein, J. "Forced Convection From Non-Isothermal Surfaces." Heat Transfer, a Symposium, University of Michigan Press, Ann Arbor, MI, 1953, pp. 211-235.

[12] Hartnett, J. Birkebak, R. Eckert, E. "Velocity distributions, Temperature Distributions, Effectiveness and Heat Transfer for Air Injected Through a Tangential Slot Into a Turbulent Boundary layer" *Journal of Heat Transfer*. August 1961, Vol. 83, pp. 293-306.

[13] Hatch, J. Papell, S. "Use of a Theoretical Flow Model to Correlate Data for Film Cooling or Heating an Adiabatic Wall by Tangential Injection of Gases of Different Fluid Properties" NASA Technical Note D-130. November 1959.

[14] Papell, S. Trout, A. "Experimental Investigation of Air Film Cooling Applied to an Adiabatic Wall by Means of an Axially Discharging Slot," NASA TND-9, August 1959.

[15] Papell, S., "Effect on Gaseous Film Cooling of Coolant Injection through Angled Slots and Normal Holes," NASA TN-D299, September 1960.

[16] Ballal, D. Lefebvre, A. "Film Cooling Effectiveness in the Near Slot Region" *Journal of Heat Transfer*, May 1973, Vol. 93, pp. 165-166.

[17] Simon, F. F., "Jet Model for Slot Film Cooling With Effect of Free-Stream and Coolant Turbulence", NASA TP 2655, October 1986.

[18] Marek, C. Tacina, R. "Effect of Free-Stream Turbulence on FilmCooling," NASA TN D-7958, June 1975.

[19] Sceza, S. Experimental Investigation of Convective Heat Transfer to Air from a Flat Plate with a Stepwise Discontinuous Surface Temperature. M.S. Thesis. University of California, Berkely. 1951.

[20] Goldstein, R. J., "Film Cooling", *Advances in Heat Transfer*, vol. 7, Academic Press, New York, 1971. Pp. 321-378.

[21] Burns, W. Stollery, J. "The Influence Foreign Gas Injection and Slot Geometry on Film Cooling Effectiveness", *International Journal of Heat and Mass Transfer*. 1969, Vol. 12, No. 9, pp. 935-951.

[22] Kacker, S. Whitelaw, J. "An Experimental Investigation of the Influence of Slot-Lip-Thickness on the Impervious-Wall Effectiveness of the Uniform-Density, Two-Dimensional Wall Jet", *Int. J. Heat Mass Transfer*. Vol. 12, pp. 1196-1201. 1969.

[23] Pederson, D. Eckert, E. Goldstein, R. "Film Cooling With Large Density Differences Between the Mainstream and the Secondary Fluid Measured by the Heat-Mass Transfer Analogy" *Journal of Heat Transfer*. Vol. 99. Nov. 1977. Pp. 621-627.

[24] Hansmann, T. Wilhelmi, H. Bohn, D. "An Experimental Investigation of the Film-Cooling Process at High Temperatures and Velocities," *AIAA Paper 93-5062*, November 1993.

[25] Jones, T., V., "Theory for the Use of Foreign Gas in Simulating Film Cooling," *International Journal of Heat and Fluid Flow*, Vol. 20, 1999, pp. 349–354.

[26] Juhasz, A. Marek, C. "Combustor Liner Film Cooling in the Presence of High Free Stream Turbulence," NASA TN D-6360. July 1971.

[27] Juhasz, A. Marek, C. "Turbulent Mixing Film Cooling Correlation" NASA Tech Brief B72-10326. December 1972.

[28] Ko, S. Liu, D.,"Experimental Investigations on Effectiveness, Heat Transfer Coefficient, and Turbulence of Film Cooling," *AIAA Journal*, Vol. 18, No. 8, 1980, pp. 907–913.

[29] Lebedev, V. Lemanov, V. Misyura, S. Terekhov, V. "Effects from Turbulence Intensity on Slot Protection Performance," *Journal of Applied Mechanics and Technical Physics*. Vol. 32, 1991, pp. 360–364.

[30] Lebedev, V. Lemanov, V. Misyura, S. Terekhov, V. "Effects of flow turbulence on film cooling efficiency" *Int. J. Heat Mass Transfer.* Vol. 38, No. 11. Pp. 2117-2125. 1995.

[31] 14Cruz, C., Marshall, A. "Surface and Gas Phase Temperature Near a Film Cooled Wall", AIAA-2004-3654, 2004.

[32] Kacker , S. Whitelaw, J. "Prediction of Wall-Jet and Wall-Wake Flows" *Journal of Mechanical Engineering Science*. Vol. 12. No. 6. Pp. 404-420. 1970.

[33] Stoll, J. and Staub, J., "Film Cooling and Heat Transfer in Nozzles", *Journal of Turbomachinery*, Vol. 110, 1988, pp. 57-64.

[34]Zhou, J. M., Salcudean, M. and Gartshore, I. S. "A Numerical Computation of Film Cooling Effectiveness", *Near-Wall Turbulent Flows*, Elsevier Science Publishers, 1993, pp. 377-386.

[35] Jansson, L. S., Davidson, L. and Olsson, E., "Calculation of Steady and Unsteady Flows in a Film-Cooling Arrangement Using a Two-Layer Algebraic Stress Model", *Numerical Heat Transfer*, Part A., vol. 25, 1994, pp. 237-258.

[36] Lakehal, D., "Near-Wall Modeling of Turbulent Convective Heat Transport in Film Cooling of Turbine Blades with the Aid of Direct Numerical Simulation Data", *ASME Journal of Turbomachinery*, Vol. 124, 2002. pp. 485-498.

[37] Sinha, A. K., Bogard, D. G., and Crawford, M. E., "Film Cooling Effectiveness Downstream of a Single Row of Holes with Variable Density Ratio" *ASME Journal of Turbomachinery*. Vol. 113. 1991. pp. 442-449.

[38] Zhang, H., Tao, W., He, Y. and Zhang, W., "Numerical Study of Liquid Film Cooling in a Rocket Combustion Chamber", *International Journal of Heat and Mass Transfer*, Vol. 49, 2006, pp. 349-358.

[39] Dellimore, K., Marshall, A. Trouvé, A. and Cadou, C. "Numerical Simulation of Subsonic Slot-Jet Film Cooling of an Adiabatic Wall" *Proceedings of 47th AIAA Aerospace Sciences Meeting Including The New Horizons Forum and Aerospace Exposition*, January 5-8, 2009, Orlando, Fl. AIAA 2009-1577.

[40] Dellimore, K. Modeling and Simulation of Mixing Layer Flows for Rocket Engine Film Cooling, PhD Dissertation, University of Maryland at College Park, May 2010.

[41] Voegele, A. Numerical Characterization and Modeling of Adiabatic Slot Film Cooling. M.S. Thesis, University of Maryland at College Park, August 2011.

[42] Voegele, A. Raffan, F. Cadou, C. Trouvé, A. Marshall, A. "RANS Adiabatic Slot Film Cooling Modeling Practices" submitted 11/2012 to *Journal of Propulsion and Power*.

[43] Guo, X. Schroder, W. Meinke, M. "Large-eddy Simulations of Film Cooling Flows," *Computers and Fluids*, Vol. 35, 2006, No. 6, pp. 587–606.

[44] Tyagi, M. and Acharya, S., "Large Eddy Simulation of Film Cooling Flow from an Incline Cylindrical Jet" *ASME Journal of Turbomachinery*, Vol. 125, 2003, pp. 734-742.

[45] Muldoon, F. and Acharya, S., "Analysis of k-ε Budgets for Film Cooling Using Direct Numerical Simulation" *AIAA Journal*, Vol. 44, No. 12, Dec. 2006. pp. 3010-3021.

[46] Konopka, M. Meinke, M. Schroder, W. "Large-Eddy Simulation of Supersonic Film Cooling" Presented at the 46th AIAA/ASME/SAE/ASEE Joint Prouplsion Conference & Exhibit. 25-28 July, 2010. Nashville, TN. AIAA Paper 2010-6792.

[47] Juhany, K. Hunt, M. Sivo, J. "Influence of Injectant Mach Number and Temperature on Supersonic Film Cooling" *Journal of Thermophysics and Heat Transfer*, Vol. 8, No. 1, 1994, pp. 59-67.

[48] Konopka, M. Meinke, M. Schroder, W. "Large-Eddy Simulation of Supersonic Film Cooling at Laminar and Turbulent Injection" Presented at the 17th AIAA International Space Planes and Hypersonic Systems and Technologies Conference. 11-14 April 20122, San Francisco, California. AIAA Paper 2011-2250.

[49] Li, N. Balaras, E. Piomelli, U. "Inflow conditions for large-eddy simulations of mixing layers," *Phys. Fluids 12*, 2000.

[50] Piomelli, U. Balaras, E. Pascarelli, A. "Turbulent structures in accelerating boundary layers," *Journal of Turbulence 1*. 2000.

[51] El-Askary, W. Schroder, W. Meinke, M. "LES of compressible wall-bounded ows," 16th AIAA Computational Fluid Dynamics Conference, Orlando, FL, 2003, AIAA Paper 2003-3554.

[52] Lund, T. S., Wu, X., and Squires, K. D., "Generation of inflow data for the spatially-developing boundary layer simulations", *Journal of Computational Physics*, Vol. 140, Issue 2, pp. 233-258, 1998.

[53] Keating, A. Piomelli, U. Balaras, E. Kaltenbach, H. "*A priori* and *a posteriori* tests of inflow conditions for large-eddy simulation" *Physics of Fluids*. Vol. 16, No. 12. Dec. 2004.

[54] Piomelli, U. Balaras, E. "Wall-Layer Models For Large-Eddy Simulations" *Annual Review of Fluid Mechanics*. 2002. Vol. 34. Pp. 349-374. 2002.

[55] Balaras, E. Benocci, C. "Subgrid-scale models in finite-difference simulations of complex wall bounded flows" *AGARD CP 551*. Pp. 2.1-2.5. Neuilly-sur-Seine, France: AGARD. 1994.

[56] Spalart, P. Jou, W. Strelets, M. Allmaras, S. "Comments on the feasibility of LES for wing and on a hybrid RANS/LES approach" *Advances in DNS/LES*. Pp. 137-148. 1997.

[57] Martini, P. Schulz, A. Bauer, H. Whitney, C. "Detached Eddy Simulation of Film Cooling Performance on the Trailing Edge Cutback of Gas Turbine Airfoils," *Transactions of*

ASME Journal of Turbomachinery, Vol. 128, 2006, pp. 292–299.

[58] Roy, S. Kapadia, S. Heidmann J. "Film Cooling Analysis Using DES Turbulence Model," ASME Turbo Expo, Paper GT 2003-38140, June 2003.

[59] Kapadia, S. Roy, S. Heidmann J. D. "First Hybrid Turbulence Modeling for Turbine Blade Cooling," *Journal of Thermophysics and Heat Transfer*, Vol. 18, No. 4, 2004, pp. 154–156.

[60] Raffan, F. Film Cooling. PhD Dissertation, University of Maryland at College Park, December 2013.

[61] Adrian, R. "Particle-imaging techniques for experimental fluid mechanics", *Annual Review of Fluid Mechanics*. Vol. 23. 1991. pp. 261-304.

[62] Bernard, P. Wallace, J. Turbulent Flow: Analysis, Measurement and Prediction. John Wiley & Sons. Hoboken, New Jersey, 2002.

[63] Schlichting, H. Gersten, K. Boundary Layer Theory. Springer. 8th Edition. 2003.

[64] Samimy, M. Lele, S. "Motion of particles with inertia in a compressible free-shear layer" *Physics of Fluids A*, Vol. 3, 1991. pp. 1915-1923.

[65] FlowMaster Software Product Manual for Davis 7.2, LaVision Gmbh, printed in Gottingen, Germany. December 2006.

[66] Keane, R. Adrian, A. "Theory of cross-correlation analysis of PIV images" *Applied Scientific Research*. Vol 49. 1992. pp. 191-215.

[67] Blevins, L. Pitts, W. "Modeling of Bare and Aspirated Thermocouples in Compartment Fires" NISTIR 6310 Report. NIST. United States Department of Commerce Technology Adminstration. 1999.

[68] Pitts, W. Braun, E. Peacock, R. Mitler, H. Johnsson, E. Reneke, P. Blevins, L. "Temperature Uncertainties for Bare-Bead and Aspirated Thermocouple Measurments in Fire Environments" *Thermal Measurements: The Foundation of Fire Standards*, ASTM STP 1427.

[69] Shaddix, C. "Practical Aspects of Correcting Thermocouple Measurements for Radiation Loss" *Western State Section/The Combustion Institute*. WSS/CI 98F-14. 1998.

[70] Marshall, A. Effects of Jet Momentum Distribution on Combustion Characteristics in Co-Swirling Flames. PhD Dissertation. University of Maryland, 1996.

[71] Ghoddoussi, R. An Investigation on Thermal Characteristics of Premixed Counterflow Flames using Microthermocouples. M.S. Thesis. University of Maryland, 2005.

[72] Brewster, M. Thermal Radiative Transfer & Properties. John Wiley & Sons, Inc. New York, NY. 1992.

[73] Modest, M. Radiative Heat Transfer. McGraw-Hill, New York, NY. 1993. pp. 200-217.

[74] Keating, A. Large-Eddy Simulation of Heat Transfer in Turbulent Channel Flow and in the Turbulent Flow Downstream of a Backward-Facing Step. PhD Dissertation. The University of Queensland. 2004.

[75] Germano, M. Piomelli, U. Moin, P. Cabot, W. "A dynamic subgrid-scale eddy viscosity model", *Phys. Fluids A*. Vol 5. pp. 1282-1284. 1991.

[76] Meneveau, C. Lund, T. Cabot, W. "A Lagrangian dynamic subgrid-scale model of turbulence" *Journal of Fluid Mechanics*. Vol. 319. pp. 353-385. 1996.

[77] Moin, P. Squires, K. Cabot, W. Lee, S. "A dynamic subgrid-scale model for compressible turbulence and scalar transport", *Phys. Fluids A*, Vol. 3. pp. 2745-2757.

[78] Pierce, C. Progress-Variable Approach for Large-Eddy Simulation of Turbulent Combustion. PhD Dissertation. Stanford University. 2001.

[79] Harlow, F. Welch, J. "Numerical Calculation of Time-Dependent Viscous Incompressible Flow of Fluid with Free Surface", *Phys. Fluids.* Vol. 8 pp. 2182-2189. 1965.

[80] Kim, J. Moin, P. "Application of a Fractional-Step Method to Incompressible Navier-Stokes Equations" *Journal of Computational Physics*. Vol. 59, pp. 308-323. 1985.

[81] Leonard, B. "A Stable and Accurate Convective Modelling Procedure Based on Quadratic Upstream Interpolation", *Computer Methods in Applied Mechanics and Engineering*. Vol. 19. pp. 59-98. 1979.

[82] Herrmann, M. Blanquart, G. Raman, V. " Flux Corrected Finite Volume Scheme for Preserving Scalar Boundedness in Reacting Large-Eddy Simulations", *AIAA Journal*. Vol. 44, No. 12. pp. 2879-2886. December 2006.

[83] Chapman, D. "Computational aerodynamics, development and outlook", *AIAA Journal*. Vol. 17. pp. 1293-1313. 1979.

[84] Kline, S. Robinson, S. "Quasi-coherent structures in the turbulent boundary layer: part I. Status report on a community-wide summary of the data", *Near-wall Turbulence,* 1990. pp. 200-207.

[85] Robinson, S. "Coherent motions in the turbulent boundary layer" *Annual Review of Fluid Mechanics*. Vol. 23. pp. 601-639.

[86] Bravo, L. Large Eddy Simulation of Boundary Layer Combustion. PhD Dissertation. University of Maryland, 2013.

[87] Moser, R. Kim, J. Mansour, N. "Direct numerical simulation of turbulent channel flow up to Re_τ=590", *Physics of Fluids*. Vol. 11, No. 4. April 1999.

[88] Nicoud, F. "Numerical study of a channel flow with variable properties", *Center for Turbulence Research Annual Research Briefs*, 1998.

[89] Batten, P. Goldberg, U. Chakravarthy, S. "Interfacing Statistical Turbulence Closures with Large-Eddy Simulation" *AIAA Journal*. Vol. 42. No. 3, March 2004. pp. 485-492.

[90] Pope, S. Turbulent Flows. Cambridge University Press, New York. 2000.

[91] Gharib, M. and Williams, K. "Study of the Origin of Three Dimensional Structures in Shear Flows through External Forcing" AFOSR Report 90-0483. 1989.

[92] George, W. "Lectures in Turbulence for the 21st Century" Chalmers University of Technology. Gothenburg, Sweden.